Hyaluronan turnover in hyaluronidase 3- and β-hexosaminidase-deficient mice

By

Vasantha Arja

A Thesis Submitted to the Faculty of Graduate Studies

in Partial Fulfillment of the Requirements for the Degree of

Doctor of Philosophy

Department of Biochemistry and Medical Genetics

Faculty of Medicine, University of Manitoba

Winnipeg, Manitoba, Canada

Thesis abstract

Hyaluronan (HA) is a glycosaminoglycan that is abundant in the extracellular matrix of vertebrate cells. Under physiological conditions HA exists in a high-molecular-weight form, whereas HA fragments accumulate at sites of tissue injury and inflammation. Hyaluronidases are a group of enzymes that initiate the breakdown of HA. In humans, six hyaluronidase-like sequences have been identified in two locations, 3p21.3 (*HYAL1, HYAL2* and *HYAL3*) and 7q31.3 (*HYAL4, SPAM1* and *HYALP1*). Deficiency of one of these enzymes, HYAL1, was identified in a patient with Mucopolysaccharidosis IX, a disorder characterized by peri-articular soft masses containing HA-filled lysosomes. Given the broad distribution of HA and the mild phenotype of the patient, it is likely that other hyaluronidases or possibly the exoglycosidases, β-hexosaminidase and β-glucuronidase, are playing a major role in HA degradation. To address the potential role of HYAL3 in HA degradation in health and disease, a *Hyal3*-deficient mouse model was generated.

Hyal3-deficient mice were viable, fertile and appeared to have no gross phenotype. The only difference observed was a subtle change in the cellularity and tissue structure of lungs from aged *Hyal3*-deficient mice. Further studies focused on analysis of HA homeostasis revealed a significant increase in HA in the airways of *Hyal3*-deficient lungs. Altered HA homeostasis is observed in rodent models of several lung conditions. In order to further study the role of Hyal3 in lungs, an ovalbumin-challenged inflammation model was generated in *Hyal3*-deficient mice. A significant increase in lung HA levels and altered distribution of HA in the airways of lungs was detected in ovalbumin-challenged *Hyal3*-deficient mice. Moreover, lung inflammation and airway resistance were increased

in *Hyal3*-deficient mice after ovalbumin-challenge compared to similarly treated *Hyal3*-control mice. This suggests HA homeostasis that is altered during *Hyal3*-deficiency might be directly or indirectly promoting inflammation and airway resistance. Because the reported level of HA accumulation was very low in *Hyal1*-deficient and *Hyal2*-deficient mice, and in our studies of *Hyal3*-deficient mice, we performed preliminary studies to assess a role for an exoglycosidase, β-hexosaminidase, in HA turnover. Our preliminary studies indicate there is no or little HA accumulation in β-hexosaminidase-deficient mouse tissues. To conclude, our study of *Hyal3*- and β-hexosaminidase-deficient mice suggests that these are not the major enzymes involved in HA degradation.

Acknowledgements

I am highly indebted to my supervisor Dr. Barb Triggs-Raine for taking me as her student and supporting me at each and every step of my Ph.D. program. I sincerely thank my advisory committee, Dr. Judy Anderson, Dr. Klaus Wrogemann, Dr. David Merz, Dr. Ganesh Srinivasan for their valuable comments and guidance all through out my Ph.D. program. I am highly thankful to my Ph.D. external examiner Dr. Carol de la Motte for reviewing my thesis and giving valuable suggestions.

I am grateful to my collaborators, Dr. Ganesh Srinivasan, Ms. Sujata Basu, Dr. Andrew Halayko, Dr. Shyamala Dakshinamurti, Dr. Alex Gutsol, Dr. Andras Nagy, Ms. Marina Gertsenstein, Dr. James Thliveris, Dr. Jude Uzonna, Dr. Dong Liu, Dr. John Gordon, Ms. Xiaobei Zhang, Dr. Sharon Byers Dr. John Mort, Dr. Solmaz Sahebjam, Dr. Volkan Seyrantepe, Dr. Alex Pshezhetsky and Dr. Euridice Carmona for their help in various experiments.

I am thankful to all my past and present co-workers, Dr. Dianna Martin, Timothy Salo, Dr. Richard Hemming, Nehal Patel, Joy Armstead, Ted Nylen, Shangbou Liu, Sunita Khatker, Lara Gushulak and Biswajit Chowdhury for their whole hearted cooperation and support throughout my Ph.D. program. I am also thankful to Ms. Xiaoli Wu for her advices during my experiments. My sincere thanks to all our departmental office staff Ms. Tuntun Sarkar, Ms. Lil Cameron, Ms. Jan Middleton and Mr. Gerhard Dyck for their constant support.

My deep sense of gratitude goes to my parents, my husband, sister, brother, uncle, aunt, cousins and my friends who have constantly encouraged and motivated me to successfully complete my studies.

I am also thankful to the Canadian Institutes of Health Research (CIHR), the CIHR Strategic Training Program, the Canadian Genetic Diseases Network, and University of Manitoba Graduate Studies for their financial support.

Dedicated to

My mother and father
For everything they have done for me

My husband
For his sacrifice and excellent care

My sister and brother
For their unconditional love and affection

My uncle's family
For their tremendous support

Table of contents

Preface:

List of tables

List of figures

List of abbreviations

©	Copyright
°C	Degree Celsius
Δ	Delta
µg	Microgram
µM	Micrometer
$Al(OH)_3$	Aluminum hydroxide
AMAC	2-aminoacridine
ANOVA	Analysis of variance
APS	Ammonium persulfate
BAL	Broncho-alveolar lavage
bp	Base pair
$CaCl_2$	Calcium Chloride
CD44	Cluster of differentiation 44
CIAP	Calf intestinal alkaline phosphatase
CPC	Cetyl pyridinium chloride
CS	Chondroitin sulfate
C_T	Threshold cycle number
DMSO	Dimethylsulfoxide
DNA	Deoxy-ribonucleic acid
dNTP	2'-deoxyribonucleotide 5' triphosphate
DS	Dermatan sulfate
DTT	Dithiothreitol
EDTA	Ethylenediamine tetraacetic acid
ELISA	Enzyme linked immuno sorbent assay
ES	Embryonic stem
FACE	Fluorophore assisted carbohydrate electrophoresis
FBS	Fetal bovine serum
g	Relative centrifugal force
GAGs	Glycosaminoglycans
GalNac	N-acetyl D-galactosamine
GluA	D-Glucuronic acid
Gluc	Glucuronidase
GlcNac	N-acetyl D-glucosamine
gm	Gram
GPI	Glycosyl-phosphatidyl inositol
H&E	Hematoxylin and Eosin
HA	Hyaluronan
HMW	High-molecular-weight
LMW	Low-molecular-weight
ECM	Extracellular matrix
HAS	Hyaluronan Synthase
HAS1	Hyaluronan Synthase-1
HAS2	Hyaluronan Synthase-2
HAS3	Hyaluronan Synthase-3

HARE	Hyaluronan receptor for endocytosis
Hex	Hexosaminidase
Hexa	Hexosaminidase a
Hexb	Hexosaminidase b
hr	Hour
HR	Homologous recombinant
HRP	Horseradish peroxidase
HS	Heparan sulfate
Hyal	Hyaluronidase
HYAL1/Hyal1	Hyaluronidase 1
HYAL2	Hyaluronidase 2
HYAL3	Hyaluronidase 3
HYAL4	Hyaluronidase 4
Hyal5	Hyaluronidase 5
IdoA	Iduronic acid
Ig	Immunoglobulin
IgG	Immunoglobulin G
IgE	Immunoglobulin E
IFN-γ	Interferon-gamma
IL	Interleukin
Kb	Kilo base
KCl	Potassium chloride
KS	Keratan sulfate
LB	Luria broth
LIF	Leukemia inhibitory factor
LYVE-1	Lymphatic vessel endothelial receptor-1
mA	Milliampere
MEFs	Mouse embryonic fibroblasts
mg	Milligram
$MgCl_2$	Magnesium chloride
ml	Milliliter
MPS	Mucopolysaccharidosis
MW	Molecular weight
NaCl	Sodium chloride
Neo	Neomycin resistance cassette
ng	Nanogram
nm	Nanometer
OD	Optical density
OVA	Ovalbumin
PAC	P1 artificial chromosome
PAGE	Polyacrylamide gel electrophoresis
PAS	Periodic acid-Schiff
PBS	Phosphate buffered saline
PCR	Polymerase chain reaction
PEEP	Positive end-expiratory pressure
PGK	Phosphoglycerate kinase
PSR	Picro-sirius red

RHAMM	Receptor for hyaluronan-mediated motility
Rn	Airway resistance
RNA	Ribonucleic acid
RT	Reverse transcription
SDS	Sodium dodecyl sulfate
SOC	Super optimal catabolite repressor medium
SSC	Saline sodium citrate
Spam1	Sperm Adhesion Molecule 1
TAE	Tris acetate EDTA
TBE	Tris borate EDTA
TBS	Tris-buffered saline
TBST	Tris-buffered saline Tween-20
TE	Tris EDTA
TEMED	Tetramethylethylenediamine
Th1	T helper-1
Th2	T helper-2
TK	Thymidine kinase
UV	Ultra violet
VILI	ventilator-induced lung injury

Chapter one: Introduction

1.1 Glycosaminoglycans and proteoglycans

Glycosaminoglycans (GAGs) are polysaccharides that consist of repeating disaccharide units of hexosamine (N-acetyl glucosamine or N-acetyl galactosamine) and uronic acid (glucuronic or iduronic acid). The monomeric units in these polymers are often modified by sulfation. GAGs are known to exist in the connective tissues of all vertebrates and also in some invertebrates. In vertebrates, GAGs are mainly found in the extracellular matrix (ECM) of cells. There are several GAGs known, including chondroitin sulfate (CS), heparin, heparan sulfate (HS), keratan sulfate (KS), dermatan sulfate (DS) and hyaluronan (HA). Among these GAGs, KS has a unique structure; it contains a galactose instead of an amino sugar. HA differs from the other GAGs in several ways, which are discussed in detail in section *1.4*. The list of GAGs, their disaccharide composition, known modifications and the location of synthesis are given in Table 1.

Most GAGs, with the exception of HA, are synthesized in the endoplasmic reticulum and golgi apparatus of the cell as proteoglycans associated with a protein core. In the golgi apparatus, GAGs are attached as tetrasaccharide structures to the serine residues of the protein core, followed by the addition of sugar units one at a time by specific glycosyltransferases. The modifications of GAGs, such as sulfation and glucuronic acid epimerization to iduronic acid, also occur while the GAGs are still in the golgi apparatus (Varki et al., 1999).

Proteoglycans are classified based on the GAGs that are attached to the protein core. These include CS/DS, heparin/HS and KS proteoglycans. CS/DS proteoglycans include aggrecan, versican, neurocan and brevican. HS proteoglycans include syndecans and betaglycan, and fibromodulin is a KS proteoglycan. After the protein core is

degraded, GAGs are degraded by multiple lysosomal endoglycosidases, exoglycosidases and sulfatases (Varki et al., 1999).

Table 1: Disaccharide composition, modification and synthesis of GAGs

GAG	Disaccharide Components	Sulfation Position	Synthesis Location
Chondroitin/ CS	GalNac GlcA	No Sulfation GalNac-4S GalNac-6S GalNac-4 & 6S	Endoplasmic reticulum & Golgi
DS	GalNac IdoA/GlcA	GalNac-4S GalNac-6S IdoA-2S	Endoplasmic reticulum & Golgi
Heparin/HS	GlcNac IdoA/GlcA	No Sulfation IdoA-2S GlcA-2S	Endoplasmic reticulum & Golgi
KS	GlcNac Gal	GlcNac-6S Gal-6S	Endoplasmic reticulum & Golgi
HA	GlcNac GlcA	No Sulfation	Cell membrane

GlcNac: N-Acetyl glucosamine, GalNac: N-Acetyl galactosamine, Gal: Galactose, GlcA: Glucuronic acid, IdoA: Iduronic acid

1.2 Mucopolysaccharidoses

Mucopolysaccharidoses (MPS) are lysosomal storage disorders characterized by the accumulation of undegraded GAGs, formerly called mucopolysaccharides, in the lysosome (Sheth et al., 2004; Neufeld and Muenzer, 2001). MPS disorders are caused by a defect in a lysosomal enzyme that degrades GAGs. Depending on the type of enzyme that is deficient, one or several of the undegraded GAGs accumulate in the tissues and are excreted in the urine of MPS patients (Wraith, 2002; Haskins et al., 2007).

The MPS disorders are classified by the enzyme deficiency. Initial classification is reviewed after the mutations involved in these disorders have been characterized, and as a consequence, MPS V and MPS VIII are no longer used to classify disorders. Except the MPS II (Robert et al., 1989), all the disorders are autosomal recessive. The name of each disease, the defective enzyme, the clinical symptoms, and the accumulated GAGs associated with the disease are listed in Table 2.

Table 2: Clinical features and defective enzymes in mucopolysaccharidoses

Disease	Defective Enzyme	Clinical Features	Accumulating GAGs
MPS I (Hurler, Hurler-Scheie, & Scheie syndromes)	α-L-iduronidase	Mental retardation, corneal clouding, glaucoma, dystosis multiplex, odontoid hypoplasia organomegaly cardiomyopathy, respiratory problems, joint stiffness.	DS, HS
MPS II (Hunter syndrome)	Iduronate-2-sulfatase	Mental retardation, symptoms similar to Hunter syndrome but milder	DS, HS

MPS III (Sanfilippo syndrome)	Heparan sulfamidase (A) or α-N- acetyl glucosaminidase (B) or Acetyl CoA: α-glucosamine N-acetyl transferase (C) or N-acetyl glucosamine-6-sulfatase (D).	Motor dysfunction, severe hyperactivity, behavioral problems	HS
MPS IV (Morquio syndrome)	N-acetyl galactos-amine-6-sulfata sulfatase (A) or β-D-galactosidase (B)	Motor dysfunction, skeletal dysplasia odontoid hypoplasia, spondylo-epiphyseal dysplasia, short stature corneal clouding	KS
MPS VI (Maroteaux-Lamy syndrome)	N-acetyl galactosamine-4-sulfatase	Short stature organomegaly, dystosis multiplex, joint stiffness, heart disease, facial dysmorphism, kyphosis, corneal clouding, sometimes mental retardation	DS, CS
MPS VII (Sly syndrome)	β-Glucuronidase	Short stature, skeletal anomalies, facial dysmorphism, organomegaly corneal clouding, developmental delay	DS, HS, CS
MPS IX (Natowicz disease)	Hyaluronidase-1	Short stature, peri-articular soft masses skeletal abnormalities, mild facial dysmorphism	HA

(Modified from Varki et al., 1999) (Russell et al., 1998; Clarke et al., 1997; Garcia et al., 2007; Li et al., 1999; Klein et al., 1978; Mikles and Stanton, 1997; Neufeld and Muenzer, 2001; Tomatsu et al., 2003; Sly et al., 1974; Volger et al., 1990; Natowicz et al., 1996; Triggs-Raine et al., 1999).

1.3 Hyaluronan (HA)

1.3.1 Structure

HA is a member of the GAG family. It is unique among GAGs as it is an unbranched molecule without any sulfate groups. Moreover, unlike other GAGs, HA is not covalently linked to a protein core. The size of HA can reach up to 4 megadaltons which consists of approximately 10,000 disaccharide units (Hascall and Laurent, 1997).

HA was first discovered in the vitreous of the eye by Meyer and Palmer (Meyer and Palmer, 1934). Approximately twenty years after that discovery, the chemical structure of HA was defined. It is composed of repeating disaccharide units of D-glucuronic acid and N-acetyl-D-glucosamine (Figure 1) (Rapport et al., 1951; Weissmann et al., 1954). The presence of uronic acid led this molecule to be named hyaluronic acid. However, now it is termed hyaluronan as *in vivo* it occurs as a polyanion rather than the protonated acid form (Laurent and Fraser, 1992a).

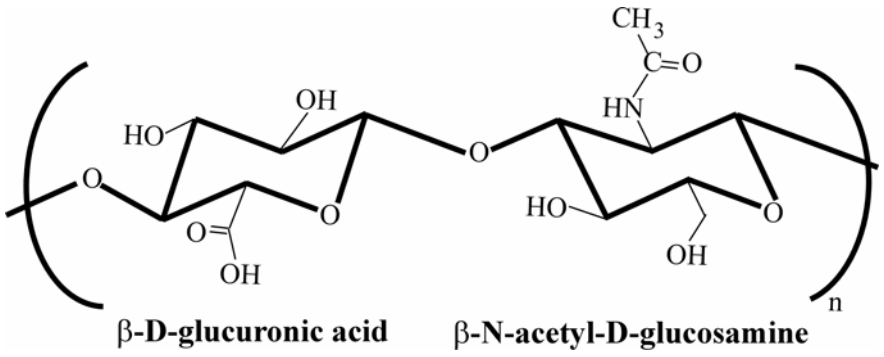

Figure 1: Disaccharide structure of HA
A schematic representation of the repeating disaccharide unit of HA polymer is shown.

1.3.2 Distribution

HA is a ubiquitous molecule distributed throughout the ECM of all vertebrate cells. The highest concentrations of HA are in the loose connective tissues such as the

umbilical cord (4100 μg/g), synovial fluid (1400-3600μg/g), vitreous humor (140-338 μg/g) and dermis (200 μg/g), and lowest in the blood serum (0.01-0.1 μg/g) (Fraser et al., 1997). Quantitative studies in rats (Reed et al., 1989) have shown that about 56% of the total HA injected intravenously is present in skin, 27% in skeleton and joints, and the remainder in muscle and viscera (Fraser et al., 1997).

The existence of a hyaluronidase-sensitive pericellular coat of HA was detected in the synovial cell culture system using an erythrocyte exclusion test (Clarris and Fraser., 1968). Moreover, HA has also been detected intracellularly (Eggli and Graber, 1995; Evanko and Wight, 1999b; Tammi et al., 2001). Inside the cell, HA was detected as diffuse staining in the cytoplasm, concentrated in the caveolae and endosomes, and also identified in the nucleus. Moreover, both intracellular HA, and a thick pericellular coat of HA were increased in dividing cells, suggesting a role for HA in mitosis (Evanko et al., 1999a; Evanko and Wight, 1999b; Evanko et al., 2004).

1.3.3 Synthesis

HA is synthesized by enzymes called HA synthases. HA synthases synthesize HA at the plasma membrane, extruding the newly synthesized HA into the extracellular space (Prehm, 1984). These enzymes are glycosyltransferases (DeAngelis, 1999) that catalyze the addition of uridine diphosphate (UDP)-linked N-acetylglucosamine and UDP-linked glucuronic acid to the growing chain of HA at the non-reducing end.

In mammals, three HA synthases, HAS1, HAS2 and HAS3 have been identified (Spicer et al., 1996; Spicer et al., 1997). These HA synthases share 55-71% similarity at amino acid level (rev. in Itano and Kimata, 2002; Itano, 1999) and are encoded by three related genes (*HAS1*, *HAS2* and *HAS3*) that are located on different chromosomes (rev. in

Volpi et al., 2009). These enzymes have unique distribution patterns (Tien and Spicer, 2005), catalytic properties, and reaction products (Itano et al., 1999).

HAS1 is least active and synthesizes high-molecular-weight (HMW) HA, where HA can reach up to 2 x 10^5 Da to 2 x 10^6 Da. *Has1*-deficient mice were generated and found to be viable and fertile (Camenisch et al., 2000).

HAS2 is more active than HAS1 and synthesizes HMW HA of 2 x 10^6 Da. In mice, *Has2*-deficiency has demonstrated that HA is important in embryonic development (Camenisch et al., 2000). Mice deficient in *Has2* die at embryonic day E9.5 due to a defect in cardiac cushion morphogenesis. These mice have a 96% reduction in HA content compared to wild-type animals. Using *Has2*-deficient mice, HA has been shown to have a role in matrix expansion and the initiation of cell migration during heart development (Camenisch et al., 2000; McDonald and Camenisch, 2002).

HAS3, which is the most active enzyme among the three synthases, synthesizes HA that varies in size from 0.2 x10^6 Da to 2 x 10^6 Da (Itano et al., 1999). *Has3*-deficient mice were also generated and characterized and were found to be viable and fertile (Camenisch et al, 2000). In addition, a role for *Has3* in the induction of the inflammatory response by *de novo* synthesis of low-molecular-weight (LMW) HA fragments was identified in a mouse model with ventilator-induced lung injury (Bai et al., 2005a).

HAS enzymes are regulated by cytokines and various growth factors. Studies using synovial fibroblasts have shown that expression of *HAS1* is increased by transforming growth factor (TGF)-β1, and *HAS3* by interleukin (IL)-1β and tumor necrosis factor (TNF)-α (Recklies et al., 2001). Moreover, *HAS1* and *HAS2* expression were increased by TGF-β in skin-derived cells of both the dermis and epidermis (Sugiyama et al., 1998).

1.3.4 Degradation

1.3.4.1 Hyaluronidases

Hyaluronidases were initially observed by Duran-Reynals as a "spreading factor" that facilitates the diffusion of subcutaneously injected vaccines, dyes and toxins (Hoffman and Duran-Reynals, 1930). These are the endoglycosidases that degrade the β-glycosidic linkage of disaccharide units of HA. In addition to HA, to a lesser extent these enzymes can also degrade other GAGs, CS and DS (Stern and Csoka, 2000).

The sequencing of the human genome has allowed six paralogous hyaluronidase-like sequences to be identified and localized as clusters on chromosomes 3p21.2 (*HYAL1, HYAL2* and *HYAL3*) and 7q31.3 (*HYAL4, SPAM1* and *HYALP1*) (Csoka et al., 1999). These two clusters have been described as candidate tumor suppressor regions (Kok et al., 1987; Pederson and Ellegaard, 1994). With the exception of *HYALP1*, which is a pseudogene in humans, the remaining five genes encode protein products.

Mouse orthologous genes were clustered on chromosomes 9 F1 (*Hyal1*, *Hyal2* and *Hyal3*) and 6 A2 (*Hyal4*, *Spam1* and *Hyalp1*) (Csoka et al., 2001). In addition to these five orthologous genes that encode proteins, in the mouse a functional *Hyalp1* and a seventh gene, *Hyal5* (Kim et al., 2005), have been identified in the chromosome 6 cluster downstream of *Spam1*. The gene cluster on chromosome 9 in mice (3 in humans) also contains an unrelated gene that encodes N-acetyl transferase, *Fus2* (Shuttleworth et al., 2002), which is embedded within *Hyal3* (Figure 2).

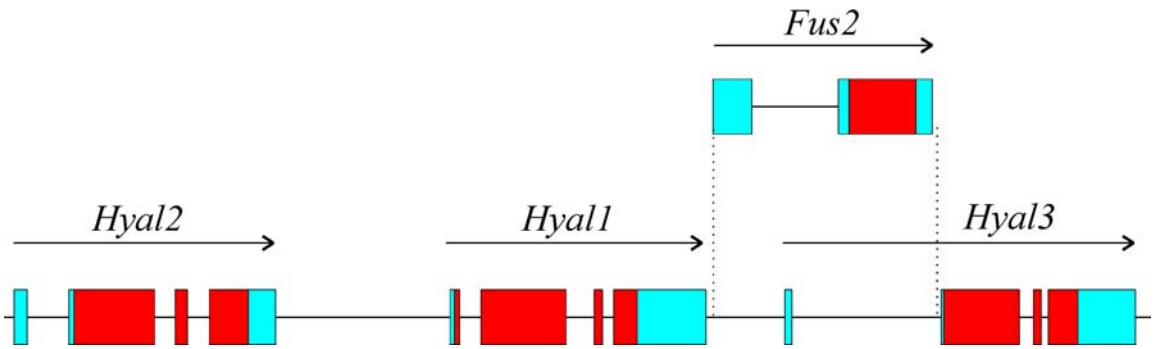

Figure 2: Organization of mouse hyaluronidases (*Hyal1*, *Hyal2* and *Hyal3*) and *Fus2*. Exons are displayed as boxes, introns and intergenic regions as lines. Red coloured boxes indicate the coding regions while blue coloured boxes indicate the untranslated regions of the genes. The direction of gene transcription is shown by arrows.

1.3.4.1.1 Hyaluronidase 1

Hyaluronidase 1 (HYAL1) is the best characterized of the somatic hyaluronidases. HYAL1 is an acid-active plasma hyaluronidase with a pH optimum of 3.8 and little activity above pH 4.5 (Frost et al., 1997). It is highly expressed in parenchymal tissues such as liver, kidney, spleen and heart. HYAL1 is a 57 kDa protein in plasma, but exists as both 57 kDa and 45 kDa forms in the urine (Csoka et al., 1999).

Mutations in the *HYAL1* gene were reported in a single patient with MPS IX (Triggs-Raine et al., 1999). The serum HA level was increased 38 to 90 fold compared to normal values, and the serum hyaluronidase activity was completely absent in this MPS IX patient. Histologically, lysosomal accumulation of HA was detected in the fibroblasts and macrophages of the patient. The clinical features of the MPS IX patient included soft masses near various joints, mild short stature, erosions of the hip joint, a flattened nasal bridge and submucosal cleft palate (Natowicz et al., 1996). The skeletal system is the primary system affected in this patient. However, compared to other MPS disorders described in *1.3*, the phenotype exhibited by the MPS IX patient is very mild. Expression

analysis of other potential hyaluronidases as compensating enzymes in the fibroblasts of the MPS IX patient showed a 2-fold increase in *HYAL2* and *HYAL3* mRNA levels (Martin D, thesis).

Recently, *Hyal1*-deficient mice have been characterized and were identified with osteoarthritis (Martin et al., 2008). *Hyal1*-deficient mice displayed increased peri-cellular and intracellular HA in the chondrocytes of articular and epiphyseal cartilages of knee joints. Proteoglycan loss, a characteristic feature of osteoarthritis, worsened with age in the *Hyal1*-deficient mice. However, the serum HA elevation that was demonstrated in the human patient was absent in the mouse model. The real-time expression studies of other potential HA degrading enzymes in these mice have indicated that *Hyal3* expression was increased by 5 fold. This suggested a role for Hyal3 as a compensating enzyme in Hyal1 deficiency (Martin et al., 2008).

1.3.4.1.2 Hyaluronidase 2

Hyaluronidase 2 (*HYAL2*) is a broadly expressed gene, with expression in all the major tissues except adult brain, where its expression is reduced after birth due to methylation of its promoter and 5'UTR regions (Lepperdinger et al., 1998, Patel et al., 2002). HYAL2 is a 60 kDa protein and was initially described as a lysosomal enzyme with a pH optimum of 3.8 (Lepperdinger et al., 1998). However, a glycosylphosphatidylinositol (GPI)-anchored form of HYAL2 was subsequently identified at the plasma membrane (Rai et al., 2001). This GPI-anchored form of HYAL2 is believed to create an acidic micro-environment at the cell surface by interacting with CD44 and a Na+/H+ exchanger (NHE1) (Bourguignon et al., 2004). Overall, the localization of HYAL2 is controversial, some studies identifying it at the cell surface (Rai

et al., 2001; Harada and Takahashi, 2007), others identifying it in the lysosomes (Lepperdinger et al., 1998) and some in both locations (Bourguignon et al., 2004; Chow et al., 2006; Monzon et al., 2008). The soluble form of HYAL2 was shown to have unique specificity towards HA, degrading HMW HA to 20 kDa HA fragments (Lepperdinger et al., 1998). These 20 kDa HA molecules, containing 50 disaccharide units, are associated with inflammation. Recently it was shown that platelet-derived HYAL2 was able to cleave HMW HA to generate HA fragments which further mediated cytokine production (de la Motte et al., 2009).

Mice deficient in *Hyal2* were characterized and shown to have skeletal and hematological defects (Jadin et al., 2008). These *Hyal2*-deficient mice had craniofacial dysmorphism with an altered fronto-nasal suture as well as intravascular hemolysis. Moreover, *Hyal2*-deficient mice have a 10-fold increase in plasma HA concentration and increased HA in the liver sinusoidal cells (Jadin et al., 2008).

1.3.4.1.3 Hyaluronidase 3

Very little is known about *HYAL3,* a broadly but weakly expressed gene with highest expression in testis and bone marrow (Csoka et al., 1999). The mouse orthologous gene has 80% identity to human HYAL3 at the amino acid level (Csoka et al., 2001). Mouse *Hyal3* also has broad expression, with highest expression among those tissues tested in liver and kidney (Shuttleworth et al., 2002).

HYAL3 mRNA levels were detected in epiphyseal cartilage (Bastow et al., 2008), in a human MG63 osteoblast cell line (Adams et al., 2006), in human bronchial epithelial cells of lungs from healthy donors (Monzon et al., 2008), and in endometrial carcinoma (Paiva et al., 2005). In a mouse model of ovarian atresia, *Hyal3* mRNA levels were

significantly increased in apoptotic granulosa cells and in atretic follicles (Orimoto et al., 2008). Increased HYAL3 protein expression has also been shown in the basal and ciliated cells of airway epithelium of asthmatics compared to the non-asthmatics (Monzon et al., 2008).

Studies using baby hamster kidney (BHK) cells overexpressing mouse *Hyal3* have shown that Hyal3 exists in multiple forms ranging in molecular weight from 45 to 56 kDa. Hyal3 has three N-linked oligosaccharides and is mostly localized in the vesicular compartments of the cell (Hemming et al., 2008). Moreover, in cell culture and in human tracheal tissue sections, HYAL3 protein was detected intracellularly in bronchial epithelial cells (Monzon et al., 2008); frequent co-localization of HYAL3 and HYAL1 was also detected in the same cells (Monzon et al., 2008).

The enzymatic activity of HYAL3 is controversial. One *in vitro* translation study indicated that HYAL3 had activity to HA (Lokeshwar et al., 2002), but activity has not been shown by any other group (Hemming et al., 2008; Harada and Takahashi, 2007). It might be that the methods employed in these studies were not sensitive enough to detect the activity of HYAL3. Increased Hyal1 activity in BHK cells overexpressing Hyal3 (Hemming et al., 2008) and increased Hyal3 expression in the fibroblasts of the HYAL1-deficient patient and the tissues of *Hyal1*-deficient mice (Martin et al., 2008) suggest that Hyal3 might be augmenting the function of Hyal1 inside the cell.

1.3.4.1.4 Hyaluronidase 4

The hyaluronidase 4 (*HYAL4*) gene encodes a 54 kDa protein with its expression limited to skeletal muscle and placenta (Csoka et al., 1999). Initially, *HYAL4* was

proposed as a chondroitinase (Csoka et al., 1999) and a very recent study has shown that it is a chondroitin sulfate hydrolase (Kaneiwa et al., 2009).

1.3.4.1.5 Hyaluronidase 5

Hyaluronidase 5 (*Hyal5*) is present in mice and rats but not in human. Hyal5 is a 55 kDa protein expressed only in the testis (Kim et al., 2005; Reitinger et al., 2007). It may be a GPI-anchored protein present in the plasma and acrosomal membranes of the sperm. HA zymography results have shown that Hyal5 is active at pH 5-7 and inactive at pH 3 and 4. Under acidic and neutral pH conditions, Hyal5 has been shown to degrade HA into small fragments (Reitinger et al., 2007). Recently, mice deficient in *Hyal5* were generated and were found to be viable and fully fertile with normal litter size (Kimura et al., 2009). Moreover, *in vitro* fertilization studies have shown that epididymal sperm from these knockout mice are functionally normal and *Hyal5* was suggested to be dispensable for fertilization (Kimura et al., 2009).

1.3.4.1.6 Hyaluronidase P1

Hyaluronidase P1 (*HYALP1*) is a broadly expressed gene at the mRNA level. However, in humans it is a pseudogene, as two premature stop codons stop the translation of this gene (Csoka et al., 1999). The mouse orthologue, *Hyalp1*, has no mutations and is expressed in testis (Miller et al., 2007) and other tissues such as liver, brain, fat, skeletal muscle, bone marrow and spleen (Reitinger et al., 2007). *Hyalp1* is predicted to be a GPI-anchored protein (Miller et al., 2007). However, the ability of *Hyalp1* to degrade HA is controversial (Reitinger et al., 2007; Miller et al., 2007)

1.3.4.1.7 Sperm adhesion molecule 1

Sperm adhesion molecule 1 (*SPAM 1*) is a non-somatic hyaluronidase expressed mainly in the testis (Jones et al., 1995). The encoded protein, PH-20, is a 64 kDa GPI-anchored protein (Thaler et al., 1995) with neutral pH activity that has been localized to the outer plasma membrane and the inner acrosome of the sperm (Myles and Primakoff, 1997). The GPI-anchored form of PH-20 has three key functions in fertilization. These include hyaluronidase activity to penetrate the HA-rich cumulus cells surrounding the oocyte (Cherr et al., 2001; Lin et al., 1994; Hunnicutt et al., 1996), receptor activity allowing binding of the zona pellucida (Myles and Primakoff, 1997) and acrosome exocytosis by inducing Ca^{2+} signaling (Cherr et al., 2001; Vandevoort et al., 1997).

An acid-active, processed form of PH-20 exists as a soluble 53 kDa protein. This protein is released after the acrosome reaction (Hunnicutt et al., 1996). Recently *SPAM1* expression was also identified in the female reproductive tract (Zhang and Martin-Deleon, 2003) and male accessory organs (Zhang et al., 2004). *SPAM1* expression in epididymis (Evans et al., 2003) has led to the prediction that it has a role in concentrating sperm fluid (Zhang et al., 2004).

A mouse deficient in PH-20 was viable and fertile. However, *in vitro* fertilization studies have shown that in the early stages after insemination, the sperm from these mice have reduced capacity to penetrate the cumulus cells of the oocyte, and thereby delay fertilization (Baba et al., 2002; Kimura et al., 2009).

1.3.4.2 Exoglycosidases

Exoglycosidases are the enzymes that remove terminal sugar units from GAGs. There are two exoglycosidases, β-hexosaminidase and β-glucuronidase, that are involved

in HA degradation (Roden et al., 1989).

1.3.4.2.1 β-Hexosaminidase

Lysosomal β-hexosaminidase is encoded by two genes, *HEXA* and *HEXB*. Each gene encodes a subunit of the enzyme, *HEXA* encodes the α-subunit and *HEXB* encodes the β-subunit. The β-hexosaminidase enzyme exists in three isoforms, β-hexosaminidase A (αβ), B (ββ) and S (αα). Mutations in *HEXA* result in deficiency of the α-subunit of β-hexosaminidase isoforms A and S, and therefore the residual activity is from β-hexosaminidase B (Suzuki et al., 1997). Mutations in *HEXB* result in deficiency of the β-subunit of β-hexosaminidase isoforms A and B, and therefore the residual activity is from β-hexosaminidase S (Suzuki et al., 1997).

In humans, mutations in *HEXA* and *HEXB* cause Tay-Sachs and Sandhoff diseases, respectively. *Hexa*$^{-/-}$ mice do not develop a phenotype but *Hexb*$^{-/-}$ mice develop symptoms similar to Sandhoff patients (Sango et al., 1995; Phaneuf et al., 1996). *Hexa*$^{-/-}$ mice accumulated gangliosides in the brain but these mice did not have a neurological phenotype (Sango et al., 1995; Phaneuf et al., 1996). However, *Hexb*$^{-/-}$ mice accumulated gangliosides and GA2 glycolipids in the brain, and these mice exhibited neurological disease, including muscle weakness, rigidity, spasticity, tremor and ataxia (Sango et al., 1995; Phaneuf et al., 1996).

Mice deficient in both subunits of β-hexosaminidase due to mutations in *Hexa* and *Hexb* genes (i.e, *Hexa*$^{-/-}$*Hexb*$^{-/-}$), had a total loss of β-hexosaminidase activity. In addition to the neurological storage disorder caused by accumulating gangliosides, the *Hexa*$^{-/-}$ *Hexb*$^{-/-}$ mice displayed an MPS-like phenotype because of accumulating GAGs in various cells and tissues (Sango et al., 1996; Suzuki et al., 1997). However, *Hexa*$^{-/-}$ *or Hexb*$^{-/-}$ mice

lack an MPS-like phenotype presumably due to the redundancy of the isoforms of β-hexosaminidases.

In *Hexa*$^{-/-}$*Hexb*$^{-/-}$ mice, vacuolated cells were identified throughout the central nervous system, sinusoidal lining cells in the spleen, and epithelial cells in the proximal renal tubules of kidney and in liver compared to *Hexa*$^{-/-}$ or *Hexb*$^{-/-}$ or wild-type control mouse tissues (Sango et al., 1996; Suzuki et al., 1997). Moreover, chondrocytes of the rib cartilage and trachea were enlarged and appeared vacuolated compared to control mouse tissues (Sango et al., 1996; Suzuki et al., 1997). In *Hexa*$^{-/-}$*Hexb*$^{-/-}$ mice, the presence of vacuoles that stain positive for alcian blue and/ or colloidal iron in various tissues confirmed the accumulation of GAGs (Sango et al., 1996; Suzuki et al., 1997). However, the GAGs accumulated in the tissues of these double knockout mice were not characterized. Only the GAGs excreted in urine have been analyzed. The fluorophore assisted carbohydrate electrophoresis (FACE) analysis on urine samples collected from *Hexa*$^{-/-}$*Hexb*$^{-/-}$ mice demonstrated the accumulated GAG as DS (Sango et al., 1996; Hepbildikler et al., 2002). The role of β-hexosaminidase in GAG degradation can be further studied using *Hexa*$^{-/-}$*Hexb*$^{-/-}$ mouse model.

1.3.4.2.2 β-Glucuronidase

β-Glucuronidase is an exoglycosidase that is encoded by the GUSB gene and the deficiency of this enzyme causes MPS VII (Sly disease) as described in *1.3*.

Both β-hexosaminidase and β-glucuronidase are believed to be involved in HA catabolism by degrading HA oligosaccharides to simple sugar units. However, studies to determine the *in vivo* contribution of these enzymes to HA degradation and overall HA

turnover are lacking. The only evidence that these enzymes participate in HA degradation is suggested by their *in vitro* activity toward HA (Longas et al., 1981).

1.3.4.3 Proposed model of HA degradation

The identification of multiple hyaluronidases has led to propose a model for HA degradation. In this proposed model (Csoka et al., 2001), HMW HA present at the cell surface is taken up by a cell surface receptor, CD44 (Culty et al., 1992), and is subsequently degraded by hyaluronidases and exoglycosidases. HYAL2 and CD44 are enriched in lipid rafts where they are believed to interact with NHE1 to create an acidic micro-environment when stimulated by HA binding (Bourguignon et al., 2004). When stimulated, HYAL2 initiates the cleavage of HMW HA to generate HA fragments of 20 kDa. These fragments are transported to endosomes and then to lysosomes where they are degraded by HYAL1 into HA oligosaccharide units. HA oligosaccharides are further degraded to simple sugars, β-D-glucuronic acid and β-N-acetyl glucosamine by the sequential action of two lysosomal exoglycosidases, β-hexosaminidase and β-glucuronidase (Csoka et al., 2001; rev. in Stern et el., 2003; Stern et al., 2004) (Figure 3).

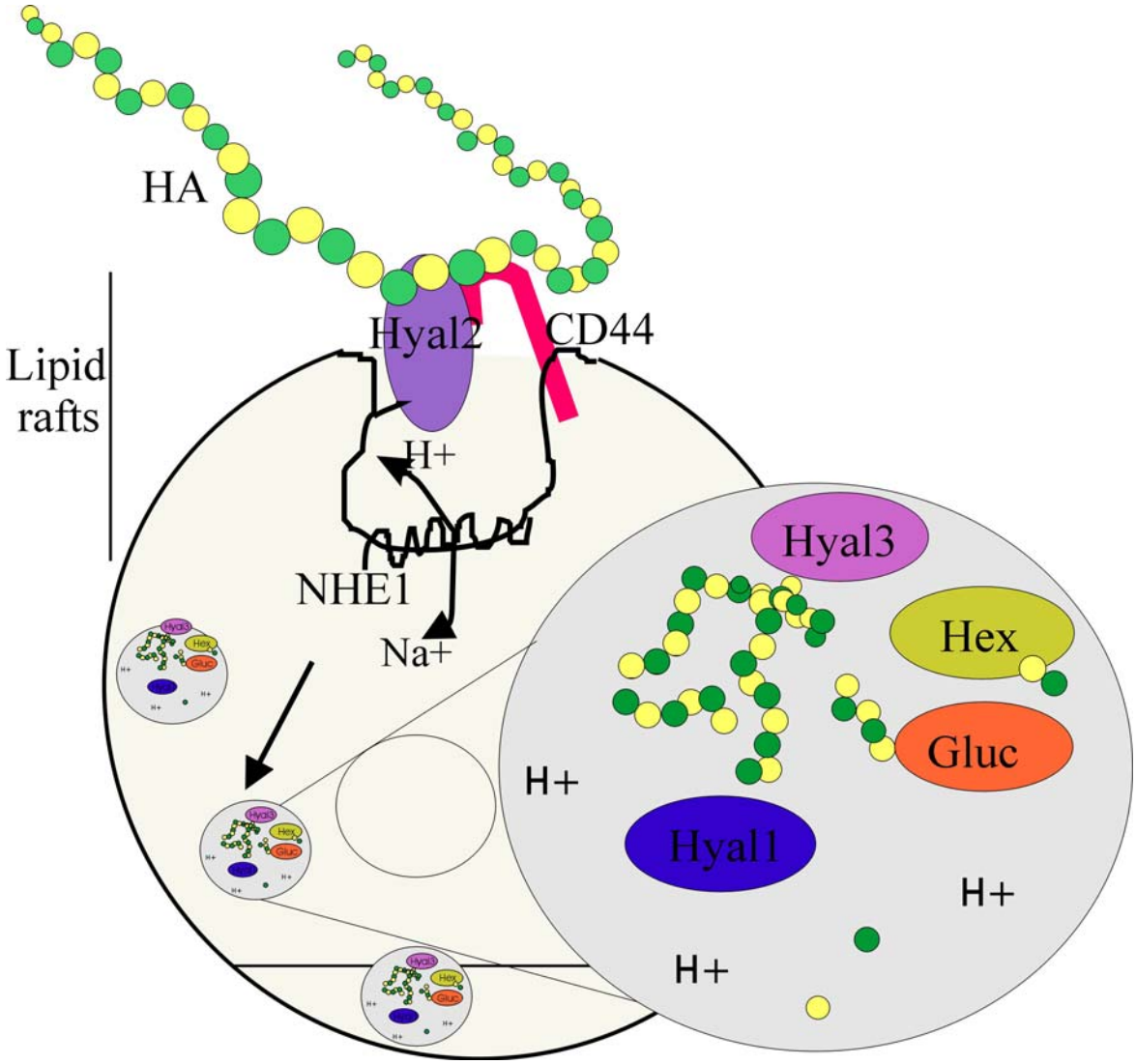

Figure 3: Proposed model of HA degradation.

Inside the lipid rafts, when HA at the cell surface binds to an HA receptor such as CD44, NHE1 is activated and creates an acidic microenvironment extracellularly. This leads to HA degradation by HYAL2. The HYAL2-generated HA fragments are further degraded to simple sugar units in the lysosomes by sequential actions of HYAL1 and β-hexosaminidase (Hex) and β-glucuronidase (Gluc). HYAL3 may also be playing a role in HA degradation inside the lysosomes. Green and yellow circles represent the monomers (N-acetyl glucosamine and glucuronic acid) of the HA molecule (This figure is modified from Csoka et al., 2001; Bourguignon et al., 2004).

1.3.4.4 Non-enzymatic HA degradation

In addition to the role of endoglycosidases and exoglycosidases in the catabolism of HA, various studies have described physiochemical methods of hydrolyzing HA (rev. in Stern et al., 2007). These methods include thermal degradation, photodegradation, ultrasonic degradation, acid and alkaline hydrolysis, free radicals and reactive oxygen species (Soltes et al., 2006). It is widely believed that free radicals are involved in HA breakdown (Uchiyama et al., 1990). However, the contribution of these physicochemical mechanisms in HA degradation are not well characterized. Recently, studies using mice deficient in extracellular superoxide dismutase (EC-SOD) showed increased lung inflammation, presumably because oxygen radicals degraded HA into smaller HA fragments that are inflammatory (Gao et al., 2008).

1.3.5 Hyaladherins

In the ECM, HA exists in both free and bound forms. Several HA-binding proteins (Knudson and Knudson, 1993), including cell surface and structural matrix proteins have been identified, and are termed as "hyaladherins" (Toole 1990). These include HA receptors (CD44, RHAMM [Receptor for hyaluronan mediated motility], LYVE-1 [Lymphatic vessel endothelial receptor-1] and HARE [HA receptor for endocytosis]), proteoglycans (aggrecan, versican, neurocan and brevican) (Hardingham and Muir, 1972; Margolis and Margolis, 1994) and other proteins such as cartilage-link protein, tumor necrosis factor stimulating gene-6 (TSG-6) and inter-α-trypsin inhibitor (IαI).

1.3.5.1 HA receptors

CD44 is highly expressed and has long been believed to be the main HA receptor.

For HA internalization, CD44 requires association with lipid rafts at the plasma membrane (Bourguignon et al., 2004). A knockout mouse model for CD44 has been generated and these mice developed normally with a subtle defect in hematopoiesis (Schmits et al., 1997). Studies of a bleomycin-induced lung injury model in *CD44*$^{-/-}$ mice showed increased inflammation and lung tissue HA accumulation compared to wild-type mice (Teder et al., 2002), suggesting impaired HA clearance in the absence of CD44.

RHAMM is a hyaladherin localized at the cell surface and also inside the cell. At the cell surface, it has been shown to be required for the locomotion of ras-transformed cells (Hardwick et al., 1992). Intracellular RHAMM is believed to have a role in mitosis as its association has been shown with microtubules and centromeres (Zhou et al., 2002; Maxwell et al., 2003). Moreover, RHAMM interactions with HA have been shown during mitosis (Evanko et al., 2004) and also during lung injury (Zaman et al., 2005).

LYVE-1, a CD44 homologue, is a transmembrane glycoprotein involved in the cellular uptake of HA (Prevo et al., 2001). LYVE-1 is localized in the endothelial cells of lymphatic vessels (Banerji et al., 1999) and also in the sinusoidal endothelial cells of liver (Mouta Carreira et al., 2001). Mice deficient in LYVE-1 were generated and characterization of these mice revealed controversial results. A study has shown that these knockouts show mild morphological changes in the lymphatic vessels and also increased interstitial lymphatic flow (Huang et al., 2006). However a subsequent study stated these mice were normal with no phenotype (Gale et al., 2007).

HARE has been identified in the sinusoidal endothelial cells of liver (Yannariello-Brown et al., 1997; Zhou et al., 2000). HARE is also localized in the medullary sinuses of lymph node, and venous sinuses of red pulp of spleen (Falkowski et al., 2003). Moreover, HARE is localized to specific cells in the bone marrow, cornea, lens, heart valves, brain

and kidney (Falkowski et al., 2003; Harris et al., 2007). HARE has been shown to bind HA and other GAGs, including CS, DS and heparin (Harris and Weigel, 2008b; Harris et al., 2008a). Studies using a blocking antibody against HARE inhibited HA clearance in liver (Weigel et al., 2003).

1.3.6 HA Turnover

HA has rapid turnover with one-third (5 gm) of the total human body HA (15 gm/70 kgm) turned over daily. Most of the HA (50 to 90%) is taken up by lymphatic vessels and then removed by lymph nodes (Fraser et al., 1988). A portion (10 to 30%) of HA is degraded locally (Laurent et al., 1991c; Laurent et al., 1992b) and the rest (~15%) enters the circulation. About 85 to 90% of circulating HA is removed by the liver and 10% by the kidney (Fraser et al., 1983; Engstrom-Laurent and Hellstrom, 1990). In liver, the uptake and degradation of HA is mainly by endothelial cells (Eriksson et al., 1983; Smedsrod et al., 1984; Fraser et al., 1985). The half life of HA varies from 2 to 5 minutes in the circulation (Fraser et al., 1981) to a few days in cartilage. Primarily, HA enters the cell by receptor-mediated endocytosis. Various HA receptors have been described in section *1.3.5.1*.

1.4 Lungs

1.4.1 Anatomy and histology

The respiratory system can be divided into conducting and respiratory regions, whose major functions are passage of air and gaseous exchange, respectively. The conducting region consists of upper airways, including the nasal cavity, nasopharynx, and larynx, as well as lower airways, including trachea, bronchi, bronchioles, and terminal

bronchioles. A combination of cartilage, elastic and collagen fibers in the conducting tissues gives structural support that allows an uninterrupted air passage through upper and lower airways to the respiratory area. As the air passes through the conducting region, it is cleaned and moistened by the mucus secreted by the goblet cells and seromucous glands. The respiratory region includes respiratory bronchioles, alveolar ducts, and alveoli. The alveoli are sac-like structures occupying the major region of the lungs where gaseous exchange occurs. Starting from bronchi to bronchioles, all the air passages are embedded within the lung parenchyma (Rev. in Junqueria and Carneiro, 2005).

The structure of the lungs changes as one moves from the conducting to the respiratory region. The epithelium of the air passages contains ciliated columnar epithelial and goblet cells, as well as mucus and serous glands. Cartilage and glands are present in the airways, but only scattered goblet cells are present in the epithelium of bronchioles. Decreasing diameter of the bronchioles is accompanied by a transition from ciliated pseudostratified columnar to cuboidal epithelium. The terminal bronchiole is divided into two or more respiratory bronchioles which are the transition between conducting and respiratory regions. The cuboidal epithelium of the respiratory bronchiole becomes continuous with the squamous alveolar lining cells. The mucosa of airways is underlaid by loose connective tissue, followed by smooth muscle cells, glands and cartilage depending on the type of airway, upper or lower (Rev. in Junqueria and Carneiro, 2005).

1.4.2 Innate immune system

The respiratory system needs an efficient innate immune system as it is in continuous contact with the external environment. The innate immune system functions to remove the microbes and particles that are inhaled through the air. The innate immune

system of the lungs includes physical barriers that stop the entry of microbes, circulating cells such as neutrophils and macrophages, as well as cytokines secreted by activated immune cells. The innate immune system recognizes microbes or molecular patterns through the pattern recognition receptors. Airway epithelial cells, alveolar macrophages and dendritic cells bear these pattern recognition receptors which recognize the pathogen associated molecular patterns on microbes or their products (Akira et al., 2006; Zaas and Schwartz, 2005). Toll-like receptors (TLRs) are the major class of pattern recognition receptors present on the epithelial cells and leukocytes (Zaas and Schwartz, 2005; Bals and Hiemstra, 2004).

The recognition of microbes or their products by the cell surface receptors leads to the activation of the innate immune system, removal of the microbes and activation of adaptive immune system. Activation of the innate immune system is mediated by resident cells such as mast cells, macrophages and dendritic cells that lead to infiltration of the injury by circulating cells to repair tissue and thereby maintain tissue homeostasis. Circulating cells reach the injury through tethering, rolling of cells to the endothelium, adhesion, and transmigration. In acute inflammation, neutrophils and macrophages are the major infiltrating cell type. Eosinophils accumulate during allergic inflammation. However, during chronic inflammation, depending on the type of injury, macrophages, lymphocytes and plasma cells accumulate in large numbers at the site of injury. The activation of the innate immune system is followed by the activation of the adaptive immune system by infiltrating lymphocytes, enabling a specific immune response to the insult. This is followed by the activation of mesenchymal cells such as fibroblasts and endothelial cells to form collagen matrix and new blood vessels.

1.4.3 Innate immune system and HA

In non-infectious lung injury, such as bleomycin-induced injury, TLRs act as mediators of tissue injury or repair. The TLRs can mediate the response through ECM component, HA. The interaction of HA with TLRs has been well studied (Jiang et al., 2002, 2005). The structural similarity of repeating disaccharide units of HA with the pathogen associated pattern molecules favours recognition of HA by pattern recognition receptors such as TLRs. However, the type of response to the injury is dependent on the size of HA that binds to the receptor. HA fragments generated at the site of tissue injury promote an inflammatory response through TLR signalling. In macrophages, when HA fragments bind to TLR-2 and TLR-4, the expression of chemokines or cytokines increases resulting in inflammatory responses. However on epithelial cells, when HMW HA binds to TLR-2 and TLR-4, it signals for the survival of epithelial cells. Therefore, during inflammation or tissue injury a balance between the levels of HMW HA and HA fragments are essential to maintain homeostasis (Jiang et al., 2005; Rev. in Jiang et al., 2006).

1.5 Physiological roles of HA

In the ECM, HA exists in both free and bound forms. HA either by itself or via interactions with hyaladherins is involved in various cellular processes such as cell-cell adhesion, cell-matrix adhesion, cell migration, proliferation and differentiation. HA acts as a molecular sieve for various proteins and contributes to tissue hydration and viscosity (Laurent and Fraser, 1986; Laurent et al., 1995; Laurent et al., 1996). It also provides structural rigidity to the cartilage and lubrication to the joints. The role of HA in embryonic development has been shown by an HA synthase (*Has2*) knockout mouse. HA

is involved in the various stages of ovarian development, ovulation and also fertilization. Recently, studies are focusing more on the size-dependent roles of HA in physiological and pathological conditions. The size-dependent roles of HA are shown in Figure 4.

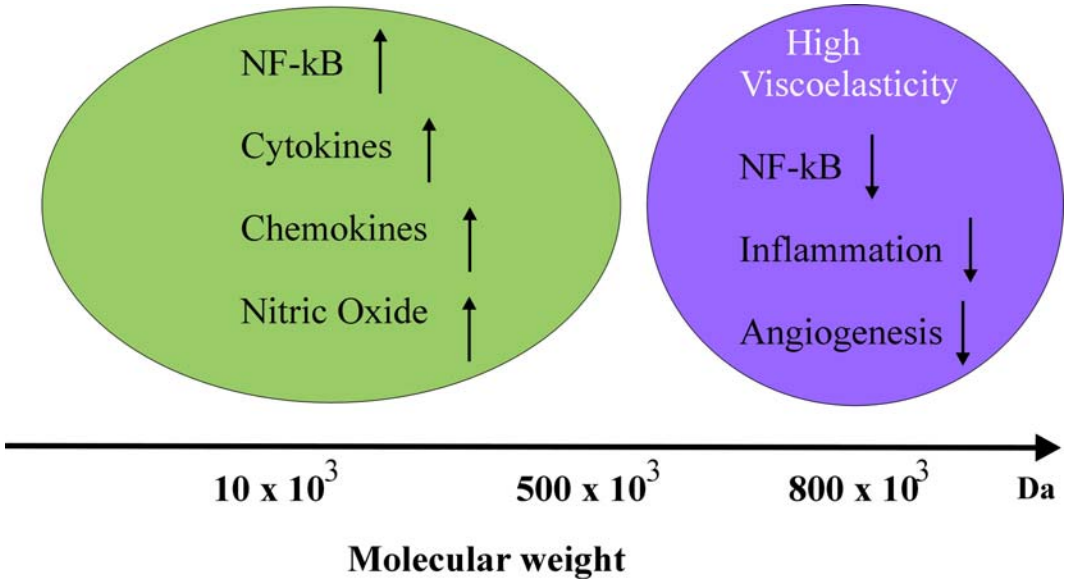

Figure 4: Size dependent roles of HA

(Modified from the original online version found at http://www.glycoforum.gr.jp/science/hyaluronan/HA12a/HA12aE.html.)

1.5.1 HMW HA

Under physiological conditions, HA exists in HMW form reaching up to 2 x 10^4 kDa, depending on the tissue type (Laurent and Fraser, 1992a). HMW HA is a space-filling molecule in the vitreous humor of the eye and acts as a lubricant and shock-absorber in the joints. HMW HA has been indicated as anti-inflammatory and immuno-suppressive (Delmage et al., 1986; McBride and Bard, 1979). The immunosuppressive effect of HMW HA has been suggested by preventing the accessibility of ligands to the cell surface receptors (rev. in Stern et al., 2006a). *In vitro* studies have shown that HMW

HA inhibits the expression of inflammatory chemokines (Jiang et al., 2005). Administration of aerosolized HMW HA (400 to 4000 kDa) has shown to prevent exercise-induced bronchoconstriction in the lungs of asthmatic patients (Petrigni and Allegra, 2006). Overall, HMW HA has been shown to have anti-inflammatory effects, even at the sites of inflammation where it acts as an immunosuppressive molecule (rev. in Stern et al., 2006a). More detailed information about the size-dependent roles of HA can be found in a review by Robert Stern and his colleagues (Stern et al., 2006a).

1.5.2 HA fragments

HA fragments, LMW HA molecules, are shown to accumulate at the site of inflammation and injury. HA fragment accumulation at the site of tissue injury has been observed in CD44 knockout mice with bleomycin-induced lung injury (Teder et al., 2002). These HA fragments have shown to increase the expression of inflammatory cytokines and chemokines (Jiang et al., 2005). Studies have also shown that HA fragments accumulate in bleomycin-induced lung injury of EC-SOD knockout mice (Gao et al., 2008). Moreover, i*n vitro* studies have indicated that HA fragments are inflammatory by stimulating the expression of chemokines and cytokines. Further *in vivo* studies aimed at determining the role of these HA fragments in tissue inflammation and injury are required.

1.5.3 HA cables

At the sites of inflammation, HA forms unusually large molecules called stress cables (rev. in Stern et al., 2006a). These HA cables arise intracellularly from more than one cell forming a long cable-like structure connecting cells. Studies have shown that HA

cables are associated with the nucleus of cells (Hascall et al., 2004). In situations of stress, HA cables are synthesized in several cell types (Majors et al., 2003; Wang and Hascall, 2004). In human intestinal smooth muscle cell cultures, HA cable-like structures were synthesized after viral infection or endoplasmic reticulum stress induced by tunicamycin (de la Motte, 1999).Moreover, studies have also shown that HA cables were also detected in the glomeruli of kidney sections during hyperglycemia (Ren et al., 2009).

The HA cable-like structures synthesized during endoplasmic reticulum stress and hyperglycemia have shown to be adhesive for mononuclear leucocytes (de la Motte, 1999; Majors et al., 2003, Ren et al., 2009). Moreover, studies have shown a role for HA hyaladherin, IαI (de la Motte et al., 2003), or cyclin D3 (Ren et al., 2009) in the formation of HA cables.

At the site of inflammation, these cables have a protective effect. HA cables bind to inflammatory cells and maintain them in an inactive state (Day and de la Motte, 2005). In contrast to HA fragments, these cables induce the expression of protective growth factors instead of pro-inflammatory markers. In addition these cables are also suggested to have an immunosuppressive role by sequestering inflammatory markers (Day and de la Motte, 2005). These cables were identified in inflammatory bowel disorders such as Crohn's disease and ulcerative colitis (de la Motte et al., 2003).

Thesis objectives and hypothesis

The objectives of my PhD thesis project were:

1. to generate and characterize mice deficient in *Hyal3*
2. to study the effect of *Hyal3* deficiency in acute and chronic lung inflammation
3. to identify the role of β-hexosaminidase in HA turnover

My hypothesis was that in health and inflammation *Hyal3* plays a major role in HA degradation in the tissues, and therefore HA will accumulate in the tissues of *Hyal3*-deficient mice where HA turnover is high.

Chapter two: Materials and methods

2.1 Preparation of bacterial media

Miller's Luria Broth (LB), low salt LB or LB agar (Invitrogen) plates were used for all bacterial cultures. To make LB agar containing ampicillin, the agar was cooled to 50°C and 100 µg/ml of ampicillin was added, and the media was poured into petri dishes. SOC media (8.5 mM NaCl, 2.5 mM KCl, 2% bacto-tryptone [Difco], 0.25 % bacto-yeast extract [Difco]) supplemented with sterile 0.01 M $MgCl_2$ and 0.02 M glucose was prepared, aliquoted and stored at -20°C.

2.2 Transformation of plasmid DNA

2.2.1 Preparation of electrocompetent cells

For preparation of electrocompetent cells, glycerol stocks of DH10B or DH5α *E.coli* bacterial cultures were streaked onto LB agar plates and the plates were incubated at 37°C overnight. A starter culture was prepared by picking a single colony from the agar plate and inoculating it into LB broth for incubation overnight at 37°C with shaking. The following morning, the starter culture was diluted (1:400) into low salt LB broth and grown at 37°C with shaking. When the OD_{600} reached 0.5 to 1.0 (~ 1 x 10^6 cells), the cells were pelleted by centrifugation at 4000 x g for 15 min at 4°C. Residual salts were removed by washing the pellet with an equal volume, followed by 0.5 and 0.2 volumes of sterile ice cold ddH_2O. The pellets were resuspended in 0.002 volumes of cold sterile 10% glycerol, aliquoted, frozen on dry ice, and stored at -80°C for subsequent use.

2.2.2 Electroporation

Plasmid DNA or ligation mixture was transformed into electrocompetent *E.coli* cells by electroporation. Frozen aliquots (50 µl) of electrocompetent DH10B or DH5α

E.coli cells were thawed, mixed with 1 ng of plasmid DNA or 1 µl of ligation mixture, and electroporated using sterile cold 1 mm gap electroporation cuvettes (BTX, Holliston, MA) at 2.5 kV resistance high voltage, 129 Ω resistance and 1.3 kV charging voltage. After electroporation, cells were recovered by incubating at 37°C for 1 hr in 960 µl of pre-warmed SOC media. Aliquots of 50, 100 or 200 µl of transformed cells were plated onto ampicillin-containing LB agar plates and the plates were incubated at 37°C overnight.

2.3 Isolation of plasmid DNA

Plasmid DNA was isolated using a QIAfilter kit (Qiagen), and following the manufacturer's instructions. Briefly, the bacterial cell pellet was lysed based on a modified alkaline lysis method (Birnboim HC, 1983) and cell debris and SDS were precipitated using potassium acetate (pH 5.5) buffer. Plasmid DNA was bound to an anion-exchange resin under low-salt and pH conditions and was eluted with high-salt buffer. DNA was precipitated with isopropanol, and the DNA pellet was washed with 70% ethanol. The DNA pellet was air dried and resuspended in ddH_2O.

2.4 Ethanol precipitation

Ethanol (95%) was typically used to precipitate all plasmid DNA samples. The DNA sample was mixed with 2.5 volumes of 95% ethanol and 0.1 volume of 3 M sodium acetate (pH 4.8), mixed well, and incubated for 30 min at -80°C. The DNA was pelleted by centrifugation at 14,000 x g for 5 min. The DNA pellet was washed with 70 % ethanol, air dried and resuspended in ddH_2O or 10 mM Tris EDTA pH 8.0 (TE) buffer.

2.5 Quantification of nucleic acids

DNA and RNA samples were quantified by measuring their absorbance at 260 nm using a Pharmacia BiotechUltraspec 1000 spectrophotometer in a 1 ml quartz cuvette. The concentrations were calculated using the following formulae:

DNA concentration (μg/ml) = Absorbance (260 nm) x 50 μg/ml x dilution factor

RNA concentration (μg/ml) = Absorbance (260 nm) x 40 μg/ml x dilution factor

2.6 Restriction enzyme digestion

Plasmid DNA or genomic DNA isolated from mouse tissues was digested with various restriction enzymes (NsiI, EcoRI, NdeI, NotI, NsiI/SalI, BamHI, NsiI/XbaI, XhoI/SalI, EcoRI/BamHI/SspI or MscI/RsrII). For each restriction enzyme digestion, the reaction was performed by adding a known amount of DNA (0.5 μg for screening clones, 5 -10 μg for preparation of vector or insert DNA for cloning, 40 μg of *Hyal3* targeting construct for electroporation, 10 μg of genomic DNA for Southern blotting) and 10 to 20 units of restriction enzyme(s) into 20, 50 or 100 μl of the restriction enzyme buffer recommended by the manufacturer (New England Biolabs). The samples were routinely incubated at 37°C for 3 hrs. However, the incubation time was extended when the DNA was not completely digested.

2.7 Preparation of vector and inserts for blunt-end ligation

2.7.1 Filling in 5' overhangs of vector and insert DNA

To create blunt ends, after restriction enzyme digestion, 5' ends of plasmid DNA were filled in using Klenow (New England Biolabs) and following the manufacturer's instructions. Plasmid DNA was ethanol precipitated and for each μg of DNA used, one

unit of DNA polymerase I enzyme and 33 μM dNTPs were added in 1 x Buffer 2 (New England Biolabs) and incubated at room temperature for 15 to 20 min. The enzyme was inactivated by incubating samples at 75°C for 10 to 20 min. Samples were stored at -20°C for further use.

2.7.2 Removal of 3' overhangs from vector DNA

To generate blunt ends, 3' overhangs from vector DNA was removed by the 3'- 5' exonuclease activity of Vent DNA polymerase (New England Biolabs). Vector DNA was ethanol precipitated, resuspended in 1 x PCR buffer, and 1 to 2 units of Vent DNA polymerase was added. The samples were incubated at 72°C for 20 min, run on an agarose gel, and gel purified.

2.7.3 Dephosphorylation of vector ends

To prevent recirculization of cloning vectors, 5' phosphates of restriction enzyme digested vector ends were removed using calf intestine alkaline phosphatase (CIAP) (New England Biolabs). Plasmid DNA was ethanol precipitated, resuspended in 1 x Buffer 3 (New England Biolabs), and 0.5 units of CIAP for each μg of plasmid DNA that was added. The samples were incubated at 37°C for 1 hr, separated on an agarose gel, and gel-purified.

2.8 Separation of nucleic acids by agarose gel electrophoresis

For DNA separation, 0.8 or 1.5% agarose gels were used depending on the sizes of the fragments to be separated. Agarose (Invitrogen) was dissolved in 100 ml of 1 x TAE (40 mM Tris-acetate and 1 mM EDTA) to make 0.8 to 1.5% agarose gels by heating in

the microwave oven for 2 to 3 min. To visualize the DNA after the molten agarose cooled to 50°C, 0.5 µg/ml of ethidium bromide was added, and the gel was poured into a gel casting tray. DNA samples and DNA molecular weight markers (Invitrogen) were mixed with 6 x DNA loading dye (0.25% bromophenol blue, 0.25% xylene xyanol and 40% sucrose) and loaded into wells created in the agarose gel. DNA was separated by electrophoresis at constant voltage of 50 to 115 V with 1 x TAE running buffer. The ethidium bromide bound DNA was visualized using UV light.

2.9 DNA extraction from agarose gels

DNA samples separated on agarose gels were isolated using QIAEX II or QIAquick (Qiagen Inc.) kits following the manufacturer's instructions. Briefly, the desired DNA fragment was excised from the gel, weighed and dissolved in a Buffer provided in the kit. The DNA in the dissolved gel was adsorbed to either the silica-gel membrane surface of a QIAquick column or beads in a QIAEXII suspension mix at high salt concentration and pH ≤7.5. Samples were washed with wash buffers, and finally the DNA was eluted in elution buffer or water.

2.10 Ligation

Vector and insert DNAs were separated on agarose gels, purified and ligated at a vector (100 ng) to insert molar ratio of 1:1 or 1:3. Ligations were performed at room temperature for 2 hrs or overnight in a 10 to 20 µl volume using T4 DNA ligase (New England Biolabs), and following the manufacturer's instructions. Ligations of the vector and insert alone were performed as negative controls.

2.11 Polymerase chain reaction (PCR) amplification

PCR was used to amplify DNA regions of interest from plasmid or genomic DNA. Each PCR reaction contained 100 ng of forward primer, 100 ng of reverse primer, 0.2 mM dNTPs, 1x PCR buffer (20 mM Tris-Cl [pH 8.4], 50 mM KCl), 1.5 mM $MgCl_2$, 2.5 units Taq DNA Polymerase (Invitrogen) and 100 ng of DNA. A reaction containing no DNA template was used as a negative control. Samples were overlaid with mineral oil and amplified using a Perkin Elmer Thermal Cycler or a MJ Research Minicycler. PCR conditions were optimized specifically for each primer set and are listed in Table 3

.

Table 3: Forward and reverse primers used for PCR amplification

Forward Primer 5'→ 3'	Forward Primer Location	Reverse Primer 5'→ 3'	Reverse Primer Location
WPG 623 ggtctccatctctgtggcat	*Hyal3* Exon 2	WPG 624 gcagcctgctcaaagctagt	*Hyal3* Exon 2
WPG 621 tggctacccgtgatattgct	Neo coding region	WPG 622 gaggctgccaggtagacttgt	Neo coding region
WPG 266 tttccatgatcaggagga	*Hyal1* 3' UTR	WPG 293 tccaactcctcggtctgccta	*Hyal1* downstream
WPG 340 caggagcagtacccaggct gactc	*Hyal3 3'* downstrea m	WPG 341 gaggctgcgctccagcagaaa gtc	*Hyal3 3'* downstream
WPG 672 ggccagatacaatcatacag	*Hexa* Exon 11	WPG 673 ctgtccacatactctccccacat	*Hexa* Exon 12
WPG 672 ggccagatacaatcatacag	*Hexa* Exon 11	WPG 658 Caccaaagaagggagccgcc ggt	PGK promoter
WPG 656 ggtttctacaagagacatcat ggc	*Hexb* Exon 2	WPG 657 caatcggtggtgcttacaggttt catc	*Hexb* Intron 2

WPG 659 gatattgctgaagagcttggcggc	Neo coding region	WPG 657 caatcggtggtgcttacaggtttcatc	*Hexb* Intron 2
Primer "A" gactctagatctgtggccaag	*Hyal3* Exon 2	Primer "B" ggtcgtccagagacaggaa	*Hyal3* Exon 2
Primer "C" ggctacccgtgatattgc	Neo coding region	Primer "D" aggtcgtccagagacaggaa	*Hyal3* exon 2 -3 junction

2.12 Phenol-chloroform purification of Hyal3 targeting constructs

To improve the quality of the linearized *Hyal3* targeting construct, the restriction enzyme digested DNA was mixed with an equal volume of phenol: chloroform: isoamyl alcohol (25:24:1), and centrifuged at 14,000 x g for 3 min and then precipitated with ethanol as described in section *2.4*.

2.13 Mouse embryonic stem (ES) cells

2.13.1 ES cell lines used for targeting

R1 ES cells that were derived from the inner cell mass of blastocyst embryos of a chinchilla *129Sv* and agouti *129Sv-CP* mice cross (Nagy et al., 1993) were used for *Hyal3* targeting in the laboratory of Dr. Andras Nagy at the Samuel Lunenfeld Research Institute, Toronto, ON.

2.13.2 ES cell culture conditions

ES cells were grown in complete ES cell medium, ES-DMEM (4.5 g/L high glucose) containing 15% ES cell qualified FBS (Hyclone), 0.1 mM non-essential amino acids, 1 mM sodium pyruvate, 0.1 mM β-mercaptoethanol, 2 mM L-glutamine, 50 U/ml

penicillin and 50 U/ml streptomycin and 1000 U/ml leukaemia inhibitory factor (LIF) at 37°C with 5% CO_2. For selection, ES cell medium was supplemented with either 150-250 μg/ml Geneticin (G418) (Gibco) and/or 2 mM gangciclovir. For long term storage of ES cells, mitotically inactivated mouse embryonic fibroblasts (MEFs) were used as feeders whereas for ES cell electroporation and during selection, gelatinized (0.1% gelatin) plates in the presence of leukemia inhibitory factor (LIF) were used. Mitomycin C treated Neo resistant MEFs were supplied by the Samuel Lunenfeld Research Institute, Toronto.

2.13.3 ES cell transfection

The *Hyal3* targeting construct was linearized by Not1 restriction digestion prior to electroporation. The construct DNA was ethanol precipitated, washed with 70% ethanol, and resuspended in sterile buffer or ddH_2O to achieve a final concentration of 1 μg/μl. After the cells reached 80% confluence (15–20 x 10^6 cells/ml in 10 cm plate), the medium was changed two hours prior to electroporation. Cells were harvested with 0.25% trypsin, and pelleted by centrifugation. The pellet was resuspended in 1 ml of electroporation buffer (Specialty Media) and the cell density was determined by haemocytometer. Cells were diluted with the same buffer to reach a density of 7 x 10^6 cells/ml. The ES cell suspension (0.8 ml) was mixed with 20 to 40 μg of *Hyal3* targeting construct DNA in a pre-cooled 4 mm gap electroporation cuvette and electroporated at 250 V and 500 μF using a Bio-Rad Gene Pulser.

2.13.4 ES cell freezing, thawing and expansion

ES cells were harvested with 0.25% trypsin in ES-DMEM and centrifuged at 1000 x g for 5 min at room temperature. The supernatant was removed and the cell pellet was

gently resuspended in 1 x ES cell freezing media (80% ES-DMEM, 10% FBS, 10% DMSO). The cell suspension was aliquoted (~ 5 x 10^6 cells/ml) into labelled cryovials and the vials were placed in a pre-cooled styrofoam box at -80°C to allow the cells to cool down gradually. After 1 – 2 days, the cryovials were stored in a liquid nitrogen tank for later use. In addition, ES clones that appeared to be correctly targeted were frozen in 96 well plates by trypsinizing, resuspending and neutralizing cells with ES-DMEM and an equal volume of 2 x ES cell freezing media (60% ES-DMEM, 20% FBS, 20% DMSO). Wells in the plates were overlaid with a thin layer of mineral oil and the plates were wrapped in parafilm and stored at -80°C for subsequent use.

ES cells frozen in cryovials and 96 well plates were thawed by quickly warming at 37°C. The contents of the cryovials were transferred to a 12 ml tube using a pipette filled with ES-DMEM. Cells were centrifuged at 1000 x g for 5 min, and the pellet was resuspended in fresh ES-DMEM and plated onto feeder fibroblasts. The following day, floating cells were removed and fresh media was added. After 2 to 3 days, ES cells were ready for passage into selective medium.

2.13.5 ES cell genomic DNA isolation

To isolate genomic DNA from ES cells grown in a 96-well plate format, the media was aspirated, and each well was washed twice with PBS and lysed overnight in a lysis buffer (10 mM Tris-Cl pH 7.5, 10 mM EDTA, 10 mM NaCl, 0.5% sarkosyl and 1 mg/ml Proteinase K) at 55°C in a humid atmosphere. The following day, DNA was isolated by adding a cold NaCl/ethanol mixture (150 µl of 5 M NaCl per 10 ml of cold 100% ethanol) to each well and incubating the plate at room temperature for 30 to 60 min. Wells were washed three times with 70% ethanol, then allowed to air dry for 10-15 min before

resuspending in restriction enzyme digestion mixture along with 100 µg/ml RNaseA and 1 mM spermidine. The plates were mixed, sealed with parafilm and incubated overnight at 37°C in a humid atmosphere. The following day, samples were used for Southern analysis.

2.14 Southern analysis

2.14.1 Preparation of DNA probes

The 430 bp 5' external probe which spans nucleotides 6488498 to 6488919 (GenBank accession # NT_039477) was generated by PCR amplification of mouse genomic DNA using primers WPG 266 and WPG 293. The 490 bp 3' external probe which spans nucleotides 6497961 to 6498439 (GenBank accession # NT_039477) was generated by PCR amplification of mouse genomic DNA using primers WPG 340 and WPG 341. All the primer sequences are listed in Table 3. The Neo probe was generated by restriction enzyme digestion of pGT-N28 plasmid (New England Biolabs) with MscI and RsrII to generate a 420 bp DNA fragment. All fragments were separated by agarose gel electrophoresis, purified by gel extraction, and quantified. The fragments were radioactively labelled with ^{32}P-dCTP using a Rediprime II (GE Healthcare) kit and the free nucleotides were removed using a ProbeQuant G-50 Micro column (GE Healthcare). The probe was only used if it had a specific activity >1 x 10^8/ ml.

2.14.2 Transfer

Genomic DNA isolated from ES cells or mouse tissues was separated by agarose gel electrophoresis and the gel was trimmed to remove excess agarose. The gel was incubated in denaturation solution (1.5 M Tris pH 7.4, 1.5 M NaCl) for 30 min at room

temperature and was equilibrated in 20 x SSC (3.0 M NaCl, 0.3 M sodium citrate pH 7.0) for 10 min. Genomic DNA in the gel was transferred by upward capillary transfer to Hybond N^+ (GE Healthcare) or Immobilon Ny^+ (Millipore) nylon membrane in 20 x SSC overnight and the membrane was UV cross-linked after a brief wash in 6 x SSC (0.9 M NaCl, 0.09 M sodium citrate pH 7.0), and following the instructions of the membrane manufacturer.

2.14.3 Hybridization

Prior to hybridization, non-specific binding of probe to the membrane was blocked by incubation in Expresshyb (Clontech) or in hybridization buffer (0.75 M NaCl, 0.075 M sodium citrate pH 7.4, 0.2% SDS, 0.1% Ficoll, 0.1% polyvinylpyrrolidone and 0.1% bovine serum albumin) containing heat denatured salmon sperm DNA (100 μg/ml) at 60°C overnight. Hybridization was done in fresh hybridization buffer containing half of the denatured ^{32}P-labelled probe by incubating at 60 - 65°C for 4 hrs or overnight. Excess probe was removed by washing the blot with wash buffer 1 (0.3 M NaCl, 0.03 M sodium citrate [pH 7.4], 0.05% SDS) at room temperature for 30 min, followed by a second wash in wash buffer 2 (0.15 M NaCl, 0.015 M sodium citrate [pH 7.4] and 0.1% SDS) at increasing temperatures until a specific signal without background was visualized on the blot by autoradiography using X-OMAT MS film (Kodak).

2.15 Protein extraction and quantification

2.15.1 Protein extraction from tissues

Liver tissue samples of approximately 30 mg were homogenized in 1 ml of lysis buffer containing 10 mM imidazole and 250 mM sucrose, and the lysates were

centrifuged to remove tissue debris. The supernatants were collected and stored to -80°C for further use.

2.15.2 Determination of protein concentration

Protein concentrations in tissue lysates were estimated by the Bradford method (Bradford, 1976) using the Bio-Rad assay kit (Bio-Rad Laboratories, Hercules, CA, USA) and following the manufacturer's instructions. Aliquots from tissue lysates and gamma globulin standards were made up to 800 µl with ddH_2O and mixed with 200 µl of Bio-Rad reagent to reach a final volume of 1 ml. Samples were incubated at room temperature for 30 min and the absorbance was read at 595 nm using a Pharmacia BiotechUltraspec 1000 spectrophotometer. The protein concentration in the tissue lysates was determined by comparison to the gamma globulin standard curve. Lysis buffer with Bio-Rad reagent was used to calibrate the absorbance to zero.

2.16 SDS and non-SDS polyacrylamide gel electrophoresis

For western blotting, protein concentrations in tissue lysates were estimated based on procedure of Bradford as described in *2.17.2* and for each sample, 50 µg of proteins were separated by polyacrylamide gel electrophoresis using 7.5% resolving and 4% stacking gels of 1.5 mm thickness. To make a 7.5% resolving gel, to a 10 ml solution containing 40 mM Tris-Cl (pH 8.8), 0.1% SDS, 7.5% acrylamide (acrylamide: bisacrylamide, 29:1) in H_2O, 75 µl of 10% ammonium persulfate (APS) and 10 µl of tetramethylethylenediamine (TEMED) was added. The gels were cast in a Mini Protean II (Bio-Rad) gel casting apparatus and allowed to polymerize at room temperature for one hour. For stacking gels, a 2.5 ml solution containing 60 mM Tris-Cl (pH 6.8), 0.1% SDS

and 4% acrylamide in H_2O was mixed with 25 µl of 10% APS and 2.5 µl of TEMED and poured on top of the resolving gel. Tissue lysates were prepared in Laemmli sample buffer (4x buffer, 0.25 M Tris-Cl [pH 6.8], 8% SDS, 100 mM DTT, 25% glycerol and 0.01% bromophenol blue) and boiled for 5 min before loading onto gels. Samples were separated by electrophoresis at constant voltage (150 V) at room temperature in running buffer containing 25 mM Tris, 0.1% SDS and 192 mM glycine (pH 8.3).

For fluorophore-assisted carbohydrate electrophoresis (FACE), 25% resolving (25% acrylamide/3.75% bisacrylamide, 0.38 M Tris pH 8.8, 1.5 ml ddH_2O, 25 µl 10% APS and 2.5 µl TEMED) and 5% stacking (5% acrylamide/ 1.5% bisacrylamide, 0.36 M Tris pH 6.8, 2.65 ml ddH_2O, 50 µl 10% APS and 5 µl TEMED) gels of 0.75 mm thickness were prepared without SDS. Fluoro-tagged samples were loaded on the gels without any further processing and the electrophoresis was performed at constant voltage of 500 V at 4°C in a running buffer containing 25 mM Tris, 0.1% SDS and 192 mM glycine (pH 8.3).

2.17 Western blotting

2.17.1 Transfer

Proteins were separated by SDS-PAGE and transferred to a nitrocellulose membrane based on procedure of Towbin. Prior to transfer, the nitrocellulose membrane and Whatmann papers were cut to the size of the gel and wet with Transfer Buffer (25 mM Tris base, 192 mM glycine, 20% methanol [pH 8.3]) along with transfer sponges. The gel and the membrane were sandwiched between Whatman papers and transfer sponges, and the assembly was placed into a transfer clamp holder. The transfer assembly was placed in a Mini Trans-Blot Cell apparatus (Bio-Rad) keeping the nitrocellulose

membrane close to the cathode. The transfer was done with ice-cold Transfer Buffer at 100 V for 1½ hr at 4°C.

2.17.2 Protein detection

The blot was stained with Ponceau S (0.2% Ponceau S in 1% acetic acid), rinsed with water, and washed with TBST (10 mM Tris-Cl [pH 7.4], 150 mM NaCl and 0.1% Tween-20) until the stain was removed. The blot was incubated for 1 hr in blocking solution (5% skim milk power in TBST) and overnight in primary rabbit anti-Hyal3 antibody (1:1000; 1% skim milk in TBST) (Hemming et al., 2008). Non-specifically bound primary antibody was removed by three-15 min washes with TBST. The blot was incubated in secondary anti-rabbit antibody conjugated to horse radish peroxidase (HRP) (Jackson Laboratories; 1:15,000) for 1 hr at room temperature, and then four washes of 10 min each were performed with TBST. Secondary antibody was detected using a chemiluminescent detection reagent (Amersham), and following the manufacturer's instructions. The blot was exposed to BioMax Light film (BioMax) and was developed using manual processing.

2.18 Selection and identification of targeted ES cells

The final *Hyal3* targeting construct was linearized with NotI restriction enzyme, and introduced into R1 embryonic stem (ES) cells derived from *129S1* mice using electroporation. On days 9 and 10 post-electroporation, 168 G418-resistant ES cell colonies were picked and grown for screening and potential storage. DNA prepared from 98 G418-resistant and gangcyclovir sensitive ES cell clones were screened for neo insertion into the *Hyal3* gene by Southern hybridization of NsiI digested DNA using the

5’ external probe. Ten putative clones (BB1, BA3, PA2, BG9, GF5, RC1, PC1, BB5, OG3 and GF5) were re-screened for Neo insertion by Southern hybridization with 3’ external and Neo probes.

2.19 Generation of hyaluronidase 3-deficient (Hyal3$^{-/-}$) mice

Three (PA2, BG9 and BB5) of the seven correctly targeted ES cell clones were aggregated with *CD1* mouse embryos and implanted in pseudo-pregnant *CD1* female mice at the Transgenic and Gene Targeting Facility (Sunnybrook Health Sciences Centre, Toronto, Ontario, Canada) (Nagy et al., 2003). Male chimeras from two ES cell clones (BG9 and BB5), transmitting the targeted *Hyal3* allele, were used to establish two independent lines of mixed background (*CD1;129S1*) by crossing with *CD1* mice obtained from Central Animal Care Services, University of Manitoba. One of the male chimeras transmitting the *Hyal3* targeted allele in their germline was also crossed with *129S1* (Charles River Laboratories, Quebec, Canada) female mice to generate a congenic line (*129S1*). Initially, the targeted allele in mice was identified by Southern hybridization of NdeI-digested liver DNA with the 5’ external probe; subsequently genotyping was performed by PCR amplification of tail-clip DNA. For the PCR amplification of the wild-type allele, the primers were WPG 623 and WPG 624 and for the amplification of the neo-targeted allele, the primers were WPG 621 and WPG 622. *Hyal3*$^{-/-}$ mice were obtained from heterozygous and homozygous crosses. Mice were maintained in Central Animal Care Services at the University of Manitoba following protocols approved by the Animal Care and Use Committee at the University of Manitoba and the guidelines of the Canadian Council on Animal Care.

2.20 Generation of β-hexosaminidase-deficient (Hexa$^{-/-}$Hexb$^{-/-}$) mice

Hexa$^{+/-}$*Hexb*$^{+/-}$ mice that were generated by intercrossing *Hexa*$^{+/-}$ and *Hexb*$^{+/-}$ mice (Phaneuf et al., 1996) were generously supplied by Alex Pshezhetsky from University of Montreal, Montreal, Quebec. Offspring of *Hexa*$^{+/-}$*Hexb*$^{+/-}$ intercrosses were genotyped to generate *Hexa*$^{-/-}$*Hexb*$^{-/-}$ mice. Genotyping was done by PCR amplification of DNA isolated from ear punch using allele-specific primers. For genotyping of *Hexa*, WPG 672 and WPG 673 were used as wild-type allele specific primers and WPG 672 and WPG 658 as neo-targeted allele specific primers. For genotyping of *Hexb*, WPG 656 and WPG 657 were used as wild-type allele specific primers and WPG 657 and WPG 659 as neo-targeted allele specific primers. All mice were maintained in Central Animal Care Services at the University of Manitoba following protocols approved by the Animal Care and Use Committee at the University of Manitoba and the guidelines of the Canadian Council on Animal Care.

2.21 Necropsy

Mice were euthanized by CO_2 asphyxiation at 6, 12 or 14 months of age for studies in chapter three and ~1 to 3 months for studies in chapters four and five. Mice were weighed and observed for gross phenotypic changes, for example, fluid filled masses on joints. Mice were dissected; blood and the major tissues were collected, weighed and examined for organomegaly. Tissues collected included, liver, lungs, lymph node, spleen, heart, brain, kidneys, skin, skeletal muscle, fat, testes, seminal vesicle, ovary, uterus and knee joints for studies in chapter three, only lungs for studies in chapter four; and liver, lungs, lymph node, spleen, heart, brain, kidneys, skin, knee joint, trachea and rib cartilage

for studies in chapter five. Tissues were either flash frozen in liquid N_2 for biochemical and molecular studies or immersed in fixatives for light and electron microscopy.

2.22 Genomic DNA isolation from mouse tails

For PCR amplification, genomic DNA was isolated from tail-clips using the salt-chloroform extraction method (Mullenbach et al., 1989). Tail-clips were digested in lysis buffer (75 mM NaCl, 25 mM EDTA [pH 8.0], 1% SDS and 200 µg/ml Proteinase K) at 55ºC overnight. Tissue debris were removed by centrifugation, and pre-warmed 6 M NaCl (saturated) was added to the supernatant and incubated at 55ºC for 5 min. After gentle mixing, 1 volume of chloroform was added, and the samples were rotated for 1 hr at room temperature. Aqueous and non-aqueous layers were separated by centrifugation at 10,000 x g for 5 min, and the top aqueous layer containing DNA was transferred to a new tube without touching the interphase or bottom layer. The genomic DNA was precipitated by adding an equal volume of isopropanol to the top aqueous layer, and gently mixed for 5 min at room temperature. DNA was pelleted by centrifugation at 14,000 x g for 5 min and the supernatant was discarded. The pellet was washed with 70 % ethanol, air dried, and resuspended in TE buffer (pH 8.0).

2.23 RNA isolation from mouse tissues

Immediately following euthanasia, mouse tissues were collected, flash frozen in liquid nitrogen and stored at -80°C to isolate RNA by guanidium thiocyanate-phenol-chloroform extraction (Chomczynski and Sacchi, 1987). To isolate total RNA, tissues were crushed and homogenized using a Potter-Elvehjem homogenizer in a lysis buffer containing 4 M guanidinium thiocyanate, 25 mM sodium citrate, 0.1 M β-

mercaptoethanol and 0.5% sarkosyl at 4°C. To the homogenate, 0.4 ml of 2 M sodium acetate (pH 4.0), 4 ml of water saturated phenol and 0.8 ml of chloroform: isoamyl alcohol (49:1) were added and incubated for 15 min on ice. The aqueous layer was collected after centrifugation at 14,000 x g for 20 min, and one volume of cold isopropanol was added. Samples were incubated at -20°C for 1 hr and the precipitated RNA was pelleted by centrifugation at 10,000 x g for 20 min at 4°C. The RNA pellet was resuspended in 1.2 ml of lysis buffer and precipitated with 2 volumes of cold ethanol for 1 hr at -20°C. The pellet was collected after centrifugation at 13,000 x g for 10 min at 4°C, and washed three times with 70% ethanol. The RNA pellet was resuspended in RNase free H_2O and the amount of RNA was quantified as described in section *2.5*.

2.24 Reverse transcription (RT) reaction

Total RNA isolated from mouse tissues was reverse transcribed to cDNA using random hexamer primers and Superscript III reverse transcriptase (Invitrogen Canada Inc., Burlington, Ontario, Canada), and following the manufacturer's instructions.

2.25 Conventional and real-time RT-PCR

For conventional RT-PCR, cDNA was PCR amplified using gene specific primers. For real-time RT-PCR, TaqMan Gene Expression Assays (Applied Biosystems Inc.[ABI]) for *Hyal1* (Mm00476206_m1), *Hyal2* (Mm0047731_m1), *Hyal3* (Mm00662097_m1), *Hyal4* (Mm01165340_m1), *Hyal5* (Mm01165333_m1), *Spam1* (Mm00486329_m1), *HexB* (Mm00599880_m1), *Fus2* (Mm01947825_S1) and Hypoxanthine-guanine Phospho Ribosyl Transferase 1 (*Hprt1)* (4352339E), or a TaqMan Custom Assay for *Hyalp1* (Primers: sense 5'-GGGAACCCTTCTGTGTTTTGGAAA-3'; antisense 5'-

CCCACTGGATAAACATGGATTGCT-3' and probe 5'-CCTTTGAGCACACTTCC-3') were used. The threshold cycle number (C_T) was determined for the transcripts of the target genes and the reference (*Hprt1*) gene in each sample (Livak and Schmittgen, 2001). ΔC_T (C_T target - C_T reference) values for each target gene were calculated and compared between the tissues of *Hyal3*$^{+/+}$ and *Hyal3*$^{-/-}$ mice. Experiments for each mouse were performed in duplicate and each sample was analyzed in triplicate. All the assays were performed using the ABI 7500 Real-time PCR system under the standard cycling conditions suggested by the manufacturer.

2.26 Antigen sensitization and challenge protocol

Hyal3$^{+/+}$ and *Hyal3*$^{-/-}$ mice (one month of age) were used for both chronic and acute inflammation models. For the chronic airway inflammation model, *Hyal3*$^{+/+}$ and *Hyal3*$^{-/-}$ mice were sensitized on days 0 and 22 with an intraperitoneal (i.p.) injection of 2 µg of ovalbumin (OVA) (Sigma-Aldrich, St. Louis, MO) conjugated with 4 mg of $Al(OH)_3$ (^{MJS}Biolynx Inc., Brockville, ON) suspended in 500 µl of 0.9% NaCl. Starting on day 29, mice were intranasally challenged with 50 µg of OVA suspended in 50 µl of 0.9% NaCl three times a week for three weeks. The acute inflammation protocol was similar to the chronic protocol except that the intranasal challenges were done for a week instead of 3 weeks. Studies of lung function, histology or lavage were performed 96 hrs after the last intranasal challenge in the chronic model and 48 hrs after the last challenge in acute model. Mice challenged with chronic and acute OVA inflammations were addressed as OVA-challenged mice or mice with acute inflammation, respectively in chapter 4 and appendix 1. Inflammation protocols are shown in Figure 5.

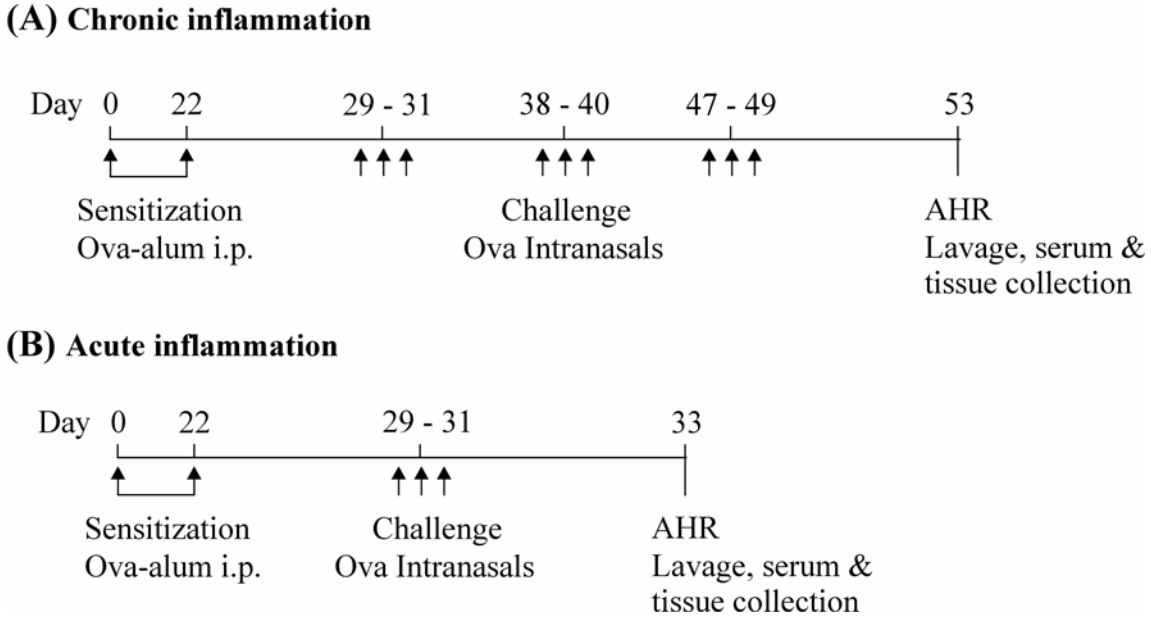

Figure 5: Schematic diagram of chronic and acute lung inflammation protocols.

2.27 Assessment of airway responsiveness

Airway resistance, Rn, to the increasing concentrations of nebulized methacholine (MCh) (0 to 25 mg/ml) was measured using a *flexi*Vent animal ventilator (SCIREQ, Montreal, Canada). Mice were anesthetized with 90-135 mg/kg of sodium pentobarbital, a tracheotomy was performed (Figure 6A) and the mice were connected to the *flexi*Vent ventilator through with a polyethylene cannula (Figure 6B). Mechanical ventilation delivered at 200 breaths/minute with a tidal volume of 10 ml/kg using a positive end-expiratory pressure, PEEP, of 3 cm H_2O. Mice were subjected to serial aerosol methacholine challenge using an Aeroneb ultrasonic nebulizer (SCIREQ) to deliver ~30 µl in 10 sec. Before each methacholine dose, the loading history was normalized by inflating to total lung capacity. Respiratory mechanics were assessed using a preset *flexi*Vent Prime-8 low frequency forced oscillation protocol to derive respiratory mechanical input impedance (Zrs), which was fit to the constant phase model to calculate

conducting Rn (Ravinc et al., 2007).

(A) Tracheotomy

(B) Lung function using *flexi*Vent ventilator

Figure 6: Tracheotomy and lung function analysis using the *flexi*Vent ventilator. Pictures showing a mouse with a **(A)** tracheotomy and **(B)** lung function testing using a *flexi*Vent ventilator.

2.28 Serum and broncho-alveolar lavage (BAL) fluid collection

Blood collected from the mice immediately following termination was allowed to clot at room temperature and the serum was collected by centrifugation at 4,000 x g for 15 min at room temperature, and stored at -80°C for HA analysis.

BAL fluid was collected by washing lungs with two 1 ml volumes of saline. Cells were collected from BAL fluid by centrifugation at 1000 x g for 10 min and the supernatant was stored at -80°C for cytokine and HA analyses.

2.29 GAG and/or HA quantification

2.29.1 Serum and lavage HA

Serum HA concentration was determined by sandwich ELISA using an HA Test Kit (Corgenix Inc., Broomfield, Colorado, USA) and following the manufacturer's instructions. Briefly, serum samples were incubated with HA-binding protein coated wells and after three washes with PBS, wells were incubated with horseradish peroxidase (HRP) conjugated HA-binding protein for 1 hr. Peroxidase activity was measured by the intensity of colour when read at 450 nm with in 30 minutes after adding substrate to the wells. HA concentration in the serum and lavage samples was calculated using a 4-parameter standard curve using known amounts of HA as a standard.

2.29.2 Tissue GAG content

Tissues to be analyzed for total GAG content were weighed immediately after dissection and frozen by immersion in liquid nitrogen. The tissues were subsequently crushed on dry ice and lyophilized using a Thermo Savant Supermodulyo Freeze Dryer until the tissues were completely dried. Total GAGs from the lyophilized tissues were

extracted into 5 volumes of 6 M urea, 50 mM Na acetate, 0.1 M Na_2EDTA and 0.1 M aminocaproic acid pH 6.5 at 4°C for 48 hrs. Tissue extracts were centrifuged at 7700 x g for 25 min at 4°C and the supernatants were applied to Q-Sepharose resin equilibrated with 50 mM Na acetate, 250 mM NaCl, 10 M formamide pH 6.0. Columns were washed with 10 volumes of the same buffer, and the samples were eluted in the same buffer but containing 5 volumes of 4 M NaCl. GAGs were quantified by uronic acid assay (Blumenkrantz and Asboe-Hansen, 1973), and the total GAG content of the tissues was normalized to the tissue wet weight.

2.29.3 Tissue HA content

Biochemically, HA present in the lung tissues of *Hyal3*$^{+/+}$ and *Hyal3*$^{-/-}$ mice was quantified by fluorophore assisted carbohydrate electrophoresis (FACE) (Plaas et al., 2001; Calabro et al., 2001; Ren et al., 2009; Karousou et al., 2004). Approximately 5 mg of lyophilized tissue was digested with Proteinase K overnight at 55°C and the enzyme was inactivated by heating samples at 95°C for 5 min. The tissue debris were removed by centrifugation at 10,000 x g for 10 min at room temperature. GAGs present in the supernatant were precipitated with ethanol at -20°C overnight and then disaccharides were derived by digesting those precipitated GAGs with 100 µl of Streptococcal hyaluronidase (50 mU/ml, Seikagaku America Inc., Rockville, MD) in ammonium acetate buffer (pH 7.3) at 37°C overnight. The enzyme digests were cooled on ice, the enzyme and the undigested GAGs were precipitated by adding 900 µl of ice cold ethanol at -20°C for 2 hrs. The precipitate was removed by spinning at 1000 x g for 20 min at 4°C and the supernatant containing disaccharides was dried by Speed Vac Lyophilization. Disaccharides were amino labelled with a fluorophore, 2-aminoacridine (AMAC;

Invitrogen), that was prepared following the manufacturer's instructions. The dried pellet was dissolved in 5 µl of AMAC and incubated at room temperature for 15 min. Later, 5 µl of freshly prepared sodium cyanoborohydride in water was added to the AMAC derived mixture and incubated overnight at 37°C. After the incubation, samples were cooled to room temperature, mixed with 32 µl of 25% glycerol and one sixth of the volume of sample was subjected to electrophoresis as described in *2.18*. Gel images were captured with a charge coupled device camera attached to a Fluor S-Max imager and the band intensity was analyzed using Quantity One Software. The band intensity of disaccharides of HA present in unknown samples was quantified by comparing with the standard curve of HA disaccharides (50, 100 and 200 pMol, Associates of Cape Cod Inc.) that were also AMAC labelled along with unknown lung samples.

2.30 Total and differential cell counts in BAL fluid

Total cell counts were determined using a hemocytometer while for differential cell counts, samples were diluted to 300,000 cells/ml, fixed on slides with a Shandon cytospin 3 (Fisher Scientific, Waltham, MA, USA) at 1000 x g for 5 min, and stained with Giemsa (HEMA 3 Stain kit, Fisher Scientific Inc.). Eosinophils, neutrophils, lymphocytes, and macrophages were identified by morphology, and a minimum of 100 cells were counted per sample.

2.31 Analyses of BAL fluid cytokines

Cytokine (IL-9, IL-4, IFN-γ and Eotaxin-1) concentrations in BAL fluid supernatants were analyzed by ELISA (Gordon et al., 2005). Undiluted BAL fluid supernatants were used and each sample was assayed in duplicate. Biotinylated detection

antibodies and the recombinant protein standards (R & D Systems Inc, Minneapolis, MN) were used for all the cytokines. The cytokine levels were calculated using their respective cytokine standard curves. The cytokine values were normalized with PBS control values and expressed as pg/ml.

2.32 Analyses of serum OVA-specific immunoglobulins

OVA-specific immunoglobulin (Ig) (IgE, IgG1 and IgG2a) levels in serum were measured by ELISA (Gordon et al., 2005). Briefly, in a 96 well plate, wells were coated with anti-mouse IgG1, IgG2a or IgE antibodies (2 μg/ml) as a capture reagent, and the serum samples diluted 1:10 (IgE) or 1:100 (IgG1, IgG2a) in PBS were added to the wells. After PBS washes, to each well, biotinylated OVA was added as a detection reagent and the optical density was read at 405 nm. PBS was used as a negative control. Each sample was assayed in duplicate and the average values were normalized to the PBS control value. The data was represented as optical density.

2.33 Light microscopy

2.33.1 Tissue fixation

Following necropsy, soft tissues listed in *2.24* were collected from *Hyal3*$^{+/+}$ and *Hyal3*$^{-/-}$ mice and the same lobe or portion of tissue from each mouse was fixed either in 4% paraformaldehyde at 4°C (chapter three studies) or formalin at room temperature (chapters four and five studies) for 24 hrs. Joint from hind knee was fixed in 0.01 M periodate-0.075 M lysine-0.037 M paraformaldehyde fixative for 1 hr at room temperature followed by overnight at 4°C. Lungs collected from *Hyal3*$^{+/+}$ and *Hyal3*$^{-/-}$ mice for studies in chapter four were inflated at a pressure of 20 cm H_2O with 10%

buffered formalin before the tissues were fixed for 24 hrs at room temperature in the same fixative. Fixed tissues except calcium-containing tissues were washed with PBS and transferred to 70% ethanol until processing. Prior to processing, tissues containing calcium (knee joints, trachea and ribs) were decalcified in Immunocal (Amersham Mastertech) at 4°C, changing solution regularly until the tissues become completely soft. After decalcification, tissues were washed under running tap H_2O for 15 min and transferred to 70% ethanol for processing.

2.33.2 Tissue processing

Tissues for studies in chapter three were processed in an automated tissue processor, Citadel 1000 (Thermo Scientific) following the protocol outlined below. The process included dehydrating tissues for 1 hr in 50% ethanol, 70% ethanol and 95% ethanol. This was followed by 1½ hr in 3 changes of 100 % ethanol, 1 hr in 100% ethanol, ½ hr in xylene, 1 hr in xylene, 1½ hr in xylene. Finally tissues were infiltrated with 2 changes of paraffin wax for 1½ hr. Lung tissues for studies in chapter four were processed following the protocol outlined below. The process included 2 changes of 70% ethanol (4 hrs each), 80% ethanol (4 hrs), 2 changes of 95% ethanol and 100 % ethanol (2 hrs each), followed by 100% ethanol/xylene (50:50) (20 min), 2 changes of xylene (20 min each) and 2 changes of paraffin wax (2 hrs each).

2.33.3 Tissue embedding and sectioning

Following processing, tissues were embedded in paraffin wax using Histocentre 3 (Thermo Scientific) maintaining the same orientation of each tissue in *Hyal3*$^{+/+}$ and *Hyal3*$^{-/-}$ mice. The blocks were stored at room temperature until sectioning. Tissues were cut into sections of 6 μm thickness using a microtome and stained with different stains.

2.33.4 Tissue staining or immunohistochemistry

2.33.4.1 Haematoxylin and eosin (H & E) staining

Tissue sections were deparafinized by 5 min incubations in two changes of xylene and re-hydrated to water by 5 min incubations in two changes of 100% ethanol and 2 changes of 95% ethanol, followed by 3 and 5 min incubations in 70% ethanol and water respectively. Sections were stained in Mayer's Haematoxylin (Sigma) for 5 to 6 min and were washed in luke warm running tap water for 15 min. Tissue sections were incubated in 80% ethanol for 1 min followed by counterstaining with Eosin Y (Sigma) for 30 sec. Excess stain was removed by a 3 min incubation in 70% ethanol and the sections were dehydrated. For dehydration, sections were incubated for 3 min in 2 changes of 95% ethanol followed by 5 min incubations in 2 changes of 100% ethanol and 2 changes of xylene prior to mounting with Permount.

2.33.4.2 Alcian blue (pH 2.5) staining

Tissue sections were deparafinized, re-hydrated to water and incubated with 3% acetic acid for 3 min before staining with 1% Alcian Tetrakis (Sigma) in 3% acetic acid (pH 2.5) for 30 min at room temperature. After washing slides under running tap water for 10 min, they were incubated in distilled water for 3 min and counterstained with 0.1% nuclear fast red solution for 3 min at room temperature. Sections were dehydrated, and mounted with Permount.

2.33.4.3 Periodic acid-Schiff (PAS) staining

Mucus secreting goblet cells present in the tissue sections were stained with Periodic acid Schiff stain. Tissue sections were re-hydrated to water and treated with

periodic acid (Sigma) for 5 min at room temperature. After several rinses in distilled water, sections were incubated in Schiff's reagent (Sigma) for 15 min at room temperature with shaking, followed by washing slides under running tap water for 5 min. Sections were stained with Gills hematoxylin (Sigma) for 90 sec and the excess stain was removed by washing slides under tap water. Finally, sections were dehydrated, and mounted using Permount. Gills hematoxylin will stain nuclei as blue while the Periodic acid and Schiff's reagent stain mucus as purple to red.

2.33.4.4 Alcian blue pH 2.5 and PAS staining

Tissue sections were de-waxed, re-hydrated to water and stained with 1% alcian blue 8GX (Sigma) in 3% acetic acid (pH 2.5) for 30 min. After washing slides under tap water for 5 min, sections were incubated with periodic acid for 5 min. Sections were rinsed several times in dH_2O and incubated in Schiff's reagent for 15 min. Sections were washed in running tap water for 5 min before and after staining with Gills hematoxylin for 90 sec followed by dehydrating and mounting slides with Permount.

2.33.4.5 Picro-Sirius red staining

Collagen present in the tissue sections was detected using picro-sirius red (PSR) staining and polarization microscopy. The bifringence of collagen fibers was increased with 1% Sirius red stain (Direct Red 80, Sigma) prepared in saturated aqueous picric acid solution (Sigma). After the paraffin embedded tissue sections were de-waxed, re-hydrated to water, tissue sections were stained with PSR for 55 min at room temperature to get near equilibrium staining. Sections were dehydrated with 70%, 95% and 100% ethanol, followed by xylene prior to mounting with Permount. Stained tissue sections were

observed under bright field and polarized light microscopes. A single plane of polarized light was used for capturing images. All the images were captured at 200x final magnification.

2.33.4.6 HA immunohistochemistry

Semi-quantitative analysis of HA present in the lung sections was done using biotinylated HA-binding protein (Seikagaku America Inc., Rockville, MD). Lung tissue sections from *Hyal3*$^{+/+}$ and *Hyal3*$^{-/-}$ mice were de-waxed, re-hydrated to H_2O and the endogenous peroxidase activity was quenched by treating the slides with 3% H_2O_2 in water for 30 min at room temperature with shaking. After three PBS washes, each for 5 min, non-specific protein binding was blocked by incubating lung sections with 10% fetal calf serum (Associates of Cape Cod Inc.) in TBST for 30 min at room temperature, followed by blocking endogenous biotin sites using an Avidin-Biotin blocking kit (Vector Laboratories, Burlingame, CA), and following the manufacturer's instructions. After all the blocking steps, lung sections were incubated with biotinylated HA-binding protein (3.3µg/ml) in TBST overnight at 4°C. Unbound biotinylated HA-binding protein was removed by washing twice in TBST for 5 min and the sections were incubated with Avidin-Biotin-HRP Complex for 1 hr at room temperature following the manufacturer's instructions (Vectastain ABC, Vector laboratories, Burlingame, CA). After washing sections twice in TBST for 5 min each, sections were incubated with DAB substrate (Vector Laboratories) for 10 min at room temperature. Excess substrate was removed with a 5 min water wash and sections were counterstained with 0.1% nuclear fast red solution for 3 to 4 min. Sections were dehydrated and mounted. Control sections were digested with *Streptomyces hyaluronidase* (50U/ml, Sigma-Aldrich) in phosphate buffered saline

(PBS) pH 7.0 at 37°C overnight prior to endogenous peroxidase quenching. HA present in the tissue sections will be detected as brown colour pigment due to the DAB substrate used for detecting peroxidase enzyme activity. All the tissue images were captured at 200x and 1000x final magnifications.

2.33.5 Semi-quantitative histology scorings

A semi-quantitative scoring system was used for assessing infiltrating inflammatory cells, goblet cell hyperplasia, collagen thickness and HA content with H & E, PAS, PSR and HA-binding protein immunohistochemistry respectively. For H&E staining, scoring was done under 200x final magnification in peri-bronchial, peri-vascular and parenchymal regions of each airway from 0 to 4 (0=none, 1=occasional, 2=few, 3=moderate and 4=high number of infiltrating inflammatory cells). For PAS staining, scoring of goblet cell number was done under 200x and 1000x final magnifications in each airway from 0 to 4 (0=<5%, 1=5 to 25%, 2=25 to 50%, 3=50 to 75% and 4=> 75% of PAS positive cells) as previously described (Mascarenhas et al., 2004). For PSR staining, under 200x final magnification, collagen thickness in each airway was given a score from 0 to 4 (0=normal lung, 1=sparse, 2=mild, 3=moderate, 4=strong fibrosis). HA staining intensity was quantitatively assessed under 200x and 1000x final magnifications in each airway using scores from 0 to 4 (0=none, 1=sparse, 2=mild, 3=moderate and 4=strong HA staining).

2.34 Electron microscopy

Tissues were fixed for 24 hr at 4°C in a glutaraldehyde-containing fixative (2% glutaraldehyde, 2% paraformaldehyde, 0.1 M cacodylate, 0.01 M $CaCl_2$ and 0.15%

ruthenium red [pH 7.2]). This was followed by washing tissues using wash buffer (0.1 M sodium cacodylate, 0.01 M $CaCl_2$, 0.15% ruthenium red and 0.7% sucrose [pH 7.2]) for 5 min, 30 min and 1 hr, respectively, for first, second and third washes at room temperature. Tissues were post-fixed for 1 hr in 1% osmium tetroxide, 0.8% potassium ferricyanide and 0.5% ruthenium red, followed by three 5 min washes with ddH_2O to remove osmium tetroxide. Tissues were stained overnight with 2% uranyl acetate in ddH_2O, and washed three times with ddH_2O. After staining with uranyl acetate, tissues were dehydrated for 5 min in 10% acetone, 30% acetone, 50% acetone, 70% acetone in ddH_2O, and 10 min in 80% acetone, 90% acetone in ddH_2O, and followed by 2 changes in 100% ethanol for 15 min each. After dehydration, tissues were infiltrated with Spurr resin for 30 min in 25% spurr, 50% Spurr and 75% Spurr in acetone, followed by 1 hr in 100% Spurr. Tissues were embedded in plastic molds filled with 100% Spurr and incubated at 70°C for 24 to 30 hrs to let the resin solidify. Sections were cut in the histology lab of the Department of Human Anatomy and Cell Science (University of Manitoba) and viewed using a Philips CM 100 transmission electron microscope.

2.35 β-Hexosaminidase activity

Liver tissues were homogenized in PBS containing 0.1% Triton X-100 and protease inhibitors (Sigma-Aldrich Canada Ltd., Oakville, Ontario, Canada). Cell debris were removed by centrifugation and the protein concentration in the supernatant was determined using a Bio-Rad assay kit (Bio-Rad) based on the method of Bradford (1976) as described in *2.17.2*. Samples were diluted in 0.01 M phosphate citrate buffer (pH 4.4) containing 0.6 % bovine serum albumin and the total β-hexosaminidase activity was measured using 4-methylumbelliferyl-2-acetamido-2-deoxy-beta-D-glucopyranoside as a

substrate, as previously described (Shapira et al., 1989). Briefly, an equal volume of 2.5 mM substrate in 0.01M phosphate citrate buffer was added to diluted tissue extracts and was incubated at 37°C for 30 min in duplicate. The reaction was stopped by adding 1.0 ml of glycine carbonate buffer (0.17 M glycine, 0.17 M sodium bicarbonate [pH 9.8]) and the fluorescence was read at 360 nm excitation and 415 nm emission wavelengths respectively. Lysis buffer was used as negative control and the nmol of fluorescent product liberated was determined by using a standard curve with 20, 50, 100, 200 and 400 nmol of methylumbelliferone. Total β-hexosaminidase activity was calculated using the formula:

Total activity (nmol/hr/mg) = [(activity x dilution factor)/protein concentration] x 2.

2.36 Flow cytometry

Lymph node, spleen and thymus from naive *Hyal3*$^{+/+}$ and *Hyal3*$^{-/-}$ mice (8 months age, n=2) were collected into Dulbecco's Modified Eagle Medium (Gibco). Under sterile conditions, single cell suspensions from each tissue were prepared as described previously using a cell strainer (BD Falcon) positioned on top of a 50 ml conical tube, and the tissue was crushed with a syringe head. This was followed by adding more medium on top of the crushed tissue to allow the single cells to enter into the conical tube along with the medium. Samples were centrifuged and the cell pellet was collected. Cells were counted with hemocytometer and 10^6 cells were incubated with different fluorochrome-labelled antibodies against CD3, CD4, CD8, CD19, DX5, CD44 and CD62L (Biolegend, San Diego, CA), to probe T cells, B cells and NK cells. Samples were sorted on a FACS Canto II flow cytometer (BD Bioscience, Mississauga, ON, Canada) and the data

collected was analyzed by FlowJo Cytometry Analysis software (Tree Star Inc, Ashland, Oregon) (Liu et al., 2009).

2.37 Statistical analysis

Comparison of the genotype distribution and sex ratios was performed by Chi-Square analysis. Comparisons of serum HA levels, tissue GAG levels, body weights, organ weights, β-hexosaminidase activity and the changes in airway resistance at each concentration of methacholine were made using two-way Analysis of Variance (ANOVA) followed by the Bonferroni post-hoc test with genotype and gender as the variables. Significance of relationship between genotypes for real-time PCR data, BAL fluid cytokine and serum Ig levels, histological and immunohistochemistry scores, total and differential cell counts, and FACE results was tested using the unpaired t-test. Data analyses were performed using the GraphPad Prism 5 software (San Diego, CA) and the differences were considered significant when $P<0.05$. The results are presented as mean and ±SD for each group.

Chapter three: Generation and characterization of Hyal3$^{-/-}$ mice

Acknowledgements:

MRC Genome Resource Facility (Toronto, ON) provided PAC clone 452D10. Tim Salo and Brandy Wicklow generated pHL3 and pHLS1 subclones, respectively. Dr. Barb Triggs-Raine designed and made the *Hyal3* targeting construct, and screened ES cells. Ms. Marina Gertsenstein and Dr. Andras Nagy (Samuel Lunenfeld Research Institute, Toronto, ON) demonstrated and taught ES cell culturing and knockout methodologies to Dr. Barb Triggs-Raine. Dr. Dianna Martin and Dr. Richard Hemming assisted in mouse tissue collection, and Dr. Richard Hemming performed the western blotting and β-hexosaminidase activity assay. Total tissue GAG content was quantified by Dr. Sharon Byers laboratory (Women's and Children's Hospital, Adelaide, SA, Australia), Australia and joint histology was performed in John Mort's laboratory (Shriner's Hopsital for Children, Montreal, QC). Dr. Judy Anderson and Dr. Jim Thliveris (University of Manitoba) reviewed light and electron microscopy sections, respectively. Dr. Alex Gutsol reviewed light microscopy lung sections. The majority of the results in this chapter were published with my maiden name as Atmuri et al., 2008.

3.1 Introduction

HA is a large unbranched GAG comprised of repeating disaccharide units of N-acetyl D-glucosamine and D-glucuronic acid. It is an abundant component of the ECM of vertebrates, where it exists in free and bound forms (Day and Prestwich, 2002). Although the ubiquitous distribution of HA has complicated investigations of its functions, clear roles for HA as a structural molecule and as a mediator of cellular signal transduction were demonstrated in mice deficient in HA synthase 2 (Camenisch et al., 2000). Given the rapid turnover rate of HA, with approximately one-third or 5 g of the human body's HA turned over each day (Laurent and Reed, 1991b), and the critical functions of HA, hyaluronidase enzymes that initiate HA degradation are presumed to be essential (Roden et al., 1989).

Hyaluronidase was initially observed by Duran-Reynals as a "spreading factor" that facilitates the diffusion of subcutaneously injected vaccines, dyes and toxins (Meyer and Palmer, 1934). Through analyses of human genome sequences, hyaluronidases have been identified as members of a multigene family comprised of six paralogs, five of which predict protein products with approximately 40% identity. These sequences are localized as two clusters, on human chromosomes 3p21.3 (*HYAL2-HYAL1-HYAL3)* and 7q31.3 (*SPAM1-HYAL4-HYALP1*) (Csoka et al., 1999; Csoka et al., 2001). The equivalent clusters are found on mouse chromosomes 9F1 – F2 and 6A2, respectively (Csoka et al., 2001). In addition, the mouse has a seventh paralogue, *Hyal5*, on chromosome 6A2, downstream of *HyalP1* (Kim et al., 2005). Except for *HYALP1*, which is a pseudogene in humans, these genes have protein products that are known or suggested to be involved in HA and/or chondroitin sulfate degradation (Stern and Jedrzejas, 2006b).

In a rat model, intravenously injected HA is found to be degraded locally (10-30%) or is cleared from the tissues and degraded through the lymph nodes (50-90%). The remaining HA enters the blood stream where it is removed by the liver, kidney and spleen (Fraser and Laurent 1989). HA receptors that are required for the uptake of HA prior to degradation have been identified in these various tissues. The degradation of HA is primarily believed to take place in the lysosome, since the addition of ammonium chloride, a weak base that disrupts lysosomal function, prevents HA degradation (Culty et al., 1992). This lysosomal HA degradation is presumably initiated through the endoglycolytic action of hyaluronidases and sustained through the action of the lysosomal exoglycosidases, β-glucuronidase and β-hexosaminidase, which are able to cleave the individual sugar residues of HA from the non-reducing terminus (Roden et al., 1989).

Evidence suggesting hyaluronidases contribute to HA degradation was strengthened with the diagnosis of a patient with MPS IX (Natowicz et al., 1996). The absence of detectable HYAL1 activity due to mutations in its gene (Triggs-Raine et al, 1999) resulted in a 38 to 90 fold increase in serum HA and lysosomes in skin fibroblasts and macrophages from the MPS IX patient were filled with HA. Compared to patients with other MPS disorders, this patient displayed mild clinical features including soft masses near various joints, mild short stature, erosions of the hip joint, a flattened nasal bridge and submucosal cleft palate. The mild phenotype of this MPS IX patient despite the broad distribution of HA, and the identification of multiple hyaluronidases, suggested that other hyaluronidases play a major role in HA degradation. Among the family of hyaluronidases, only *HYAL1*, *HYAL2* and *HYAL3* are broadly expressed (Csoka et al, 1999). The identification of HYAL2 as a GPI-linked protein that is found in the plasma membrane of some cells (Rai et al., 2001) made HYAL3 a good candidate to play a role

in HA degradation based on its intracellular localization. We generated a mouse model with a deficiency of HYAL3 in order to evaluate its role in HA degradation. Herein we have characterized the basic macroscopic and microscopic characteristics of this model, focusing on the tissues with high *Hyal3* expression (Csoka et al., 1999) and/or high HA turnover (Fraser et al., 1997) for evidence of HA accumulation.

This chapter describes the design and construction of a *Hyal3* targeting construct, and the generation and phenotypic characterization of *Hyal3*$^{-/-}$ mice. The *Hyal3*$^{-/-}$ mice that were generated by this approach were apparently normal and no GAG accumulation was detectable, suggesting that under normal circumstances, *HYAL3* does not contribute significantly to HA degradation.

3.2 Results

3.2.1 Design and construction of the Hyal3 targeting vector

The construction of a *Hyal3* targeting vector (Figure 7) was facilitated by the availability of a previously mapped mouse genomic *129S1* PAC clone, 452D10, containing mouse *Hyal1*, *Hyal2* and *Hyal3* genes (Shuttleworth et al., 2002). Subclones from this clone, an 8.75 kb SalI/PmeI subclone containing *Hyal3*, pHL3, and a 10.8 kb SalI subclone containing *Hyal1*, pHLS1, were used as sources for the homologous arms of the targeting vector. The p*Hyal3*/TK/Neo targeting construct was designed to disrupt *Hyal3,* while having minimal impact on an overlapping gene, *Fus2* (N-acetyltransferase 6) (Shuttleworth et al., 2002). The second exon of *Fus2* is embedded within the first intron of *Hyal3*.

The *Hyal3* gene was disrupted by introducing a positive selection marker, a Neo cassette, under the control of the PGK promoter, into exon 2 of the *Hyal3* gene. The insertion was into an NsiI site, 40 bp downstream of the *Hyal3* initiation codon. This NsiI site was located downstream of the last exon of *Fus2*, and the insertion was expected to allow normal transcription of *Fus2* and *Hyal3*. However, the *Hyal3* transcripts would be abnormal and would not encode a functional protein. As a negative selection marker, the herpes simplex virus type I TK gene under the control of the PGK promoter was isolated from pGEM7TK (Adra et al., 1987), and introduced at the 3' end of the targeting vector. To increase the 5' homology to 3.7 kb, a 2.7 kb fragment from pHLS1 was inserted upstream of the *Hyal3* gene. The final p*Hyal3*/TK/Neo targeting construct contained 3.7 kb and 4.5 kb of 5' and 3' homology, respectively.

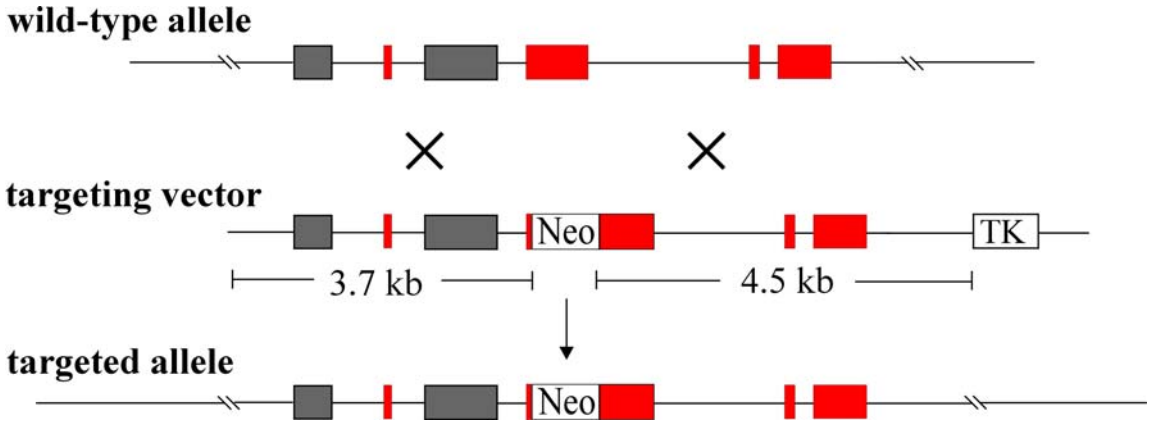

Figure 7: *Hyal3* targeting construct.

The *Hyal3* wild-type allele, targeting vector and targeted allele are represented as consecutive lines. Red and grey solid boxes, respectively, represent the exons of the *Hyal3* and *Fus2* genes; black lines represent the introns of *Hyal3* and *Fus2* genes. Inserted Neo and TK cassettes used as positive and negative selection markers are depicted as labeled open boxes. The regions of homology are indicated as 3.7 and 4.5 kb. "//' represents a break in the sequence. This figure is not drawn to scale.

The cloning procedure to construct the *Hyal3* targeting construct is shown schematically in Figure 8.

3.2.1.1 pHL3/TK

The first step in the construction of the targeting vector was the generation of the pHL3/TK by introducing a negative selection marker, TK, into a vector containing mouse *Hyal3,* pHL3. An 8.8 kb fragment from the pHL3 clone was prepared by restriction digestion with NotI, CIAP treatment to prevent recirculization of the plasmid, followed by fill-in of the 5' overhangs with DNA polymerase I. The 3.0 kb TK insert was prepared by digestion of pGEM7TK with restriction enzymes EcoRI and BamHI, followed by fill-in with DNA polymerase I, and gel purification. A 11.8 kb pHL3/TK plasmid was generated after ligation of the TK insert and the modified pHL3 plasmid (Figure 8, Step I). After

confirmation of the correct orientation of TK using SacI restriction enzyme, the clone was used for the second step.

3.2.1.2 pHL3/TK/Neo

The second step in the construction of the targeting vector was the introduction of a positive selection marker, Neo, to generate the pHL3/TK/Neo plasmid. A 4.6 kb Neo insert was prepared from the pGTN28 vector (New England Biolabs, Beverly, MA, USA) by restriction digestion with BamHI and CIAP treatment, followed by filling the in 5' overhangs with DNA polymerase I. A 12.1 kb pHL3/TK/Neo plasmid was generated by blunt-end ligation of the Neo insert with pHL3/TK plasmid that was modified with restriction enzymes, NsiI and SalI and filled in (Figure 8, Step II). After confirmation of a clone containing the Neo insert in the forward direction using SacI or BamHI/EagI restriction digestion, the clone was used for the third step.

3.2.1.3 pHL3/TK/Neo modified

The third step in the construction of the *Hyal3* targeting vector was the introduction of the 5' end of exon 2 of *Hyal3* immediately before the Neo cassette. A blunt-ended 1.2 kb fragment of exon 2 of *Hyal3* was generated by restriction digestion of pHL3 with NsiI/XbaI, followed by the removal of 3' overhangs using Vent DNA polymerase. A 13.3 kb modified pHL3/TK/Neo plasmid was generated by ligation of the *Hyal3* exon 2 insert and pHL3/TK/Neo plasmid digested with XhoI and filled in (Figure 8, Step III).

3.2.1.4 pHyal3/TK/Neo targeting construct

The final step in the generation of the *Hyal3* targeting construct was to increase the length of the 5' homologous arm to 3.7 kb. A 2.7 kb EcoRI/SalI fragment of pHLS1 was inserted into the pHL3/TK/Neo modified plasmid digested by NsiI/SalI and filled in. A clone with the correct orientation of the pHLS1 insert was identified by BamHI and NotI/SalI digestion. The final p*Hyal3*/TK/Neo targeting construct of 16 kb was generated (Figure 8, Step IV).

The final *Hyal3* targeting construct containing 3.7 kb and 4.5 kb of 5' and 3' homology, respectively, was linearized with NotI enzyme prior to electroporation into the ES cells.

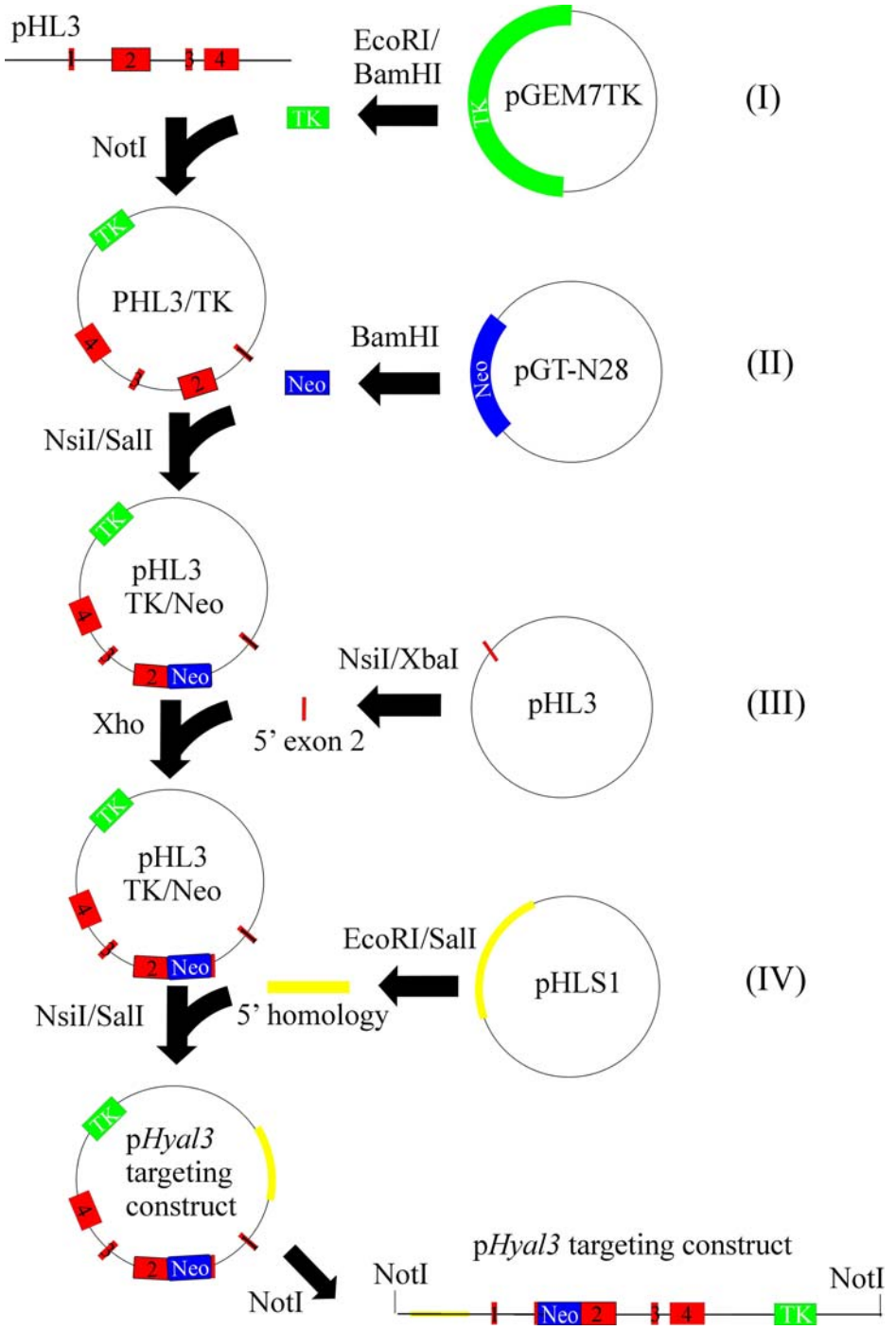

Figure 8: Cloning strategy of p*Hyal3*/TK/Neo targeting construct.

Red coloured boxes with numbers denote exons of *Hyal3* gene while blue or green coloured boxes represent positive and negative selection markers. The yellow lines denote the extended 5' region of homology. Restriction enzymes used in generating insert or vector fragments are indicated above solid black arrows. Roman numbers indicate the cloning step as described as described in *3.2.1*. This figure is not drawn to scale.

A screening strategy to identify ES cell clones in which the *Hyal3* locus had been correctly targeted was designed using NdeI and NsiI restriction enzyme digestions of genomic DNA, followed by Southern analyses using 3' external, 5' external and Neo probes (Figure 9). In NdeI-digests, correctly targeted clones were identified by an increase in the DNA fragment size from 10.9 kb to 12.9 kb because of the insertion of a 2 kb Neo cassette. The targeted and wild-type alleles were identified by the presence of 12.9 kb and 10.9 kb NdeI digested fragments, respectively, using the 5'and 3' external probes. In NsiI digests, correctly targeted clones were identified by the loss of an NsiI site in exon 2 of *Hyal3*, resulting in 18.4 kb fragment.

The results were also confirmed by Southern analysis of NsiI digested genomic DNA using 5'and 3' external probes and a Neo probe. The targeted and wild-type alleles were identified by the presence of 18.4 kb and 4.4 kb bands using the 5' external probe and the presence of 18.4 kb and 12 kb fragments with the 3' external probe (Figure 9). The occurrence of only one Neo-integration per cell was confirmed by the presence of one 12.9 kb NdeI and one 18.4 kb NsiI band using the Neo probe (Figure 9). No band is detected in the wild-type allele using the Neo probe.

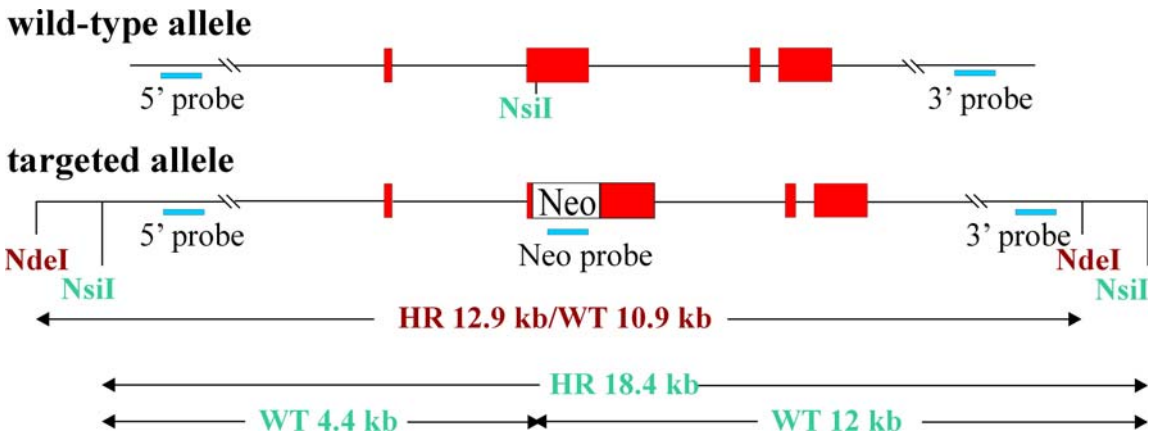

Figure 9: *Hyal3* screening strategy.

The *Hyal3* wild-type allele, targeting vector and targeted allele are represented as consecutive lines. Large red solid boxes and black lines represent the exons and introns of the *Hyal3* gene. Inserted Neo and TK cassettes used as positive and negative selection markers are depicted as labeled open boxes. Small blue solid boxes below the lines represent the probes used for Southern hybridization. NdeI and NsiI are the restriction enzyme digestion sites used to generate DNA fragments of sizes listed for wild-type (WT) and homologous recombinant (HR) alleles. "//' represents a break in the sequence.

3.2.2 ES cell targeting and confirmation

The final *Hyal3* targeting construct was introduced into R1 ES cells and the DNA isolated from 98 G418-resistant gangcyclovir sensitive clones were screened for the Neo targeted allele using the 5' external probe (data not shown). Ten putative clones containing the targeted allele were identified, and were re-screened with the 3' external (Figure 10A and B) and the Neo probes (Figure 10A and C). Out of ten clones re-screened, seven clones (BB1, PA2, BG9, RC1, PC1, BB5 and GF5) were identified as correctly targeted by the presence of an 18.4 kb NsiI digested fragment using the 3' external (Figure 10A and B; wild-type fragment is 12 kb) and Neo (Figure 10A and C; no wild-type fragment) probes. The frequency of homologous recombination that occurred was identified to be about 8%. Only three clones were used subsequently to generate

Hyal3$^{-/-}$ mice.

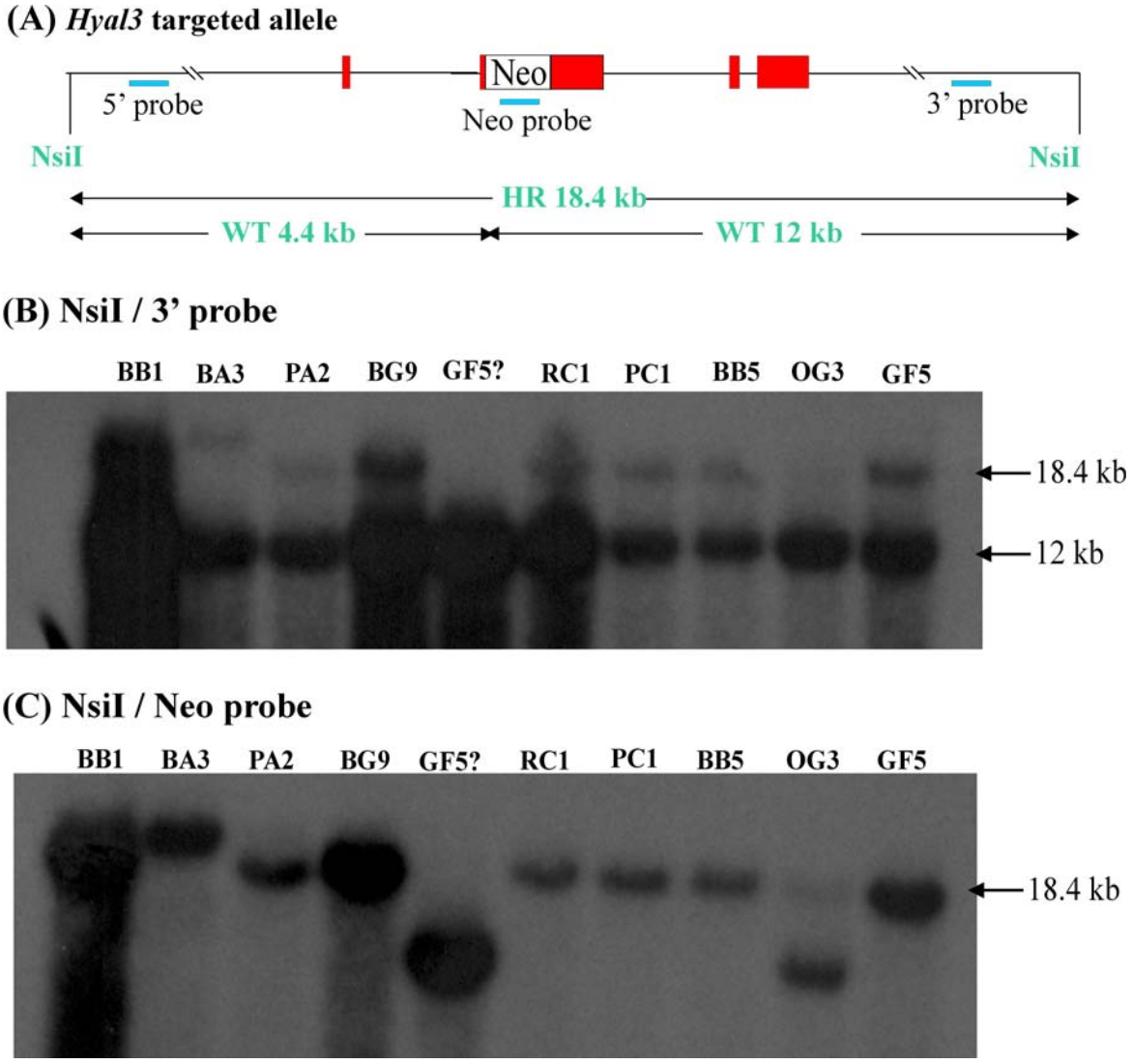

Figure 10: Screening of *Hyal3* targeted ES cells by Southern analysis.

(A) A schematic representation of the *Hyal3* screening strategy and the expected fragment sizes with NsiI restriction enzyme digestion of the WT and HR alleles are shown. Large orange solid boxes and black lines, respectively, represent the exons and the introns of the *Hyal3* gene. The Neo cassette is depicted as a labeled open box and the small solid blue boxes below the lines represent the probes used for Southern analyses. "//" represents a break in the sequence. **(B** and **C)** DNA isolated from 10 putative correctly targeted ES cell clones are digested with NsiI and screened for the correct targeting event using the **(B)** 3' external and the **(C)** "Neo" probes. ES cell clones with the *Hyal3*-targeted allele were identified by the presence of 18.4 and 12 kb bands and only the 18.4 kb and using the "Neo" probe.

3.2.3 Generation of Hyal3$^{-/-}$ mice

Three independently targeted ES cell lines (*129S1*), BG9, BB5 and PA2, were aggregated with *CD1* embryos and implanted into pseudo-pregnant *CD1* female mice at the Sunnybrook Health Sciences Centre, Toronto, Ontario, Canada. For BG9 and BB5 cell lines, chimeras with germ line transmission of the targeted *Hyal3* allele were obtained. No chimeras with germ line transmission of the targeted allele were obtained for PA2. Once the germ line transmitting chimeras (BB5 and BG9) were identified, they were shipped to Central Animal Care Services at the University of Manitoba. BG9 and BB5 chimeras were crossed with *CD1* female mice to generate two independent lines of mixed background (*CD1;129S1*). The BG9 chimera was also crossed with *129S1* female mice (Charles River Laboratories, Quebec, Canada) to generate a congenic *129S1* line.

The genotypes of offspring mice were initially identified by Southern analysis of DNA isolated from liver tissue. The *Hyal3* targeted and wild-type alleles in these *Hyal3* mice were identified using NdeI (Figure 11) and NsiI (Figure 12) restriction enzyme digestions by 5' and 3' external probes and the Neo Probe. The occurrence of only one Neo-integration per cell was confirmed by the presence of one 12.9 kb (Figure 11D) or 18.4 kb (Figure 12D) fragment, respectively, using the Neo probe after NdeI or NsiI restriction enzyme digestion.

Using the NdeI restriction enzyme, the genotypes of mice were identified by the presence of only the 10.9 kb wild-type band (*Hyal3*$^{+/+}$), only the 12.9 kb neo-targeted band (*Hyal3*$^{-/-}$) or both the 12.9 and 10.9 kb bands (*Hyal3*$^{+/-}$). Using the NsiI restriction enzyme, the genotypes of mice were identified by the presence of only the 4.4 kb/12 kb wild-type band (Hyal3$^{+/+}$), only the 18.4 kb Neo-targeted band (Hyal3$^{-/-}$) or both the 4.4 kb/12 kb and 18.4 kb bands (Hyal3$^{+/-}$).

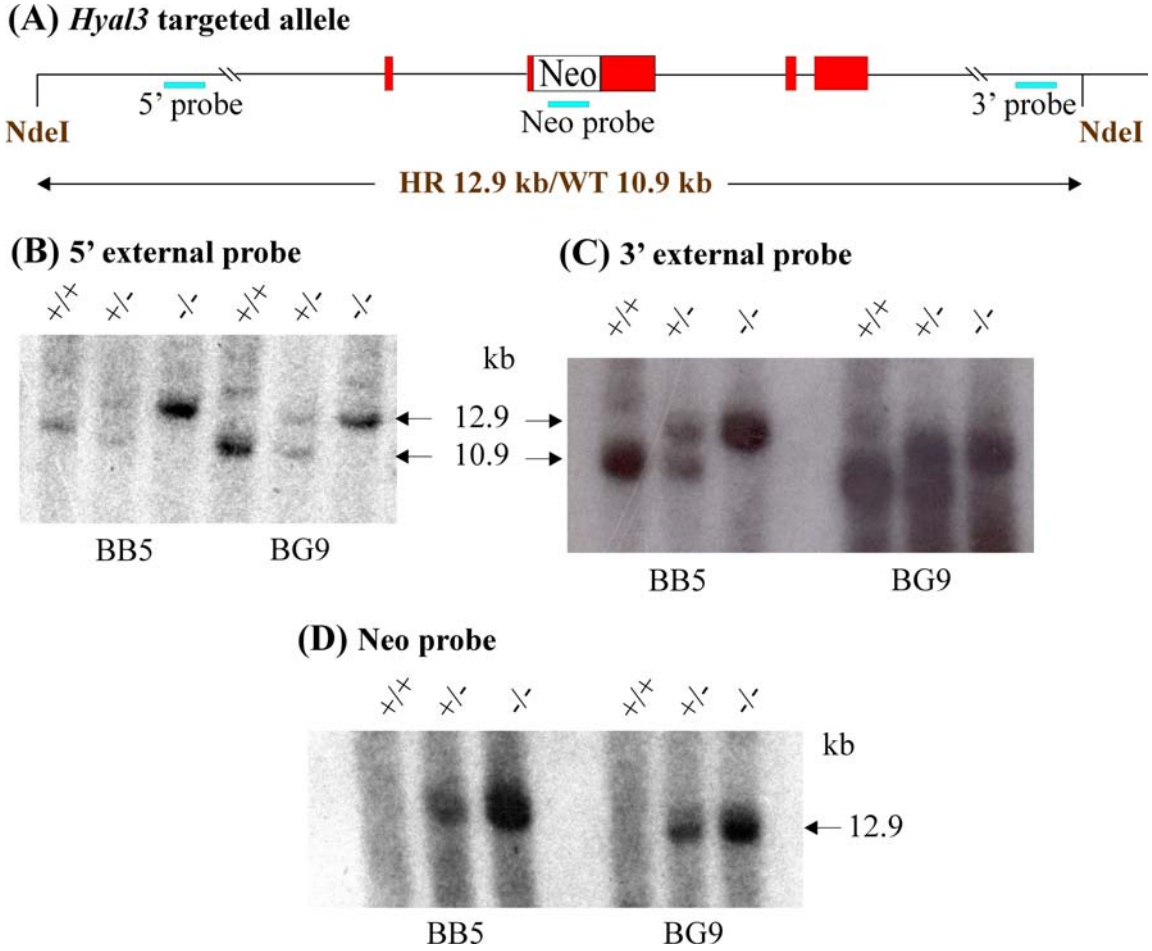

Figure 11: Characterization of the *Hyal3* targeted mutation by Southern analysis (NdeI digestion). (A) A schematic representation of the *Hyal3* screening strategy and the expected fragment sizes for WT and HR alleles with NdeI restriction enzyme digestion. Large orange solid boxes and black lines, respectively, represent the exons and the introns of the *Hyal3* gene. The Neo cassette is depicted as a labeled open box and the labelled small blue solid boxes below the lines represents the probes used for Southern analyses of genomic DNA isolated from mouse liver, and digested with NdeI restriction enzyme. Using the 5' **(B)** and 3' **(C)** external probes, the HR allele was detected as a 12.9 kb band and the WT allele as a 10.9 kb band. Mice were identified as +/+ (only 10.9 kb band), -/- (only 12.9 kb band) and +/- (both 12.9 and 10.9 kb bands). **(D)** Using the "Neo" probe, the HR allele was detected as a 12.9 kb band in +/- and -/- mice and no band in +/+ mice. BB5 and BG9 represent correctly targeted ES cell clones used to generate two independent lines of mice.

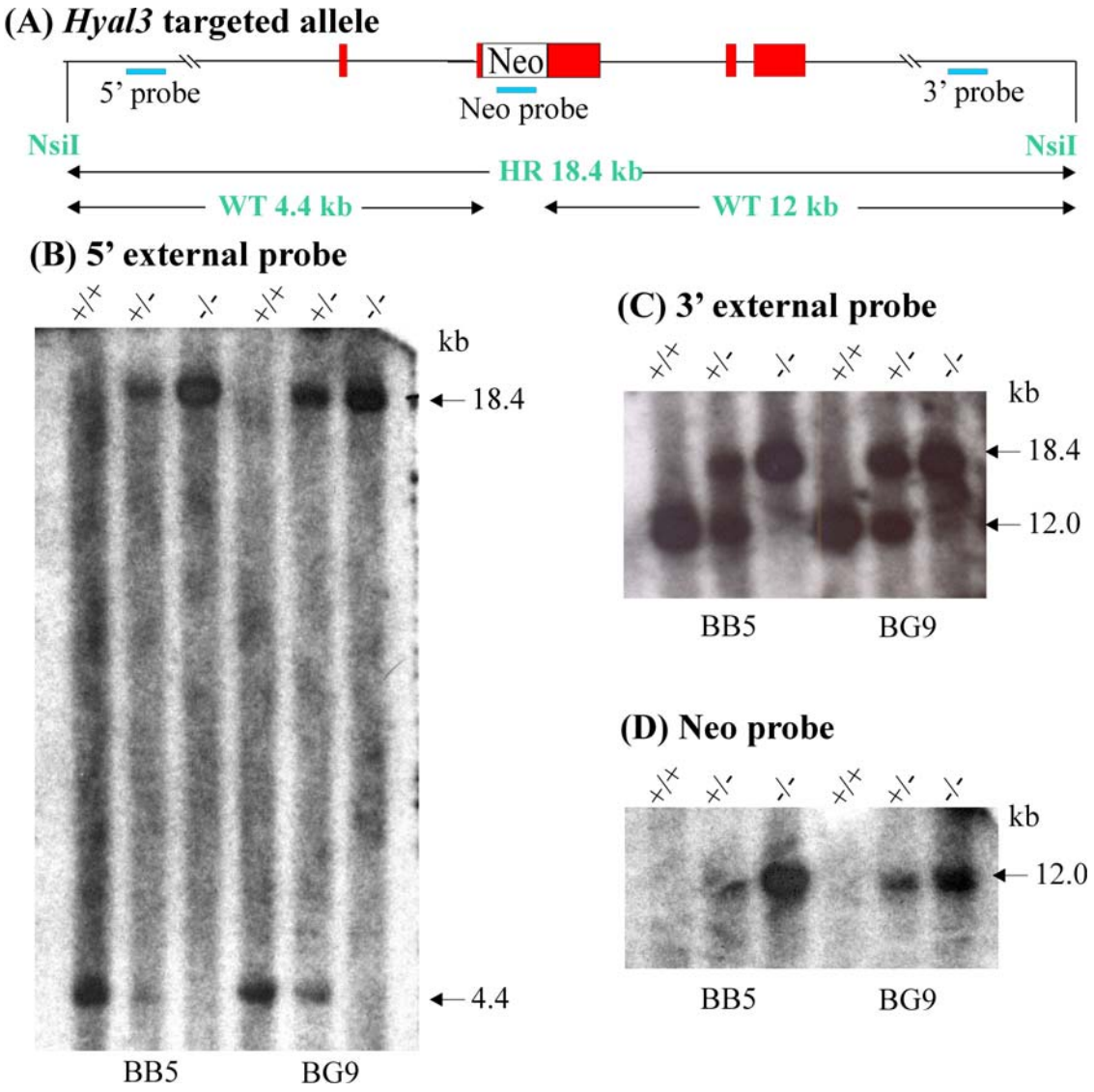

Figure 12: Characterization of the *Hyal3* targeted mutation by Southern analysis (NsiI digestion). (A) A schematic representation of the *Hyal3* screening strategy and the expected fragment sizes for WT and HR alleles with NsiI restriction enzyme digestion. Large orange solid boxes and black lines, respectively, represent the exons and the introns of the *Hyal3* gene. The inserted Neo cassette is depicted as a labeled open box and the labelled small blue solid boxes below the lines represent the probes used for Southern analyses of NsiI-digested genomic DNA isolated from mouse liver. **(B)** Using the 5' external probe, the HR allele was detected as an 18.4 kb band, and the WT allele as a 4.4 kb band. Mice were identified as +/+ (only 4.4 kb band), -/- (only 18.4 kb band) and +/- (both 4.4 and 18.4 kb bands). **(C)** Using the 3' external probe, the HR allele was identified as an 18.4 kb band while the WT allele produced a 12 kb band. Mice were identified as +/+ (only 12.0 kb band), -/- (only 18.4 kb band) and +/- (both 12.0 and 18.4 kb bands). **(D)** Using the "Neo" probe, the HR allele was detected with only the 18.4 kb band in +/- and -/- mice and no band in +/+ mice. BB5 and BG9 represent correctly targeted ES cell clones used to generate two independent lines of *Hyal3* mice.

Southern analysis was later replaced by PCR amplification of tail-clip DNA for routine genotyping. PCR amplification using allele-specific primers identified the *Hyal3*-targeted and wild-type alleles as 1.0 kb and 0.5 kb bands respectively (Figure 13). The genotypes of mice were identified by the presence of only the 0.5 kb wild-type band ($Hyal3^{+/+}$), only the 1.0 kb neo-targeted band ($Hyal3^{-/-}$) or both the 0.5 and 1.0 kb bands ($Hyal3^{+/-}$).

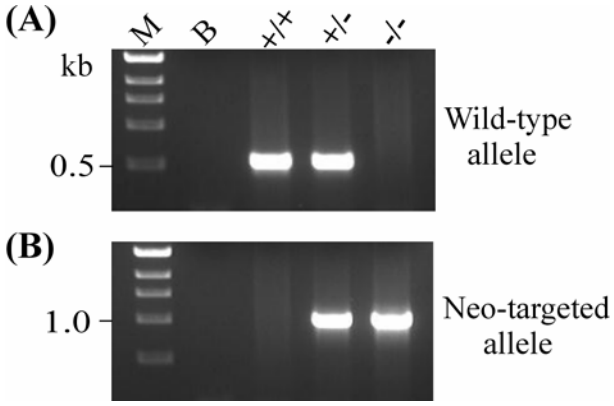

Figure 13: Genotyping of *Hyal3* mice.

The genotypes of *Hyal3* mice were determined by PCR amplification of tail-clip genomic DNA with **(A)** wild-type allele specific primers (WPG 623 and WPG 624) and **(B)** neo-targeted allele specific primers (WPG 621 and WPG 622). Genotypes of mice were identified by the presence of only the 0.5 kb fragment (+/+), only the 1.0 kb fragment (-/-) or both 0.5 and 1.0 kb fragments (+/-). M- molecular-weight marker; B- no template control.

3.2.4 Analysis of the expression of Hyal3 and Fus2 from the targeted locus

To determine how the *Hyal3*-targeting event affected the expression of *Hyal3* and *Fus2*, transcript levels of these genes were examined by real-time RT-PCR using total RNA isolated from testis and liver of 8 to 12 month-old $Hyal3^{-/-}$ and $Hyal3^{+/+}$ mice as templates. Testis was chosen because this tissue has a high level of both *Hyal3* and *Fus2*

expression; liver was chosen as the non-reproductive tissue with the highest expression of both *Hyal3* and *Fus2* (Shuttleworth et al., 2002).

3.2.4.1 Analysis of Hyal3 expression

Real-time RT-PCR studies with primers that span the boundary between exon 2 and exon 3 of *Hyal3* (Taqman assay; Mm00662097_m1) were used to demonstrate the *Hyal3* transcript levels in the testis and liver tissues of $Hyal3^{+/+}$ and $Hyal3^{-/-}$ mice. The expression levels of *Hyal3* in the testis and liver of $Hyal3^{+/+}$ and $Hyal3^{-/-}$ mice were calculated and represented by the mean (±SD) ΔC_T values of *Hyal3* transcripts in $Hyal3^{-/-}$ mice as a proportion of the mean (±SD) ΔC_T values of *Hyal3* transcripts in $Hyal3^{+/+}$ mice. In the testis, the level of *Hyal3* transcripts was reduced by approximately one-third in the testis of $Hyal3^{-/-}$ mice (mean 0.69 ± SD 0.03) compared to $Hyal3^{+/+}$ controls (1.0 ± 0.08) (Figure 14A, n=3, **P=0.001). However, in the liver, the levels of *Hyal3* transcripts detected in $Hyal3^{-/-}$ mice (1.10 ± 0.09) were not significantly different from $Hyal3^{+/+}$ mice (1.0 ± 0.11) (Figure 14A, n=4, P=0.23). This real-time RT-PCR data suggests that $Hyal3^{-/-}$ mice still have either reduced or normal levels of *Hyal3* transcripts.

The presence of *Hyal3* transcripts in $Hyal3^{-/-}$ mice was expected, but in order to confirm that these were aberrant *Hyal3* transcripts, they were characterized by conventional reverse transcription (RT)-PCR. Using sense and antisense primers flanking the *neo* insertion site, and within exon 2 (primers A and B in Figure 14B), PCR products (920 bp) were generated only from the cDNA of $Hyal3^{+/+}$ mice (Figure 14C, top panel). PCR products were not generated from the cDNA of the $Hyal3^{-/-}$ mice under any of the conditions that were tested, indicating that normal *Hyal3* transcripts are absent in the $Hyal3^{-/-}$ mice. To confirm that the *Hyal3* transcripts produced in the $Hyal3^{-/-}$ mice

contained some part of *neo*, the cDNA was amplified with a sense primer (Primer "C" in Figure 14B) within *neo* and an antisense primer (Primer "D" in Figure 14B) that spanned the junction of *Hyal3* exons 2 and 3. Amplification using these primers was only detected in the cDNA generated from *Hyal3*$^{-/-}$ testis and not *Hyal3*$^{+/+}$ testis (Figure 14C, bottom panel).

Taken together, the real-time and conventional RT-PCR data showed that the testis and liver of *Hyal3*$^{-/-}$ mice contained no detectable normal *Hyal3* transcripts, but did have *Hyal3* transcripts containing the neo insertion.

3.2.4.2 Analysis of Fus2 expression

To determine how the *Hyal3*-targeting event affected the expression of *Fus2*, a gene that is embedded with in *Hyal3* gene, real-time RT-PCR studies were performed using primers within exon 2 of *Fus2* (Taqman assay, Mm01947825_S1). Real-time RT-PCR studies demonstrated that *Fus2* transcripts in the testis of *Hyal3*$^{-/-}$ mice (0.50 ± 0.27) were not significantly altered compared to the transcript levels in *Hyal3*$^{+/+}$ testis (1.0 ± 0.49) (Figure 14D, n=3, P=0.22). However, the levels of *Fus2* transcripts in the liver of *Hyal3*$^{-/-}$ mice (0.80 ± 0.12) were reduced by approximately 20% compared to the transcript levels in the liver of *Hyal3*$^{+/+}$ mice (1.0 ± 0.06) (Figure 14D, n=4, P=0.03). This reduced *Fus2* trascript levels in liver should be considered while assessing *Hyal3*-deficient mouse phenotype.

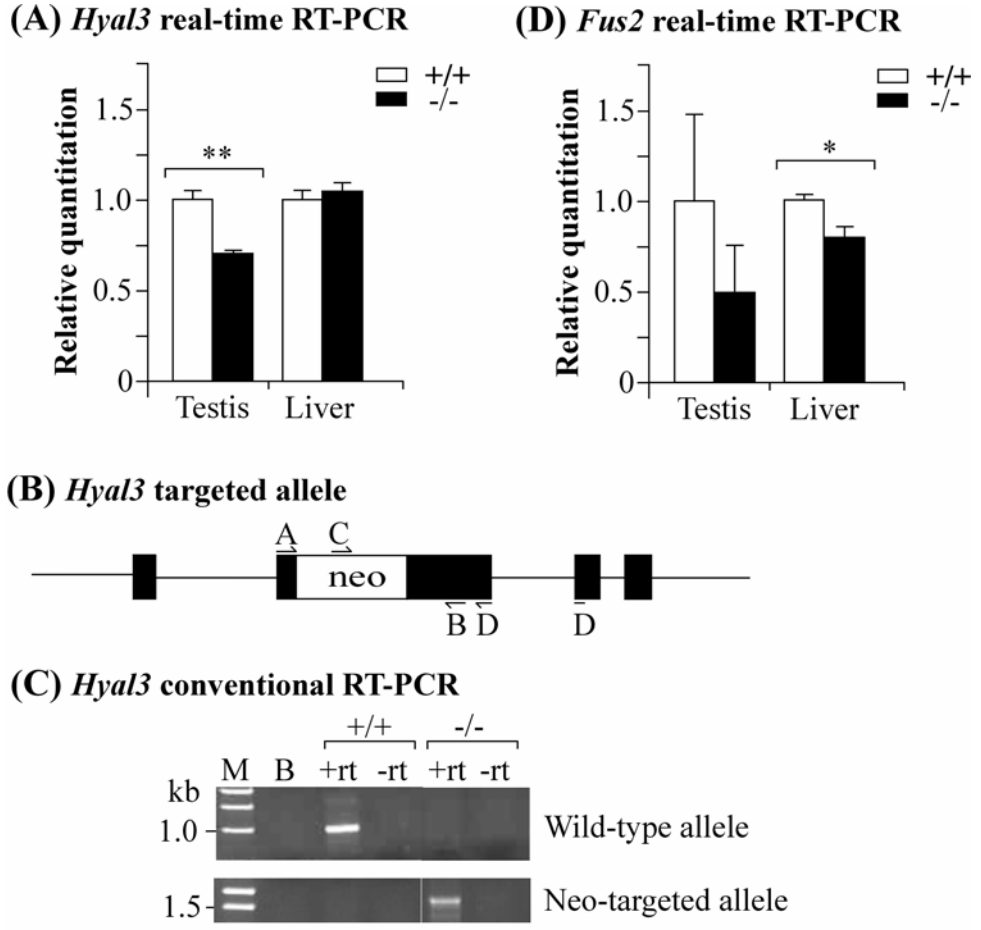

Figure 14: Characterization of *Hyal3* and *Fus2* transcripts.

(A) Expression levels of *Hyal3* in the testis and liver of $Hyal3^{+/+}$ and $Hyal3^{-/-}$ mice are represented by the mean (±SD) ΔC_T values of *Hyal3* transcripts in $Hyal3^{-/-}$ mice as a proportion of the mean (±SD) ΔC_T values of *Hyal3* transcripts in $Hyal3^{+/+}$ mice (n=3, **P=0.001 [testis]; P=0.23 [liver]). "n" represents the number of animals from each group. In each animal, each sample was analyzed in triplicate two times. **(B)** Schematic of the positions of PCR primers used to characterize the neo-targeted *Hyal3* allele by conventional RT-PCR. Exons are shown as solid boxes, introns as straight lines and the neo insertion as an open box. The position of primers are shown as arrows and labeled as "A", "B", "C" and 'D". **(C)** Characterization of *Hyal3* transcripts by conventional RT-PCR. Total RNA isolated from the testis of $Hyal3^{+/+}$ and $Hyal3^{-/-}$ mice was reverse-transcribed and PCR-amplified using primer sets specific for the wild-type (A and B) and the targeted allele (C and D). M- 1 kb DNA ladder, B- control without cDNA, -rt - cDNA without reverse transcriptase and +rt - cDNA with reverse transcriptase. **(D)** Expression levels of *Fus2* in the liver and testis of $Hyal3^{+/+}$ and $Hyal3^{-/-}$ mice represented by the mean (±SD) ΔC_T values of *Fus2* transcripts in $Hyal3^{-/-}$ mice as a proportion of the mean (±SD) ΔC_T values of *Fus2* transcripts in $Hyal3^{+/+}$ mice (n=3; P=0.22 [testis], *P=0.03 [liver]). "n" represents the number of animals from each group. In each animal, each sample was analyzed twice and in triplicates.

3.2.5 Analysis of Hyal3 protein levels in Hyal3$^{+/+}$ and Hyal3$^{-/-}$ mice

Studies showing the presence of abnormal *Hyal3* transcripts in *Hyal3*$^{-/-}$ mice led us to try to confirm the absence of Hyal3 at the protein level. It is likely that the *Hyal3* transcripts detected in *Hyal3*$^{-/-}$ mice originate in the neomycin resistance gene, under the control of the PGK promoter. These transcripts would not have exon 1 or the beginning of exon 2 of *Hyal3,* since this is where the neo cassette is inserted. The abnormal transcripts would not direct the synthesis of any normal Hyal3 protein. Unfortunately, Hyal3 protein levels in normal mice were not sufficient to convincingly detect the protein using western blot analysis. Using an anti-Hyal3 antibody, no differences could be detected in the protein profiles of tissues from *Hyal3*$^{+/+}$ and *Hyal3*$^{-/-}$ mice. Therefore, the absence of Hyal3 could not be confirmed in *Hyal3*$^{-/-}$ mouse tissues by western analysis (Figure 15).

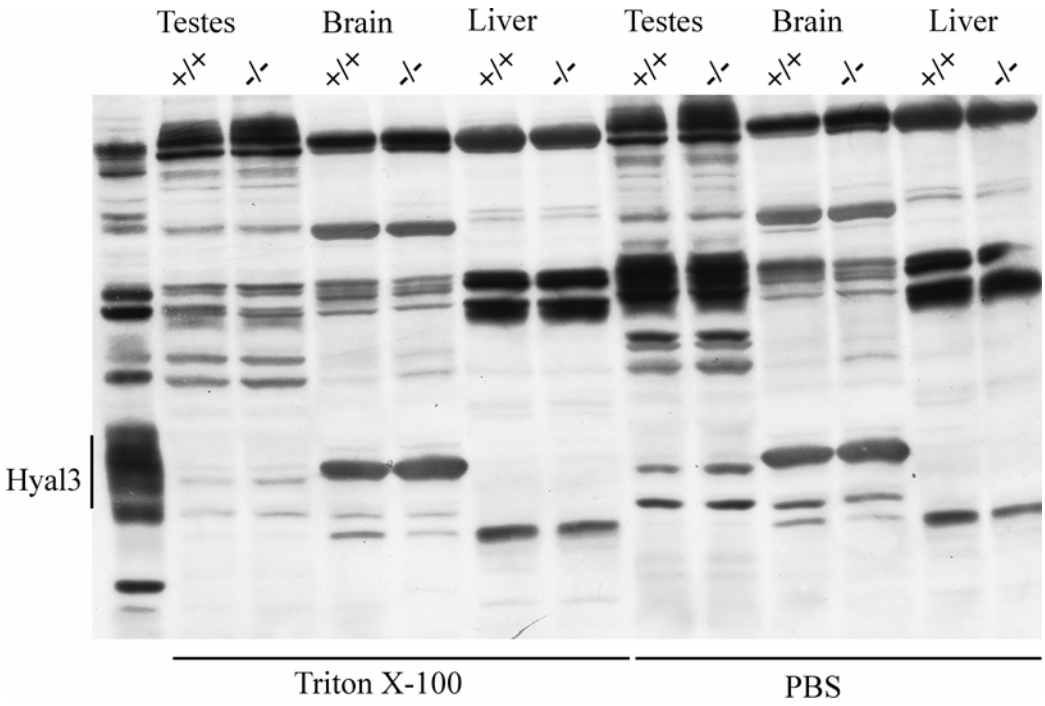

Figure 15: Western analysis of Hyal3 protein in *Hyal3*$^{+/+}$ and *Hyal3*$^{-/-}$ mice.
Extracts prepared from *Hyal3*$^{+/+}$ and *Hyal3*$^{-/-}$ mice tissues were immunoblotted with an anti-Hyal3 antibody. No difference was identified between the proteins detected in any of the tissues examined indicating the endogenous Hyal3 protein could not be detected even in wild-type tissues.

3.2.6 Macroscopic phenotype of Hyal3$^{-/-}$ mice

Hyal3$^{-/-}$ mice of both *CD1;129S1* and *129S1* background appeared healthy and normal in appearance up to 18 months-of-age, the latest time point examined. Both males and females were fertile and litter sizes appeared normal. Combined data from crosses between *Hyal3* heterozygotes (+/-) of both mixed and congenic background resulted in offspring with a normal Mendelian ratio of *Hyal3*$^{+/+}$, *Hyal3*$^{+/-}$ and *Hyal3*$^{-/-}$ mice (χ^2=0.45, P=0.80, n=146). There was no difference from the expected 1-to-1 ratio of affected male to female offspring (χ^2=1.34, P=0.25, n=146). X-ray analysis of the skeleton of 12 to 14 month-old *Hyal3*$^{+/+}$ and *Hyal3*$^{-/-}$mice (n=5), and visual examination of joints did not reveal any obvious abnormalities.

The total body weights of *Hyal3*$^{+/+}$ and *Hyal3*$^{-/-}$ mice aged for 6 months and 12 months were also analyzed. At 6 months age, there was no difference between the total body weights of male (n=6, mean 39.18 g ± SD 7.41) or female (n=7, mean 36.45 g ± SD 5.05) *Hyal3*$^{-/-}$ mice compared to male (n=6, mean 38.5 g ± SD 3.0) or female (n=7, mean 36.1 g ± SD 3.7) *Hyal3*$^{+/+}$ mice, respectively (P>0.05, Figure16). In addition, total body weigths of 12 month-old mice were also analyzed. No significant difference was observed in the total body weigths of male *Hyal3*$^{+/+}$ (n=6, mean 46.7 g ± SD 3.99) and *Hyal3*$^{-/-}$ (n=6, mean 44.77 g ± SD 3.47) mice or female *Hyal3*$^{+/+}$ (n=5, mean 38.89 g ± SD 3.65 and *Hyal3*$^{-/-}$ (n=5, mean 42.82 g ± SD 2.22) mice (P>0.05, Figure 16).

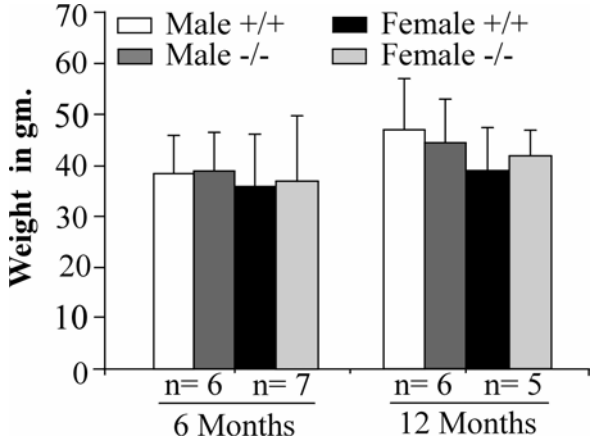

Figure 16: Total body weights of *Hyal3*$^{+/+}$ and *Hyal3*$^{-/-}$ mice.

The total body weights of *Hyal3*$^{+/+}$ and *Hyal3*$^{-/-}$ mice aged for 6 months or 12 months were weighed at the time of termination and no difference was observed between genotypes in male or female mice. "n" represents the number of animals in each group. Data represent the mean ±SD ($p>0.05$).

At necropsy, organ morphology and size appeared normal. Organs collected from *Hyal3*$^{+/+}$ and *Hyal3*$^{-/-}$ mice at the time of mouse euthanasia were weighed and analyzed. Weights of brain (n=11, 0.48 g ± 0.03), heart (n=11, 0.20 g ± 0.07), liver (n=10, 1.37 g ± 0.34), lungs (n=11, 0.22 g ± 0.04), kidneys (n=11, 0.54 g ± 0.10), spleen (n=10, 0.125 g ± 0.10) and testes (n=6, 0.248 g ± 0.05) from *Hyal3*$^{+/+}$ mice were comparable to the weights of brain (n=15, 0.46 g ± 0.03), heart (n=11, 0.207 g ± 0.07), liver (n=11, 1.48 g ± 0.34), lungs (n=11, 0.24 g ± 0.04), kidneys (n=11, 0.53 g ± 0.10), spleen (n=11, 0.146 g ± 0.10) and testes (n=6, 0.265 g ± 0.05) from *Hyal3*$^{-/-}$ mice ($P>0.05$, Figure 17). There was no difference observed in any of the organ weights analyzed indicates that there was no organomegaly in *Hyal3*$^{-/-}$ mice at 12 months-of-age. Thus, *Hyal3*$^{-/-}$ mice have no obvious gross phenotype and lack the skeletal features that were identified in the MPS IX patient.

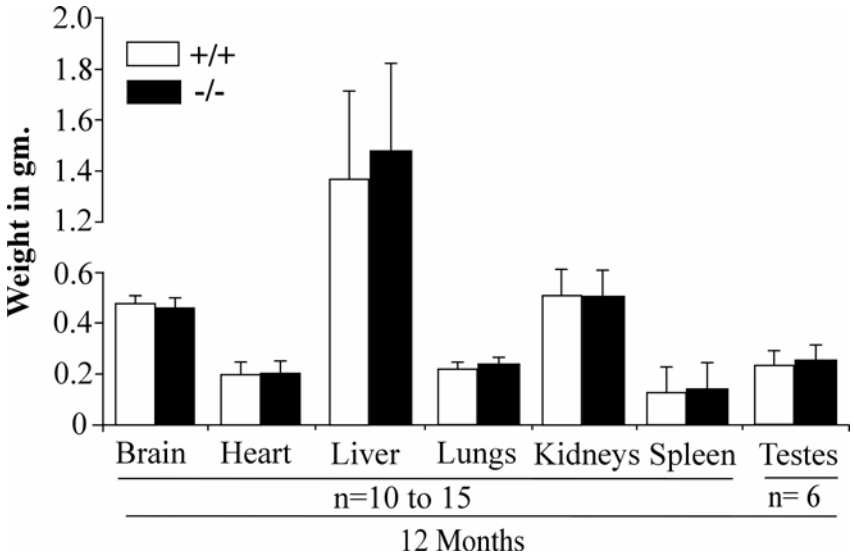

Figure 17: Organ weights of *Hyal3*$^{+/+}$ and *Hyal3*$^{-/-}$ mice.

Organs of *Hyal3*$^{+/+}$ and *Hyal3*$^{-/-}$ mice aged for 12 months were collected at the time of mouse euthanasia and weighed. No significant difference was observed between the organ weights of *Hyal3*$^{+/+}$ and *Hyal3*$^{-/-}$ mice. Data represent the mean ±SD (P>0.05). "n" represents the number of animals in each group.

3.2.7 Analysis of serum and tissue GAG and/or HA accumulation

3.2.7.1 ***Serum HA concentration***

The elevated serum HA level (38 to 90 fold normal) in the MPS IX patient suggested that serum HA concentration would be a reliable indicator of HA accumulation. Therefore, to analyze serum HA, blood samples were collected from *Hyal3*$^{+/+}$ and *Hyal3*$^{-/-}$ mice of both mixed and congenic background at the time of mouse euthanasia by heart puncture and serum samples were prepared. HA levels in serum samples collected from *Hyal3*$^{+/+}$ and *Hyal3*$^{-/-}$ mice were analyzed using a HA-binding protein based sandwich ELISA assay. Serum HA levels of the mixed line exhibited large variations making these results difficult to compare. However, no statistically significant elevation in HA ($p>0.05$) was identified in *Hyal3*$^{-/-}$ mice compared to *Hyal3*$^{+/+}$ mice matched for age, strain and

gender even in the congenic *129S1* mice that exhibited less individual variation (Figure 18). These results indicate that *Hyal3*$^{-/-}$ mice lack the serum HA elevation characteristic of the MPS IX patient.

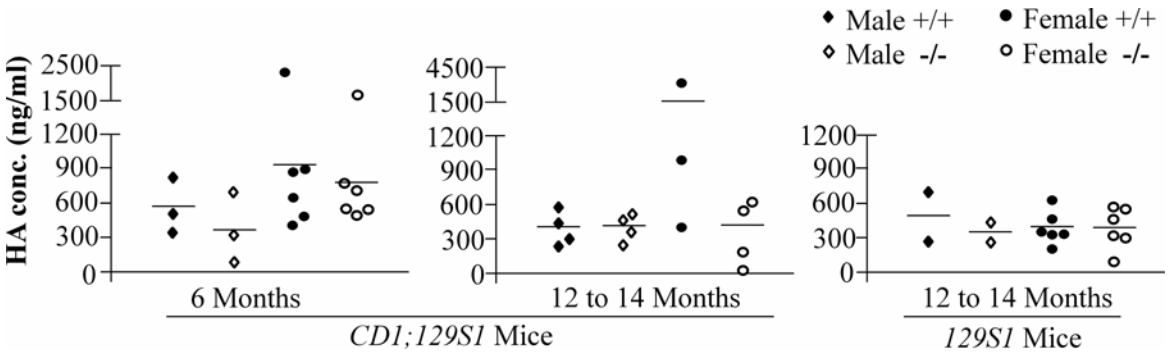

Figure 18: Analysis of serum HA in *Hyal3*$^{+/+}$ and *Hyal3*$^{-/-}$ mice.

HA levels in serum samples of *Hyal3*$^{+/+}$ and *Hyal3*$^{-/-}$ mice from *CD1;129S1* and *129S1* lines were analyzed using HA-binding protein based ELISA. Each point in the graph represents the value of an individual animal and the horizontal line represents the mean value. No difference was observed in the HA levels between the serum samples of *Hyal3*$^{+/+}$ and *Hyal3*$^{-/-}$ mice (P>0.05).

3.2.7.2 ***Tissue GAG concentration***

Tissue GAG content was examined to determine whether any tissues from the *Hyal3*$^{-/-}$ mice exhibited GAGs accumulation. Total GAGs were determined in tissues with high rates of HA turnover (liver, kidney, spleen and skin) and *Hyal3* expression (testis) (Shuttleworth et al., 2002), as well as lung, fat and seminal vesicle. GAG content was estimated using an assay for uronic acid that would detect both HA and chondroitin sulfate, the two substrates of hyaluronidase (Stern and Jedrzejas, 2006b). The GAG content in the tissues of 12-14 month-old *Hyal3*$^{+/+}$ and *Hyal3*$^{-/-}$ mice of *CD1;129S1* line were analyzed. The GAG content in liver (n=6, 34.65 µg ± 21.05), lungs (n=6, 52.8 µg ±

75.72), kidneys (n=4, 35.1 µg ± 17.41), spleen (n=4, 52.16 µg ± 48.26), skin (n=4, 19.0 µg ± 2.43), fat (n=4, 7.53 µg ± 4.54), testes (n=3, 27.5 µg ± 18.41), seminal vesicles (n=3, 25.89 µg ± 17.13) of *Hyal3*$^{+/+}$ mice were comparable to the GAG content in the liver (n=6, 32.8 µg ± 6.78), lungs (n=6, 105.4 µg ± 86.7), kidneys (n=4, 50.55 µg ± 38.79), spleen (n=4, 117.85 µg ± 46.58), skin (n=4, 35.13 µg ± 22.95), fat (n=4, 14.99 µg ± 8.58), testes (n=3, 158.31 µg ± 97.49) and seminal vesicles (n=3, 53.03 µg ± 21.74) of *Hyal3*$^{-/-}$ mice (P>0.05, Figure 19).

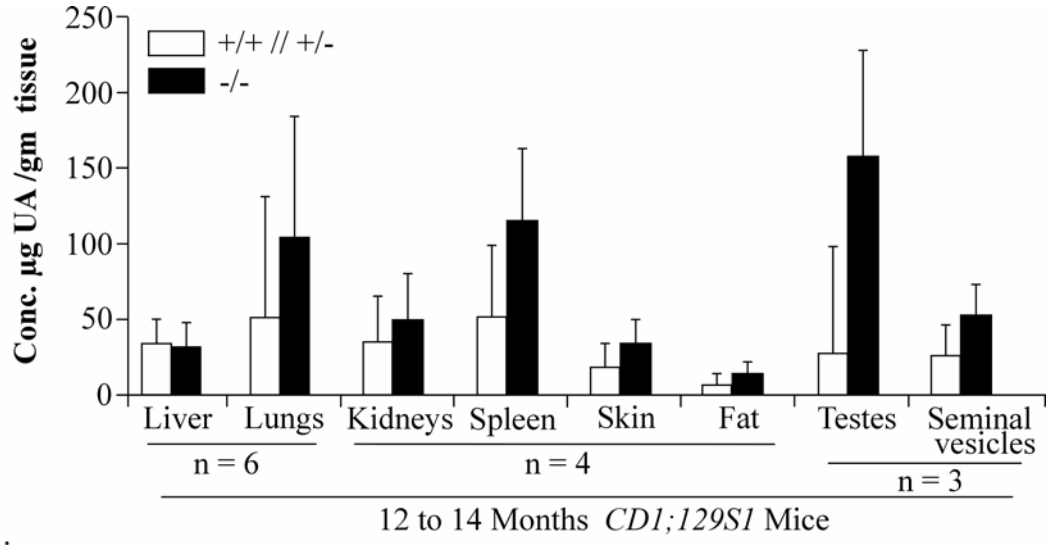

Figure 19: Analysis of total tissue GAGs in *Hyal3*$^{+/+}$ and *Hyal3*$^{-/-}$ mice.

Total tissue GAGs content in *Hyal3*$^{+/+}$ and *Hyal3*$^{-/-}$ mice of *CD1;129S1* line was determined by uronic acid assay and no significant difference between the genotypes was observed in any of the tissues analyzed. However, GAGs content in lungs, spleen and testes appeared to be elevated in *Hyal3*$^{-/-}$ mice compared to *Hyal3*$^{+/+}$ mouse tissues. Data represent the mean ±SD (p>0.05). "n" represents the number of animals in each group.

3.2.8 Histological studies

A broad range of tissues were collected from *Hyal3*$^{+/+}$ and *Hyal3*$^{-/-}$ mice that were aged for 6 months or 12-14 months. The tissue sections that were stained with

hematoxylin and eosin were analyzed by light microscopy. The tissues included for the analyses were liver, skin, lung, brain, fat, testis, seminal vesicle, ovary, uterus, kidney, heart, muscle, eye and lymph node. Sagittal sections of cerebellum, fore brain, heart, testes, kidney, uterus, spleen and transverse sections of eye, skin, liver, lymph node, skeletal muscle, seminal vesicle and joints were analyzed from *Hyal3*$^{+/+}$ and *Hyal3*$^{-/-}$ mice. In each tissue of *Hyal3*$^{+/+}$ and *Hyal3*$^{-/-}$ mice, general tissue morphology, with particular scrutiny for extracellular or intracellular vacuolation (HA accumulation) was examined. No evidence of vacuolation was identified in any of the tissues from *Hyal3*$^{-/-}$ mice that were analyzed. In addition, no consistent difference in the overall tissue organization or the connective tissue organization, thickness or cellularity was identified between the tissues of *Hyal3*$^{-/-}$ and *Hyal3*$^{+/+}$ mice except subtle changes in the lung. A representative field selected from each tissue analyzed from one of the *Hyal3*$^{+/+}$ and *Hyal3*$^{-/-}$ mice (12-14 month-old) is shown in Figure 20.

The skeletal system is often affected in mucopolysaccharidoses because of the abundance of GAGs in skeletal tissues. Indeed, the MPS IX patient displayed acetabular erosion and nearby fluid-filled masses. The role of *Hyal3* in joints was assessed by examining sections of knee-joint tissues from *Hyal3*$^{-/-}$ mice at 12-14 months-of-age (*CD1;129S1*, n=3). Joint sections were stained with toluidine blue which detects tissue proteoglycans (Figure 20). Joint-tissue sections were also stained for proteoglycans with Safranin O (n=1, data not shown) or for HA by immunostaining for HA-binding protein (n=1, data not shown). Overall, no difference was observed between the knee-joint tissues from the *Hyal3*$^{+/+}$ and *Hyal3*$^{-/-}$ mice, indicating that HYAL3 does not have a major role in GAG degradation in the joints.

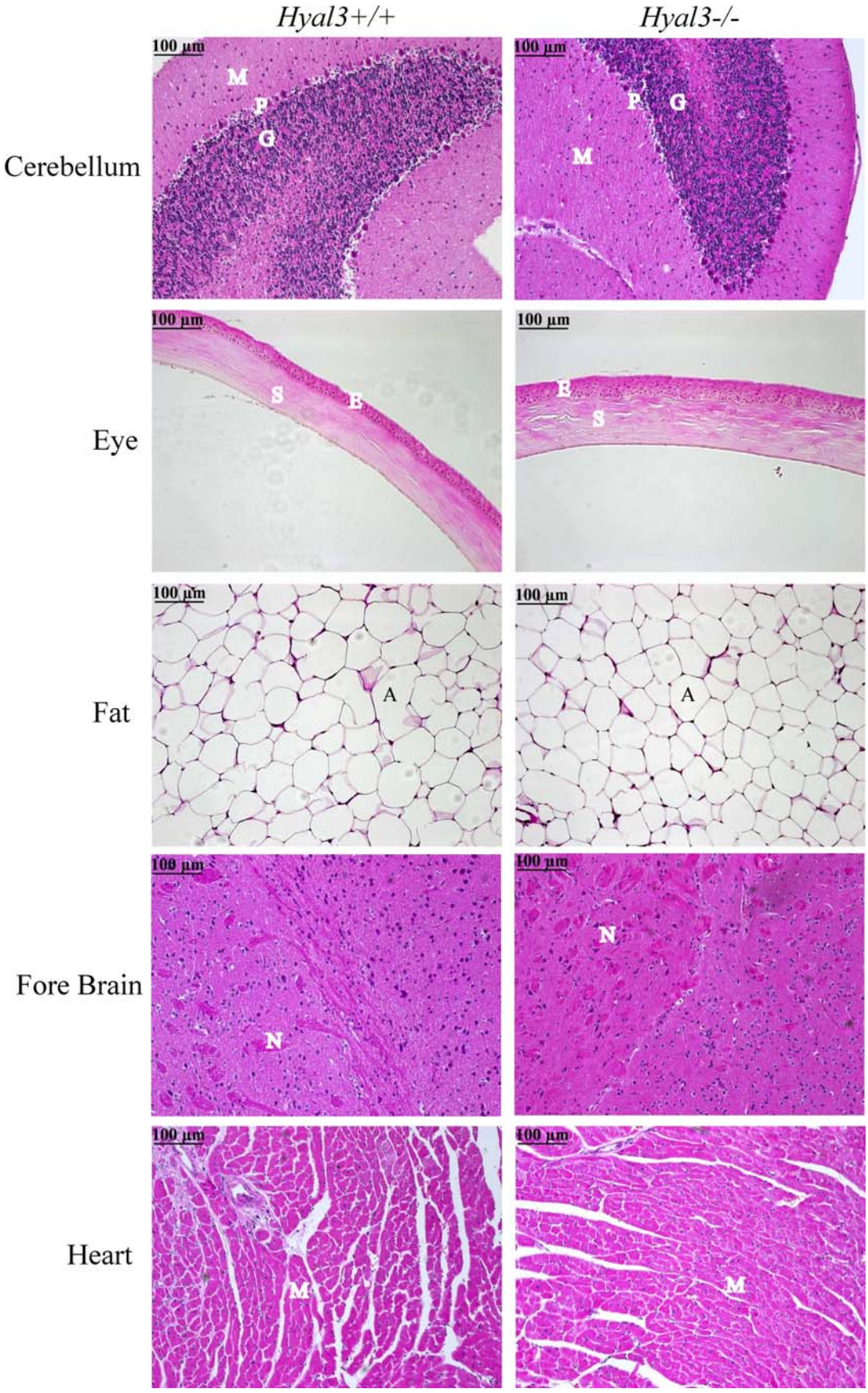
Hyal3+/+
Hyal3-/-
Cerebellum
Eye
Fat
Fore Brain
Heart
100 µm
M
P
G
S
E
A
N

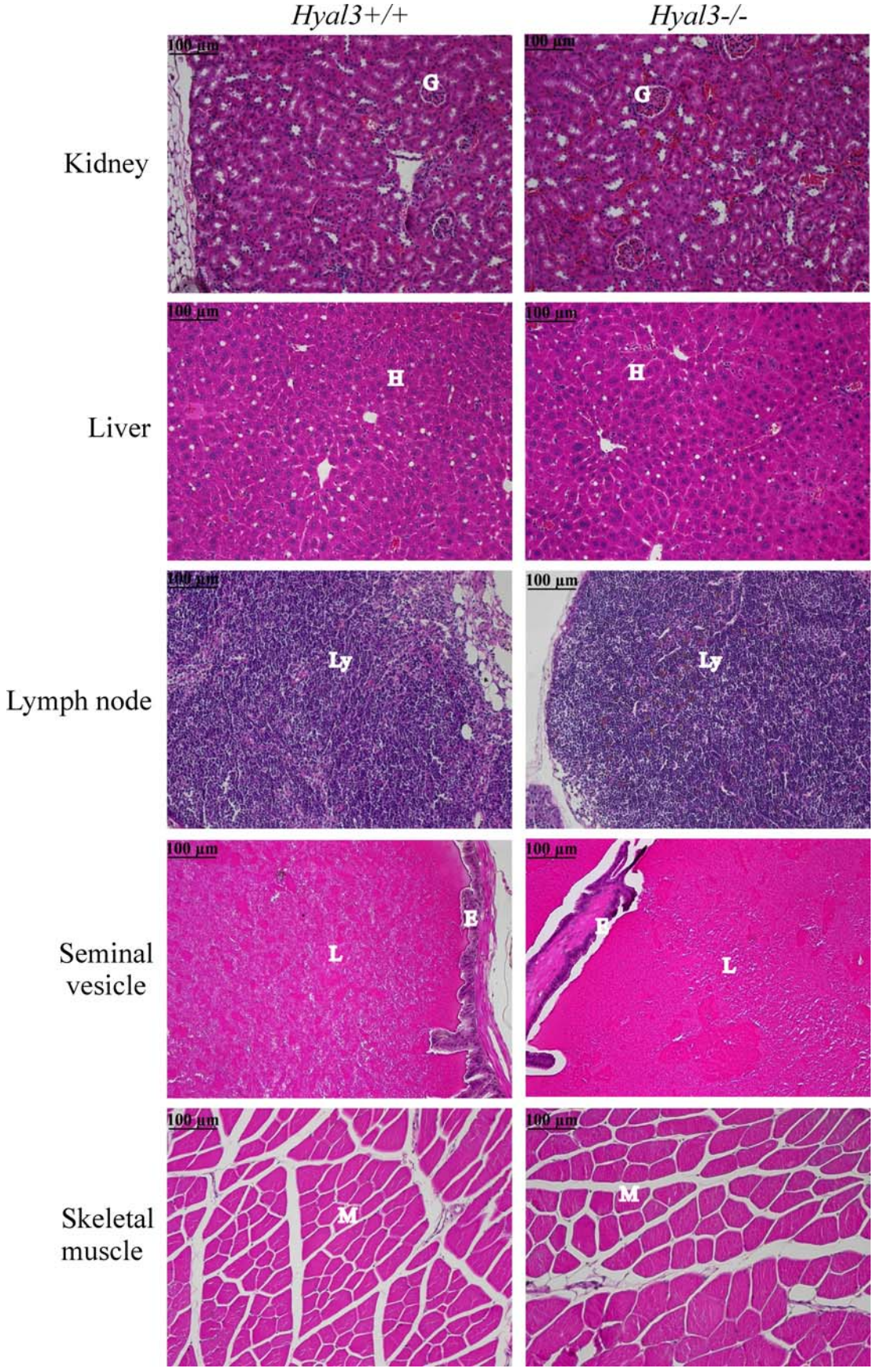
Hyal3+/+
Hyal3-/-
Kidney
Liver
Lymph node
Seminal vesicle
Skeletal muscle
100 µm
G
H
Ly
E
L
M

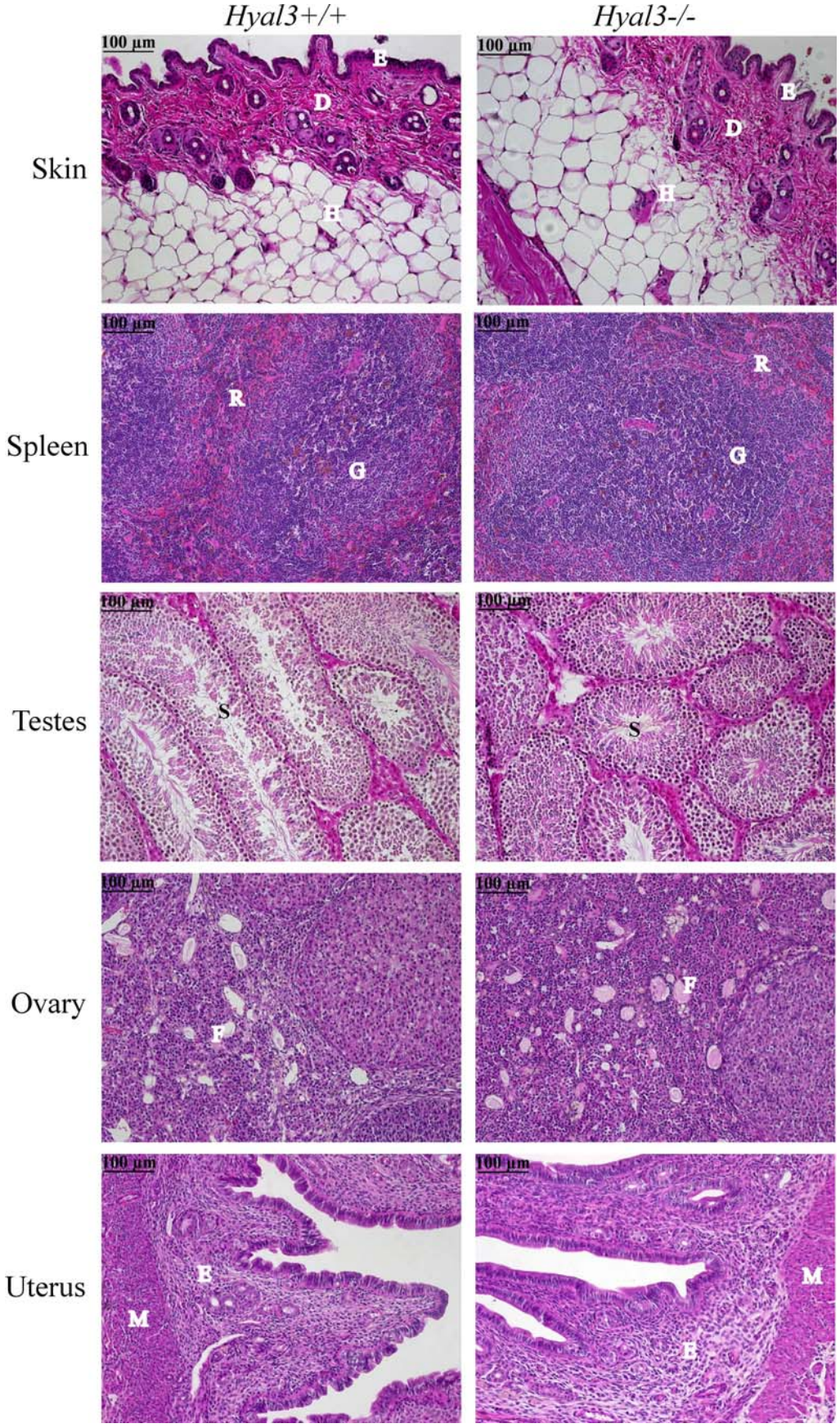
Hyal3+/+
Hyal3-/-
Skin
Spleen
Testes
Ovary
Uterus
100 μm
E
D
H
R
G
S
F
M

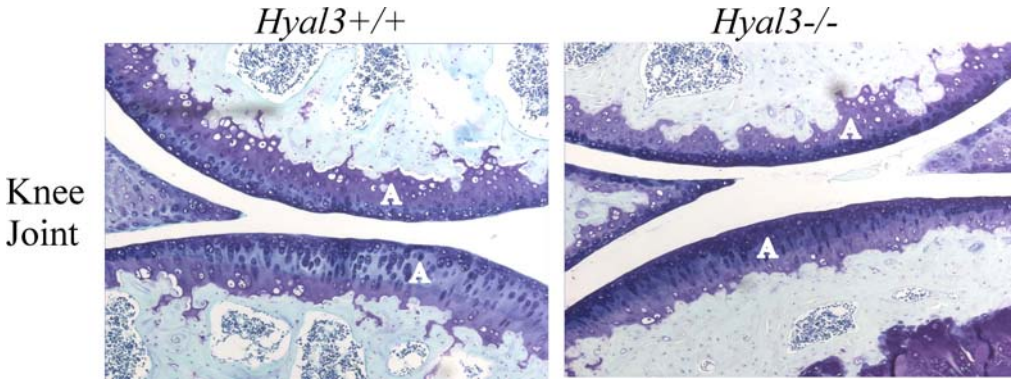

Figure 20: Light microscopy of all major tissues of *Hyal3*$^{+/+}$ and *Hyal3*$^{-/-}$ mice.

No obvious difference was observed in the histology of any of the tissues analyzed in *Hyal3*$^{+/+}$ and *Hyal3*$^{-/-}$ mice (12 to 14 month-old, n=6). "n" represents the number of animals from each group. One representative field from *Hyal3*$^{+/+}$ and *Hyal3*$^{-/-}$ mouse tissues such as cerebellum (G-granule cell layer, M-molecular cell layer and P-Purkinje cells), eye (S-corneal stroma and E-epithelium), fat (A-adipocytes), fore brain (N-neurons), heart (M-cardiac myocytes), kidney cortex (G-glomerulus), liver (H-hepatocytes), lymph node (Ly-lymphocytes in lymphatic nodule), seminal vesicle (L-lumen and E-epithelium), skeletal muscle (M-muscle fibres), skin (E-epidermis, D-dermis and H-hypodermis), spleen (R-red pulp and G-germinative centre), testes (S-seminiferous tubules), ovary (F-follicles), uterus (E-endometrium and M-myometrium) and knee joint (A-articular cartilage) are shown. All the tissues, except knee joint, were stained with hematoxylin and eosin and knee joints were stained with toluidine blue.

Lung tissues from 12-14 month-old *Hyal3*$^{+/+}$ and *Hyal3*$^{-/-}$ mice (*129S1*, n=6) were analyzed for structural changes and cellular vacuolation. In each lung from an individual animal, atleast 10 fields with well spread alveoli were selected randomly and analyzed in a blinded fashion to compare between the genotypes. Although there was no evidence of cellular vacuolation, lungs from 12-14 month-old *Hyal3*$^{-/-}$ mice displayed air space enlargement (Figure 21B) compared to lungs from *Hyal3*$^{+/+}$ mice (Figure 21A). The proportion of the lungs with thickened interstitium was large in *Hyal3*$^{-/-}$ mice (Figure 21C) compared to the lungs in *Hyal3*$^{+/+}$ mice.

In addition, preliminary studies were also performed on lung tissues from *Hyal3*$^{+/+}$ and *Hyal3*$^{-/-}$ mice at 6 months-of-age (*CD1;129S1,* n=2). Lung sections of *Hyal3*$^{-/-}$ mice showed more alveoli without septae (Figure 21E) compared to the lungs from *Hyal3*$^{+/+}$ mice (Figure 21D).However, quantitative studies were not possible as the lungs from 6 month-old and 12-14 month-old mice were not inflated for fixation. Further studies are required to confirm and extend these findings.

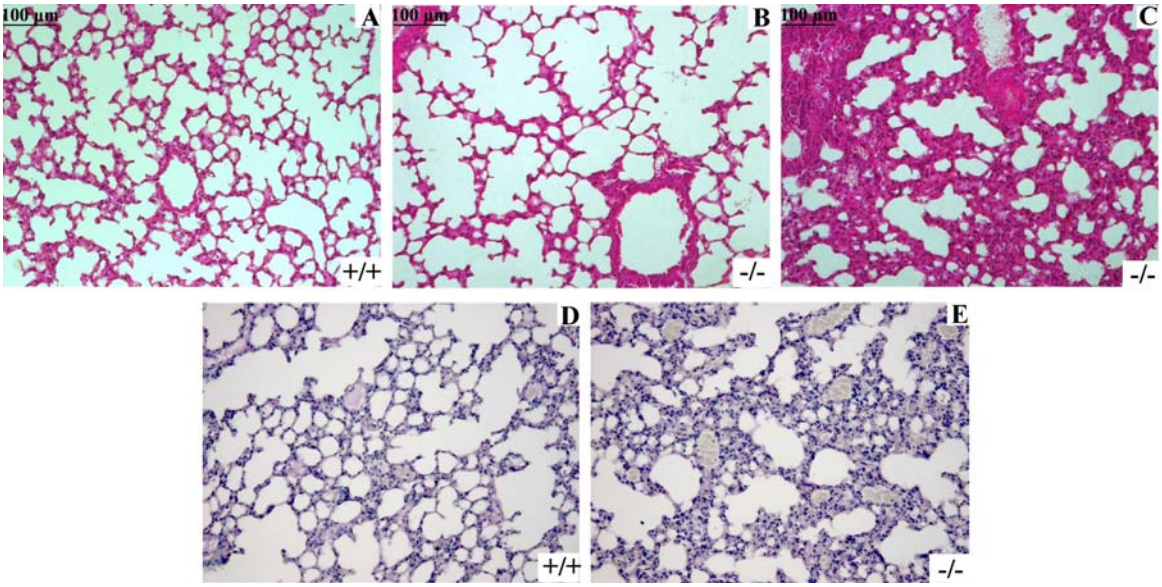

Figure 21: Histology of *Hyal3*$^{+/+}$ and *Hyal3*$^{-/-}$ mouse lungs.

A comparison of lung tissues from 12 to14 month-old **(A)** *Hyal3*$^{+/+}$ and **(B, C)** *Hyal3*$^{-/-}$ mice revealed **(B)** air space enlargement and more areas of **(C)** thickened ECM in *Hyal3*$^{-/-}$ lungs compared to *Hyal3*$^{+/+}$ lungs (n=6). A comparison of lung tissues from 6 month-old *Hyal3*$^{+/+}$ mice **(D)** and *Hyal3*$^{-/-}$ mice **(E)** revealed more alveoli without septae in *Hyal3*$^{-/-}$ mice compared to *Hyal3*$^{+/+}$ mice (n=2). "n" represents the number of animals from each group and in each animal atleast 10 fields were analyzed in a blinded fashion. One representative field of each tissue from *Hyal3*$^{+/+}$ and *Hyal3*$^{-/-}$ mice is shown.

Subsets of the tissues with high rates of HA turnover (lymph node and liver) in addition to the lung tissue were collected from *Hyal3*$^{+/+}$ and *Hyal3*$^{-/-}$ mice and processed for transmission electron microscopy. These tissues were analyzed for the ultra structural

changes. There was no evidence of cellular vacuolation in any of the *Hyal3*$^{-/-}$ tissues analyzed from 12-14 month-old *Hyal3*$^{-/-}$ mice (Figure 22) where HA accumulation would expected to be greatest.

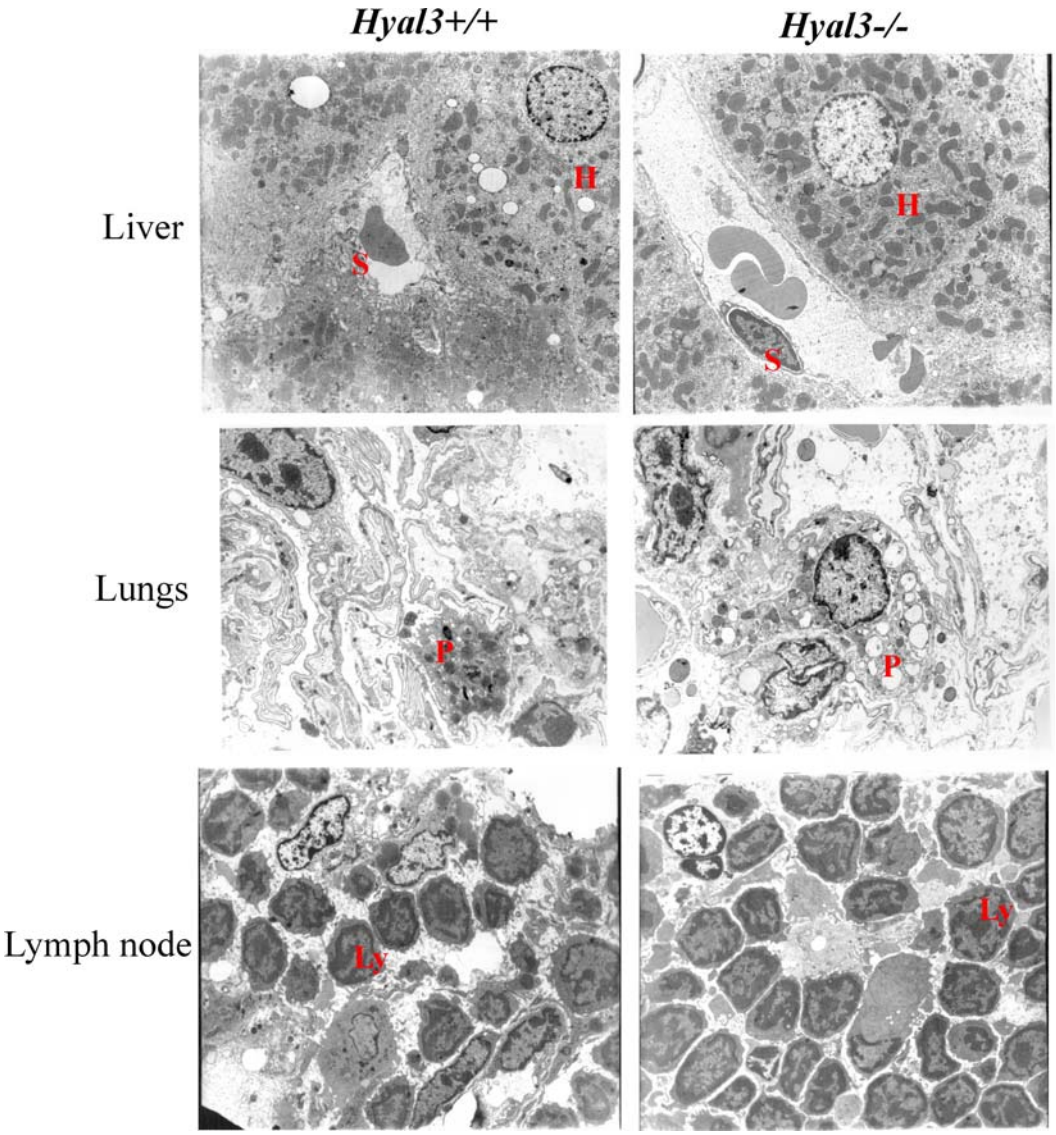

Figure 22: Transmission electron microscopy of *Hyal3*$^{+/+}$ and *Hyal3*$^{-/-}$ mouse tissues. No evidence of cellular vacuolation was observed in the *Hyal3*$^{-/-}$ tissues analyzed compared to the tissues of *Hyal3*$^{+/+}$ mice (12-14 month-old, n=4 to 6) by transmission electron microscopy. "n" represents the number of animals from each group and in each animal atleast 10 fields were analyzed. One representative field in *Hyal3*$^{+/+}$ and *Hyal3*$^{-/-}$ mouse tissues such as liver (H-hepatocytes and S-sinusoidal cells), lungs (P-type II pneumocytes) and lymph node (Ly-lymphocytes) are shown. Images were taken at magnification of either 3400x or 2600x.

3.2.9 Analysis of expression of other hyaluronidases

HA accumulation was not detected in any of the examined tissues or serum from *Hyal3*$^{-/-}$ mice, despite the absence of normal *Hyal3* transcripts. To determine if a HYAL3 deficiency was compensated by other genes involved in HA breakdown, we analyzed the expression of two broadly expressed hyaluronidases (*Hyal1* and *Hyal2*) and other hyaluronidases that are expressed in testes (*Hyal4*, *Hyal5*, *Spam1* and *Hyalp1*) by real-time RT-PCR. The expression of these genes was analyzed in testis and liver tissues from 8-12 month-old *Hyal3*$^{-/-}$ and *Hyal3*$^{+/+}$ mice (*CD1;129S1*).

The mean (± SD) ΔC_T values of the transcripts of individual genes in *Hyal3*$^{-/-}$ mice were calculated as a proportion of their mean ΔC_T values in *Hyal3*$^{+/+}$ mice. In testis, the mean ΔC_T values of the transcripts of *Hyal1* (1.18 ± 0.12), *Hyal2* (1.19 ± 0.41), *Hyal4* (0.83 ± 0.13), *Hyal5* (0.58 ± 0.19), *Hyapl1* (0.79 ± 0.02), *Spam1* (0.67 ± 0.12) in *Hyal3*$^{-/-}$ mice were comparable to the proportion of their respective mean ΔC_T values in *Hyal3*$^{+/+}$ mice. Therefore, there was no difference observed in the expression of *Hyal1* (P=0.08), *Hyal2* (P=0.42), *Hyal4* (P=0.13), *Hyal5* (P=0.12), *Hyalp1* (0.06) and *Spam1* (P=0.23) in the testis of *Hyal3*$^{+/+}$ and *Hyal3*$^{-/-}$ mice (Figure 22A, n=3).

In the liver tissue, the mean ΔC_T values of the transcripts of *Hyal1* (0.40 ± 0.15) in *Hyal3*$^{-/-}$ mice was reduced by 60% to the proportion of their mean ΔC_T value in *Hyal3*$^{+/+}$ mice (Figure 23B, *P=0.02, n=4). However, the mean ΔC_T values of the transcripts of *Hyal2* (1.19 ± 0.41) in *Hyal3*$^{-/-}$ mice was unchanged to the proportion of their mean ΔC_T value in *Hyal3*$^{+/+}$ mice (Figure 23B, P=0.06, n=4).

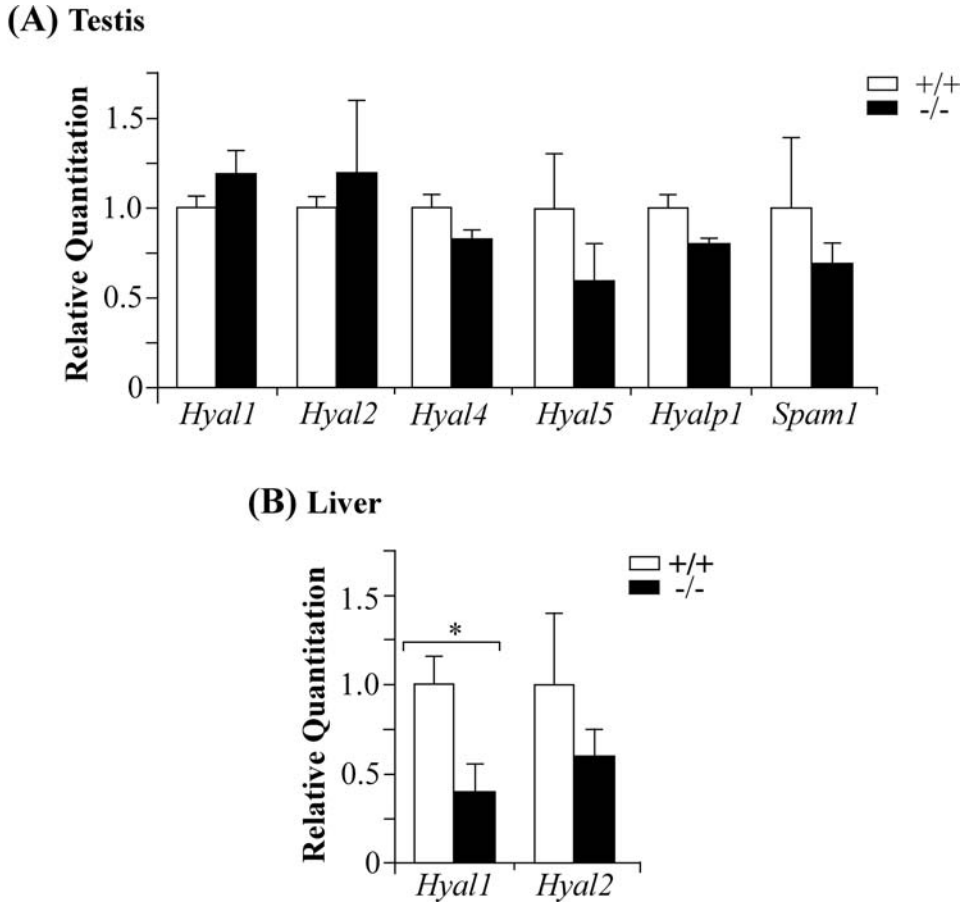

Figure 23: Real-time PCR results showing the expression levels of other hyaluronidases in the testis and liver from *Hyal3*$^{+/+}$ and *Hyal3*$^{-/-}$ mice.

(A) No significant difference was observed in the expression levels of hyaluronidases *Hyal1*, *Hyal2*, *Hyal4*, *Hyal5*, *Hyalp1* and *Spam1* in the testis of *Hyal3*$^{+/+}$ and *Hyal3*$^{-/-}$ mice (*CD1;129S1*, n=3; P=0.08 [*Hyal1*], P=0.42 [*Hyal2*], P=0.13 [*Hyal4*], P=0.12 [*Hyal5*], P=0.06 [*Hyap1*], P=0.23 [*Spam1*]). **(B)** In the liver, significant difference in the expression levels of *Hyal1* (n=4, P=0.02) and no difference in *Hyal2* (n=4, P= 0.09) were observed between *Hyal3*$^{+/+}$ and *Hyal3*$^{-/-}$ mice. Data was shown as the mean (±SD) ΔC_T values of the transcripts of the individual genes in *Hyal3*$^{-/-}$ mice represented as a proportion of their mean (±SD) ΔC_T values in *Hyal3*$^{+/+}$ mice. "n" represents the number of animals from each group. In each animal, each sample was analyzed in triplicate two times.

3.2.10 Analyses of expression and activity of an exoglycosidase

The exoglycosidases, β-hexosaminidase and β-glucuronidase are the enzymes that release terminal sugar moieties from the HA-breakdown products of hyaluronidases, and could also compensate for a hyaluronidase deficiency. The expression of *HexB*, a gene encoding α-subunit of β-hexosaminidase, was analyzed in the testis and liver tissues of *Hyal3*$^{-/-}$ and *Hyal3*$^{+/+}$ mice by real-time RT-PCR and the total β-hexosaminidase activity was analyzed by an enzymatic assay.

The mean (± SD) ΔC_T values of the transcripts of *HexB* in testis (0.90 ± 0.06) and liver (1.02 ± 0.26) of *Hyal3*$^{-/-}$ mice were comparable to the proportion of the mean ΔC_T values of the transcripts of *HexB* in testis (1.0 ± 0.17) and liver (1.0 ± 0.18) of *Hyal3*$^{+/+}$ mice (Figure 24A). Therefore, no difference in *HexB* expression was observed in either testis (n=3, P=0.50) or liver (n=4, P=0.90).

Furthermore, β- hexosaminidase activity was also analyzed in the liver tissues of 12-14 month-old *Hyal3*$^{+/+}$ and *Hyal3*$^{-/-}$ mice using an enzymatic assay. Again, total β-hexosaminidase activity in the liver tissues of both female and male *Hyal3*$^{+/+}$ and *Hyal3*$^{-/-}$ mice was unchanged (Figure 24B *CD1;129S1,* n=8, p=0.14).

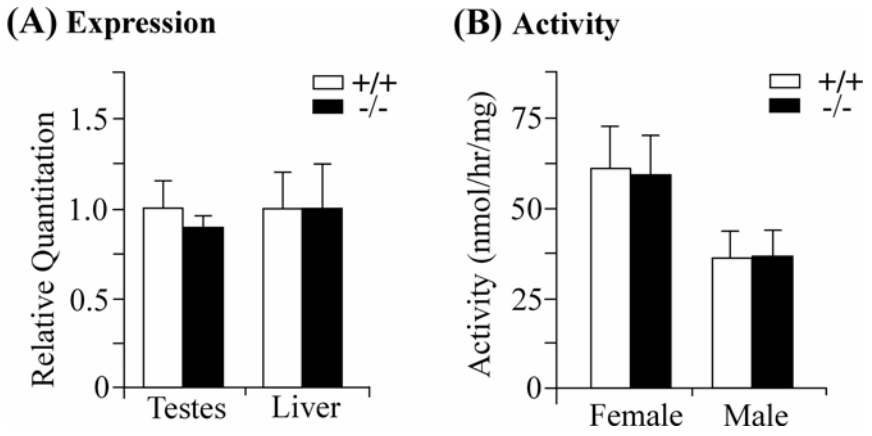

Figure 24: *HexB* expression and the total β-hexosaminidase activity in *Hyal3*$^{+/+}$ and *Hyal3*$^{-/-}$ mouse tissues.

(A) Expression levels of *HexB* in testis (n=3, P=0.5) and liver (n=4. P=0.90) of *Hyal3*$^{+/+}$ and *Hyal3*$^{-/-}$ mice. Data are shown as the mean (±SD) ΔC_T value of the transcripts of *HexB* in *Hyal3*$^{-/-}$ mice represented as a proportion of their mean (±SD) ΔC_T values in *Hyal3*$^{+/+}$ mice. **(B)** Total β-hexosaminidase activity in the liver tissues of *Hyal3*$^{+/+}$ and *Hyal3*$^{-/-}$ was unchanged (n=8, P=0.14).

Overall, the absence of elevation in any of the other hyaluronidases or exoglycosidase analyzed suggested that these enzymes are not compensating for *Hyal3* deficiency in *Hyal3*$^{-/-}$ mice.

3.3 Conclusions and discussion

The mild phenotype found in a HYAL1-deficient patient, despite the broad distribution and rapid turnover of HA, suggests that other hyaluronidases play an important role in HA degradation. Among the other hyaluronidases, we considered HYAL3 as the most likely hyaluronidase to participate in HA degradation because of its broad expression (Shuttleworth et al., 2002) and intracellular localization (Hemming et al., 2008). HYAL2 is also broadly expressed, but its localization is controversial (Chow et al., 2006; Miller, 2003). HYAL2 also appears to be active only toward high molecular-weight HA (Lepperdinger et al., 1998), making it unlikely to play a major role in intracellular HA breakdown. We have now generated and characterized a Hyal3 deficient mouse model. Based on comprehensive studies of our model, HYAL3 does not have a major role in the constitutive degradation of HA.

Our studies employed a *Hyal3* targeting construct that was an interruption-type vector, designed to insert a Neo cassette into exon 2 of *Hyal3* which is a major coding region of the gene. The *Hyal3* targeting vector was designed to disrupt *Hyal3* function while maintaining normal transcription of an overlapping gene, *Fus2*. The targeting construct introduced into the ES cells was inserted into the ES cell genome by homologous recombination. The frequency of homologous recombination that occurred was found to be approximately 8%.

In *Hyal3* $^{-/-}$ mice, transcripts were produced from *Hyal3*, but they were abnormal and did not include the full exon 2 coding sequence. The abnormal transcript would not encode a functional HYAL3 protein as exon 2 is highly conserved among all of the hyaluronidases and the site-directed mutagenesis studies have demonstrated that the key

active-site residues are within this region (Arming et al., 1997). Furthermore, changes as small as single amino acid substitutions can lead to misfolding of glycoproteins. If any parts of the HYAL3 protein are translated from the abnormal transcripts, they would not have a signal sequence, would not be glycosylated, and thereby could not fold to form a functional protein.

Real-time RT-PCR demonstrated that the transcription of the overlapping gene, *Fus2,* was preserved in the testis of the new model of *Hyal3*$^{-/-}$ mice used for this study, although *Fus2* transcripts in the liver were reduced by 20% compared to the level in wild-type mouse liver (Figure 14D). Therefore the targeting construct was successful in disrupting *Hyal3* while maintaining substantial levels of *Fus2* expression. Interestingly, the level of *Hyal1* expression was also slightly reduced in the liver. There are many co-transcripts in the liver that include *Hyal1* and/or *Fus2* and/or *Hyal3* (Shuttleworth et al., 2002). The disruption of normal *Hyal3* transcription may interfere with the expression of these co-transcripts and therefore both *Hyal1* and *Fus2* transcripts would be lowered. This interference could be due to the destabilization of the transcripts or it may be the indirect results of Hyal3 deficiency. In previous work, our laboratory showed that overexpression of *Hyal3* increased *Hyal1* expression (Hemming et al., 2008), suggesting that a feedback loop exists; therefore a decrease in *Hyal3* transcripts could decrease *Hyal1* and *Fus2* transcripts. *Fus2* encodes a cytoplasmic N-acetyl transferase, and has been localized in a region associated with lung-cancer susceptibility (Zegerman et al., 2000). Given this, changes in *Fus2* expression must be considered as a possible confounding variable in the interpretation of the lung phenotype in the *Hyal3*$^{-/-}$ mice.

HA is broadly distributed, and the highest concentrations are found in connective tissues. Accordingly, while evidence of HA accumulation was investigated in a broad

range of tissues, the present survey placed the greatest emphasis on the tissues where high turnover of HA is expected or *Hyal3* expression is high. Neither biochemical nor histological approaches detected any evidence of GAG accumulation. These results indicate that HYAL3 is not a major contributing enzyme to the constitutive degradation of any GAG, including HA. This new information now directs future studies toward alternative explanations that would account for the mild phenotype in MPS IX.

The skeletal system was most affected in the HYAL1-deficient human (Natowicz et al., 1996) and was the only system where HA accumulation was detected in *Hyal1* $^{-/-}$ mice (Martin et al., 2008). Considering the high HA turnover in joint tissue, we specifically examined the knee joint in *Hyal3*$^{-/-}$ mice, but there was no evidence of HA accumulation. This finding indicates that HYAL3 does not have a major role in the constitutive degradation of HA, even in high-turnover tissues.

Despite the lack of HA accumulation in skeletal and non-skeletal tissues of *Hyal3* $^{-/-}$ mice, the lung-tissue morphology was abnormal. Lung tissue from aged *Hyal3* $^{-/-}$ mice displayed large alveoli and a larger proportion of lung area had a thickened interstitium compared to lung tissue from age-matched wild-type mice. In preliminary studies of young *Hyal3*$^{-/-}$ mice, fewer septa were identified between alveoli, suggesting HYAL3 deficiency may lead to age-dependent development of an alveolar-septal defect. Unfortunately, quantitative studies were not possible as the lungs were not inflated to a set pressure prior to fixation. Detailed analysis of lung histology and *Fus2* expression in this tissue is necessary to confirm that these findings are due to HYAL3 deficiency. It is interesting to note, however, that *HYAL1*, *HYAL2*, and *HYAL3* all exhibit relatively high expression in the lung, consistent with the important role of HA in maintaining normal lung function (Jiang et al., 2005).

The absence of GAG accumulation in *Hyal3*$^{-/-}$ mouse tissues was not surprising since recent work from our lab using HYAL3 over-expressing cells (Hemming et al., 2008) and the work of others (Harada and Takahashi, 2007) indicate that HYAL3 lacks hyaluronidase activity. Of note, although HYAL3 did not have intrinsic enzymatic activity, HYAL1 activity was increased in HYAL3 over-expressing cells (Hemming et al., 2008). This putative non-enzymatic role for HYAL3 in HA metabolism is supported by other recent work from our laboratory on HYAL1-deficient mice, which have an approximate 5-fold increase in *Hyal3* mRNA (Martin et al., 2008). This reciprocal interplay between HYAL1 activity and *Hyal3* expression indicates a cooperative role for HYAL1 and HYAL3 in HA metabolism. It is also possible that HYAL3's function depends on the presence of a co-factor that is only present in specific cell types and would not have been present in the cell lines used for *in vitro* expression analysis. Given that 60% of the monocytes/macrophages in the body are found in the lung tissue, it is possible that monocytes contain such a co-factor, and therefore a deficiency of *HYAL3* would be most evident in the lungs.

We analyzed the transcripts of other enzymes that might contribute to HA degradation in *Hyal3*$^{-/-}$ mice tissues since these enzymes might be upregulated to compensate for HYAL3 deficiency in the testis tissue where *Hyal3* expression is normally highest. No increase in the expression of any of the hyaluronidases or the exoglycosidase, β-hexosaminidase, was identified. This may not be extremely surprising given the very low expression level of *Hyal3* compared to the other hyaluronidases. HYAL2 may still be a reasonable candidate to compensate for loss of HYAL1 activity, especially when combined with the very abundant lysosomal exoglycosidases, β-glucuronidase, and β-Hex. Although HYAL2 has a GPI-linked cell surface form, some enzyme is found in

early endosomes, suggesting that it could play a role in both extracellular and intracellular HA catabolism.

Present studies of *Hyal3*$^{-/-}$ mice indicate that HYAL3 is not a major contributor to constitutive HA degradation. Together with other studies, these findings suggest that HYAL3 is not a classic hyaluronidase but instead has another role in HA metabolism. However, it is clear from this study and that of HYAL1 deficient mice (Martin et al., 2008) that there is still much to be understood about the mechanism of HA degradation. Studies of double knockouts of *Hyal1* and *Hyal3* will be essential to unravel some of the unanswered questions in HA catabolism and MPS pathophysiology.

Chapter four: Analyses of HA turnover and airway inflammation in Hyal3$^{-/-}$ mice

Acknowledgements:

Special thanks to Ms.Sujata Basu for technical assistance and performing lung function analysis and thanks to Dr. Ganesh Srinivasan for discussing his thoughts regarding this project. Serum Ig and BAL fluid cytokine levels were analyzed in Dr. John Gordon's laboratory (University of Saskatchewan, Saskatoon) and immunophenotyping in Dr. Jude Uzonna's laboratory (University of Manitoba) by Dong Liu. Special thanks to Dr. Andrew Halayko for critical review of the results presented in this chapter. Experiments conducted in naive (unsensitized) and chronic inflammation model (addressed as OVA-challenged *Hyal3* mice) are presented in this chapter. A similar set of experiments performed in an acute inflammation model of *Hyal3* mice are not included in this chapter but provided as appendix 1, because the results are not significant.

4.1 Introduction

HA is a GAG that is ubiquitously distributed in the ECM of vertebrate cells. HA typically exists as a HMW form which is associated with tissue integrity and homeostasis. However, during tissue injury and inflammation, HA is broken down to LMW HA fragments (Jiang et al., 2005; rev. in Stern et al., 2007), which impact immune responses by increasing the expression of inflammatory chemokines and cytokines (Turino and Cantor, 2003; Noble et al., 2006; Scheibner et al., 2006; Jiang et al., 2006). Surprisingly, exogenous HMW HA has been successfully used to protect lungs from injury (Petrigni and Allegra, 2006; Cantor and Turino, 2004; Liu et al., 2008). However, the mechanisms that control the size of HA to promote or protect from inflammation are poorly understood (rev. in Stern et al., 2006).

Susceptibility to lung inflammation in several rodent models is mediated by alterations in HA metabolism. For example, when ventilator-induced lung injury was examined in HA synthase-3 deficient mice, the inflammatory response was reduced (Bai et al., 2005a; Mrabat et al., 2009), presumably because HA fragments normally synthesized by HA synthase-3 are absent. A role for oxygen radicals in HA fragment generation has been suggested by increased HA and inflammation in lung injury models of extracellular superoxide dismutase-deficient mice (Gao et al., 2008; Garantziotis et al., 2009; Bracke et al., 2009). Further, in mice deficient in the HA receptor CD44, lung injury leads to unresolved inflammation because HA fragments are not cleared from the lungs (Teder et al., 2002).

Hyaluronidases are endoglycosidases required to initiate HA degradation and are presumed to contribute to the generation of HA fragments; however, no direct role for them has been confirmed except *in vitro* where platelet-derived hyaluronidase 2 (Hyal2)

was shown to degrade HA into pro-inflammatory fragments (de la Motte et al., 2009). In humans and mice, there are three broadly expressed hyaluronidases (*Hyal1*, *Hyal2* and *Hyal3*) that are present in the lungs (Csoka et al., 1999; Shuttleworth et al., 2002; Monzon et al., 2008).

Csoka and colleagues (Csoka et al., 2001) have proposed that HMW HA can be bound by a cell surface receptor and then broken down into HA fragments by a GPI-anchored form of HYAL2. HA fragments are thought to be internalized and transported to endosomes and finally to the lysosomes where they are further degraded into oligosaccharides by HYAL1 and two lysosomal exoglycosidases, β-glucuronidase and β-hexosaminidase (rev. in Stern, 2003; Stern, 2004). Studies using individual hyaluronidase-deficient mice reveal the existence of mild and differing phenotypes; *Hyal1*$^{-/-}$ mice develop mild osteoarthritis and HA accumulation in the cartilage of knee joints (Martin et al., 2008); *Hyal2*$^{-/-}$ mice exhibit skeletal and hematological defects (Jadin et al., 2008); and *Hyal3*$^{-/-}$ mice exhibit mildly abnormal cellular structure in the lungs (Atmuri et al., 2008).

The basis of the abnormal lung structure in *Hyal3*$^{-/-}$ mice is not clear as very little is known about HYAL3, a broadly but weakly expressed gene in humans (Csoka et al., 1999) and mice (Shuttleworth et al., 2002). *In vitro* studies using lysates of mouse Hyal3 over-expressing cells show that it localizes to a vesicular compartment(s) in the cell and leads to Hyal1 activity increases (Hemming et al., 2008); however, intrinsic Hyal3/HYAL3 activity has not been detected (Harada and Takahashi, 2007; Hemming et al., 2008). Despite this, in *Hyal1*$^{-/-}$ mice *Hyal3* transcript levels are increased (Martin et al., 2008) suggesting regulation of Hyal3 is a fundamental component of HA homeostasis. Collectively, these findings suggest expression and activity of different hyaluronidases are

complex.

In the current study to determine if Hyal3 is involved in HA homeostasis or whether it might be involved in the generation of pro-inflammatory HA fragments, we examined HA levels in the lungs of *Hyal3*$^{-/-}$ mice and assessed the effects of *Hyal3*-deficiency on ovalbumin (OVA)-induced airway inflammation. We demonstrate that *Hyal3*-deficiency alters HA levels, and, in response to allergen exposure, HA distribution and levels were changed and lung-inflammation was increased.

4.2 Results

4.2.1 Hyal3$^{-/-}$ mice have increased HA in lungs

In an initial survey of the GAGs content of tissues from *Hyal3*$^{-/-}$ mice using histological and biochemical approaches, no significant accumulation was detected in any of the tissues analyzed (Atmuri et al., 2008). However, subtle histological changes in the alveolar structure of lungs from *Hyal3*$^{-/-}$ mice suggested an important role for Hyal3 in this tissue. To further assess HA homeostasis in the lungs of *Hyal3*$^{-/-}$ mice, we detected HA levels by immunohistochemistry using a biotinylated HA-binding protein. HA detection using HA-binding protein is a more specific approach than the uronic acid assay performed for studies in chapter 3. This HA detection method clearly demonstrated an increase in HA in the ECM of airways of *Hyal3*$^{-/-}$ lungs compared to *Hyal3*$^{+/+}$ lungs. *Streptomyces* hyaluronidase-treated sections confirmed that the staining was specific (Figure 25A). HA present in the lung sections was detected as brown colour with the peroxidase substrate, diaminobenzidine (DAB) that was used. HA levels detected in the peri-bronchial region of airways from *Hyal3*$^{+/+}$ and *Hyal3*$^{-/-}$ mouse lungs by immunohistochemistry (Figure 25A) were quantified. In each animal, HA levels in the peri-bronchial region were analyzed in atleast 10 airways on a 5-point score system under 200x and 1000x final magnification. This semi-quantitative approach demonstrated an increase in HA levels in the peri-bronchial region of *Hyal3*$^{-/-}$ mouse airways (HA score mean 4.0 ± SD 0.0) compared to *Hyal3*$^{+/+}$ airways (HA score mean 2.3 ± SD 1.03) (Figure 25B, n=3, P=0.046).

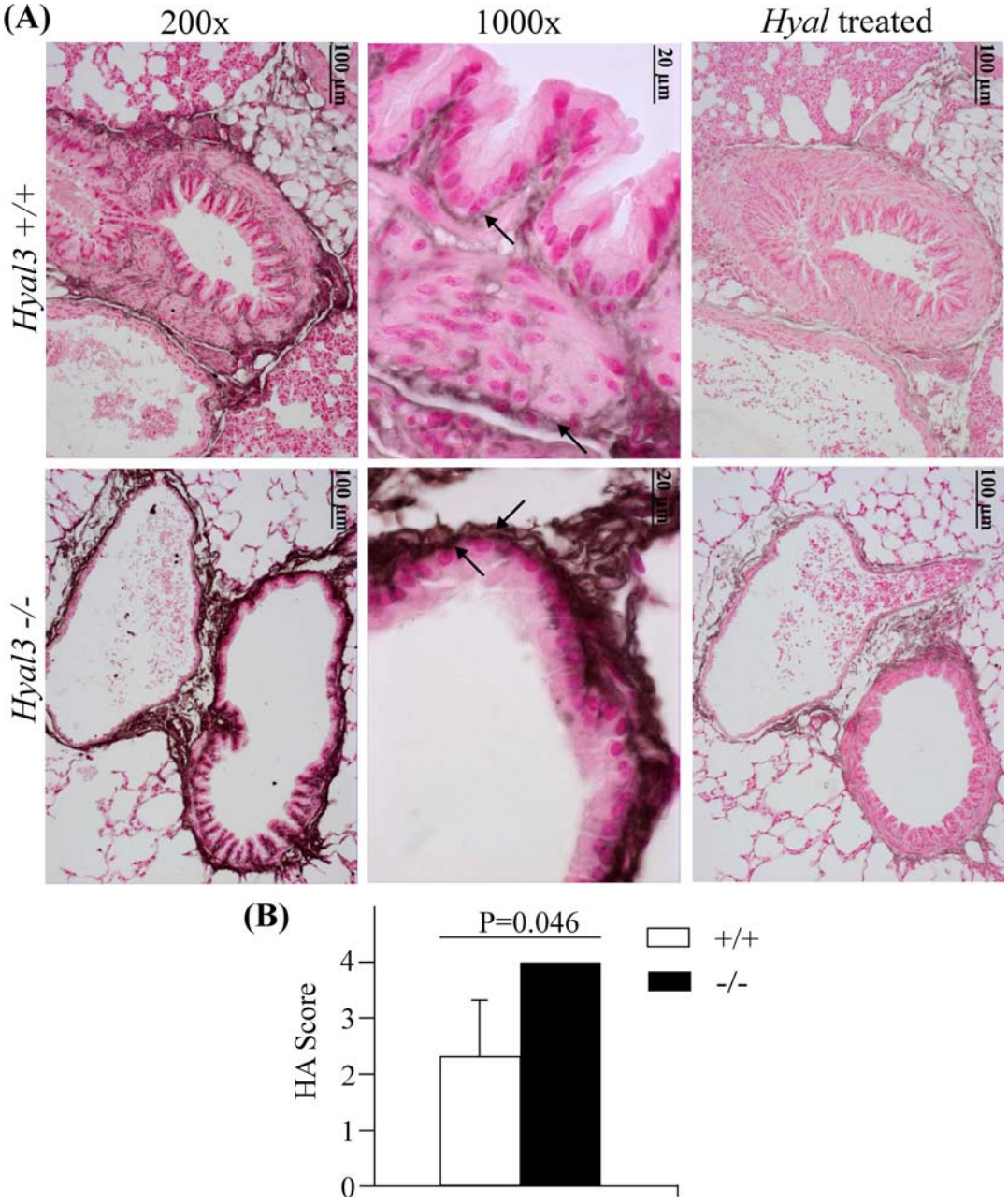

Figure 25: Semi-quantitative analysis of HA in the lung sections of naive *Hyal3*$^{+/+}$ and *Hyal3*$^{-/-}$ by immunohistochemistry. **(A)** Lung tissue sections of *Hyal3*$^{+/+}$ and *Hyal3*$^{-/-}$ mice stained for HA using biotinylated HA-binding protein by immunohistochemistry. The brown staining represents the specific staining for HA. Peri-bronchial HA in the airways of *Hyal3*$^{+/+}$ and *Hyal3*$^{-/-}$ mice is denoted by arrows. *Hyal3*$^{-/-}$ mouse lung sections showing increased peri-bronchial HA (arrows) compared to *Hyal3*$^{+/+}$ lung airways. *Streptomyces* hyaluronidase treated sections are included as negative control. **(B)** A representation of the semi-quantified data of peri-bronchial HA in *Hyal3*$^{+/+}$ and *Hyal3*$^{-/-}$ lungs sections. Data shows the mean ± SD (n=3). "n" represents the number of animals in each group and in each animal atleast 10 fields were analyzed.

4.2.2 HA distribution in Hyal3$^{-/-}$ mice is altered during inflammation

We expected that the elevated HA in the lungs of the *Hyal3*$^{-/-}$ mice could alter the susceptibility of this model to inflammation because accumulation of HA in the ECM is associated with several lung conditions (Jiang et al., 2007). After OVA-sensitization and challenge, we evaluated HA present in lung tissues of *Hyal3*$^{+/+}$ and *Hyal3*$^{-/-}$ mice using immunohistochemistry and fluorophore assisted carbohydrate electrophoresis (FACE) analyses.

HA levels were identified in the airways of OVA-challenged *Hyal3*$^{+/+}$ and *Hyal3*$^{-/-}$ mice (Figure 26A) and quantified on a 5-point scale system. In each animal, HA levels in the peri-bronchial region were analyzed in atleast 10 airways under 200x and 1000x final magnification. This semi-quantitative approach determined an increase in HA levels in the peri-bronchial region of OVA-challenged *Hyal3*$^{-/-}$ mouse airways (HA score mean 3.0 ± SD 0.4) compared to OVA-challenged *Hyal3*$^{+/+}$ airways (HA score mean 1.25 ± SD 0.5) (Figure 26B, n=4, P=0.002). Interestingly, OVA-challenged *Hyal3*$^{-/-}$ airways also exhibited intra-epithelial HA, a feature that was completely absent in the OVA-challenged *Hyal3*$^{+/+}$ mice (Figure 26A, n=4), and also naive *Hyal3*$^{+/+}$ and *Hyal3*$^{-/-}$ mice (Figure 25A, n=3); *Streptomyces* hyaluronidase-treated sections confirmed that the staining was specific to HA (Figure 26A).

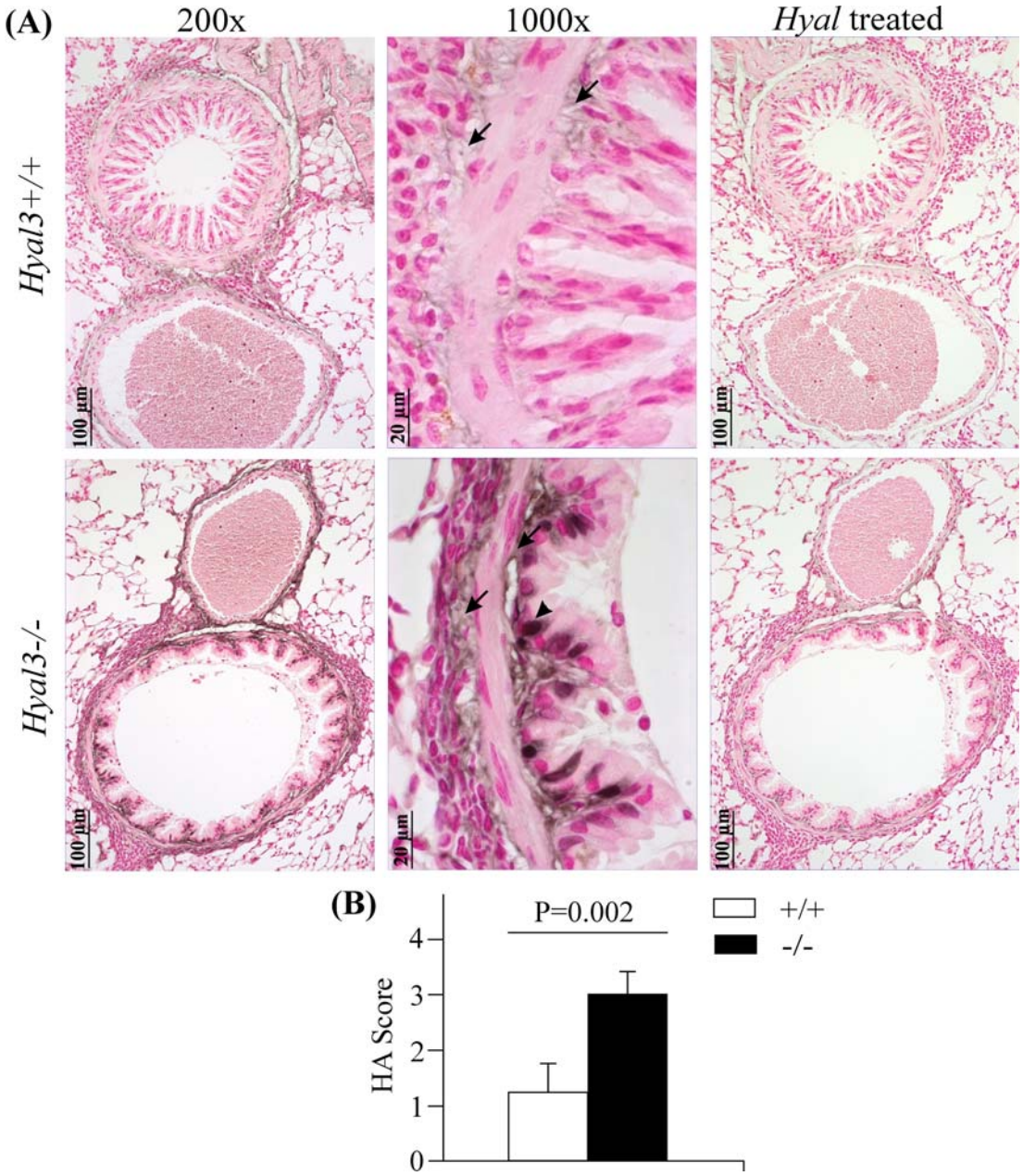

Figure 26: Semi-quantitative analysis of HA in the lung sections of OVA-challenged *Hyal3*$^{+/+}$ and *Hyal3*$^{-/-}$ mice by immunohistochemistry. (A) Lung sections of OVA-challenged *Hyal3*$^{+/+}$ and *Hyal3*$^{-/-}$ mice stained for HA using biotinylated HA-binding protein. Peri-bronchial HA staining was increased in OVA-challenged *Hyal3*$^{-/-}$ mice compared to similarly treated control mice. Arrows denote the brown staining specific for HA. Arrow head indicate the intra-epithelial HA staining. *Hyal*-treated sections are included as a negative control. **(B)** A semi-quantified representation of peri-bronchial HA in OVA-challenged *Hyal3*$^{+/+}$ and *Hyal3*$^{-/-}$ lung sections. A significant increase in peri-bronchial HA was observed in the airways of OVA-challenged *Hyal3*$^{-/-}$ mice compared to *Hyal3*$^{+/+}$ mice. Data represent the mean ± SD (n=4). "n" represents the number of animals in each group and in each animal atleast 10 fields were analyzed.

To further confirm that HA was increased in the lungs of OVA-challenged *Hyal3*$^{-/-}$ mice, we also quantified HA by FACE. The lung tissue lysates of OVA-challenged *Hyal3*$^{+/+}$ and *Hyal3*$^{-/-}$ mice were analyzed for HA content by FACE. The data showed a trend toward increased HA in OVA-challenged *Hyal3*$^{-/-}$ mice (mean 108.8 ± SD 91.17) compared to similarly treated *Hyal3*$^{+/+}$ mice (mean 39.7 ± SD 12.93), but it was not a statistically significant difference (Figure 27A, n=6, P=0.096). In addition, HA present in the broncho-alveolar lavage (BAL) fluid of OVA-challenged *Hyal3*$^{-/-}$ mice also showed a trend toward increased HA compared to *Hyal3*$^{+/+}$ mice (Figure 27B, n=4).

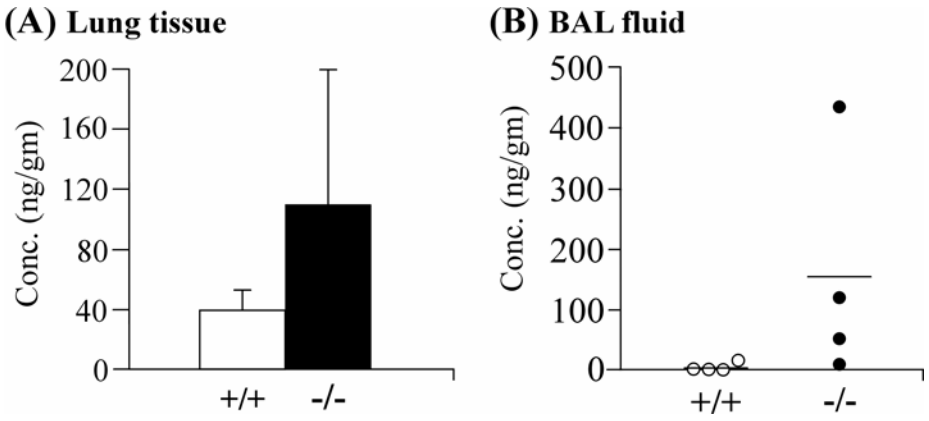

Figure 27: HA concentration in the lung tissue and BAL fluid of OVA-challenged *Hyal3*$^{+/+}$ and *Hyal3*$^{-/-}$ mice.

(A) FACE analysis showed a trend towards an increase in HA in the lung tissues of OVA-challenged *Hyal3*$^{-/-}$ mice compared to similarly treated *Hyal3*$^{+/+}$ mice. Data represent the mean ± SD (n=6, P=0.096). **(B)** HA levels in the BAL fluid of OVA-challenged *Hyal3*$^{+/+}$ and *Hyal3*$^{-/-}$ mice were analyzed by ELISA (n=4). Each data point is equal to an individual animal and horizontal lines represent the mean. The data represents an increase in the HA levels in OVA-challenged *Hyal3*$^{-/-}$ mice compared to OVA-challenged *Hyal3*$^{+/+}$ mice. "n" represents the number of animals in each group.

4.2.3 Increased airway inflammation in OVA-challenged Hyal3$^{-/-}$ mice

To determine if the accumulated HA in OVA-challenged *Hyal3*$^{-/-}$ mice lungs had any effect on airway inflammation, we analyzed the number and type of inflammatory cells in the broncho-alveolar lavage (BAL) fluid collected from the lungs of OVA-challenged *Hyal3*$^{+/+}$ and *Hyal3*$^{-/-}$ mice.

The total cell counts were analyzed by hemocytometer and the data indicates that the total cell count was significantly increased in the BAL fluid of OVA-challenged *Hyal3*$^{-/-}$ mice (mean 73.75 x 10^4 cells ±SD 17.85, n=4) compared to those in similarly treated *Hyal3*$^{+/+}$ mice (mean 28.7 x 10^4 cells ± SD 18.3, n=4) (Figure 28A, P=0.013).

To determine the cell type responsible for the increase in total cell count in the BAL fluid of OVA-challenged *Hyal3*$^{-/-}$ mice, different cells were identified based on morphology. An equal number of cells from the BAL fluid of OVA-challenged *Hyal3*$^{+/+}$ and *Hyal3*$^{-/-}$ mice were subjected to cytospin and stained. The percentage of each type of cells presents in the BAL fluid of OVA-challenged *Hyal3*$^{+/+}$ and *Hyal3*$^{-/-}$ mice was determined. The greater increase in the total cell count in BAL fluid of OVA-challenged *Hyal3*$^{-/-}$ mice appears to be associated with a fractional increase in both eosinophils and neutrophils compared to OVA-challenged *Hyal3*$^{+/+}$ mice, although no significant difference was observed in any cell type (Figure 28B, n=4, P>0.05).

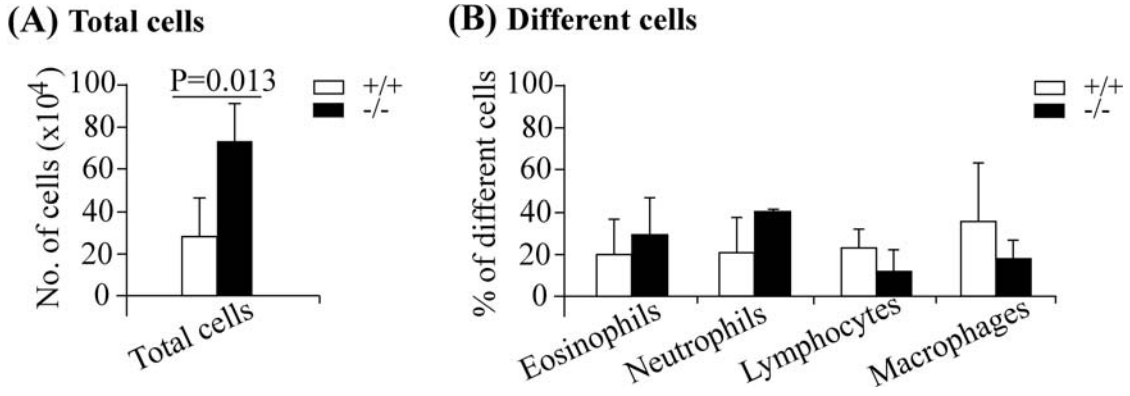

Figure 28: Total and differential cell counts in the BAL fluid of OVA-challenged *Hyal3*$^{+/+}$ and *Hyal3*$^{-/-}$ mice.

(A) Total cell counts in the BAL fluid of OVA-challenged *Hyal3*$^{+/+}$ and *Hyal3*$^{-/-}$ mice were analyzed. A significant increase in the total cell count was observed in the BAL fluid of OVA-challenged *Hyal3*$^{-/-}$ mice compared to OVA-challenged *Hyal3*$^{+/+}$ mice. Data represent the mean ± SD (n=4, P=0.013). **(B)** The different cells in the BAL fluid of OVA-challenged *Hyal3*$^{+/+}$ and *Hyal3*$^{-/-}$ mice were analyzed. A trend toward an increase in the percentage of eosinophils and neutrophils was observed in the BAL fluid of OVA-challenged *Hyal3*$^{-/-}$ mice compared to similarly treated *Hyal3*$^{+/+}$ mice. Data represent the mean ± SD (n=4, P>0.05). "n" represents the number of animals in each group.

As a sign of inflammation, in addition to the analysis of total cells in BAL fluid of OVA-challenged *Hyal3*$^{+/+}$ and *Hyal3*$^{-/-}$ mice, lung tissue sections were analyzed for infiltrated cells in the peri-bronchial, peri-vascular and parenchymal regions. Lung sections of OVA-challenged *Hyal3*$^{+/+}$ and *Hyal3*$^{-/-}$ mice stained with hematoxylin and eosin (H & E) were used to analyze the infiltrated cells. The infiltrated cells in each region of the lung were examined in OVA-challenged *Hyal3*$^{+/+}$ and *Hyal3*$^{-/-}$ mice using a 5-point scale system for quantification. In each lung tissue from an individual animal, atleast 5 to 10 fields were analyzed and average mean of all the animals in a group was used for the calculation. The infiltrated score was significantly increased in the peri-bronchial (mean score 3.25 ± SD 0.28), peri-vascular (3.35 ± 0.58) and parenchymal (1.81

± 0.21) regions in the lung sections of OVA-challenged *Hyal3*$^{-/-}$ mice compared to the infiltrated score in the peri-bronchial (0.90 ± 1.05), peri-vascular (0.65 ± 0.789) and parenchymal (0.685 ± 0.27) regions of lung sections from similarly treated OVA-challenged *Hyal3*$^{+/+}$ mice. This data has shown that in OVA-challenged *Hyal3*$^{-/-}$ lung sections, there was a significantly greater number of infiltrating inflammatory cells associated with peri-bronchial (P=0.005), peri-vascular (P=0.0015) and parenchymal (P=0.0007) regions compared to OVA-challenged *Hyal3*$^{+/+}$ mice (Figure 29, n=4).

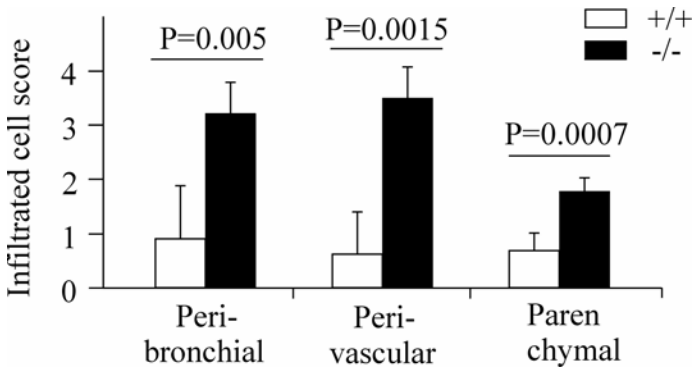

Figure 29: Semi-quantified data representing the increase in infiltrating cells in OVA-challenged *Hyal3*$^{+/+}$ and *Hyal3*$^{-/-}$ mouse lungs.

Infiltrated cells in the peri-bronchial, peri-vascular and parenchymal regions of the lung sections of OVA-challenged *Hyal3*$^{+/+}$ and *Hyal3*$^{-/-}$ mice were quantified based on a 5-point scale system. A significant increase in infiltrating cells was identified in OVA-challenged *Hyal3*$^{-/-}$ lungs compared to similarly treated *Hyal3*$^{+/+}$ lungs. Data represent the mean ± SD (n=4). "n" represents the number of animals in each group and in each animal atleast 10 fields were analyzed under 200x and 1000x final magnifications.

One representative field from each of H&E stained lung sections of OVA-challenged *Hyal3*$^{+/+}$ and *Hyal3*$^{-/-}$ mice indicating the final infiltrated score of that genotype is shown in Figure 30.

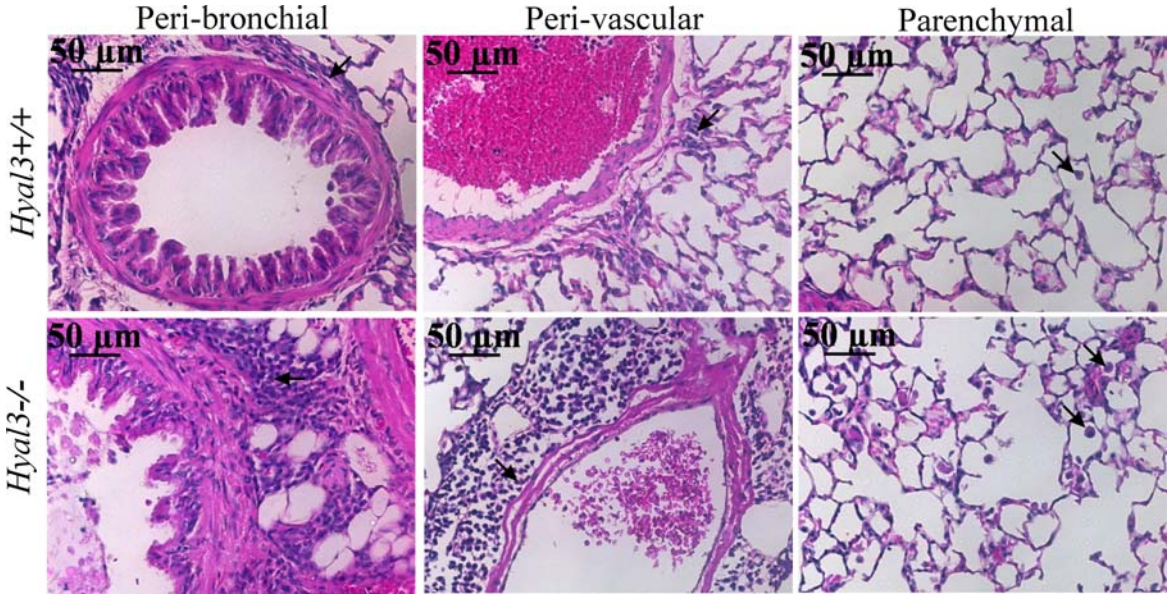

Figure 30: H & E-stained lung sections of OVA-challenged *Hyal3*$^{+/+}$ and *Hyal3*$^{-/-}$ mice. Lung tissue sections of OVA-challenged *Hyal3*$^{+/+}$ and *Hyal3*$^{-/-}$ mice stained with hematoxylin and eosin were used for analyzing infiltrated cells. A significant increase in infiltrated cells was observed in the peri-bronchial, peri-vascular and parenchymal regions of *Hyal3*$^{-/-}$ lung sections compared to their respective regions in similarly treated *Hyal3*$^{+/+}$ lungs. Arrows in peri-bronchial, peri-vascular and parenchymal regions of lung sections indicate the infiltrated cells. One representative field of lung tissues is shown (n=4). "n" represents the number of animals from each group and in each animal atleast 10 fields were analyzed under 200x and 1000x final magnification. Shown is 200x magnification.

In order to assess whether the increase in infiltrating cells in lungs of OVA-challenged *Hyal3*$^{-/-}$ mice pre-existed in these mice when there was no inflammation, we analyzed inflammatory cells in the H & E-stained lung tissue sections of naive *Hyal3*$^{+/+}$ and *Hyal3*$^{-/-}$ mice. The number of infiltrated cells in the peri-bronchial, peri-vascular and parenchymal regions of lung sections from naive *Hyal3*$^{+/+}$ and *Hyal3*$^{-/-}$ mice were comparable (Figure 31, n=3).

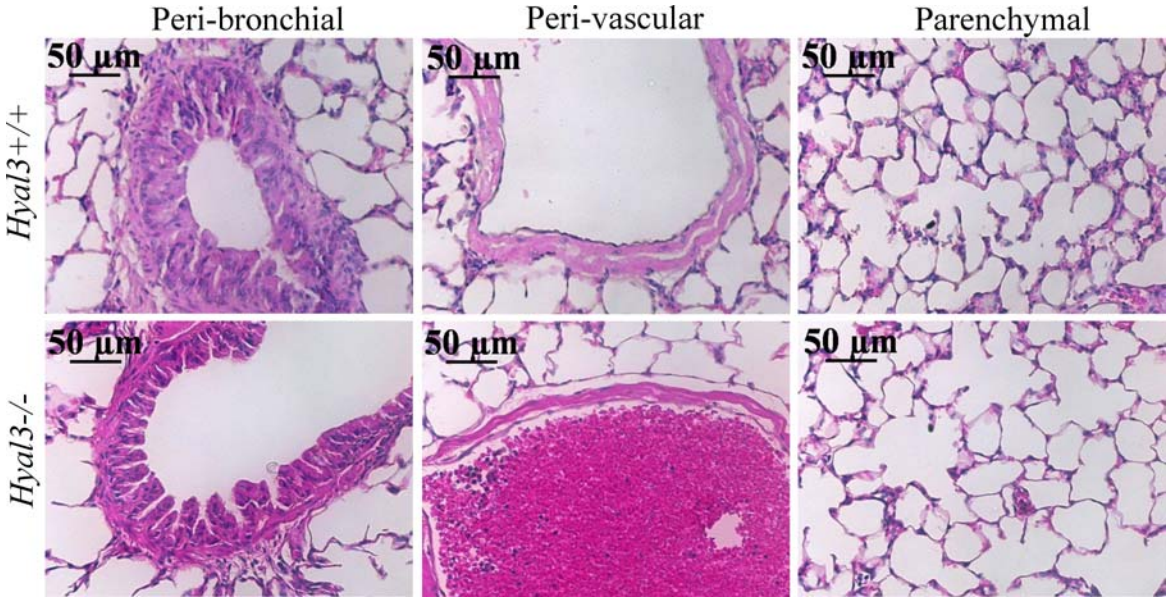

Figure 31: H & E-stained lung sections of naive *Hyal3*$^{+/+}$ and *Hyal3*$^{-/-}$ mice.

Lung sections of naive *Hyal3*$^{+/+}$ and *Hyal3*$^{-/-}$ mice stained with H & E were used to analyze the number of infiltrated cells in peri-bronchial, peri-vascular and parenchymal regions. No difference in the number of infiltrating cells was observed in peri-bronchial, peri-vascular and parenchymal regions of naive *Hyal3*$^{+/+}$ and *Hyal3*$^{-/-}$ mice (n=3). "n" represents the number of animals from each group and in each animal atleast 10 fields were analyzed under 200x and 1000x final magnification. Shown is 200x magnification.

As an index of acute local inflammation, lung sections of OVA-challenged *Hyal3*$^{+/+}$ and *Hyal3*$^{-/-}$ mice were also stained with periodic acid-Schiff (PAS) stain to identify mucus secreting goblet cells in the airways. Red to purple coloured staining in the airways of OVA-challenged *Hyal3*$^{+/+}$ and *Hyal3*$^{-/-}$ mice represent the mucus secreting goblet cells (Figure 32A). The abundance of these PAS-positive cells were assessed in the airways of OVA-challenged *Hyal3*$^{+/+}$ and *Hyal3*$^{-/-}$ mice semi-quantitatively following a 5-point scale system as previously described (McMillan et al., 2002). In each animal in a group, atleast 10 airways were analyzed and the mean PAS-score of all the animals of *Hyal3*$^{-/-}$ mice (mean score 2.67 ± SD 0.559) was compared to the mean PAS-score of all

the animals of *Hyal3*$^{+/+}$ mice (mean score 0.233 ± SD 0.16). The percentage of PAS-positive goblet cells in the airways of OVA-challenged *Hyal3*$^{-/-}$ mice were markedly higher compared to OVA-challenged *Hyal3*$^{+/+}$ mice (Figure 32B, n=4, P=0002), suggesting *Hyal3*-deficiency promotes goblet cell hyperplasia in response to allergen challenge. This is consistent with the increased airway inflammation observed in OVA-challenged *Hyal3*$^{-/-}$ mice.

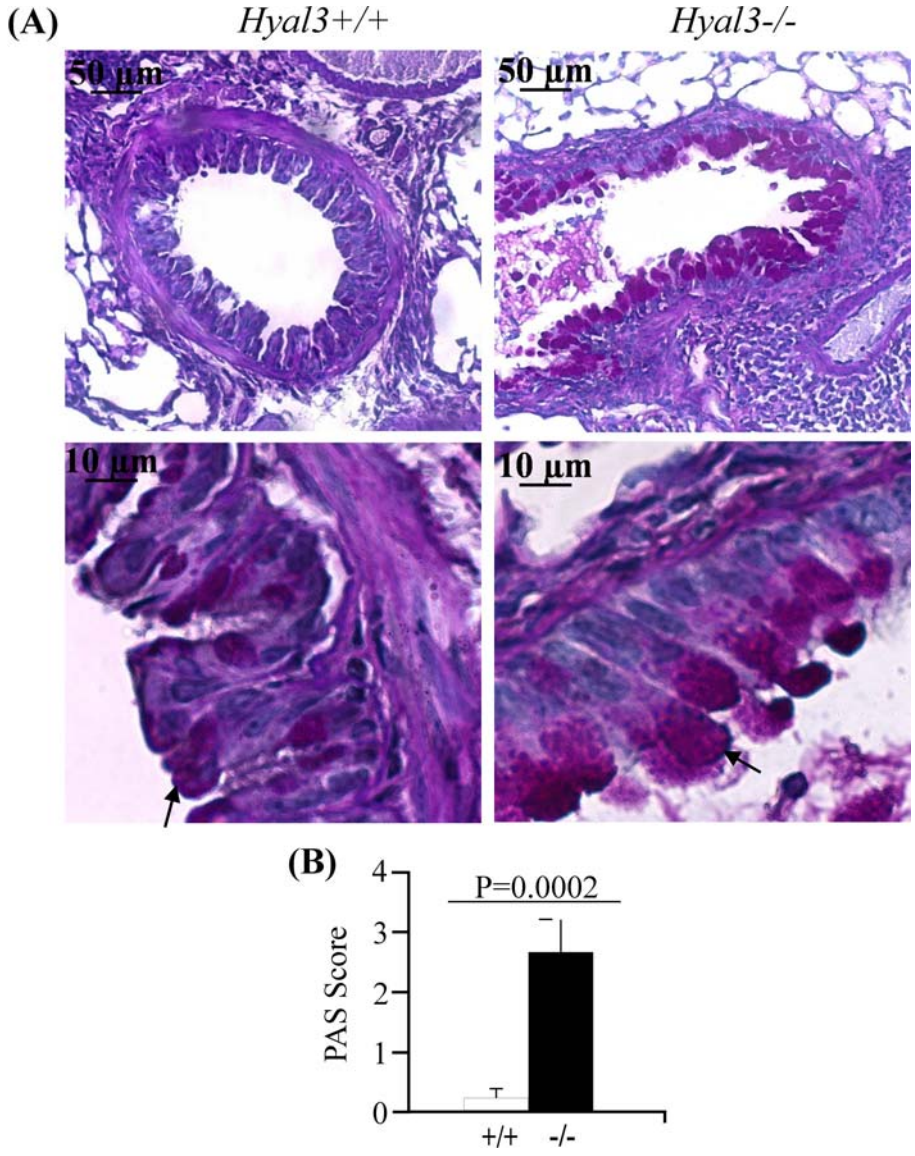

Figure 32: PAS-stained lung sections of OVA-challenged *Hyal3*$^{+/+}$ and *Hyal3*$^{-/-}$ mice. **(A)** Lung sections of OVA-challenged *Hyal3*$^{+/+}$ and *Hyal3*$^{-/-}$ airways were stained with periodic acid Schiff (PAS) stain for mucus secreting goblet cells. Red boxes indicate the region shown under higher magnification in the lower panel and the arrows represent a goblet cell that is stained with PAS. **(B)** The number of PAS-positive goblet cells in the airways of OVA-challenged *Hyal3*$^{+/+}$ and *Hyal3*$^{-/-}$ mouse lungs was quantified using a 5-point scale system. A significant increase in PAS-score was observed in OVA-challenged *Hyal3*$^{-/-}$ mice compared to OVA-challenged *Hyal3*$^{+/+}$ mice. Data represent the mean ± SD (n=4). "n" represents the number of animals in each group and in each animal atleast 10 fields were analyzed under 200x and 1000x final magnification.

To confirm that the goblet cell hyperplasia observed in OVA-challenged *Hyal3*$^{-/-}$ mice was specific to the inflammation and was not present prior to the antigen sensitization, we performed PAS staining for goblet cells on naive *Hyal3*$^{+/+}$ and *Hyal3*$^{-/-}$ lung sections. The results showed no PAS-positive goblet cells in the airways of either genotype (Figure 33, n=3).

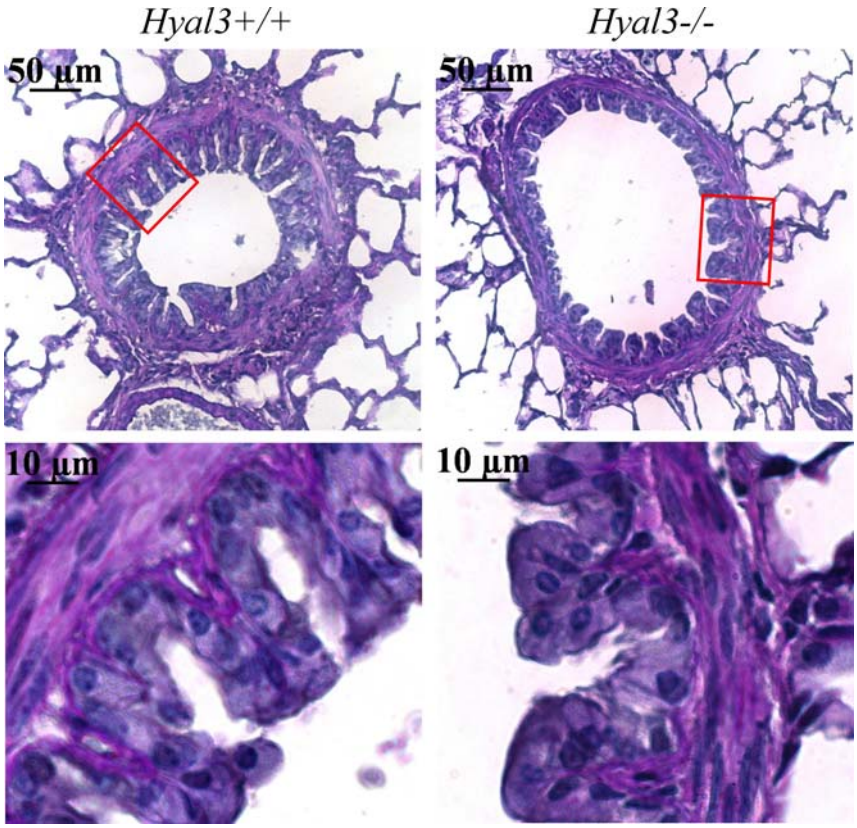

Figure 33: PAS-stained lung sections of naive *Hyal3*$^{+/+}$ and *Hyal3*$^{-/-}$ mice.
Lung sections of naive *Hyal3*$^{+/+}$ and *Hyal3*$^{-/-}$ mice were stained with periodic acid-Schiff (PAS) stain. No PAS-positive goblet cells were identified in either section. Red boxes indicate the region shown under higher magnification in the lower panel. A representative section in each genotype is shown (n=3). "n" represents the number of animals and in each animal atleast 10 fields were analyzed.

Collectively, H & E- and PAS-stained lung sections data indicate *Hyal3*$^{-/-}$ mice exhibited an increase in airway inflammation in response to OVA sensitization and challenge which was absent prior to the antigen sensitization.

4.2.4 Immunophenotyping of naive Hyal3$^{+/+}$ and Hyal3$^{-/-}$ mice

To determine if the differences in the response of *Hyal3*$^{+/+}$ and *Hyal3*$^{-/-}$ mice to allergen sensitization and challenge may be due, in part, to differences in the cellular composition of their immune system prior to allergen challenge, we performed comprehensive immunophenotyping analyses of primary and secondary lymphoid organs by flow cytometry.

First we investigated whether disruption of *Hyal3* affected the development and generation of mature T cells in the thymus. There was no difference in the percentages of CD4+, CD8+, CD4+CD8+ and CD4-CD8- T cells in the thymi of *Hyal3*$^{+/+}$ and *Hyal3*$^{-/-}$ mice (Figure 34, n=2), suggesting that the absence of *Hyal3* does not discernibly affect positive or negative selection of T cells in the thymus.

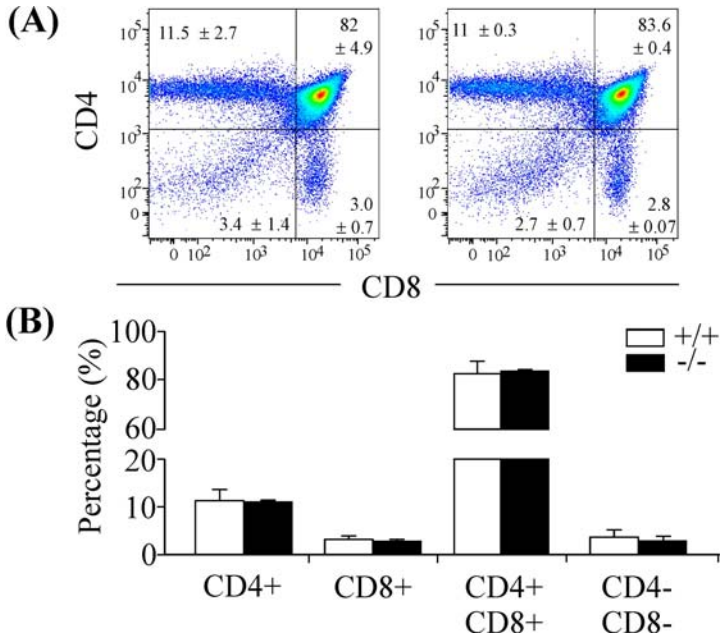

Figure 34: Flow cytometry results showing the percentage of CD4+, CD8+, CD4+CD8+ and CD4-CD8- cells in the thymi of naive *Hyal3*$^{+/+}$ and *Hyal3*$^{-/-}$ mice.

(A, B) No difference was observed in the percentage of CD4+, CD8+, CD4+CD8+, CD4-CD8- cells in thymus of *Hyal3*$^{+/+}$ and *Hyal3*$^{-/-}$ mice. Data represent the mean ± SD (n=2). "n" represents the numer of animals in each group.

Next, we assessed the percentages of mature differentiated lymphocyte subsets in the periphery by determining their numbers in the secondary lymphoid organs. The percentages of T (total, CD3+ and differential, CD4+ and CD8+), B cells (CD19+) and NK cells (DX5+) cells were comparable in the lymph nodes (Figure 35A and B, n=2) and spleens (Figure 35C and D, n=2) of *Hyal3*$^{+/+}$ and *Hyal3*$^{-/-}$ mice, suggesting that the absence of *Hyal3* does not affect the survival of mature lymphocytes in the periphery.

In T cells, CD62L is a lymph node homing receptor which allows them to enter the high endothelial venules and is down-regulated upon activation of T cells (Andersson et al., 1994). When combined with staining of CD44, T cells can be divided into three distinct subsets (naive, memory and effector) by the expression of CD44 and CD62L. Our results of CD44 and CD62L expression on CD4+ T cells and CD8+ cells in lymph node (Figure 36A and B) and spleen (Figure 36C and D) of *Hyal3*$^{+/+}$ and *Hyal3*$^{-/-}$ mice were not significantly different, suggesting that *Hyal3* deficiency does not affect generation and differentiation of naive or memory lymphocytes.

Collectively, our analyses indicate that differences in airway inflammation that developed between *Hyal3*$^{-/-}$ and *Hyal3*$^{+/+}$ mice after OVA-challenge are not the result of disparity in the basal immune status of these animals.

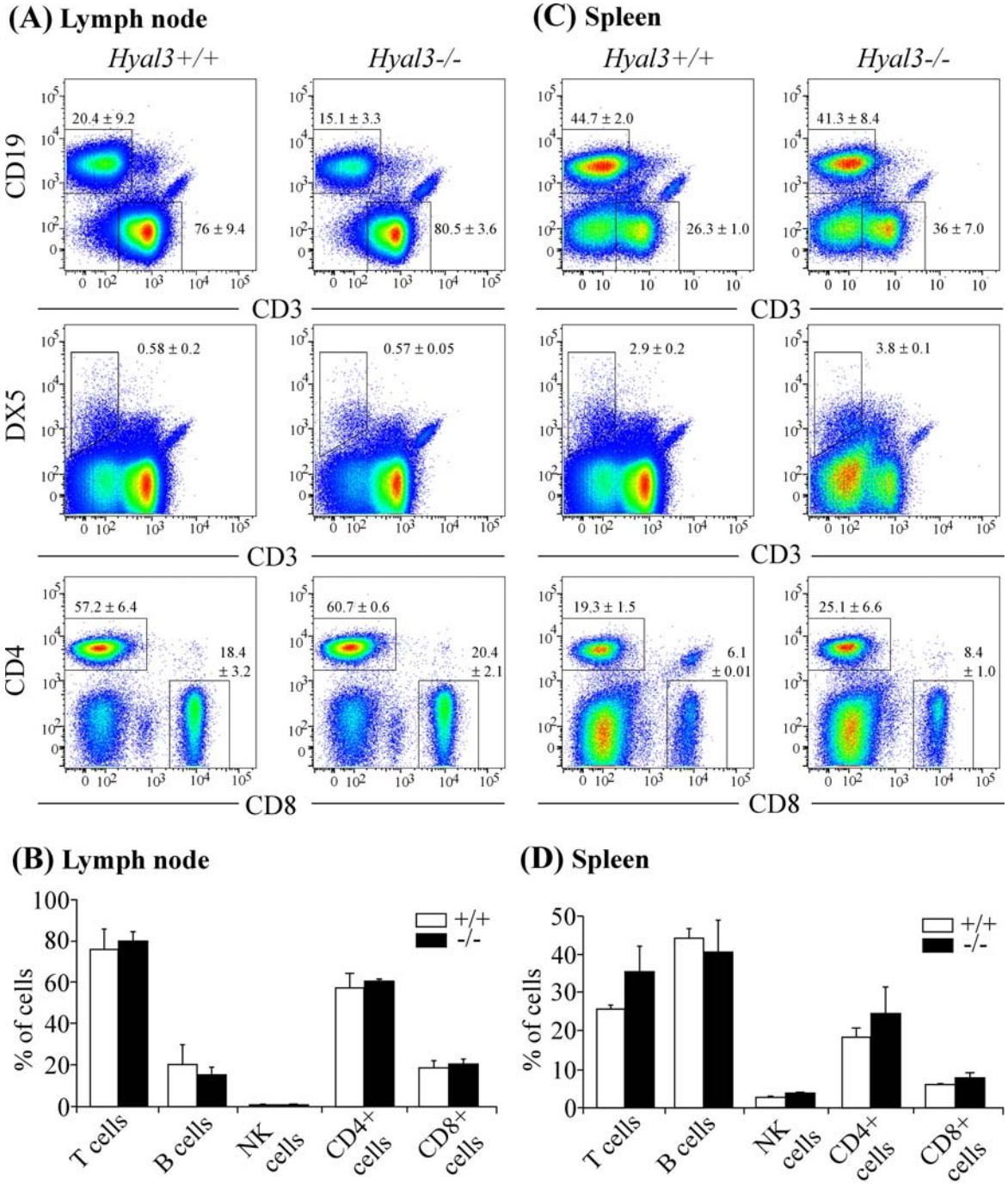

Figure 35: Flow cytometry results showing the percentages of lymphocytes in the lymph nodes and spleens of naive *Hyal3*$^{+/+}$ and *Hyal3*$^{-/-}$ mice.

No significant difference was observed in the percentages of different lymphocytes in **(A** and **B)** lymph nodes and **(C** and **D)** spleens of naive *Hyal3*$^{+/+}$ and *Hyal3*$^{-/-}$ mice. Data represent the mean ± SD (n=2). "n" represents the number of animals in each group.

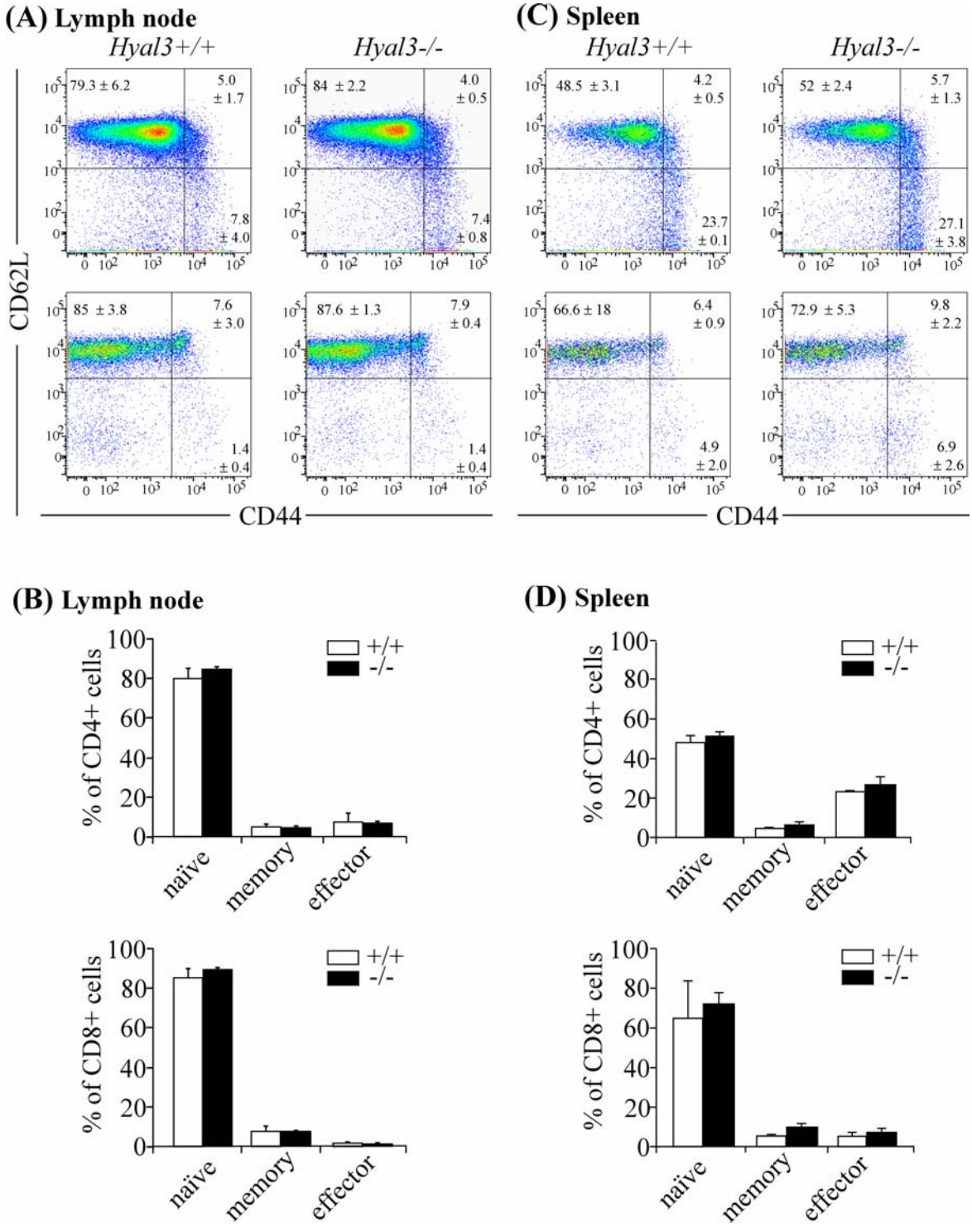

Figure 36: Flow cytometry results showing the percentages of subsets of CD4+ and CD8+ cells in the lymph nodes and spleens of naive *Hyal3*$^{+/+}$ and *Hyal3*$^{-/-}$ mice.

No significant difference was observed in the percentages of different subsets of CD4+ or CD8+ cells in **(A** and **B)** lymph nodes and **(C** and **D)** spleens of naive *Hyal3*$^{+/+}$ and *Hyal3*$^{-/-}$ mice. Data represent the mean ± SD (n=2). "n" represents the number of animals.

4.2.5 Analyses of serum OVA-specific Ig levels in OVA-challenged Hyal3$^{-/-}$ mice.

To confirm that the increased inflammation in OVA-challenged *Hyal3*$^{-/-}$ mice was antigen-specific, OVA-specific IgE, IgG1 and IgG2a levels in serum samples of OVA-challenged *Hyal3*$^{+/+}$ and *Hyal3*$^{-/-}$ mice were assayed by ELISA. The OVA-specific IgE levels (Figure 37A) and the ratio of IgG1/IgG2a (Figure 37B) were significantly increased in OVA-challenged *Hyal3*$^{-/-}$ mice compared to in OVA-challenged *Hyal3*$^{+/+}$ mice.

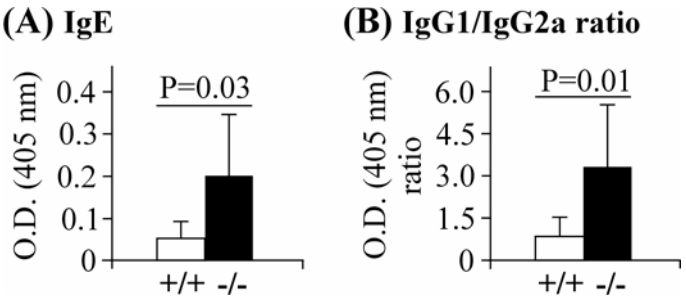

Figure 37: Ig levels in the serum of OVA-challenged *Hyal3*$^{+/+}$ and *Hyal3*$^{-/-}$ mice.
OVA-specific immunoglobulin levels were analyzed in the serum samples of OVA-challenged *Hyal3*$^{+/+}$ and *Hyal3*$^{-/-}$ mice by ELISA. A significant increase in the levels of OVA-specific **(A)** IgE and **(B)** the ratio of IgG1/IgG2a was observed in the serum samples of OVA-challenged *Hyal3*$^{-/-}$ mice compared to similarly treated *Hyal3*$^{+/+}$ mice. Data represent the mean ± SD (n=8). "n" represents the number of animals in each group and in each animal serum samples were analyzed in duplicates.

4.2.6 Analysis of BAL fluid cytokine levels in OVA-challenged Hyal3$^{-/-}$ mice

To further elucidate the cellular basis for increased inflammation in *Hyal3*$^{-/-}$ mice, markers for T-helper 1, (IFN-γ) and T-helper 2 (IL-9 and IL-4) cells and also the eosinophil chemo-attractant (eotaxin-1) were analyzed in the BAL fluid by ELISA. No significant difference was observed in any of the cytokines analyzed between the BAL fluid samples of *Hyal3*$^{+/+}$ and *Hyal3*$^{-/-}$ mice (Figure 38).

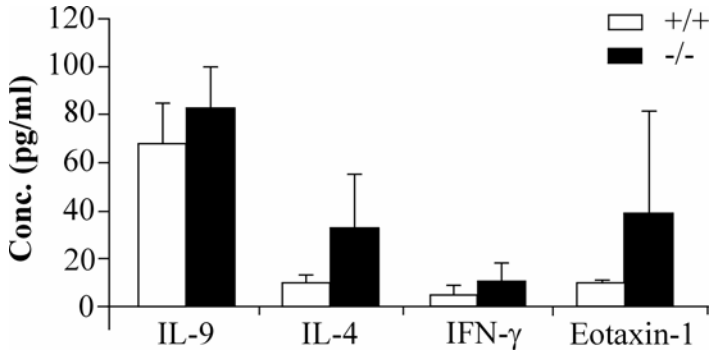

Figure 38: Cytokine levels in the BAL fluid of OVA-challenged *Hyal3*$^{+/+}$ and *Hyal3*$^{-/-}$ mice.

Cytokine levels were analyzed in the BAL fluid of OVA-challenged *Hyal3*$^{+/+}$ and *Hyal3*$^{-/-}$ mice by ELISA. No significant difference in the levels of cytokines (IL-9, IL-4, IFN-γ and eotaxin-1) analyzed was observed between the genotypes. Data represent the mean ± SD (n=4). "n" represents the number of animals in each group and in each sample was analyzed as duplicates.

4.2.7 Analysis of collagen thickness in Hyal3$^{+/+}$ *and Hyal3*$^{-/-}$ *mice*

Chronic airway inflammation is typically associated with airway remodeling (Yamauchi, 2006; Bergeron et al., 2009; Bai and Knight, 2005b). Alterations in the content and organization of the subepithelial ECM of airways is another common feature in allergic diseases such as asthma, the most common being subepithelial fibrosis (Bergeron et al., 2009; Tormanen et al., 2005; Postma and Timens, 2006).

To elucidate the effect of *Hyal3*-deficiency on collagen deposition in our inflammation model, lung sections of OVA-challenged *Hyal3*$^{+/+}$ and *Hyal3*$^{-/-}$ mice were stained for collagen with Picro-Sirius red stain (Figure 39A). To quantitate collagen deposition, the semi-quantitative analyses on the polarized images of Picro-Sirius red (PSR)-stained lung sections (Simoes et al., 2009) of OVA-challenged *Hyal3*$^{+/+}$ and *Hyal3*$^{-/-}$ mice was performed. In each group 4 animals and in each animal atleast 10 airways were used for quantification performed under 200x final magnification. The

quantification was done on a 5-point scale system and the mean PSR-score of OVA-challenged *Hyal3*$^{+/+}$ mice (mean PSR-score 2.22 ± SD 0.33) was significantly increased compared to the mean PSR-score of OVA-challenged *Hyal3*$^{+/+}$ mice (mean PSR-score 1.10 ± SD 0.60) (Figure 39B, n=4, 0.02). Notably, staining for peri-bronchial collagen in OVA-challenged *Hyal3*$^{-/-}$ mice was approximately double of that we measured in similarly treated *Hyal3*$^{+/+}$ mice.

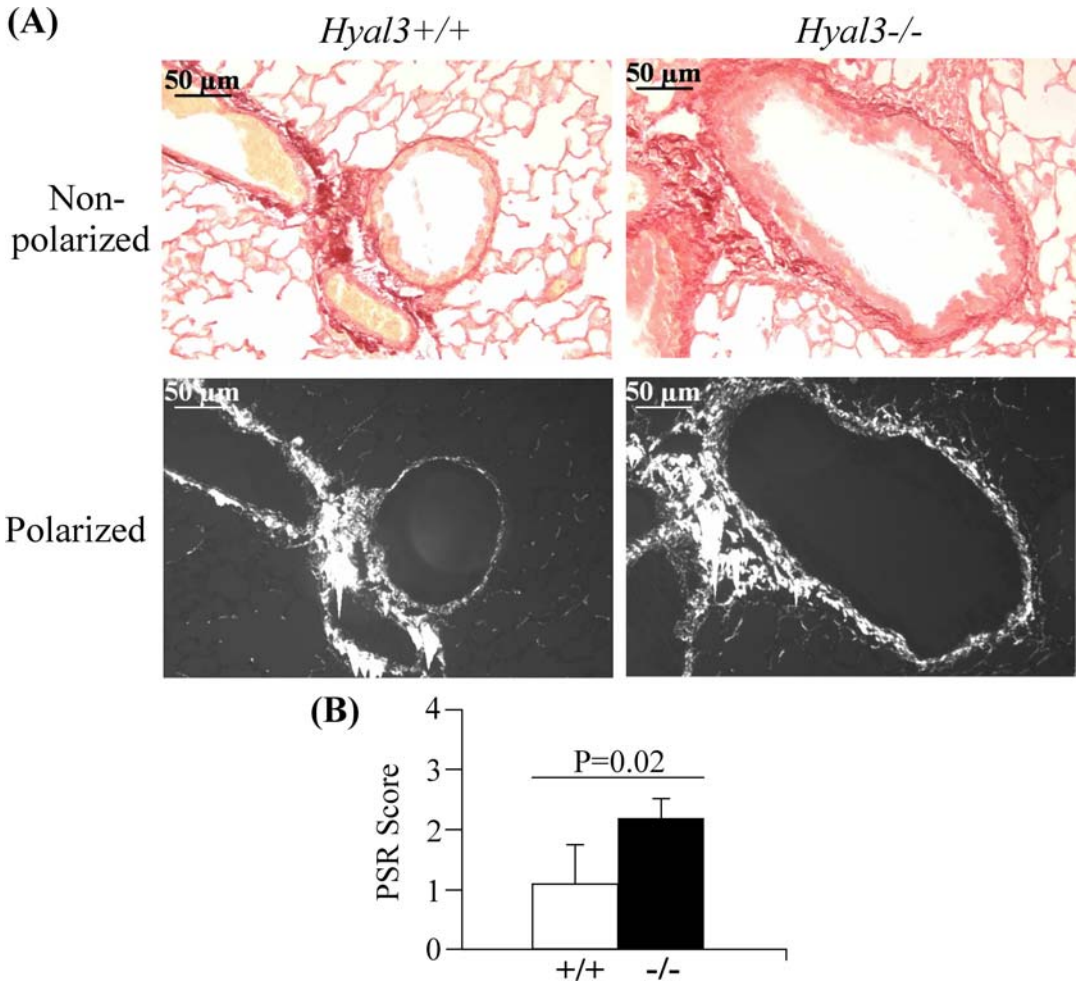

Figure 39: PSR-stained lung sections of OVA-challenged *Hyal3*$^{+/+}$ and *Hyal3*$^{-/-}$ mice.
(A) Lung sections of OVA-challenged *Hyal3*$^{+/+}$ and *Hyal3*$^{-/-}$ mice stained with Picro-Sirius red (PSR) and representative image of a non-polarized and polarized view is shown. **(B)** The semi-quantified data representing the increased peri-bronchial collagen thickness in the airways of OVA-challenged *Hyal3*$^{-/-}$ mice compared to the airways of similarly treated *Hyal3*$^{+/+}$ mice. Data represents the mean ± SD (n=4 animals per group).

To assess whether collagen thickness was already increased in naive *Hyal3*$^{-/-}$ mice, we analyzed PSR-stained lung sections of naive *Hyal3*$^{+/+}$ and *Hyal3*$^{-/-}$ mice (Figure 40A). Semi-quantitative data indicated that there was no difference in collagen thickness between the genotypes (Figure 40B, n=3, P=0.23).

Overall, PSR-stained lung sections data suggests that in response to antigen challenge collagen thickness was increased in *Hyal3*$^{-/-}$ mice

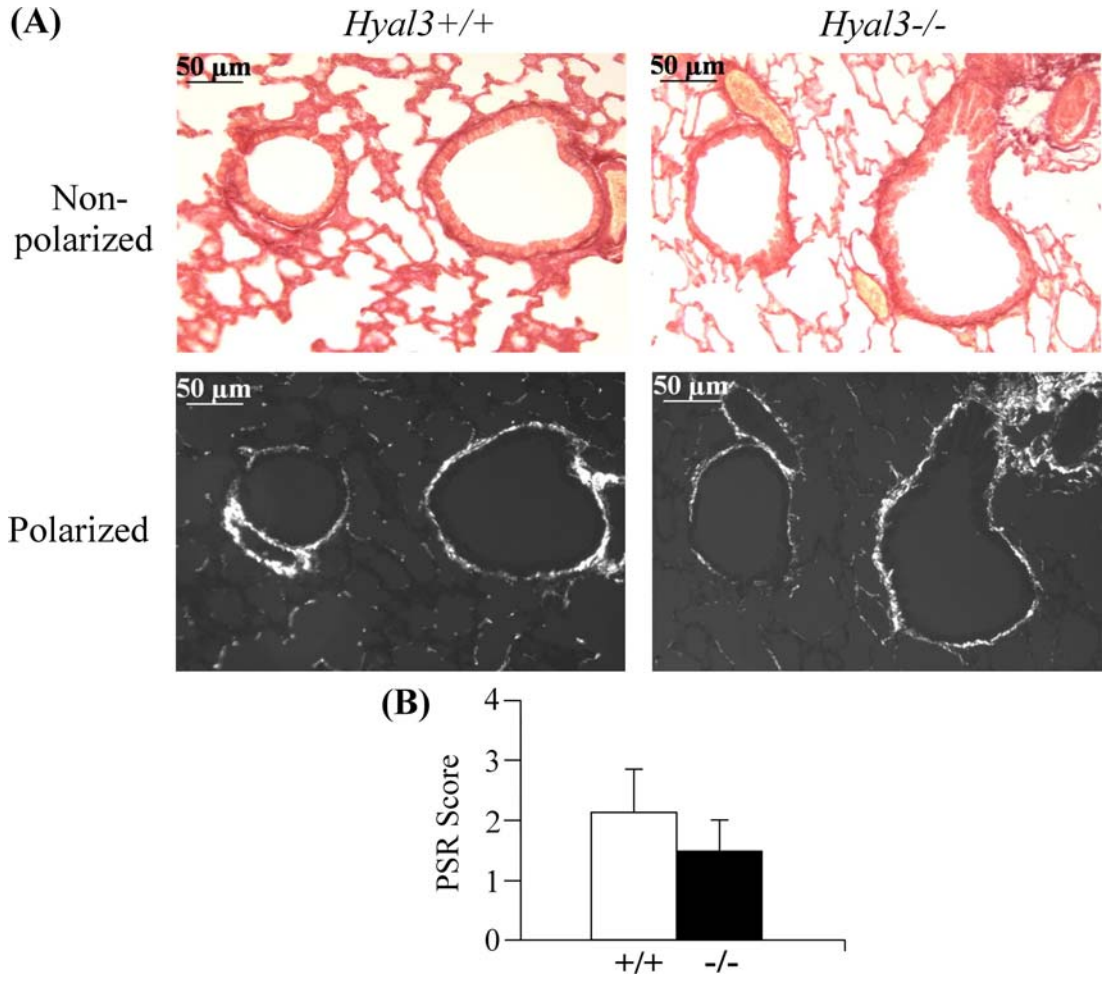

Figure 40: PSR-stained lung sections of naive *Hyal3*$^{+/+}$ and *Hyal3*$^{-/-}$ mice.

(A) Non-polarized and polarized images of airways from naive *Hyal3*$^{+/+}$ and *Hyal3*$^{-/-}$ mouse lung sections stained with PSR. **(B)** A representation of the semi-quantified data of collagen thickness in lung sections. No significant difference was observed in the collagen thickness of *Hyal3*$^{+/+}$ and *Hyal3*$^{-/-}$ airways. Data represent the mean ± SD (n=3). "n" represents the number of animals in each group.

4.2.8 Airway resistance in Hyal3$^{+/+}$ and Hyal3$^{-/-}$ mice

As in human asthma, development of airway hyperresponsiveness to inhaled broncho-constrictors such as methacholine is a characteristic feature of mice in which allergic airway inflammation has been induced (Berend et al., 2008 and Pascual and Peters, 2005). Thus, we next determined changes in respiratory mechanics using low frequency forced oscillation that allowed discrimination of the difference in airway resistance between *Hyal3*$^{-/-}$ and *Hyal3*$^{+/+}$ mice.

OVA-challenged *Hyal3*$^{-/-}$ mice exhibited significantly increased airway resistance at concentrations 12.5 mg/ml ($P<0.001$) and 25 mg/ml ($P<0.01$) of methacholine compared to similarly treated *Hyal3*$^{+/+}$ mice. This indicated that the airways in *Hyal3*$^{-/-}$ mice were hyper-reactive to methacholine (Figure 41A, n=8).

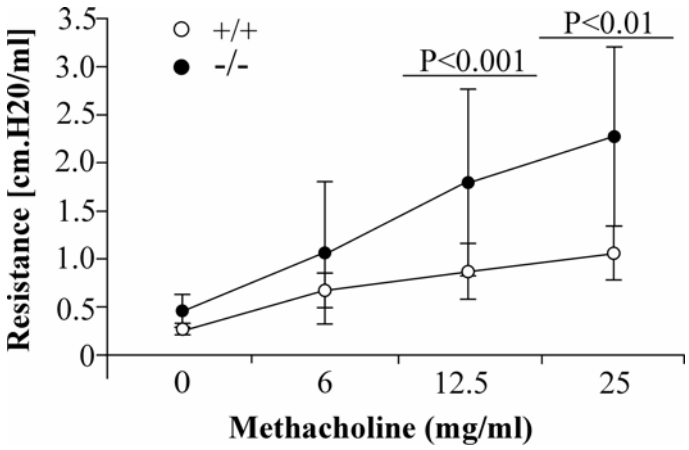

Figure 41: Airway resistance of OVA-challenged *Hyal3*$^{+/+}$ and *Hyal3*$^{-/-}$ mice.
A significant increase in airway resistance in response to methacholine was observed in *Hyal3*$^{-/-}$ mice compared to *Hyal3*$^{+/+}$ mice. Data represent the mean ± SD (n=8). "n" represents the number of animals in each group.

In order to assess if the higher airway resistance observed in OVA-challenged *Hyal3*$^{-/-}$ mice was present in *Hyal3*$^{-/-}$ mice before inflammation, we analyzed airway resistance in naive *Hyal3*$^{+/+}$ and *Hyal3*$^{-/-}$ mice. There was no difference in airway resistance between naive *Hyal3*$^{+/+}$ and *Hyal3*$^{-/-}$ animals (Figure 42, n=3, P>0.05).

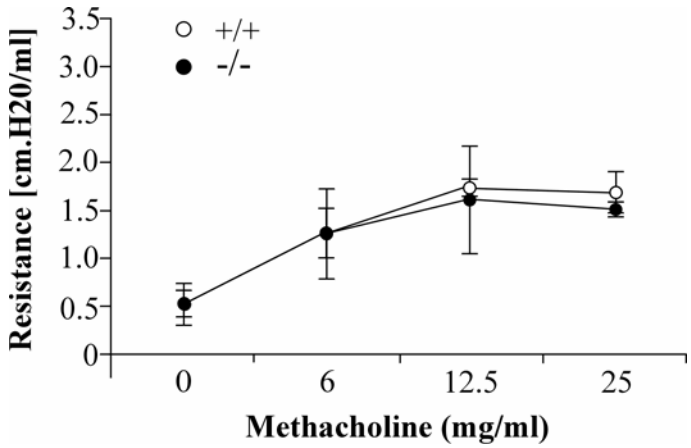

Figure 42: Airway resistance of naive *Hyal3*$^{+/+}$ and *Hyal3*$^{-/-}$ mice.
No significant difference was observed in the airway resistance of *Hyal3*$^{+/+}$ and *Hyal3*$^{-/-}$ mice. Data represent the mean of ± SD (n=3). "n" represents the number of animals in each group.

Collectively, these data reveal that after OVA-challenge to induce airway inflammation, *Hyal3*$^{-/-}$ mice exhibited a greater airway hyperresponsiveness to methacholine than *Hyal3*$^{+/+}$ mice that express *Hyal3*.

4.3 Conclusions and discussion

Lung injury and inflammation are associated with damage, repair and remodeling of the ECM (Jiang et al., 2005; rev. in Jiang et al., 2007). HA is one of several ECM components that is altered during tissue injury and inflammation. Hyal3 is one of the three somatic hyaluronidases that are presumed to play a major role in HA homeostasis. We have shown that *Hyal3* is important in maintaining healthy lungs, presumably through a mechanism that involves regulating the level, sizes and distribution of HA. In *Hyal3*$^{-/-}$ mice, the level of HA in airways was both increased and differently distributed in lung inflammation (Figure 26), suggesting altered HA homeostasis. This is the first *in vivo* report demonstrating a role for *Hyal3* in HA metabolism.

The absence of *Hyal3* is associated with greater susceptibility to an "asthma-like" phenotype when sensitized and challenged with allergen, but this is not associated with alterations in basal immune status. The asthma-like phenotype in the *Hyal3*$^{-/-}$ mice included increased airway inflammation and responsiveness compared to their control littermates. OVA-challenged *Hyal3*$^{-/-}$ mice were shown to exhibit profoundly increased goblet cell hyperplasia compared to *Hyal3*$^{+/+}$ mice, and we also detected a doubling in collagen deposition in the airways. In combination with increased infiltration of inflammatory cells in *Hyal3*$^{-/-}$ mice, structural changes in the airways likely contribute significantly to altered lung function that is manifested as airway hyperresponsiveness to inhaled methacholine. The increased airway inflammation and airway responsiveness that we observed in *Hyal3*$^{-/-}$ mice was not found in naive *Hyal3*$^{+/+}$ and *Hyal3*$^{-/-}$ mice. Therefore, the OVA-induced inflammation and associated airway hyper-responsiveness that we observed in *Hyal3*$^{-/-}$ mice likely reflect differences in the lung microenvironment that promote inflammation. Of note, we are able to rule out the possibility that *Hyal3*

depletion substantially modifies the immune system as we saw no differences in the capacity of *Hyal3*$^{-/-}$ mice to generate and mature thymic T cells or in the relative percentages of lymphocyte subpopulations (B, T and NK cells) in the peripheral lymphoid organs. Thus, our data suggest that increased airway inflammation and airway responsiveness that develop in *Hyal3*$^{-/-}$ mice after allergen challenge is the result of changes in inflammatory responses, including inflammatory cell recruitment, localized to the lung in *Hyal3*$^{-/-}$ mice.

The present studies of lung inflammation in *Hyal3*$^{-/-}$ mice suggest that hyaluronidases play a major role in the constitutive degradation of HA and that Hyal3 is acting either as an enzyme or functioning along with other hyaluronidases, in HA turnover in inflammatory conditions. Indeed, we observed an increased HA concentration in BAL fluid and in lung tissues of *Hyal3*$^{-/-}$ mice after OVA challenge. Moreover, immunohistochemistry of *Hyal3*$^{-/-}$ lungs showed HA accumulation in the peri-bronchial region and in some cases, inside the epithelial cells of airways. These increases in HA suggest that *Hyal3*$^{-/-}$ mice have altered HA metabolism. Despite our observations, the attribution of an important and specific role for the enzyme activity of Hyal3 has been controversial. There is one report of acidic activity of Hyal3 *in vitro* (Lokeshwar et al., 2002), however, previous studies in our lab and others have failed to detect activity intrinsic to Hyal3 (Hemming et al., 2008; Harada and Takahashi, 2007). This might be due to insufficient sensitivity to detect Hyal3 activity, or, a primary role for Hyal3 may not encompass its direct enzyme catalytic potential but rather it may function in a currently unknown manner to support HA degradation.

We had expected that if Hyal3 was involved in any aspect of HA degradation, its deficiency would lead to protection from inflammation as LMW fragments of HA are

associated with inflammation. Our finding that Hyal3 deficiency is associated with increased HA and increased airway inflammation suggests that the accumulating HA is promoting inflammation. It is possible that in the absence of Hyal3, HA accumulates in the matrix around the cell and provides additional substrate for Hyal2 which is known to function outside the cell (Rai et al., 2001; Harada and Takahashi et al., 2007). Hyal2 may then produce pro-inflammatory HA fragments (de la Motte et al., 2009) from the accumulating HA. It is possible that any pathway that leads to accumulation of HA in the ECM where Hyal2 would have access to it, would lead to inflammation. For example, a deficiency in the HA receptor, CD44, was previously shown to promote lung inflammation because HA was not cleared (Teder et al., 2002). Therefore, we speculate that Hyal3 is important for some aspect(s) of HA clearance.

HA is widely used in medical devices and treatments involving the joints (Moreland., 2003; Jüni et al., 2007; Brzusek and Petron, 2008), eyes and skin; and studies have indicated its use in treating lung disorders. Consistent with a role for HMW HA in tissue homeostasis, HMW HA has been shown to prevent bronchoconstriction (Jiang et al., 2005; Jiang et al., 2007; Brzusek and Petron, 2008; Petrigni and Allegra, 2006) in both humans and mice, and to protect from emphysema (Cantor and Turino, 2004) whereas HA fragments have promoted bronchoconstriction (Petrigni and Allegra 2006). A better understanding of how exogenously added HA is handled might be important given that our results suggest that failure to break down HA leads to increased inflammation. It is possible however, that the HA has to be integral to the matrix to become a substrate for degradation, and that exogenously added HA is not a substrate for the processes that produce pro-inflammatory HA fragments.

These studies show for the first time, a potential role for one of the hyaluronidases, Hyal3, in protecting from inflammation. With the additional mouse models of hyaluronidase deficiency that are now available, it will be possible to assess how their deficiency or dysregulation could lead to inflammation.

Chapter five: Analyses of HA levels in Hexa$^{-/-}$Hexb$^{-/-}$ mice

Acknowledgements:

Special thanks to Volkan Seyrantepe and Alex Pshezhetsky from the University of Montreal (Montreal, QC) for crossing *Hexa* and *Hexb* to generate *Hexa*$^{+/-}$ *Hexb*$^{+/-}$ mice and providing those mice for our studies.

5.1 Introduction

HA is ubiquitously present in all vertebrates. Its turnover is rapid, with a half-life varying from a few minutes to a few days. Hyaluronidases are presumed to play a key role in the rapid turnover of HA. However, very little HA accumulation was detected in *Hyal3*$^{-/-}$ mice, and the tissue accumulation of HA in *Hyal1*$^{-/-}$ and *Hyal2*$^{-/-}$ mice was restricted to the joint and liver, respectively. *Hyal1*$^{-/-}$ mice exhibited proteoglycan loss characteristic of osteoarthritis but no other signs of HA accumulation (Martin et al., 2008). *Hyal2*$^{-/-}$ mice displayed skeletal and hematological defects (Jadin et al., 2008) but a direct relationship to HA accumulation was not identified. This evidence suggests that hyaluronidases are not key to HA catabolism when considered in the context of the broad distribution and rapid turnover of HA. This idea suggests inturn that either the hyaluronidases are redundant or that other enzymes involved in HA degradation, the exoglycosidases, may play a major role in HA degradation.

In human and mice, three main somatic hyaluronidases (*Hyal1*, *Hyal2* and *Hyal3*) are broadly expressed and their expression overlaps in most of the tissues (Csoka et al., 1999; Shuttleworth et al., 2002). Studies have shown that in *Hyal1*$^{-/-}$ mice, *Hyal3* mRNA levels (Martin et al., 2008), and in *Hyal2*$^{-/-}$ mice *Hyal1* mRNA levels (Jadin et al., 2008) were increased. Moreover, *Hyal3* overexpression results in increased Hyal1 activity. This evidence suggests that hyaluronidases function together or have redundant roles. However, the very close location of these genes in the chromosome has hindered intercrossing these hyaluronidase knockout mice to generate double- or triple-gene knockouts, and therefore has led us to explore the role of exoglycosidases in HA turnover.

The exoglycosidases, β-hexosaminidase and β-glucuronidase, are the two lysosomal enzymes that remove terminal β-N-acetyl hexosamine and β-glucuronic acid

moieties from GAGs containing these molecules. *In vitro* activity studies have shown that these enzymes can remove terminal sugar units from the non-reducing ends of HA (Longas et al., 1981). However, the contribution of these exoglycosidases to HA degradation is yet to be determined. Mouse models completely deficient in lysosomal β-hexosaminidase were described with MPS-like pathology in addition to the neurological phenotype (Sango et al., 1996; Suzuki et al., 1997). The presence of GAG-filled vacuoles, characteristic of MPS pathology (Sheth et al., 2004), was noticed in the brain and visceral organs of these mice. GAG accumulation was demonstrated by the existence of vacuoles stained with colloidal iron and/or alcian blue in various cells and tissues of *Hexa*$^{-/-}$*Hexb*$^{-/-}$ mice. Moreover, a 50-fold increase in the levels of GAGs in the urine of *Hexa*$^{-/-}$*Hexb*$^{-/-}$ mice compared to either *Hexa*$^{-/-}$ or *Hexb*$^{-/-}$ mice was demonstrated. To date, the individual GAGs accumulated in *Hexa*$^{-/-}$*Hexb*$^{-/-}$ mice have not been analyzed, except in the urine (Hepbildikler et al., 2002).

In the urine of *Hexa*$^{-/-}$*Hexb*$^{-/-}$ mice, GAG levels were increased compared to control mice samples. FACE studies have demonstrated that DS is the main GAG detected in urine of *Hexa*$^{-/-}$*Hexb*$^{-/-}$ mice (Hepbildikler et al., 2002). However, to date, there is no evidence for HA excretion in the urine of the MPS IX patient which displayed increased HA in serum. This suggests the possibility that HA may have accumulated in the tissues of *Hexa*$^{-/-}$*Hexb*$^{-/-}$ mice, and prompted us to determine if HA is one of the GAGs accumulated in the tissues of *Hexa*$^{-/-}$*Hexb*$^{-/-}$ mice. Using this approach, we wanted to determine whether there is a role for β-hexosaminidase, and in turn the contribution of exoglycosidases, in overall HA degradation in tissues.

5.2 Results

5.2.1 Generation of Hexa$^{-/-}$Hexb$^{-/-}$ mice

Hexa$^{-/-}$*Hexb*$^{-/-}$ mice were generated by intercrossing *Hexa*$^{+/-}$*Hexb*$^{+/-}$ mice that were generously supplied by Volkan Seyrantepe and Alex Pshezhetsky from the University of Montreal. The mutations in the *Hexa* and *Hexb* genes were originally introduced by inserting a Neo-cassette in exon 11 or exon 2, respectively (Phaneuf et al., 1996). The mutations in *Hexa* and *Hexb* genes result in the loss of both subunits of β-hexosaminidase, which causes a complete loss of β-hexosaminidase activity.

Genotypes of mice were identified by PCR amplification of DNA isolated from ear-clip samples. Using gene specific primers, wild-type and neo-targeted alleles of *Hexa* gene were identified as 420 bp and 219 bp DNA fragments (Figure 43), while wild-type and neo-targeted alleles of *Hexb* gene were identified as 141 bp and 700 bp DNA fragments, respectively (Figure 43). Mice were considered *Hexa*$^{-/-}$*Hexb*$^{-/-}$, when only with Neo-targeted allele-specific primers for *Hexa* (219 bp) and *Hexb* (700 bp) genes produced amplification products (Figure 43).

5.2.2 Gross phenotype of Hexa$^{-/-}$Hexb$^{-/-}$ mice

The loss of activity of all the isoforms of β-hexosaminidase in *Hexa*$^{-/-}$*Hexb*$^{-/-}$ mice resulted in a severe phenotype in these mice compared to either *Hexa*$^{-/-}$ or *Hexb*$^{-/-}$ or wild-type control mice (Sango et al., 1996; Suzuki et al., 19997). Both *Hexa*$^{-/-}$ and *Hexb*$^{-/-}$ mice accumulate gangliosides in the brain, although *Hexb*$^{-/-}$ mice accumulate more gangliosides and also accumulate glycolipids (Sango et al., 1995; Phaneuf et al., 1996). *Hexb*$^{-/-}$ mice develop a neurological disorder with symptoms that include muscle weakness, spasticity and tremors, however, *Hexa*$^{-/-}$ mice lack these features due to the alternative degradation

pathway that exists in mice in the absence of *Hexa* (Sango et al., 1995; Phaneuf et al., 1996).

The *Hexa*$^{-/-}$*Hexb*$^{-/-}$ mice, which lack the complete activity of β-hexosaminidase, exhibit both a neurological disorder and MPS-like pathology (Sango et al., 1996; Suzuki et al., 1997). These mice displayed extensive accumulation of gangliosides and also evidence for the accumulation of mucopolysaccharides. The severity of the phenotype in these *Hexa*$^{-/-}$*Hexb*$^{-/-}$ mice results in their early death (Sango et al., 1996; Suzuki et al., 19997), with phenotypic presentation by 4 weeks of age and a maximum life span of 4 months. For this reason, *Hexa*$^{-/-}$*Hexb*$^{-/-}$ mice used in this study were typically 5 weeks-old.

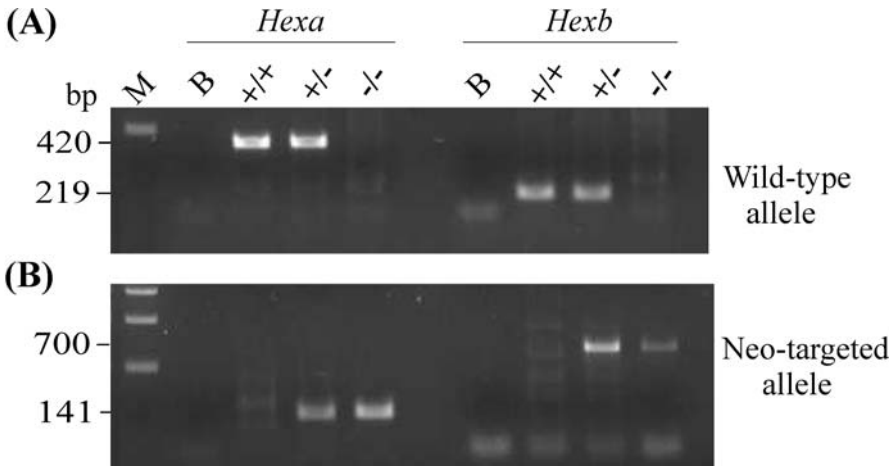

Figure 43: Genotyping of *HexaHexb* mice.

The genotypes of *HexaHexb* mice were determined by PCR amplification of DNA isolated from ear-punch with **(A)** wild-type allele specific primers (WPG 672 and WPG 673 for *Hexa*; WPG 656 and WPG 657 for *Hexb*) and **(B)** neo-targeted allele specific primers (WPG 672 and WPG 658 for *Hexa*; WPG 657 and WPG 659 for *Hexb*). Genotypes of *Hexa* mice were identified by the presence of only 420 bp (+/+), only 141 bp (-/-) or both 420 bp and 141 bp fragments (+/-). Genotypes of *Hexb* mice were identified by the presence of only 219 bp (+/+), only 700 bp (-/-), or both 219 bp and 700 bp fragments (+/-). M- molecular weight marker; B- no template control.

5.2.3 Analysis of Hexa$^{-/-}$Hexb$^{-/-}$ mouse tissues by H & E staining

Studies of *Hexa*$^{-/-}$*Hexb*$^{-/-}$ mice by two different groups (Sango et al., 1996 and Suzuki et al., 1992) showed vacuolated cytoplasm in various cells and tissues of these mice. The vacuolated cells were identified throughout the central nervous system, sinusoidal lining cells in the spleen, epithelial cells in the proximal renal tubules of kidney and in the liver. Moreover, chondrocytes of rib cartilage and trachea of *Hexa*$^{-/-}$*Hexb*$^{-/-}$ mice were enlarged and appeared vacuolated compared to tissues of *Hexa*$^{-/-}$or *Hexb*$^{-/-}$ or wild-type mice.

Prior to characterizing the accumulating GAGs in double knockouts, experiments were performed to confirm the presence of vacuolated cells in the tissues. In addition to the tissues analyzed previously, tissues with high levels of HA, lymph node and the articular and epiphyseal cartilage from knee joints were included. H & E-stained tissue sections of *Hexa*$^{-/-}$*Hexb*$^{-/-}$ and wild-type mice (n=2) were analyzed for the presence of vacuoles.

Among the numerous tissues analyzed, prominent vacuolation was identified in the spleen, liver, cortex of kidney and brain of *Hexa*$^{-/-}$*Hexb*$^{-/-}$ mice compared to wild-type mice tissues (Figure 44). The enlarged chondrocytes were detected in the rib cartilage of *Hexa*$^{-/-}$*Hexb*$^{-/-}$ mice (Figure 44) as described previously (Sango et al., 1997; Suzuki et al, 1996). The only tissue where our preliminary studies failed to detect the phenotype described previously (Suzuki et al., 1996) was the trachea of *Hexa*$^{-/-}$*Hexb*$^{-/-}$ mice where enlarged chondrocytes were not readily apparent (Figure 44).

Our studies also detected enlarged chondrocytes with clear cytoplasm in the articular cartilage, and enlarged chondrocytes with vacuolated cytoplasm in the epiphyseal cartilage of knee joints (Figure 44) that had not been previously described

(Sango et al., 1997; Suzuki et al, 1996). The phenotype is more severe in the articular cartilage compared to the epiphyseal plate of the knockouts (Figure 44).

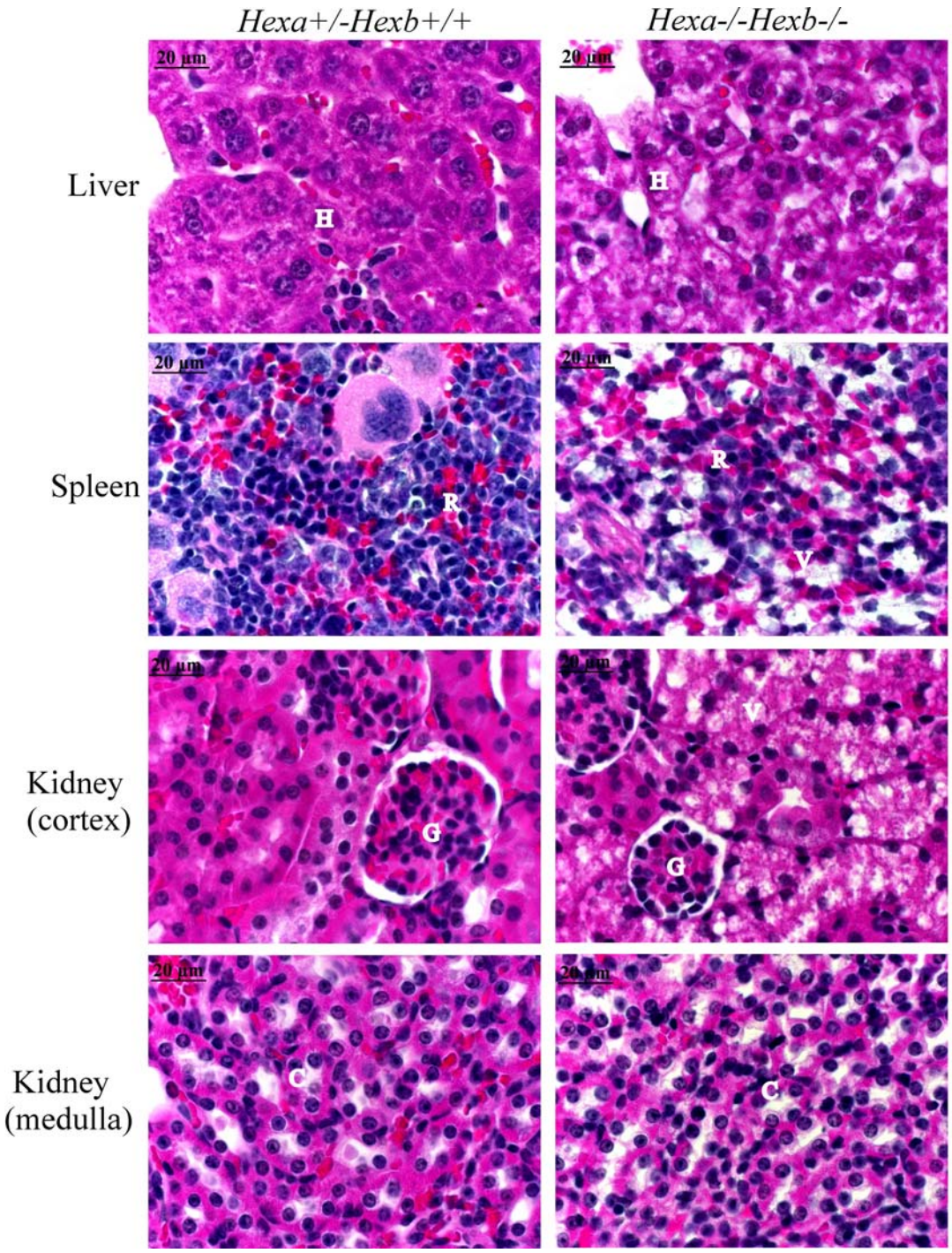

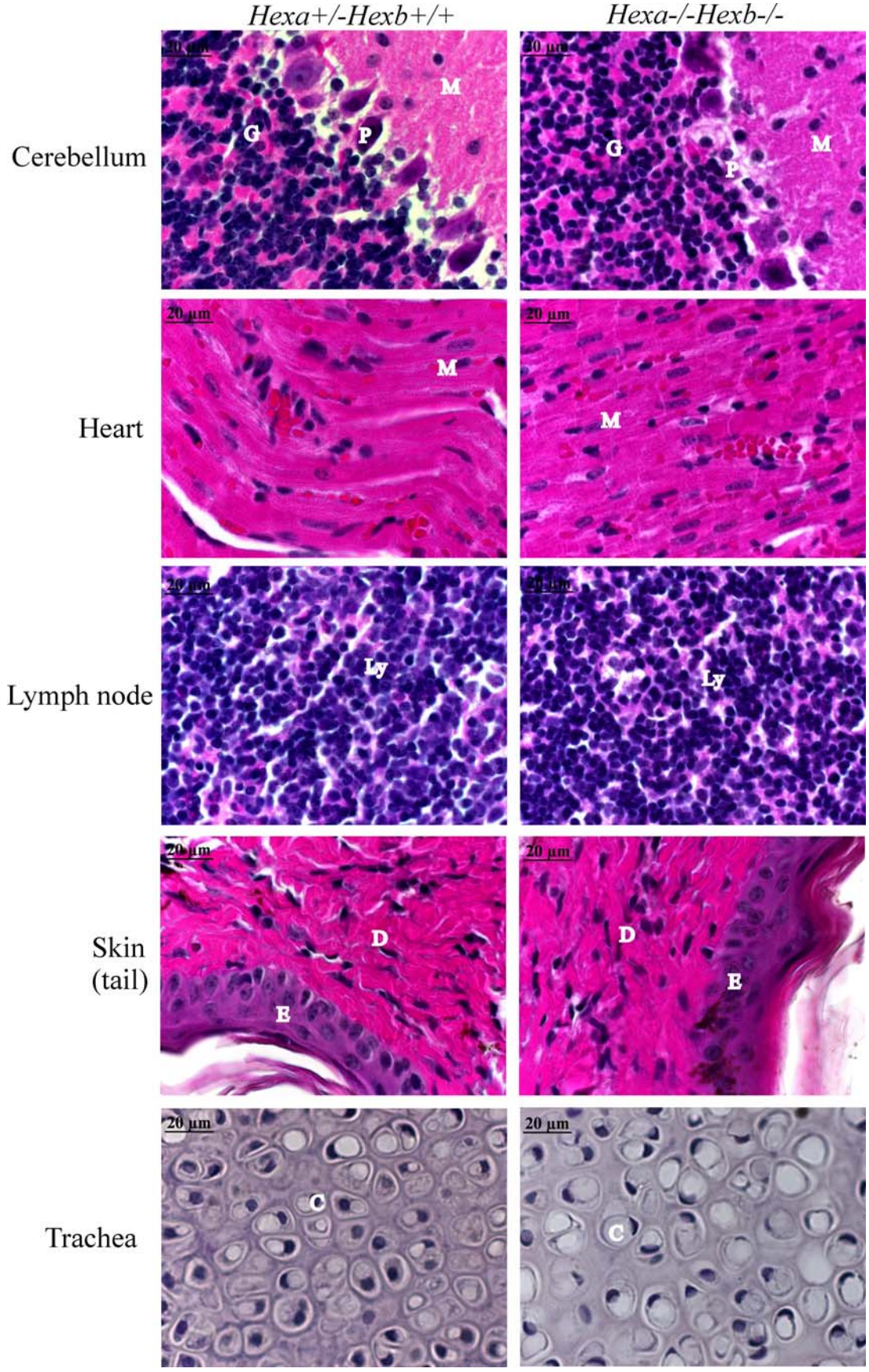
Hexa+/-Hexb+/+
Hexa-/-Hexb-/-
Cerebellum
Heart
Lymph node
Skin (tail)
Trachea
20 µm
M
G
P
Ly
D
E
C

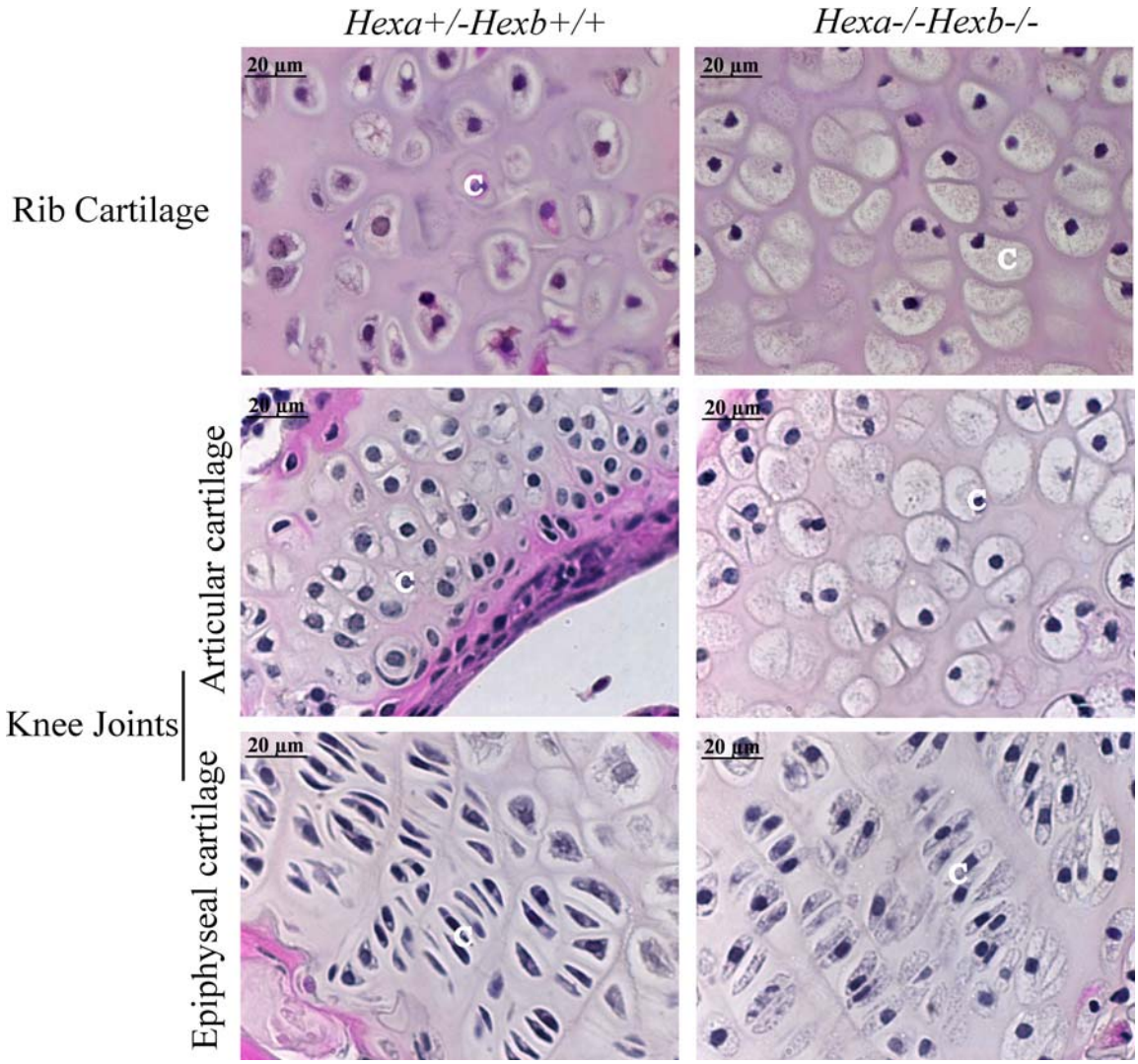

Figure 44: **H & E-stained tissue sections of *Hexa*$^{-/-}$*Hexb*$^{-/-}$ and control mice.**

Intracellular vacuoles were observed in the hepatocytes (H) of liver, renal proximal cells (V) in kidney cortex, sinusoidal cells in the red pulp (R) of spleen, and enlarged chondrocytes (C) in the articular cartilage from ribs and knee joints, as well as enlarged and vacuolated chondrocytes (C) in the epiphyseal cartilage of knee joints. No difference was identified in the cerebellum (G-granule cell layer, P-purkinje cells, M-molecular layer), kidney cortex (G-glomerulus), kidney medulla (C-collecting ducts, skin (E-epidermis and D-dermis), cartilage of trachea (C-chondrocytes), heart (M-cardiac myocytes) and lymph node (ly-lymphocytes in lymphatic nodule) of *Hexa*$^{-/-}$*Hexb*$^{-/-}$ and control mice.

5.2.4 Analysis of GAG concentration in Hexa$^{-/-}$Hexb$^{-/-}$ mouse tissues

Two different groups have demonstrated the accumulation of GAGs in the vacuoles by identifying colloidal iron- and Alcian blue-positive cells in various tissues (Suzuki et al., 1996; Sango et al., 1997). To reproduce the phenotype before characterizing the accumulating GAGs, *Hexa*$^{-/-}$*Hexb*$^{-/-}$ mouse tissues were stained with alcian blue. Increased staining was observed in the sinusoidal cells of the liver, in spleen and also in the lymph node of *Hexa*$^{-/-}$*Hexb*$^{-/-}$ mice compared to wild-type control mice (Figure 45). The vacuolated cytoplasm of renal proximal tubular cells also stained with alcian blue demonstrating GAG accumulation, although no difference in the staining was observed in the glomerulus of the kidney. In addition, the intensity of alcian blue staining was increased in the lungs of *Hexa*$^{-/-}$*Hexb*$^{-/-}$ mice (Figure 45). However, no difference in the intensity of alcian blue staining was observed in the chondrocytes of cartilage in the trachea, knee joints or ribs (Figure 45).

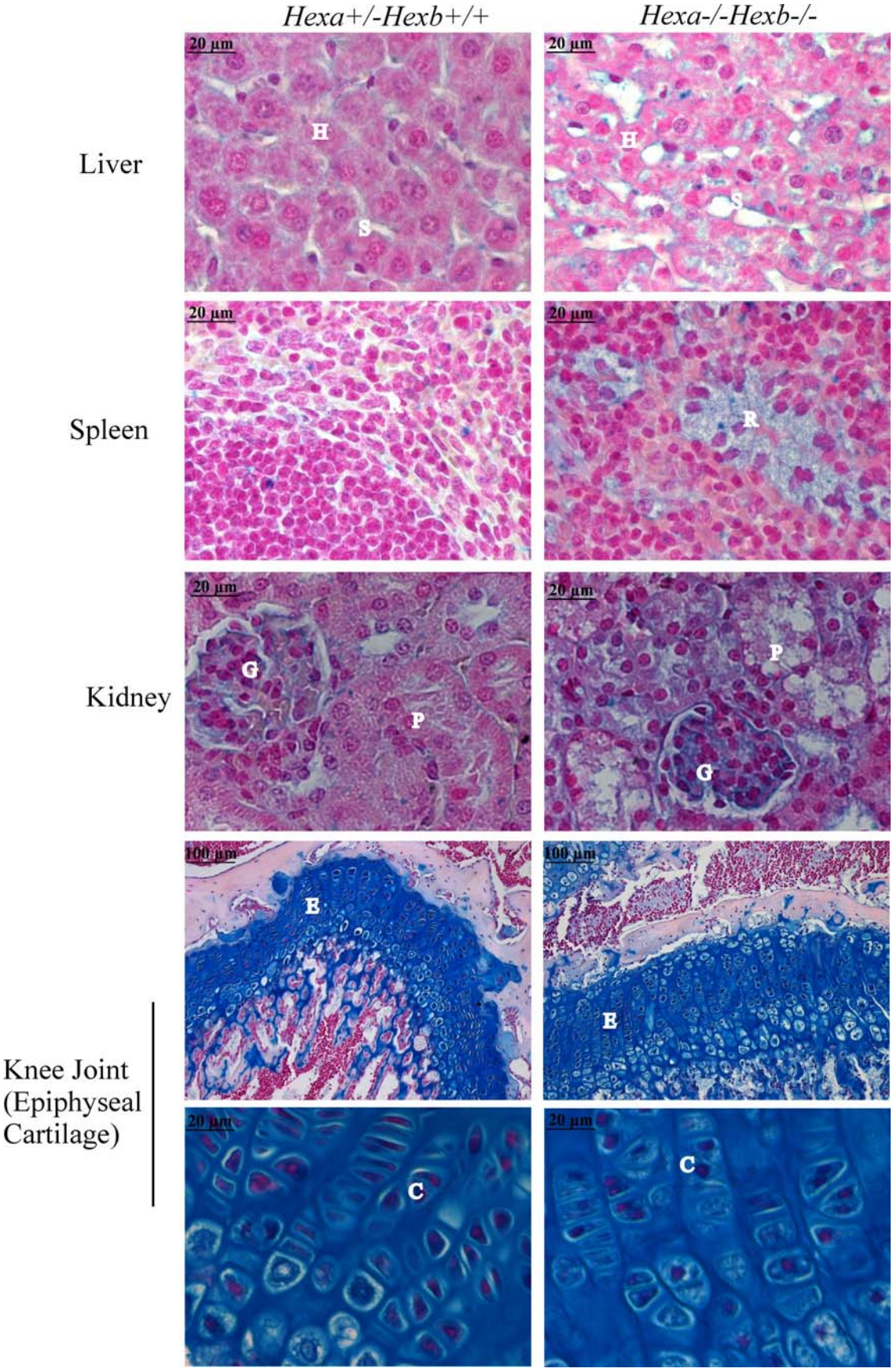
Hexa+/-Hexb+/+
Hexa-/-Hexb-/-
Liver
Spleen
Kidney
Knee Joint
(Epiphyseal
Cartilage)
20 µm
100 µm
H
S
R
G
P
E
C

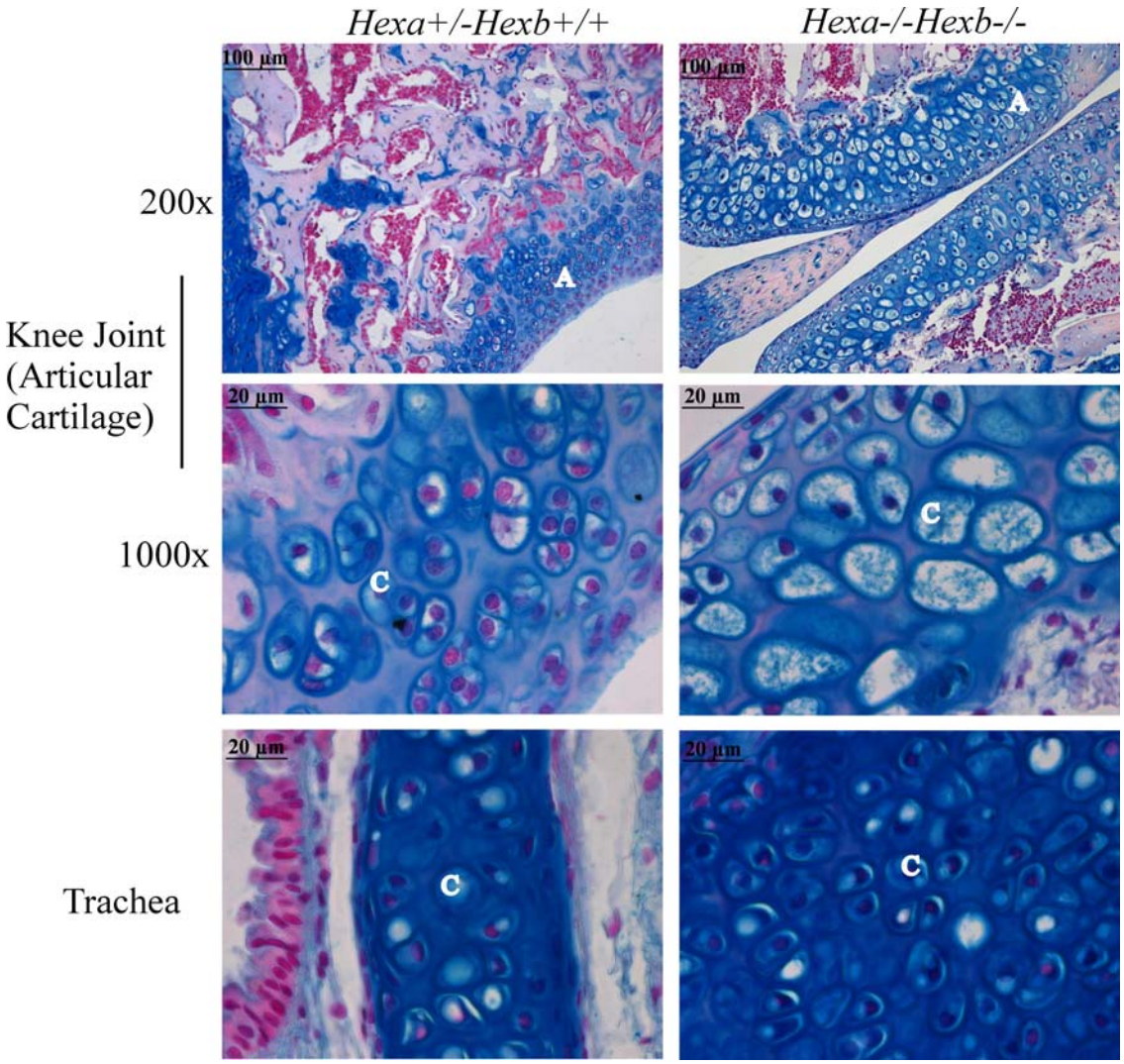

Figure 45: Alcian blue-stained tissue sections of *Hexa*$^{-/-}$*Hexb*$^{-/-}$ and control mice.

Increased alcian blue staining was noticed in the sinusoidal cells in the red pulp (R) of spleen and in the liver (H-hepatocytes) in *Hexa*$^{-/-}$*Hexb*$^{-/-}$ mice compared to the tissues of control mice. Vacuolated renal proximal epithelial cells (P) in the cortex of kidney from *Hexa*$^{-/-}$*Hexb*$^{-/-}$ mice were also stained slightly positive with alcian blue compared to the kidney from control mice. No difference in the intensity of alcian blue staining was observed between the genotypes in the chondrocytes (C) of epiphyseal and articular cartilages of knee joints, and the cartilage of trachea. One representative field from each tissue of *Hexa*$^{-/-}$*Hexb*$^{-/-}$ and control mice is shown (n=2). "n" represents the number of animals in each group.

5.2.5 Analysis of HA content in Hexa$^{-/-}$Hexb$^{-/-}$ mouse tissues

The tissues that were identified with GAG accumulation were further characterized to determine if any of the accumulating GAGs in *Hexa*$^{-/-}$*Hexb*$^{-/-}$ mice was HA. The presence of HA was analyzed in the spleen, liver, lymph node, lungs, tracheal cartilage and articular and epiphyseal cartilage of knee joints by immunohistochemistry using the HA-binding protein. Preliminary results from the tissues revealed that there was no HA accumulation in spleen, lymph node, lungs and liver of *Hexa*$^{-/-}$*Hexb*$^{-/-}$ mice compared to control mice (Figure 46). However further studies are required to confirm these details by immunohistochemistry and also biochemically by FACE.

Our preliminary studies also included the analysis of HA accumulation in the cartilage of trachea and in the knee joints. These results indicated that there was no difference in the intensity of HA staining in the chondrocytes of cartilage of the trachea (Figure 46). Chondrocytes of articular cartilage from knee joints were observed with more peri-cellular HA staining, but overall the intensity of staining was not altered in *Hexa*$^{-/-}$ *Hexb*$^{-/-}$ mice (Figure 46). However, very little staining was noticed in the chondrocytes of the epiphyseal plate.

Surprisingly, the cell layer following the closure of epiphyseal cartilage and the beginning of the bone were stained intensively for HA. The intensity of staining was increased in *Hexa*$^{-/-}$*Hexb*$^{-/-}$ mice compared to wild-type controls (Figure 46). The cells that were intensely stained for HA appear to be osteoblasts, which are precursors for osteocytes. However, further studies are required to confirm this HA accumulation and also to clearly identify the cell type.

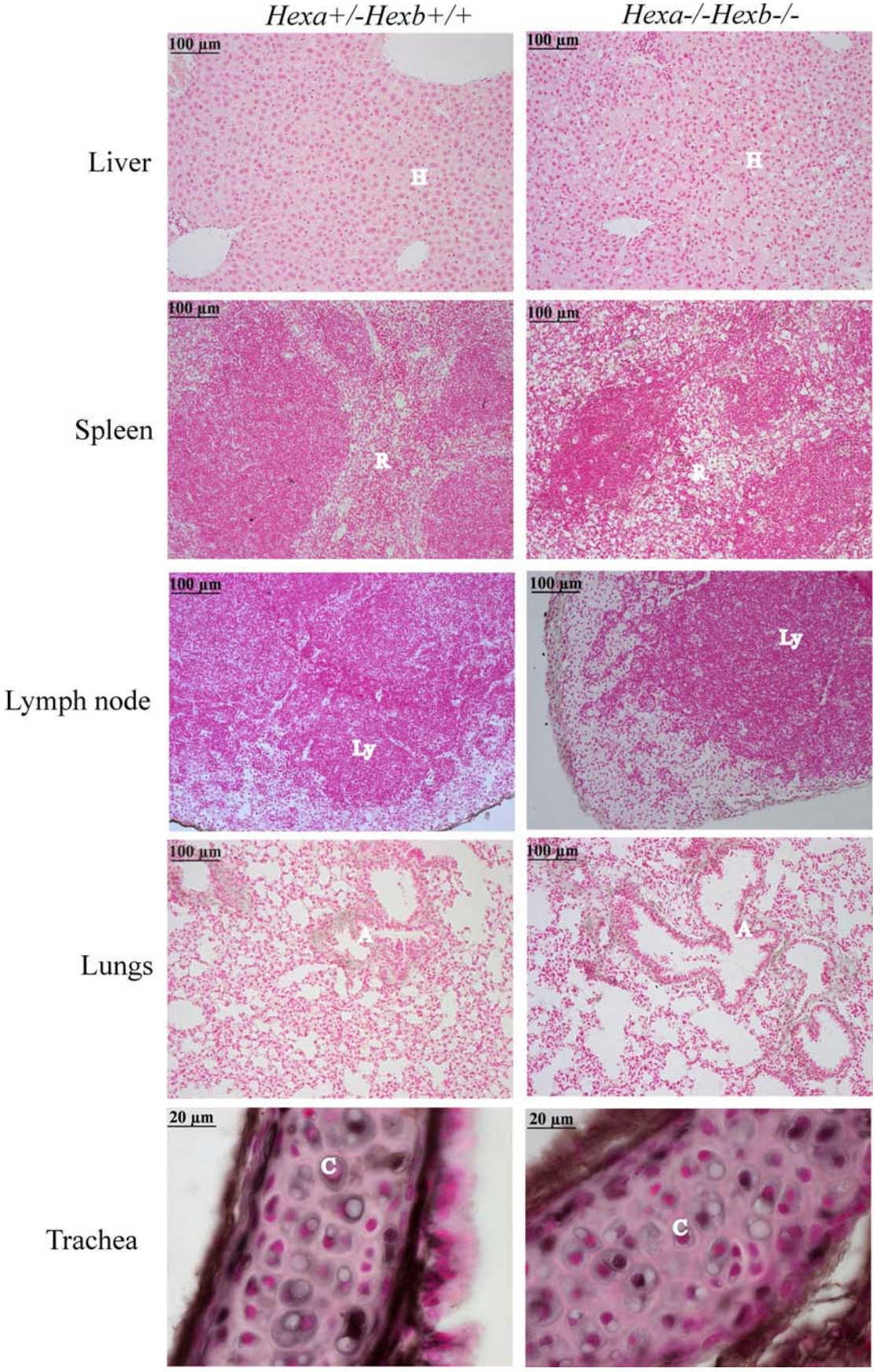
Hexa+/-Hexb+/+
Hexa-/-Hexb-/-
Liver
Spleen
Lymph node
Lungs
Trachea
100 µm
20 µm
H
R
Ly
A
C

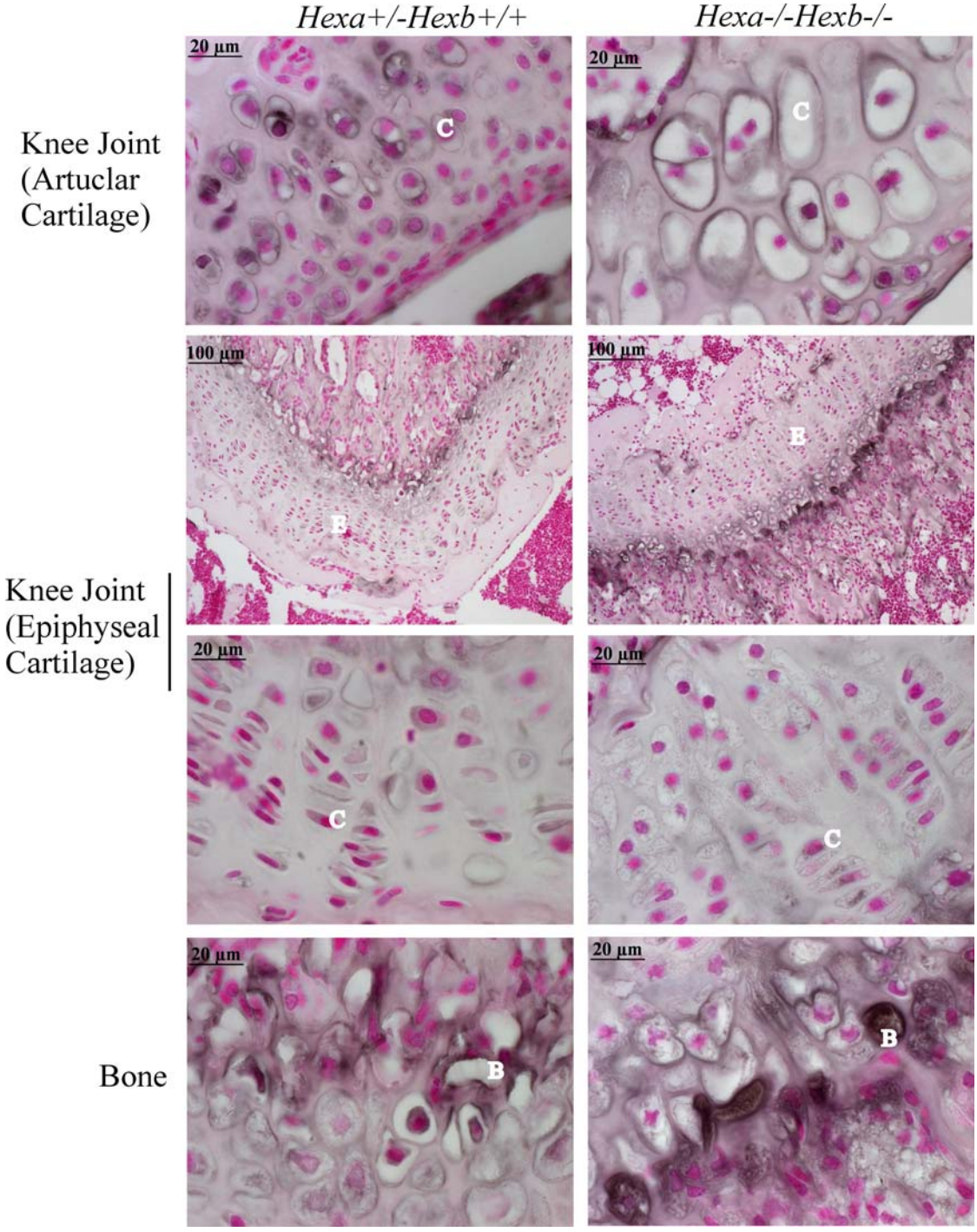

Figure 46: Analysis of HA in the tissue sections of *Hexa*$^{-/-}$*Hexb*$^{-/-}$ and control mice by immunohistochemistry

No difference in HA staining was identified in liver (H-hepatocytes), lymph node (ly-lymphatic nodule), lungs (A-airway), spleen (R-red pulp), cartilage of trachea (C-chondrocytes) and knee joints (E-epiphyseal cartilage, C-chondrocytes) of *Hexa*$^{-/-}$*Hexb*$^{-/-}$ and control mice except increased HA staining in the bone (B-bone cells).

5.3 Conclusions and discussion

Hexa$^{-/-}$*Hexb*$^{-/-}$ mice deficient in both α-and β-subunits of β-hexosaminidase, and therefore having a complete loss of β-hexosaminidase activity, were identified with MPS-like pathology (Suzuki et al., 1996; Sango et al., 1997). The present study has also confirmed that the *Hexa*$^{-/-}$*Hexb*$^{-/-}$ mice exhibit MPS-like pathology with vacuolation in various tissues (brain, spleen, joint, liver and kidney). The alcian blue stained tissue sections have confirmed that vacuolated cells in the tissues accumulated GAGs. However, using the HA-binding protein in the present study either no or little HA accumulation was detected in the absence of *Hexa* and *Hexb* genes. Overall, the present studies were able to reproduce the MPS-like pathology that has been described previously (Suzuki et al., 1996; Sango et al., 1997).

The MPS-like pathology is present only in *Hexa*$^{-/-}$*Hexb*$^{-/-}$ mice, not in mice lacking either α-or β- subunit alone, although a small amount of GAGs are detected in *Hexb*$^{-/-}$ mice (Suzuki et al., 1996). In *Hexb*$^{-/-}$ mice, PAS and/or colloidal iron positive cells representing GAG accumulation were detected in the macrophages of liver; GAGs were also detected in the urine (Suzuki et al., 1996). In these *Hexb*$^{-/-}$ mice, the residual activity due to the β-hexosaminidase S is sufficient to suppress the MPS-like phenotype observed in *Hexa*$^{-/-}$*Hexb*$^{-/-}$ mice. In *Hexa*$^{-/-}$*Hexb*$^{-/-}$ mice, deficiency of the activity of all three isoforms of β-hexosaminidase activity resulted in an MPS-like phenotype that is absent or mild in *Hexa*$^{-/-}$ or *Hexb*$^{-/-}$ mice.

The present studies demonstrated the vacuolation in various tissues as had been described previously (Sango et al., 1997; Suzuki et al., 1996). The only tissue where the difference described by Suzuki and colleagues was not reproduced in the present study was the trachea, where enlarged chondrocytes containing vacuoles in the cartilage of the trachea were not identified. In addition, for the first time these studies also demonstrated

vacuolation in the chondrocytes of articular and epiphyseal cartilage of knee joints from *Hexa*$^{-/-}$*Hexb*$^{-/-}$ mice.

Previously, studies have shown that the vacuoles identified in *Hexa*$^{-/-}$*Hexb*$^{-/-}$ mice were GAG-filled as they stained intensely with alcian blue and/or colloidal iron. My preliminary studies also able to demonstrate GAG accumulation in the vacuoles of various tissues obtained from *Hexa*$^{-/-}$*Hexb*$^{-/-}$ mice. However, the alcian blue stained chondrocytes in the articular cartilage were largely empty in the *Hexa*$^{-/-}$*Hexb*$^{-/-}$ mice knee joints compared to wild-type controls. The present studies were unable to demonstrate whether the large empty chondrocytes in articular cartilage were the result of loss of GAGs during tissue processing, or that accumulating gangliosides in these cells were somehow hindering or masking the staining.

Ganglioside accumulation was observed in the brain and visceral organs of *Hexa*$^{-/-}$ *Hexb*$^{-/-}$ mice, where the complete loss of β-hexosaminidase activity resulted in the severe form compared to *Hexa*$^{-/-}$ or *Hexb*$^{-/-}$ or wild-type mice. The ganglioside accumulation also appears as vacuoles inside the cells, similar to MPS-pathology. To better understand if the enlarged and empty chondrocytes observed in *Hexa*$^{-/-}$*Hexb*$^{-/-}$ mice are specifically accumulating either GAGs or gangliosides, studies are required to compare *Hexa*$^{-/-}$*Hexb*$^{-/-}$ mice tissues with *Hexb*$^{-/-}$ tissues. Previous studies used *Hexa*$^{-/-}$ or *Hexb*$^{-/-}$ or wild-type mice for comparison, however, my preliminary studies employed only wild-type controls. Specifically, the use of *Hexb*$^{-/-}$ mice which have an accumulation of gangliosides similar to *Hexa*$^{-/-}$*Hexb*$^{-/-}$ mice, but have very little GAG accumulation, will aid in confirming the vacuoles as either GAG- or ganglioside-specific.

The only analysis performed to analyze the accumulated GAGs in the *Hexa*$^{-/-}$*Hexb*$^{-/-}$ mice was in urine samples analyzed by FACE. The FACE studies have demonstrated

that the accumulating GAG in the urine of *Hexa*$^{-/-}$*Hexb*$^{-/-}$ mice was DS (Sango et al., 1997; Hepbildikler et al., 2002). My studies used a sensitive method to determine if HA is one of the GAGs accumulating in the *Hexa*$^{-/-}$*Hexb*$^{-/-}$ mice tissues. The HA detection was performed by a specific semi-quantitative method using the HA-binding protein. My preliminary studies have shown no HA accumulation in the spleen, liver, lymph node and lungs of *Hexa*$^{-/-}$*Hexb*$^{-/-}$ mice compared to wild-type controls. However, the overall staining in these tissues appeared weak. Further studies with additional animals are needed to assess HA levels. Very weak staining was detected inside the chondrocytes of articular and epiphyseal cartilage, and therefore, I cannot rule out the possibility that this is due to the lack of accessibility of antigen to the antibody. The only tissue that was observed to have more HA staining was in the bone. Osteoblasts in the bone of *Hexa*$^{-/-}$ *Hexb*$^{-/-}$ mice appeared to be filled with more HA than wild-type controls. Overall, these preliminary results indicate that there is little or no HA accumulation in the *Hexa*$^{-/-}$*Hexb*$^{-/-}$ mice, with the exception of HA accumulation in the osteoblasts of the bone. However, further studies are needed to confirm this by both immunohistochemistry and by FACE analysis.

These preliminary results indicate that β-hexosaminidase is not playing a major role in HA turnover. However I cannot rule out the possibility that subtle accumulation was missed during HA detection or that the presence of gangliosides masked or hindered HA detection.

Chapter six: Conclusions, discussion and future directions

6.1 Conclusions and discussion

HA is an omnipresent molecule in vertebrates that is rapidly turned over. Hyaluronidases are the enzymes that are believed to play a major role in HA degradation. Of the six hyaluronidases in humans, *Hyal1*, *Hyal2* and *Hyal3* are the three broadly expressed somatic hyaluronidases. However, the role and contribution of these enzymes in the constitutive degradation of HA are not completely understood. The first *in vivo* evidence supporting a role for hyaluronidases in HA degradation was shown in an MPS IX patient with mutations in *HYAL1*. The patient displayed HA accumulation in blood and in the lysosomes of fibroblasts and macrophages. Despite the broad distribution and rapid turnover of HA, the MPS IX patient exhibited a mild phenotype compared to the other MPS disorders. This suggested that other hyaluronidases, HYAL2 and/or HYAL3, may play a major role in HA catabolism by compensating for the loss of HYAL1 in the MPS IX patient.

Studies demonstrating a close relationship between *HYAL3* and *HYAL1*, as well as a similar sub cellular localization of HYAL1 and HYAL3, led us to speculate that HYAL3 plays a major role in HA degradation. *HYAL3* mRNA expression was shown to be increased in the fibroblasts of an MPS IX patient (Dianna Martin, unpublished data) and the tissues of *Hyal1*$^{-/-}$ mice (Martin et al., 2008). However, the enzymatic activity of HYAL3 is controversial (Lokeshwar et al., 2002; Harada and Takahashi, 2007; Hemming et al., 2008). To date, very little is known about the role of *Hyal3*; to better understand this protein, *Hyal3*$^{-/-}$ mice were generated by introducing a mutation into exon 2 of *Hyal3*.

The *Hyal3*$^{-/-}$ mice appeared normal with no sign of cellular vacuolation and no obvious phenotype in any of the major tissues analyzed, except a subtle lung phenotype in aged mice. Lungs of 12-14 month-old *Hyal3*$^{-/-}$ mice appeared to have large alveolar spaces

similar to that seen in an emphysema-like condition. In addition, 6 month-old *Hyal3*$^{-/-}$ mice appeared to have an alveolar septal defect in their lungs. However, it is not uncommon to have an alveolar size or septal defect when the ECM of lungs is altered. Mouse models deficient in matrix proteinases have been described with enlarged alveolar spaces and/ or an alveolar septal defect (Irie et al., 2005; Leco et al., 2001). The knockout mice for membrane-type matrix metalloproteinase 1 (MT1-MMP) developed abnormally large and smooth alveolar spaces (Irie et al., 2005). Moreover, the knockout mice for tissue inhibitor of metalloproteinase-3 (TIMP-3) developed spontaneous air space enlargement that progressed with age (Leco et al., 2001) and also appeared to have disruption of alveologenesis (Gill et al., 2009). In these mouse models, the turnover of ECM components is altered, which suggests that in *Hyal3*$^{-/-}$ mice, the deficiency of *Hyal3* is leading to changes in ECM. Total GAG content in lungs and various other tissues of *Hyal3*$^{-/-}$ mice was analyzed to assess changes in its turnover in the absence of *Hyal3* using a uronic acid assay. However, the uronic acid assay results failed to demonstrate any difference between *Hyal3*$^{+/+}$ and *Hyal3*$^{-/-}$ mice. This indicates that *Hyal3* probably does not have a major role in HA degradation but does appear to have some role in the lung. The down-regulation of *Fus2,* a gene embedded within *Hyal3*, in the liver of *Hyal3*$^{-/-}$ mice can not be ruled out as a contributing factor to the lung phenotype. It would be interesting to examine the expression levels of *Fus2* in *Hyal3*$^{-/-}$ mouse lungs.

The lung phenotype observed in *Hyal3*$^{-/-}$ mice was subtle, but an important role for hyaluronidases in the lungs was supported by the detection of all three major somatic hyaluronidases (HYAL1, HYAL2 and HYAL3) in human and mouse lungs (Csoka et al., 1999; Shuttleworth et al., 2002). Further, mRNA and protein for all three hyaluronidases were detected in human bronchial epithelial cells (Monzon et al., 2008). The HYAL2

protein was detected both intracellularly and at the cell surface. However, HYAL1 and HYAL3 proteins were only detected inside the cells, with frequent co-localization of these proteins. This was shown in a bronchial epithelial cell culture system and in tracheal sections obtained from healthy individuals (Monzon et al., 2008). Moreover, HYAL3 protein expression was increased in the epithelial cells of tracheal sections from asthmatics compared to healthy individuals. This suggests a role for HYAL3 in maintaining healthy lungs.

In order to elucidate a role for *Hyal3* in HA homeostasis in lungs, lung tissue sections from naive *Hyal3*$^{+/+}$ and *Hyal3*$^{-/-}$ mice were stained specifically for HA using HA-binding protein. There was a significant increase in HA in the ECM of airways of naive *Hyal3*$^{-/-}$ mice compared to naive *Hyal3*$^{+/+}$ mice. This suggests that *Hyal3*-deficiency results in an imbalance in the metabolism of HA. Despite this apparent imbalance in HA homeostasis, the enzymatic activity of Hyal3 is controversial. At this point it is unclear whether Hyal3 is acting as an enzyme or whether it is playing another as yet unknown role in the degradation pathway.

Lung is a tissue with high turnover of ECM components. HA is one of the ECM components that accumulate in several lung conditions. Studies of *Hyal3*$^{-/-}$ mice showing a subtle lung phenotype and altered HA homeostasis in the airways of naive *Hyal3*$^{-/-}$ mice, as well as studies indicating an increase in HYAL3 protein levels in asthmatics, led us to study the effect of *Hyal3*-deficiency in an asthma-like model generated by OVA-sensitization and challenges.

In OVA-challenged *Hyal3*$^{+/+}$ and *Hyal3*$^{-/-}$ mice, the HA quantification studies showed a significant increase in the levels of HA present in the *Hyal3*$^{-/-}$ lungs compared to *Hyal3*$^{+/+}$ lungs. The increased HA was observed in the BAL fluid, ECM of airways of

lungs and also in the total lung tissue lysate of OVA-challenged *Hyal3*$^{-/-}$ mice. Surprisingly, in addition to the overall HA increase, our studies have shown that the organization of HA differed between the OVA-challenged *Hyal3*$^{+/+}$ and *Hyal3*$^{-/-}$ mice. The airway epithelial cells of OVA-challenged *Hyal3*$^{-/-}$ mice contained intracellular HA that was completely absent in similarly treated *Hyal3*$^{+/+}$ mice (Figure 26A), and also in naive *Hyal3*$^{+/+}$ and *Hyal3*$^{-/-}$ mice (Figure 25A). These changes in the content and distribution of HA in OVA-challenged *Hyal3*$^{-/-}$ mouse lungs suggests that HA homeostasis is altered by *Hyal3*-deficiency.

In addition to the altered HA homeostasis, increased lung inflammation was also observed in OVA-challenged *Hyal3*$^{-/-}$ mice, suggesting altered HA homeostasis and lung inflammation were associated in these mice. Altered HA homeostasis has previously been shown to affect inflammation in several lung inflammation models. Some studies have shown that HA accumulating at the site of inflammation is not the HMW HA that exists in healthy state but rather LMW HA fragments that are pro-inflammatory or very large HA structures called HA cables that may have a protective role at the inflammation site.

In several lung injury models, LMW HA fragments were shown to have pro-inflammatory effects. Moreover, the studies have shown that LMW HA fragments but not HMW HA induces inflammatory responses in lung cells (Jiang et al., 2005; McKee et al., 1996; McKee et al., 1997; Noble et al., 1996). The LMW HA fragments that accumulate at the site of tissue injury promote the inflammatory response by stimulating cytokine and chemokine expression in macrophages (Jiang et al., 2005; rev. in Jiang et al., 2006). A role for toll-like receptor (TLR)-2 and TLR-4 as receptors for HA in mediating the signals to increase the expression of inflammatory cytokines and chemokines has been identified using knockout mouse models of TLR-2 and TLR-4. The role of HA fragments is in

contrast to the role for HMW HA during injury where HMW HA present at the surface of epithelial cells protects the cells from undergoing apoptosis by basal activation of NF-kB through TLR-2 and TLR-4 (Jiang et al., 2005; rev. in Jiang et al., 2006).

Studies have also shown that during inflammatory conditions, as a protective mechanism, HA forms large cable-like structures that are adhesive for monocytes. There is a proposed model suggesting that in response to stress or inflammatory conditions, intracellular HA synthase that may be present in association with endoplasmic reticulum or nuclear membrane, synthesizes HA cables inside the cell. These HA cables are extended into the ECM which further promotes the adhesion of leukocytes to them. This is suggested to block the access of ligands to the inflammatory signals, thereby inhibiting further inflammation (rev. in Hascall et al., 2004).

In OVA-challenged *Hyal3*$^{-/-}$ mice, it is possible that either HA fragments and/ or HA cables are accumulating at the site of inflammation. If HA fragments accumulate, these fragments further mediated the inflammatory response by inducing the expression of inflammatory cytokines and chemokines, and thereby increasing lung inflammation in OVA-challenged *Hyal3*$^{-/-}$ mice. It is also possible that HA cables are synthesized in these mice to protect them from inflammatory response. However, we can not exclude the existence of both mechanisms during *Hyal3*-deficiency. The undegraded HA accumulated during *Hyal3*-deficiency may become a substrate for Hyal2, which degrades HA to generate pro-inflammatory HA fragments. These HA fragments further mediate inflammatory responses and in turn promote the environment to form HA cables that inhibit increased inflammation. Despite these studies suggesting a role for Hyal3 in HA degradation, the enzymatic activity of Hyal3 is controversial.

The *Hyal3*$^{-/-}$ mouse studies (Atmuri et al., 2008; Arja et al., manuscript in preparation), together with studies of *Hyal1*$^{-/-}$ and *Hyal2*$^{-/-}$ mice indicated that the phenotypes exhibited by these mice were mild compared to the broad distribution and rapid turnover of HA. This suggested a role for the exoglycosidases in the turnover of HA. However, preliminary analysis of HA levels in the tissues of *Hexa*$^{-/-}$*Hexb*$^{-/-}$ mice indicated that there was no or very little accumulation of HA. This suggests that exoglycosidases may be not playing a major role in HA degradation, although we can not rule out redundancy with hyaluronidases. It is not uncommon to have these redundancies as increased β-hexosaminidase activity was detected in mice deficient in β-glucuronidase (Tomatsu et al., 2003).

Our present studies provide a basis for further studies aimed at evaluating the contribution of all the enzymes involved in tissue HA degradation.

6.2 Future directions

Hyal3$^{-/-}$ mice were generated by targeted disruption of *Hyal3*. These mice appeared normal except with subtle differences in the cellularity and structure of lungs. In humans and mice, *Fus2*, a gene that encodes for N-acetyl transferase, is embedded within *Hyal3*. The experiments conducted to analyze the expression levels of *Fus2* resulted in a reduction in the transcript levels in liver. Further experiments should be conducted to rule out the possibility that this reduced *Fus2* transcript level has an impact on the lung phenotype that was observed in *Hyal3*$^{-/-}$ mice. This could be done by analyzing the expression levels of *Fus2* in the lung tissue of *Hyal3*$^{-/-}$ mice. The mRNA levels of *Fus2* can be studied by performing real-time RT-PCR.

Studies of *Hyal3*$^{-/-}$ mice described in chapter 3 did not detect any significant accumulation of HA in these mice using a uronic acid assay. However, when the HA analysis was performed using biotinylated HA-binding protein, a more sensitive method than the uronic acid assay, an increase in HA was detected in the lungs of *Hyal3*$^{-/-}$ mice. Based on this observation, future studies should be conducted using the biotinylated HA-binding protein to detect levels of HA in all the other tissues of *Hyal3*$^{-/-}$ mice. HA levels in other tissues might be identified by following the basic HA immunohistochemistry protocol employed for lung tissues. These studies could also be followed up with FACE if areas of highly elevated HA are identified in any tissue(s). Based on the HA levels estimated in various tissues of *Hyal3*$^{-/-}$ mice by HA immunohistochemistry and FACE, *Hyal3* may eventually be found to play a role in HA turnover in additional tissues.

Increased HA levels in the lungs of *Hyal3*$^{-/-}$ mice suggested that Hyal3 has a role in HA degradation. However, to date no enzymatic activity has been detected for Hyal3, except in an *in vitro* study. Studies by Hemming et al (Hemming et al., 2008) have tested

Hyal3 enzyme activity on HMW HA. Further studies should be conducted to test Hyal3 activity on HA fragments of different sizes in an *in vitro* assay. The MEFs or lung tissue lysates of *Hyal3*$^{+/+}$ and *Hyal3*$^{-/-}$ mice could be used for this purpose. The more ideal source of enzyme would be to use Hyal1-deficient cells overexpressing Hyal3, since the activity of Hyal1 was increased when Hyal3 was over expressed in BHK cells (Hemming et al., 2008). The enzyme activity should be tested at different pHs by incubating Hyal3 samples with HA fragments at 37°C. The activity can be measured by a colorimetric assay using p-dimethylaminobenzaldehyde as a substrate. The absorbance of Hyal3 samples can be measured at 585 nm and compared with a substrate standard curve to estimate the enzyme activity. The difference between samples with and without Hyal3 would indicate the level of Hyal3 activity at that particular pH.

Despite the increased HA levels identified in *Hyal3*$^{-/-}$ lungs, the techniques we employed did not detect the sizes of HA that were accumulated. The size(s) of HA that accumulated in *Hyal3*$^{-/-}$ mice should be determined to assist in finding Hyal3's role in the proposed HA degradation pathway. There are different approaches to detect the sizes of HA present in tissue, serum or BAL fluid samples. A simple and sensitive agarose gel electrophoresis based method described previously (Lee and Cowman, 1994) could be used after total GAGs are isolated and purified from samples (Bracke et al., 2009, Bitter and Muir, 1962). A known amount of purified GAGs would be subjected to agarose gel electrophoresis along with HA molecular weight markers (Lee and Cowman, 1994) and stained. Alternatively, HA can be transferred to nylon membrane by electroblotting. HA on the membrane can then be detected using biotinylated-HABP (Sigma-Aldrich), followed by HRP conjugated Streptavidin, and finally the peroxidase activity can be produced by chemiluminescent detection using the Western Lighting ^{TM} Detection Kit

(Perkin-Elmer, Shelton, CT). The molecular weight of HA in unknown samples will be estimated by comparing with known HA molecular weight standards. Using this approach, the size of HA accumulated in *Hyal3*$^{-/-}$ lungs can be analyzed to determine if it is a probable substrate for Hyal3.

The intracellular HA accumulation in *Hyal3*$^{-/-}$ airway epithelial cells after OVA-challenge could also be due to HA cables deposited in the absence of Hyal3. However, the HA detection system used in studies described in chapter 4 did not identify accumulated HA as cables. HA cables should be detected in tissue sections and cell cultures using biotinylated HA-binding protein and subsequent fluorescent detection system (de la Motte., 2003; Selbi et al., 2006; Lauer et al., 2009). Tissue sections or cell cultures would be subjected to fluorescence histochemistry using biotinylated HA-binding protein, followed by fluorescein-tagged streptavidin for HA detection (Vector Laboratories, Burlingame, CA, USA), and finally analysis of samples by confocal microscopy (de la Motte., 2003; Selbi et al., 2006; Lauer et al., 2009).

In order to employ any method to detect HA quantitatively in tissue sections, one should eliminate the possibility that its detection is underestimated. HA exists in the ECM of tissues as bound and unbound forms. Most of the unbound HA is lost during normal tissue processing conditions as it is a water soluble molecule. This suggests that there is a possibility for underestimating HA detected by immunohistochemistry in studies described in chapter 4. Further studies are required to prevent the loss of HA during tissue processing and then estimating HA levels quantitatively. This can be achieved by using cetylpyridinium chloride (CPC), a cationic quaternary ammonium compound that acts as a precipitating agent, all throughout the tissue processing, followed by the method described previously (Nilsson et al., 1990). One percent CPC should be added during

tissue fixation, washing and dehydration steps, followed by HA detection using immunohistochemistry. This method should give the actual HA levels that are present in the tissue sections. Moreover, analyzing HA levels by FACE would also solve this problem as frozen tissue samples are used in this method.

In addition to the increased HA levels, increased inflammation was identified in *Hyal3*$^{-/-}$ lungs. However, to look at the HA homeostasis during inflammation our studies employed only an OVA-challenged inflammation model. Future studies should be conducted using other lung inflammation models in *Hyal3*$^{-/-}$ mice. For example, other possibilities for lung inflammation models include bleomycin- and ventilator-induced lung injuries, following protocols described previously (Teder et al., 2002; Bai et al., 2005). In addition, future studies should also focus on inflammation models of other tissues. A good example will be a colon inflammation model of *Hyal3*$^{-/-}$ mice as the ECM of colon is rich in HA and also the remodeling of ECM components occurs rapidly in the colon. Moreover, an established colitis model for HA analysis has already been used by other groups in the HA field. In mice, colon inflammation (colitis) could be established by providing 5% dextran sulfate sodium through their drinking water (Bandyopadhyay et al., 2008). Using additional inflammation models for these experiments could provide a strong indication of a role for Hyal3 in HA homeostasis during inflammation.

In preliminary studies of β-hexosaminidase-deficient mice, HA levels may have also been underestimated using the biotinylated HA-binding protein. Further studies should be performed to estimate the levels of HA in various CPC fixed tissues of β-hexosaminidase-deficient mice using biotinylated HA-binding protein. HA accumulation identified in any of the tissues should be confirmed by FACE. These experiments would

indicate whether we underestimated the levels of HA that had accumulated in β-hexosaminidase-deficient mice.

In our studies of *Hyal3*$^{-/-}$ or β-hexosaminidase-deficient mice, we observed very little or no HA accumulation, suggesting redundancies among the HA-degrading enzymes. Future studies should be performed to analyze which hyaluronidases and/ or exoglycosidases are altered in each enzyme deficiency. This can be studied by analyzing mRNA expression levels of hyaluronidases and exoglycosidases by real-time RT-PCR. Moreover, future studies should be conducted to evaluate the role of the HA-degrading enzymes in HA turnover by generating cell lines and/ or mice that are deficient in these enzymes in different combinations. Various combinations of these enzyme-deficient cell lines can be established *in vitro* using siRNA. Based on HA levels estimated in the cells that are deficient in multiple HA-degrading enzymes, hyaluronidases and/ or exoglycosidases may be found to play a major role in HA turnover.

Our OVA-challenged *Hyal3*$^{-/-}$ mice studies indicated a role for Hyal3 in inflammation. However, roles for other hyaluronidases in HA turnover during inflammation have not been examined except a study indicating Hyal2 generates pro-inflammatory HA fragments (de la Motte et al., 2009). Further studies are required to evaluate roles played by other hyaluronidases in HA turnover during inflammation. Inflammation models in *Hyal1*$^{-/-}$ or *Hyal2*$^{-/-}$ mice should be generated in lung or other tissues and the levels of HA and inflammation could be analyzed. From *Hyal1*$^{-/-}$ mice inflammation studies, we could expect the same phenotype exhibited by *Hyal3*$^{-/-}$ mice. This is because of the suggested intracellular role of Hyal1 in degrading pro-inflammatory HA fragments. In contrast, *Hyal2*$^{-/-}$ mice probably could exhibit decreased inflammation due to the absence of Hyal2-generated pro-inflammatory HA fragments. However, in any

of these models, we can not rule out the contribution of other hyaluronidases, exoglycosidases and/ or other physical mechanisms in the degradation of HA.

References

1. Adams JR, Sander G and Byers S. Expression of hyaluronan synthases and hyaluronidases in the MG63 osteoblast cell line. *Matrix Biol* 2006;25:40-6.

2. Adra CN, Boer PH, Mcburney MW. Cloning and expression of the mouse pgk-1 gene and the nucleotide sequence of its promoter. *Gene* 1987;60:65-74.

3. Akira S, Uematsu S and Takeuchi O. Pathogen recognition and innate immunity. *Cell* 2006;124:783-801.

4. Arming S, Strobl B, Wechselberger C and Kreil G. In vitro mutagenesis of PH-20 hyaluronidase from human sperm. *Eur J Biochem* 1997;247:810-14.

5. Atmuri V, Martin DC, Hemming R, Gutsol A, Byers S, Sahebjam S, Thliveris JA, Mort JS, Carmona E, Anderson JE, Dakshinamurti S and Triggs-Raine B. Hyaluronidase 3 (HYAL3) knockout mice do not display evidence of hyaluronan accumulation. *Matrix Biol* 2008;27:653-60.

6. Baba D, Kashiwabara S, Honda A, Yamagata K, Wu Q, Ikawa M, Okabe M and Baba T. Mouse sperm lacking cell surface hyaluronidase PH-20 can pass through the layer of cumulus cells and fertilize the egg. *J Biol Chem* 2002;277:30310-14.

7. Bai KJ, Spicer AP, Mascarenhas MM, Yu L, Ochoa CD, Garg HG and Quinn DA. The role of hyaluronan synthase 3 in ventilator-induced lung injury. *Am J Respir Crit Care Med* 2005a;172:92-8.

8. Bai TR and Knight DA. Structural changes in the airways in asthma: observations and consequences. Clin Sci 2005b;108:463-77.

9. Bals R and Hiemstra PS. Innate immunity in the lung: how epithelial cells fight against respiratory pathogens. *Eur Respir J* 2004;23:327-33.

10. Bandyopadhyay SK, de la Motte CA, Kessler SP, Hascall VC, Hill DR and Strong SA. Hyaluronan-mediated leukocyte adhesion and dextran sulfate sodium-induced colitis are attenuated in the absence of signal transducer and activator of transcription 1. *Am J Pathol*. 2008;173:1361-8.

11. Banerji S, Ni J, Wang SX, Clasper S, Su J, Tammi R, Jones M and Jackson DG. LYVE-1, new homolog of the CD44 glycoprotein, is a lymph-specific receptor for hyaluronan. *J Cell Biol* 1999;144:789-801.

12. Bastow ER, Byers S, Golub SB, Clarkin CE, Pitsillides AA and Fosang AJ. Hyaluronan synthesis and degradation in cartilage and bone. *Cell Mol Life Sci*. 2008;65:395-413.

13. Berend N, Salome CM and King GG. Mechanisms of airway hyperresponsiveness in asthma. *Respirology* 2008;13:624-31

14. Bergeron C, Al-Ramli W and Hamid Q. Remodeling in Asthma. *Proc Am Thorac Soc* 2009;6:301-5.

15. Bitter, T and Muir HM. A modified uronic acid carbazole reaction. *Anal Biochem*. 1962;4:330-4.

16. Birnboim HC. A rapid alkaline extraction method for the isolating of plasmid DNA. *Meth Enzymol* 1983;100:243-55.

17. Blumenkrantz N and Asboe-Hansen G. New method for quantitative determination of uronic acids. *Anal Biochem* 1973;54:484-9.

18. Bourguignon LY, Singleton PA, Diedrich F, Stern R and Gilaad E. CD44 interaction with Na+-H+ exchanger creates acidic microenvironments leading to hyaluronidase-2 and cathepsin B activation and breast tumor cell invasion. *J Biol Chem* 2004;279:26991-27007.

19. Bracke KR, Dentener MA, Papakonstantinou E, Vernooy JH, Demoor T, Pauwels NS, Cleutjens J, van Suylen R, Joos GF, Brusselle GG and Wouters EF. Enhanced deposition of low weight hyaluronan in lungs of cigarette smoke-exposed mice. *Am J Respir Cell Mol Biol*. (In press)

20. Bradford MM. A rapid and sensitive method for the quantitation of microgram quantities of protein utilizing the principle of protein-dye binding. *Anal Biochem* 1976;72:248-54.

21. Brzusek D and Petron D. Treating knee osteoarthritis with intra-articular hyaluronans. *Curr Med Res Opin* 2008;24:3307-22.

22. Calabro A, Midura R, Wang A, West L, Plaas A and Hascall VC. Fluorophore-assisted carbohydrate electrophoresis (FACE) of glycosaminoglycans. *Osteoarthritis Cartilage* 2001;9 SupplA:S16-S22.

23. Camenisch TD, Spicer AP, Brehm-Gibson T, Biesterfeldt J, Augustine ML, Calabro A Jr, Kubalak S, Klewer SE and McDonald JA. Disruption of hyaluronan synthase-2 abrogates normal cardiac morphogenesis and hyaluronan-mediated transformation of epithelium to mesenchyme. *J Clin Invest* 2000;106:349-60.

24. Cantor JO and Turino GM. Can exogenously administered hyaluronan improve respiratory function in patients with pulmonary emphysema? *Chest* 2004;125:288-92.

25. Cherr GN, Yudin AI and Overstreet JW. The dual functions of GPI-anchored PH-20: hyaluronidase and transcellular signaling. *Matrix Biol* 2001;20:515-25.

26. Chomczynski P and Sacchi N. Single-step method of RNA isolation by acid guanidinium thiocyanate-phenol-chloroform extraction. *Anal Biochem* 1987;162:156-9.

27. Chow G, Knudson CB and Knudson W. Expression and cellular localization of human hyaluronidase-2 in articular chondrocytes and cultured cell lines. *Osteoarthritis Cartilage* 2006;14:849-58.

28. Clarris BJ and Fraser JR. On the pericellular zone of some mammalian cells in vitro. *Exp Cell Res* 1968;49:181-93.

29. Csoka AB, Frost GI and Stern R. The six hyaluronidase-like genes in the human and mouse genomes. *Matrix Biol* 2001;20:499-508.

30. Csoka AB, Scherer SE and Stern R. Expression analysis of six paralogous human hyaluronidase genes clustered on chromosomes 3p21 and 7q31. *Genomics* 1999;60:356-61.

31. Culty M, Nguyen HA and Underhill CB. The hyaluronan receptor (CD44) participates in the uptake and degradation of hyaluronan. *J Cell Biol* 1992;116:1055-62.

32. Clarke LA, Russell CS, Pownall S, Warrington CL, Borowski A, Dimmick JE, Toone J and Jirik FR. Murine mucopolysaccharidosis type I: targeted disruption of the murine alpha-L-iduronidase gene. *Hum Mol Genet* 1997;6:503-511.

33. Day AJ and de la Motte CA. Hyaluronan cross-linking: a protective mechanism in inflammation? *Trends Immunol* 2005;26:637-43.

34. Day AJ and Prestwich GD. Hyaluronan-binding proteins: typing up the giant. *J Biol Chem* 2002;277:4585-8.

35. DeAngelis PL. Hyaluronan synthases: fascinating glycosyltransferases from vertebrates, bacterial pathogens, and algal viruses. *Cell Mol Life Sci* 1999;56:670-82.

36. Delmage JM, Powars DR, Jaynes PK and Allerton SE. The selective suppression of immunogenicity by hyaluronic acid. *Ann Clin Lab Sci* 1986;16:303-10.

37. de la Motte CA, Hascall VC, Drazba J, Bandyopadhyay SK and Strong SA. Mononuclear leukocytes preferentially bind via CD44 to hyaluronan on human intestinal mucosal smooth muscle cells after virus infection or treatment with poly(I.C). *J Biol Chem* 1999;274:30747-55.

38. de la Motte CA, Hascall VC, Drazba J, Bandyopadhyay SK and Strong SA. Mononuclear leucocytes bind to specific hyaluronan structures on colon mucosal smooth muscle cells treated with polyinosinic acid:polycytidylic acid: inter-alpha-trypsin inhibitor is crucial to structure and function. *Am J Pathol* 2003;163:121-33.

39. de la Motte C, Nigro J, Vasanji A, Rho H, Kessler S, Bandyopadhyay S, Danese S, Fiocchi C and Stern R. Platelet-derived hyaluronidase 2 cleaves hyaluronan into fragments that trigger monocyte-mediated production of proinflammatory cytokines. *Am J Pathol* 2009;174:2254-64.
40. Eggli PS and Graber W. Association of hyaluronan with rat vascular endothelial and smooth muscle cells. *J Histochem Cytochem* 1995;43:689-97.

41. Engström-Laurent A and Hellström S. The role of liver and kidneys in the removal of circulating hyaluronan. An experimental study in the rat. *Connect Tissue Res* 1990;24:219-24.

42. Eriksson S, Fraser JR, Laurent TC, Pertoft H and Smedsrød B. Endothelial cells are a site of uptake and degradation of hyaluronic acid in the liver. *Exp Cell Res* 1983;144:223-8.

43. Evanko SP, Angello JC and Wight TN. Formation of hyaluronan- and versican-rich pericellular matrix is required for proliferation and migration of vascular smooth muscle cells. *Arterioscler Thromb Vasc Biol* 1999a;19:1004-13.

44. Evanko SP, Parks WT and Wight TN. Intracellular hyaluronan in arterial smooth muscle cells: association with microtubules, Rhamm, and the mitotic spindle. *J Histochem Cytochem* 2004;52:1525-35.

45. Evanko SP and Wight TN. Intracellular localization of hyaluronan in proliferating cells. *J Histochem Cytochem* 1999b;47:1331-42.

46. Evans EA, Zhang H and Martin-Deleon PA. SPAM1 (PH-20) protein and mRNA expression in the epididymides of humans and macaques: utilizing laser microdissection/RT-PCR. *Reprod Biol Endocrinol* 2003;1:54.

47. Falkowski M, Schledzewski K, Hansen B and Goerdt S. Expression of stabilin-2, a novel fasciclin-like hyaluronan receptor protein, in murine sinusoidal endothelia, avascular tissues, and at solid/liquid interfaces. *Histochem Cell Biol* 2003;120:361-9.

48. Fraser JR, Alcorn D, Laurent TC, Robinson AD and Ryan GB. Uptake of circulating hyaluronic acid by the rat liver. Cellular localization in situ. *Cell Tissue Res.* 1985;242:505-10.

49. Fraser JR, Appelgren LE and Laurent TC. Tissue uptake of circulating hyaluronic acid. A whole body autoradiographic study. *Cell Tissue Res* 1983;233:285-93.

50. Fraser JRE, Laurent TC and Laurent UBG. Hyaluronan: its nature, distribution, functions and turnover. *J Intern Med* 1997;242:27-33.

51. Fraser JRE and Laurent TC. Turnover and metabolism of hyaluronan. *Ciba Found Symp* 1989;143:41-59.

52. Fraser JR, Laurent TC, Pertoft H and Baxter E. Plasma clearance, tissue distribution and metabolism of hyaluronic acid injected intravenously in the rabbit. *Biochem J* 1981;200:415-24.

53. Fraser JR, Kimpton WG, Laurent TC, Cahill RN and Vakakis N. Uptake and degradation of hyaluronan in lymphatic tissue. *Biochem J* 1988;256:153-8.

54. Gale NW, Gale NW, Prevo R, Espinosa J, Ferguson DJ, Dominguez MG, Yancopoulos GD, Thurston G and Jackson DG. Normal lymphatic development and function in mice deficient for the lymphatic hyaluronan receptor LYVE-1. *Mol Cell Biol* 2007;27:595-604.

55. Gao F, Koenitzer JR, Tobolewski JM, Jiang D, Liang J, Noble PW and Oury TD. Extracellular superoxide dismutase inhibits inflammation by preventing oxidative fragmentation of hyaluronan. *J Biol Chem* 2008;283:6058-66.

56. Garantziotis S, Li Z, Potts EN, Kimata K, Zhuo L, Morgan DL, Savani RC, Noble PW, Foster WM, Schwartz DA and Hollingsworth JW. Hyaluronan mediates ozone-induced airway hyperresponsiveness in mice. *J Biol Chem* 2009; 284:11309-17.

57. Garcia Ar, Pan J, Lamsa JC and Muenzer J. The characterization of a murine model of mucopolysaccharidosis II (Hunter syndrome). *J Inherit Metab Dis* 2007;30:924-34.

58. Gill SE, Pape MC and Leco KJ. Absence of tissue inhibitor of metalloproteinases 3 disrupts alveologenesis in the mouse. *Dev Growth Differ*. 2009;51:17-24.

59. Gordon JR, Li F, Nayyar A, Xiang J and Zhang X. CD8+, but Not CD8{alpha}-, Dendritic Cells Tolerize Th2 Responses via Contact-Dependent and Independent Mechanisms, and Reverse Airway Hyperresponsiveness, Th2, and Eosinophil Responses in a Mouse Model of Asthma. *J Immunol* 2005;175:1516-22.

60. Harada H and Takahashi M. CD44-dependent intracellular and extracellular catabolism of hyaluronic acid by hyaluronidase-1 and -2. *J Biol Chem* 2007;282:5597-5607.

61. Hardingham TE and Muir H. The specific interaction of hyaluronic acid with cartillage proteoglycans. *Biochim Biophys Acta* 1972;279:401-5.

62. Hardwick C, Hoare K, Owens R, Hohn HP, Hook M, Moore D, Cripps V, Austen L, Nance DM and Turley EA. Molecular cloning of a novel hyaluronan receptor that mediates tumor cell motility. *J Cell Biol* 1992;117:1343-50.

63. Harris EN, Kyosseva SV, Weigel JA and Weigel PH. Expression, processing and glycosaminoglycan binding activity of the recombinant human 315-kDa hyaluronic acid receptor for endocytosis (HARE). *J Biol Chem* 2007;282:2785-97.

64. Harris EN, Weigel JA and Weigel PH. The human hyaluronan receptor for endocytosis (HARE/Stabilin-2) is a systemic clearance receptor for heparin. *J Biol Chem* 2008a;283:17341-50.

65. Harris EN and Weigel PH. The ligand-binding profile of HARE: hyaluronan and chondroitin sulfates A, C, and D bind to overlapping sites distinct from the sites for heparin, acetylated low-density lipoprotein, dermatan sulfate, and CS-E. *Glycobiology* 2008b;18:638-48.

66. Hascall VC and Laurent TC. Hyaluronan: structure and physical properties. *Hyaluronan today, Glycoforum,* 1997. www.glycoforum.gr.jp.

67. Hascall VC, Majors AK, de la Motte CA, Evanko SP, Wang A, Drazba JA, Strong SA and Wight TN. Intracellular hyaluronan: a new frontier for inflammation? *Biochim Biophys Acta* 2004;1673:3-12.

68. Haskins ME. Animal models for mucopolysaccharidosis disorders and their clinical relevance. *Acta Paediatr Suppl* 2007;96:56-62.

69. Hemming R, Martin DC, Slominski E, Nagy JI, Halayko AJ, Pind S and Triggs-Raine B. Mouse Hyal3 encodes a 45-to-56-kDa glycoprotein whose overexpression increases hyaluronidase 1 activity in cultured cells. *Glycobiology* 2008;18:280-9.

70. Hepbildikler ST, Sandhoff R, Kolzer M, Proia RL and Sandhoff K. Physiological substrates for human lysosomal beta-hexosaminidase S. *J Biol Chem* 2002;277:2562-72.

71. Hoffman, DC and Duran-Reynals F. The mechanism of enhancement of infections by testicle extract. *Science* 1930;72:508.

72. Huang SS, Liu IH, Smith T, Shah MR, Johnson FE and Huang JS. Crsbp-1/Lyve-L-null mice exhibit identifiable morphological and functional alterations of lymphatic capillary vessels. *FEBS Lett* 2006;580:6259-68.

73. Hunnicutt GR, Mahan K, Lathrop WF, Ramarao CS, Myles DG and Primakoff P. Structural relationship of sperm soluble hyaluronidase to the sperm membrane protein Ph-20. *Biol Reprod* 1996;54:1343-9.

74. Irie K, Komori K, Seiki M, Tsuruga E, Sakakura Y, Kaku T and Yajima T. Impaired alveolization in mice deficient in membrane-type matrix metalloproteinase 1 (MT1-MMP). *Med Mol Morphol*. 2005;38:43-6.

75. Itano N and Kimata K. Mammalian hyaluronan synthases. *IUBMB Life* 2002;54:195-9.

76. Itano N, Sawai T, Yoshida M, Lenas P, Yamada Y, Imagawa M, Shinomura T, Hamaguchi M, Yoshida Y, Ohnuki Y, Miyauchi S, Spicer AP and McDonald JA and Kimata K. Three isoforms of mammalian hyaluronan synthases have distinct enzymatic properties. *J Biol Chem* 1999;274:25085-92.

77. Jadin L, Wu X, Ding H, Frost GI, Onclinx C, Triggs-Raine B and Flamion B. Skeletal and hematological anomalies in HYAL2-deficient mice: a second type of mucopolysaccharidosis IX?. *FASEB J* 2008;22:4316-26.

78. Jiang D, Liang J, Fan J, Yu S, Chen S, Luo Y, Prestwich GD, Mascarenhas MM, Garg HG, Quinn DA, Homer RJ, Goldstein DR, Bucala R, Lee PJ, Medzhitov R and Noble PW. Regulation of lung injury and repair by Toll-like receptors and hyaluronan. *Nat Med* 2005;11:1173-9.

79. Jiang D, Liang J, Li Y and Noble PW. The role of Toll-like receptors in non-infectious lung injury. *Cell Res* 2006;16:693-701.

80. Jiang D, Liang J and Noble PW. Hyaluronan in tissue injury and repair. *Annu Rev Cell Dev Biol* 2007;23:435-61.

81. Johnson LA, Prevo R, Clasper S and Jackson DG. Inflammation-induced uptake and degradation of the lymphatic endothelial hyaluronan receptor LYVE-1. J *Biol Chem* 2007;282:33671-80.

82. Jones MH, Davey PM, Aplin H and Affara NA. Expression analysis, genomic structure, and mapping to 7q31 of the human sperm adhesion molecule gene Spam1. *Genomics* 1995;29:796-800.

83. Jüni P, Reichenbach S, Trelle S, Tschannen B, Wandel S, Jordi B, Züllig M, Guetg R, Häuselmann HJ, Schwarz H, Theiler R, Ziswiler HR, Dieppe PA, Villiger PM and Egger M; Swiss Viscosupplementation Trial Group. Efficacy and safety of intracellular hylan or hyaluronic acids for osteoarthritis of the knee: a randomized controlled trial. *Arthritis Rheum* 2007;56:3610-19.

84. Junqueira LC and Carneiro J. Basic histology text and atlas. McGraw-Hill Medical publicshing divison, 2005;340-359.

85. Kaneiwa T, Mizumoto S, Sugahara K and Yamada S. Identification of human hyaluronidase-4 as a novel chondroitin sulfate hydrolase that preferentially cleaves the galactosaminidic linkage in the trisulfated tetrasaccharide sequence. *Glycobiology*. (In press)

86. Karousou EG, Porta G, De LG and Passi A. Analysis of fluorophore-labelled hyaluronan and chondroitin sulfate disaccharides in biological samples. *J Pharm Biomed Anal* 2004;34:791-5.

87. Kim E, Baba D, Kimura M, Yamashita M, Kashiwabara S and Baba T. Identification of a hyaluronidase, Hyal5, involved in penetration of mouse sperm through cumulus mass. *Proc Natl Acad Sci* 2005;102:18028-33.

88. Kimura M, Kim E, Kang W, Yamashita M, Saigo M, Yamazaki T, Nakanishi T, Kashiwabara S and Baba T. Functional roles of mouse sperm hyaluronidases, HYAL5 and SPAM1, in fertilization. *Biol Reprod* 2009;81:939-47

89. Klein U, Kresse H and Von Figura K. Sanfilippo syndrome type C: deficiency of acetyl-CoA:alpha-glucoaminide N-acetyltransferase in skin fibroblasts. *Proc Natl Acad Sci* 1978;75:5185-9.

90. Knudson CB and Knudson W. Hyaluronan binding proteins in development, tissue homeostasis, and disease. *FASEB J* 1993;7:1233-41.

91. Kohan M, Breuer R and Berkman N. Osteopontin induces airway remodeling and lung fibroblast activation in a murine model of asthma. *Am J Respir Cell Mol Biol*. (In press)

92. Kok K, Osinga J, Carritt B, Davis MB, van der Hout AH, van der Veen AY, Landsvater RM, de Leij LF, Berendsen HH, Postmus PE and et al. Deletion of a DNA sequence at the chromosomal region 3p21 in all major types of lung cancer. *Nature* 1987;330:578-81.

93. Laurent TC, Johnson-Wells G, Hellstrom S, Engstrom-Laurent A and Wells AF. Localization of hyaluronan in various muscular tissues. A morphological study in the rat. *Cell Tissue Res* 1991a;263:201-5.

94. Laurent TC and Fraser JR. The properties and turnover of hyaluronan. *Ciba Found Symp* 1986;124:9-29.

95. Laurent TC and Fraser JR. Hyaluronan. *FASEB J* 1992a;6:2397-2404.

96. Laurent TC, Laurent UB and Fraser JR. Functions of hyaluronan. *Ann Rheum Dis* 1995;54:429-32.

97. Laurent TC. Laurent UB and Fraser JR. The structure and function of hyaluronan: an overview. *Immunol Cell Biol* 1996;74:A1-A7.

98. Laurent UBG and Reed RK. Turnover of hyaluronan in the tissues. *Adv Drug Delivery Rev* 1991b;7:237-56.

99. Laurent UB, Dahl LB and Reed RK. Catabolism of hyaluronan in rabbit skin takes place locally, in lymph nodes and liver. *Exp Physiol* 1991c;76:695-703.

100. Laurent UB, Fraser JR, Engstrom-Laurent A, Reed RK, Dahl LB and Laurent TC. Catabolism of hyaluronan in knee joint of the rabbit. *Matrix* 1992b;12:130-36.

101. Leco KJ, Waterhouse P, Sanchez OH, Gowing KL, Poole AR, Wakeham A, Mak TW and Khokha R. Spontaneous air space enlargement in the lungs of mice lacking tissue inhibitor of metalloproteinase-2 (TIMP-3*)*. *J Clin Invest*. 2001;108:817-29. Erratum in: *J Clin Invest* 2001;108:1405. Comment in: *J Clin Invest*. 2001;108:799-800.

102. Lee HG and Cowman MK. An agarose gel electrophoretic method for analysis of hyaluronan molecular weight distribution. *Anal Biochem*.1994;219:278-87.

103. Lepperdinger G, Strobl B and Kreil G. *HYAL2*, a human gene expressed in many cells, encodes a lysosomal hyaluronidase with a novel type of specificity. *J Biol Chem* 1998;273:22466-70.

104. Li HH, Yu WH, Rozengurt N, Zhao HZ, Lyons KM, Anagnostaras S, Fanselow MS, Suzuki K, Vanier MT and Neufeld EF. Mouse model of Sanfilippo syndrome type B produced by targeted disruption of the gene encoding alpha-N-acetylglucosaminidase. *Proc Natl Acad Sci* 1999;96:14505-10.

105. Lin Y, Mahan K, Lathrop WF, Myles DG and Primakoff P. A hyaluronidase activity of the sperm plasma membrane protein Ph-20 enables sperm to penetrate the cumulus cell layer surrounding the egg. *J Cell Biol* 1994;125:1157-63.

106. Liu D, Zhang T, Marshall AJ, Okkenhaug K, Vanhaesebroeck B and Uzonna JE. The p110{delta} Isoform of phosphatidylinositol 3-kinase controls susceptibility to leishmania major by regulating expression and tissue homing of regulatory T cells. *J Immunol* 2009;183:1921-33.

107. Livak KJ and Schmittgen TD. Analysis of relative gene expression data using real-time quantitative PCR and the 2(-Delta Delta C(T)) method. *Methods* 2001;25:402-8.

108. Lokeshwar VB, Schroeder GL, Carey RI, Soloway MS and Iida N. Regulation of hyaluronidase activity by alternative mRNA splicing. *J Biol Chem* 2002;277:33654-63.

109. Longas MO and Meyer K. Sequential hydrolysis of hyaluronate by beta-glucuronidase and beta-hexosaminidase. *Biochem J* 1981;197:275-82.

110. Majors AK, Austin RC, de la Motte CA, Pyeritz RE, Hascall VC, Kessler SP, Sen G and Strong SA. Endoplasmic reticulum stress induces hyaluronan deposition and leucocyte adhesion. *J Biol Chem* 2003;278:47223-31.

111. Margolis RU and Margolis RK. Aggrecan-versican-neurocan family proteoglycans. *Methods Enzymol* 1994;245:105-26.

112. Martin DC, Atmuri V, Hemming RJ, Farley J, Mort JS, Byers S, Hombach-Klonisch S, Csoka AB, Stern R and Triggs-Raine BL. A mouse model of human

mucopolysaccharidosis IX exhibits osteoarthritis. *Hum Mol Genet* 2008;17:1904-15. Erratum in: *Hum Mol Genet*. 2008;17:2919. Csoka AB [added].

113. Mascarenhas MM, Day RM, Ochoa CD, Choi WI, Yu L, Ouyang B, Garg HG, Hales CA and Quinn DA. Low molecular weight hyaluronan from stretched lung enhances interleukin-8 expression. *Am J Respir cell Mol Biol* 2004;30:51-60.

114. Maxwell CA, Keats JJ, Crainie M, Sun X, Yen T, Shibuya E, Hendzel M, Chan G and Pilarski LM. Rhamm is a centrosomal protein that interacts with dynein and maintains spindle pole stability. *Mol Biol Cell* 2003;14:2262-76.

115. McBride WH and Bard JB. Hyaluronidase-sensitive halos around adherent cells. Their role in blocking lymphocyte-mediated cytolysis. *J Exp Med* 1979;149:507-15.

116. McDonald JA and Camenisch TD. Hyaluronan: genetics insights into the complex biology of a simple polysaccharide. *Glycoconj J* 2002;19:331-9.

117. McKee CM, Penno MB, Cowman M, Burdick MD, Strieter RM, Bao C and Noble PW. Hyaluronan (HA) fragments induce chemokine gene expression in alveolar macrophages. The role of HA size and CD44. *J Clin Invest* 1996;98:2403-13.

118. Meyer K and Palmer JW. The polysaccharide of vitreous humor. *J Biol Chem* 1934;107:629-634.

119. Mikles M and Stanton RP. A review of Morquio syndrome. *Am J Orthop* 1997;26:533-40.

120. Miller AD. Identification of Hyal2 as the cell-surface receptor for jaagsiekte sheep retrovirus and ovine nasal adenocarcinoma virus. *Curr Top Microbiol Immunol* 2003;275:179-99.

121. Miller KA, Shao MH and Martin-Deleon PA. Hyalp1 in murine sperm function: Evidence for unique and overlapping functions with other reproductive hyaluronidases. *J Androl* 2007;28:67-76.

122. Monzon ME, Manzanares D, Schmid N, Casalino-Matsuda SM and Forteza RM. Hyaluronidase expression and activity is regulated by pro-inflammatory cytokines in human airway epithelial cells. *Am J Respir Cell Mol Biol* 2008;39:289-95.

123. Moreland LW. Intra-articular hyaluronan (hyaluronic acid) and hylans for the treatment of osteoarthritis: mechanisms of action. *Arthritis Res Ther* 2003;5:54-67.

124. Mouta Carreira C, Nasser SM, di Tomaso E, Padera TP, Boucher Y, Tomarev SI and Jain RK. LYVE-1 is not restricted to the lymph vessels: expression in normal liver blood sinusoids and down-regulation in human liver cancer and cirrhosis. *Cancer Res* 2001;61:8079-84.

125. Mrabat H, Beagle J, Hang Z, Garg HG, Hales CA and Quinn DA. Inhibition of HA synthase 3 mRNA expression, with a phosphodiesterase 3 inhibitor, blocks lung injury in a septic ventilated rat model. *Lung* 2009;187:233-9.

126. Mullenbach R, Lagoda PJL and Welter C. An efficient salt-chloroform extraction of DNA from blood and tissues. *Trends Genet* 1989;5:391.

127. Myles DG and Primakoff P. Why did the sperm cross the cumulus? to get to the oocyte. Functions of the sperm surface proteins Ph-20 and fertilin in arriving at, and fusing with, the egg. *Biol Reprod* 1997;56:320-7.

128. Nagy A, Gertsenstein M, Vintersten K and Behringer R. Manipulating the mouse embryo: a laboratory manual. *Cold Spring Harbor, NY: Cold Spring Harbor Laboratory Press* 2003.

129. Nagy A, Rossant J, Nagy R, Abramow-Newerly W and Roder JC. Derivation of completely cell culture-derived mice from early-passage embryonic stem cells. *Proc Natl Acad Sci USA* 1993;90:8424-28.

130. Natowicz MR, Short MP, Wang Y, Dickersin GR, Gebhardt MC, Rosenthal DI, Sims KB and Rosenberg AE. Clinical and biochemical manifestations of hyaluronidase deficiency. *New Engl J Med* 1996;335:1029-33.

131. Neufeld ES and Muenzer J. The mucopolysaccharidoses. In: *Online Metabolic and Molecular Bases of Inherited Disease* (Scriver, C.R. et al., eds), 2001;3421-52 (chapter 136, McGraw-Hill, New York).

132. Nilsson K, Henriksson R, Hellström S, Tengblad A and Bjermer L. Hyaluronan reflects the pre-fibrotic inflammation in irradiated rat lung: concomitant analysis of parenchymal tissues and bronchoalveolar lavage. *Int J Radiat Biol*. 1990;58:519-30.

133. Noble PW and Jiang D. Matrix regulation of lung injury, inflammation, and repair: the role of innate immunity. *Proc Am Thorac Soc* 2006;3:401-4.

134. Orimoto AM, Dumaresq-Doiron K, Jiang J, Tanphaichitr N, Tsang BK and Carmona E. Mammalian hyaluronidase induces ovarian granulosa cell apoptosis and is involved in follicular atresia. *Endocrinology* 2008;149:5835-47.

135. Paiva P, Van Damme MP, Tellbach M, Jones RL, Jobling T and Salamonsen LA. Expression patterns of hyaluronan, hyaluronan synthases and hyaluronidases indicate a role for hyaluronan in the progression of endometrial cancer. *Gynecol Oncol* 2005;98:193-202.

136. Pascual RM and Peters SP. Airway remodeling contributes to the progressive loss of lung function in asthma: An overview. *J Allergy Clin Immunol* 2005;116:477-86.

137. Petrigni G and Allegra L. Aerosolised hyaluronic acid prevents exercise-induced bronchoconstriction, suggesting novel hypotheses on the correction of matrix defects in asthma. *Pulm Pharmacol Ther* 2006;19:166-71.

138. Phaneuf D, Wakamatsu N, Huang JQ, Borowski A, Peterson AC, Fortunato SR, Ritter G, Igdoura SA, Morales CR, Benoit G, Akerman BR, Leclerc D, Hanai N, Marth JD, Trasler JM and Gravel RA. Dramatically different phenotypes in mouse models of human Tay-Sachs and Sandhoff diseases. *Hum Mol Genet* 1996;5:1-14.

139. Plaas AH, West L, Midura RJ and Hascall VC. Disaccharide composition of hyaluronan and chondroitin/dermatan sulfate. Analysis with fluorophore-assisted carbohydrate electrophoresis. *Methods Mol Biol* 2001;171:117-28.

140. Postma DS and Timens W. Remodeling in Asthma and Chronic Obstructive Pulmonary Disease. *Proc Am Thorac Soc* 2006;3:434-9.

141. Prehm P. Hyaluronate is synthesized at plasma membranes. *Biochem J* 1984;220:597-600.

142. Prevo R, Banerji S, Ferguson DJ, Clasper S and Jackson DG. Mouse LYVE-1 is an endocytic receptor for hyaluronan in lymphatic endothelium. *J Biol Chem* 2001;276:19420-30.

143. Rai SK, Duh FM, Vigdorovich V, Danilkovitch-Miagkova A, Lerman MI and Miller AD. Candidate tumor suppressor HYAL2 is a sheep retrovirus, the envelope protein of which mediates oncogenic transformation. *Proc Natl Acad Sci* 2001;98:4443-8.

144. Rapport MM, Weissmann B, Linker A and Meyer K. Isolation of a crystalline disaccharide, hyalbiuronic acid, from hyaluronic acid. *Nature* 1951;168:996-7.

145. Ravinc DJ, Konerding MA, Pratt JP, Wolloscheck T, Huss HT and Mentzer SJ. The murine bronchopulmonary microcirculation in hapten-induced inflammation. *J Thorac Cardiovasc Surg* 2007;133:97-103.

146. Recklies AD, White C, Melching L and Roughley PJ. Differential regulation and expression of hyaluronan synthases in human articular chondrocytes, synovial cells and osteosarcoma cells. *Biochem J* 2001;354:17-24.

147. Reed RK, Lilja K and Laurent TC. Hyaluronan in the rat with special reference to the skin. *Acta Physiol Scand* 1989;134:405-11.

148. Reitinger S, Laschober GT, Fehrer C, Greiderer B and Lepperdinger G. Mouse testicular hyaluronidase-like protein SPAM1 and HYAL5 but not HYALP1 degrade hyaluronan. *Biochem J* 2007;401:79-85.

149. Ren J, Hascall VC and Wang A. Cyclin D3 mediates synthesis of a hyaluronan matrix that is adhesive for monocytes in mesangial cells stimulated to divide in hyperglycemic medium. *J Biol Chem* 2009;284:16621-32

150. Roden L, Campbell P, Fraser JRE, Laurent TC, Pertoft H and Thompson JN. Enzymatic pathways of hyaluronan catabolism. *Ciba Found Symp* 1989;143:60-86.

151. Russell C, Hendson G, Jevon G, Matlock T, Yu J, Aklujkar M, Ng KY and Clarke LA. Murine MPS I: insights into the pathogenesis of Hurler syndrome. *Clin Genet* 1998;53:349-61.

152. Sango K, McDonald MP, Crawley JN, Mack ML, Tifft CJ, Skop E, Starr CM, Hoffmann A, Sandhoff K, Suzuki and Proia RL. Mice lacking both subunits of lysosomal beta-hexosaminidase display gangliosidosis and mucopolysaccharidosis. *Nat Genet* 1996;14:348-52.

153. Sango K, Yamanaka S, Hoffmann A, Okuda Y, Grinberg A, Westphal H, McDonald MP, Crawley JN, Sandhoff K, Suzuki K and Proia RL. Mouse models of Tay-Sachs and Sandhoff diseases differ in neurologic phenotype and gangliosides metabolism. *Nat Genet* 1995;11:170-6.

154. Scheibner KA, Lutz MA, Boodoo S, Fenton MJ, Powell JD and Horton MR. Hyaluronan fragments act as an endogenous danger signal by engaging TLR2. *J Immunol* 2006;177:1272-81.

155. Schmits R, Filmus J, Gerwin N, Senaldi G, Kiefer F, Kundig T, Wakeham A, Shahinian A, Catzavelos C, Rak J, Furlonger C, Zakarian A, Simard JJ, Ohashi PS, Paige CJ, Gutierrez-Ramos JC and Mak TW. CD44 regulates hematopoietic progenitor distribution, granuloma formation, and tumorigenicity. *Blood* 1997;90:2217-33.

156. Selbi W, Day AJ, Rugg MS, Fülöp C, de la Motte CA, Bowen T, Hascall VC and Phillips AO. Overexpression of hyaluronan synthase 2 alters hyaluronan distribution and function in proximal tubular epithelial cells. *J Am Soc Nephrol.* 2006;17:1553-67.

157. Shapira E, Blitzer MG, Miller JB and Africk DK. Biochemical genetics:a laboratory manual. 1989; *Oxford University Press, Oxford, NY*.

158. Sheth J, Patel P, Sheth F and Shah R. Lysosomal storage disorders. *Indian Paediatr* 2004;41:260-5.

159. Shuttleworth TL, Wilson MD, Wicklow BA, Wilkins JA and Triggs-Raine BL. Characterization of the murine hyaluronidase gene region reveals complex organization and cotranscription of Hyal1 with downstream genes, Fus2 and Hyal3. *J Biol Chem* 2002;277:23008-18.

160. Simoes DC, Xanthou G, Petrochilou K, Panoutsakopoulou V, Roussos C and Gratziou C. Osteopontin deficiency protects against airway remodeling and hyperresponsiveness in chronic asthma. *Am J Respir Crit Care Med* 2009;179:894-902.

161. Sly WS, Brot FE, Glaser J, Stahl PD, Quinton BA, Rimoin DL and McAlister WH. Beta-glucuronidase deficiency mucopolysaccharidosis. *Birth Defects Orig Artic Ser* 1974;10:239-45.

162. Smedsrod B, Pertoft H, Eriksson S, Fraser JR and Laurent TC. Studies in vitro on the uptake and degradation of sodium hyaluronate in rat liver endothelial cells. *Biochem J* 1984;223:617-26.

163. Soltes L, Mendichi R, Kogan G, Schiller J, Stankovska M and Arnhold J. Degradative action of reactive oxygen species on hyaluronan. *Biomacromolecules* 2006;7:659-68.

164. Spicer AP, Augustine ML and McDonald JA. Molecular cloning and characterization of a putative mouse hyaluronan synthase. *J Biol Chem* 1996;271:23400-6.

165. Spicer AP, Seldin MF, Olsen AS, Brown N, Wells DE, Doggett NA, Itano N, Kimata K, Inazawa J and McDonald JA. Chromosomal localization of the human and mouse hyaluronan synthase genes. *Genomics* 1997;41:493-7.

166. Stern R. Devising a pathway for hyaluronan catabolism: are we there yet? *Glycobiology* 2003;13:105R-115R.

167. Stern R. Hyaluronan catabolism: a new metabolic pathway. *Eur J Cell Biol* 2004;83:317-25.

168. Stern R and Csoka AB. Mammalian hyaluronidases. *Hyaluronan today, Glycoforum*, 2000. www.glycoforum.gr.jp.

169. Stern R, Asari AA and Sugahara KN. Hyaluronan fragments: An information-rich system. *Euro J Cell Biol* 2006a;85:699-715.

170. Stern R and Jedrzejas MJ. Hyaluronidases: their genomics, structures, and mechanisms of action. *Chem Rev* 2006b;106:818-39.

171. Stern R, Kogan G, Jedrzejas MJ and Soltes L. The many ways to cleave hyaluronan. *Biotechnol Adv* 2007;25:537-57.

172. Sugiyama Y, Shimada A, Sayo T, Sakai S and Inoue S. Putative hyaluronan synthase mRNA are expressed in mouse skin and TGF- beta upregulates their expression in cultured human skin cells [published erratum appears in *J Invest Dermatol* 1998;110:991]. *J Invest Dermatol* 1998;110:116-21.

173. Suzuki K, Sango K, Prio RL and Langaman C. Mice deficient in all forms of lysosomal beta-hexosaminidase show mucopolysaccharidosis-like pathology. *J Neuropathol Exp Neurol* 1997;56:693-703.

174. Tammi R, Rilla K, Pienimaki JP, MacCallum DK, Hogg M, Luukkonen M, Hascall VC and Tammi M. Hyaluronan enters keratinocytes by a novel endocytic route of catabolism. *J Biol Chem* 2001;276:35111-22.

175. Teder P, Vandivier RW, Jiang D, Liang J, Cohn L, Puré E, Henson PM and Noble PW. Resolution of lung inflammation by CD44. *Science* 2002;296:155-8.

176. Thaler CD and Cardullo RA. Biochemical characterization of a glycosylphosphatidylinositol-linked hyaluronidase on mouse sperm. *Biochem* 1995;34:7788-95.

177. Tien JY and Spicer AP. Three vertebrate hyaluronan synthases are expressed during mouse development in distinct spatial and temporal patterns. *Dev Dyn* 2005;233:30-41.

178. Tomatsu S, Orii KO, Vogler C, Nakayama J, Levy B, Grubb JH, Gutierrez MA, Shim S, Yamaguchi S, Nishioka T, Montano AM, Noguchi A, Orii T, Kondo N and Sly WS. Mouse model of N-acetylgalactosamine-6-sulfate sulfatase deficiency (Galns-/-) produced by targeted disruption of the gene defective in Morquio A disease. *Hum Mol Genet* 2003;12:3349-58.

179. Toole BP. Hyaluronan and its binding proteins, the hyaladherins. *Curr Opi Cell Biol*. 1990;2:839-44.

180. Triggs-Raine B, Salo T, Zhang H, Wicklow BA and Natowicz M. Mutations in *HYAL1*, a member of a tandemly distributed multigene family encoding disparate hyaluronidase activities, cause a newly described lysosomal disorder, mucopolysaccharidosis IX. *Proc Natl Acad Sci* 1999;96:6296-300.

181. Turino GM and Cantor JO. Hyaluronan in respiratory injury and repair. *Am J Respir Crit Care Med* 2003;167:1169-75.

182. Uchiyama H, Dobashi Y, Ohkouchi K and Nagasawa K. Chemical change involved in the oxidative reductive depolymerization of hyaluronic acid. *J Biol Chem* 1990;265:7753-9.

183. Vandevoort CA, Cherr GN and Overstreet JW. Hyaluronic acid enhances the zona pellucida-induced acrosome reaction of Macaque sperm. *J Androl* 1997;18:1-5.

184. Varki A, Cummings R, Esko J, Freeze H, Hart G and Marth J. *Essentials of glycobiology* 1999 Cold Spring Harbor Laboratory Press. ISBN 0-87969-560-9.

185. Vogler C, Birkenmeier EH, Sly WS, Levy B, Pegors C, Kyle JW and Beamer WG. A murine model of mucopolysaccharidosis VII. Gross and microscopic findings in beta-glucuronidase-deficient mice. *Am J Pathol* 1990;136:207-217.

186. Volpi N, Schiller J, Stern R and Soltés L. Role, metabolism, chemical modifications and applications of hyaluronan. *Curr Med Chem* 2009;16:1718-45.

187. Wang A and Hascall VC. Hyaluronan structures synthesized by rat mesangial cells in response to hyperglycemia induce monocyte adhesion. *J Biol Chem* 2004;279:10279-85.

188. Weissmann B and Meyer K. The structure of hyalobiuronic acid of hyaluronic acid from umbilical Cord. *J Am Chem Soc* 1954;76:1753-7.

189. Weigel JA, Raymond RC, McGary C, Singh A and Weigel PH. A blocking antibody to the hyaluronan receptor for endocytosis (HARE) inhibits hyaluronan clearance by perfused liver. *J Biol Chem* 2003;278:9808-12.

190. Wraith JE. Lysosomal disorders. *Semi Neonatol* 2002;7:75-83.

191. Yamauchi K. Airway remodeling in asthma and its influence on clinical pathophysiology. *Tohoku J Exp Med* 2006;209:75-87.

192. Yannariello-Brown J, Zhou B and Weigel PH. Identification of a 175 Kda protein as the ligand-binding subunit of the rat liver sinusoidal endothelial cell hyaluronan receptor. *Glycobiology* 1997;7:15-21.

193. Zaas AK and Schwartz DA. Innate immunity and the lung: defense at the interface between host and environment. *Trends Cardiovasc Med* 2005;15:195-202.

194. Zaman A, Cui Z, Foley JP, Zhao H, Grimm PC, Delisser HM and Savani RC. Expression and role of the hyaluronan receptor RHAMM in inflammation after bleomycin injury. *Am J Respir Cell Mol Biol* 2005;33:447-54.

195. Zegerman P, Bannister AJ and Kouzarides T. The putative tumour suppressor Fus-2 is an N-acetyltransferase. *Oncogene* 2000;19:161-3.

196. Zhang H and Martin-Deleon PA. Mouse Spam1 (PH-20) is a multifunctional protein: evidence for its expression in the female reproductive tract. *Biol Reprod* 2003;69:446-54.

197. Zhang H, Morales CR, Badran H, El Alfy M and Martin-Deleon PA. Spam1 (PH-20) expression in the extratesticular duct and accessory organs of the mouse: a possible role in sperm fluid reabsorption. *Biol Reprod* 2004;71:1101-7.

198. Zhou B, Weigel JA, Fauss L and Weigel PH. Identification of the hyaluronan receptor for endocytosis (HARE). *J Biol Chem* 2000;275:37733-41.

199. Zhou R, Wu X and Skalli O. The hyaluronan receptor Rhamm/Ihabp in astrocytoma cells: expression of a tumor-specific variant and association with microtubules. *J Neurooncol* 2002;59:15-26.

Appendix 1

Analysis of acute airway inflammation model

The repeated OVA-challenges used for the chronic inflammation model (addressed as OVA-challenged mice in chapter 4) resulted in an increase in airway inflammation and airway resistance in *Hyal3*$^{-/-}$ mice. In order to assess if the increased inflammation in *Hyal3*$^{-/-}$ mice also results with only a few OVA-challenges, an acute airway inflammation model was generated. In the acute model, we analyzed all the parameters that we analyzed in the chronic model. This was not included in chapter 4 because all the results were not significant, nor consistent. This inconsistency was due to the differences between *Hyal3*$^{+/+}$ and *Hyal3*$^{-/-}$ in their time of euthanasia after the last intranasal challenge with OVA.

1.1 HA quantification in the airways of Hyal3$^{-/-}$ *mice with acute inflammation*

We studied HA levels in the lung tissues of *Hyal3*$^{+/+}$ and *Hyal3*$^{-/-}$ mice with acute inflammation by immunohistochemistry and FACE. HA immunohistochemistry was performed on lung sections of *Hyal3*$^{+/+}$ and *Hyal3*$^{-/-}$ mice using biotinylated HA-binding protein (Figure 47A), and HA detected in the ECM of airways was analyzed semi-quantitatively in these lung sections (Figure 47B). These mice did not show a significant difference. Interestingly, in this acute model a few epithelial cells of airways *Hyal3*$^{-/-}$ mice had intracellular HA which was completely absent in the *Hyal3*$^{+/+}$ mice; hyaluronidase-treated sections confirmed that the staining was specific (Figure 46A). Moreover, total HA present in lungs was quantified by FACE, and showed a significant increase in *Hyal3*$^{-/-}$ mice compared to *Hyal3*$^{+/+}$ mice (Figure 47C).

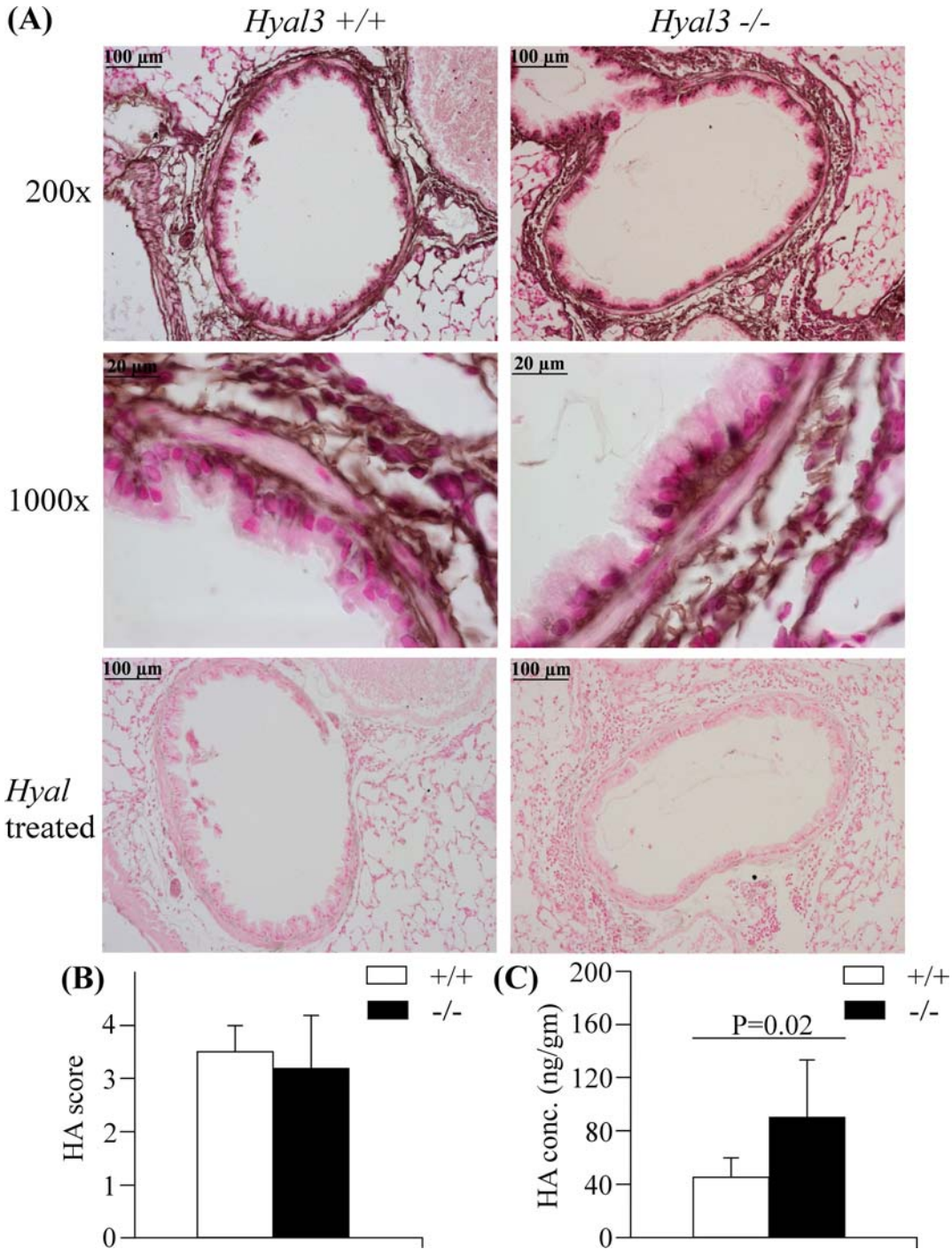

Figure 47: Semi-quantitative analysis of HA in the lung sections of *Hyal3*$^{+/+}$ and *Hyal3*$^{-/-}$ mice with acute inflammation by immunohistochemistry and FACE.

(A) *Hyal3*$^{-/-}$ mice displayed an increase in HA staining in the peri-bronchial and intra-epithelial regions of airways of lungs compared to *Hyal3*$^{+/+}$ mice. *Hyal*-treated sections are a negative control. **(B)** A semi-quantified representation of peri-bronchial HA in lung sections (n=4) and **(C)** the total HA in lung tissues measured by FACE (n=8). Data represent the mean ± SD. "n" represents the number of animals in each group.

1.2 Increased airway inflammation in Hyal3$^{-/-}$ mice with acute inflammation

To determine if *Hyal3* deficiency also increases airway inflammation in an acute inflammation model, we analyzed the number and type of inflammatory cells in the BAL fluid and lung tissue of *Hyal3*$^{+/+}$ and *Hyal3*$^{-/-}$ mice. No difference in total cell count was observed between *Hyal3*$^{+/+}$ and *Hyal3*$^{-/-}$ mice with acute inflammation (Figure 48A, n=4, P>0.05). However, a significant increase was observed in the number of eosinophils in the BAL fluid of *Hyal3*$^{-/-}$ mice with acute inflammation compared to similarly treated *Hyal3*$^{+/+}$ mice (Figure 48B, n=4, P=0.03).

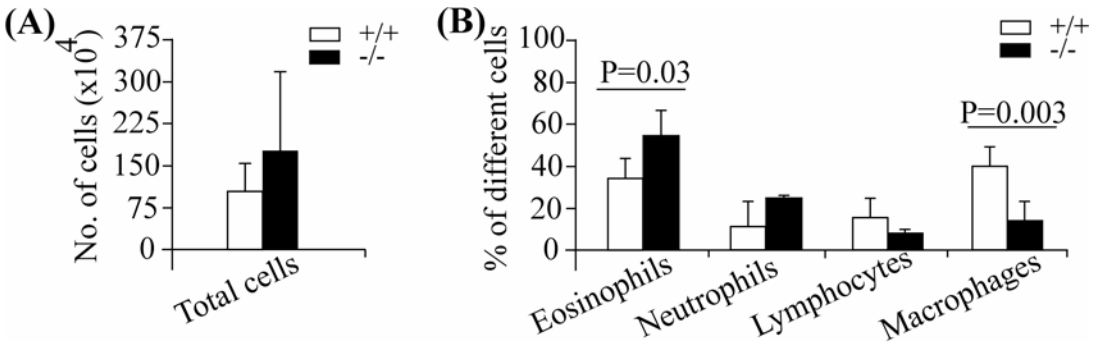

Figure 48: Total and differential cell counts in the BAL fluid of *Hyal3*$^{+/+}$ and *Hyal3*$^{-/-}$ mice with acute inflammation.

BAL fluid of *Hyal3*$^{-/-}$ mice compared to *Hyal3*$^{+/+}$ mice showed (A) a trend towards increased total cell count and (B) significantly increased eosinophils. Data represent the mean ± SD (n=4).

As an index of inflammation, infiltrating inflammatory cells in H & E-stained lung sections of *Hyal3*$^{+/+}$ and *Hyal3*$^{-/-}$ mice with acute inflammation were analyzed. Compared to *Hyal3*$^{+/+}$ lungs, *Hyal3*$^{-/-}$ lung sections displayed a mild increase in the number of infiltrating inflammatory cells in peri-bronchial, peri-vascular and parenchymal regions (Figure 49).

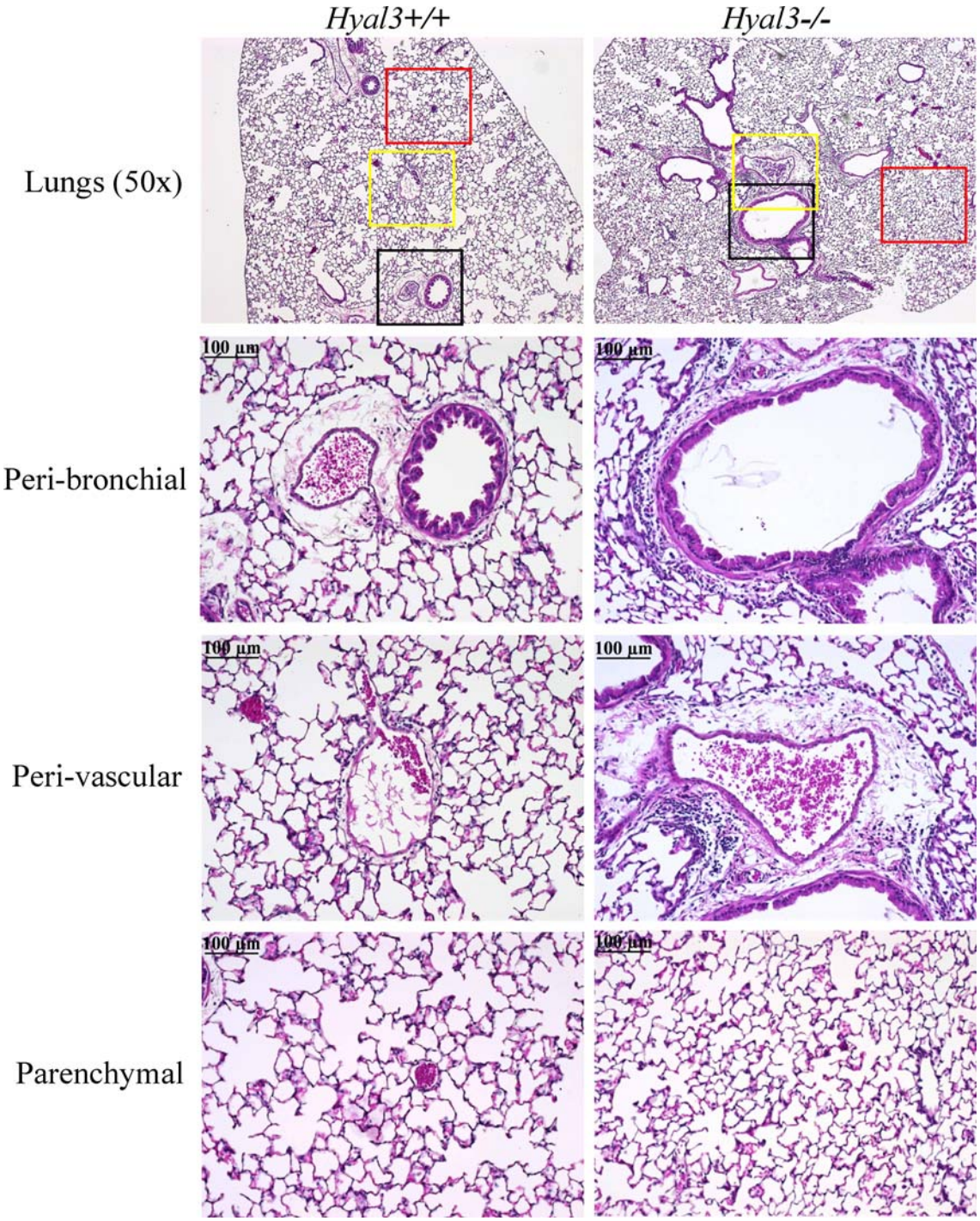

Figure 49: H & E-stained lung sections of *Hyal3*$^{+/+}$ and *Hyal3*$^{-/-}$ mice with acute inflammation.

A mild increase in infiltrated cells in the peri-bronchial, peri-vascular and parenchymal regions of *Hyal3*$^{-/-}$ lung sections compared to *Hyal3*$^{+/+}$ lungs highlighted as black, yellow and red squares respectively in whole lung section under 50x final magnification. One representative field of lung tissue was shown (n=4).

To assess the effect of *Hyal3*-deficiency on goblet cell number, *Hyal3*$^{+/+}$ and *Hyal3*$^{-/-}$ mice lung sections stained with PAS were analyzed (Kohan et al., 2009) (Figure 50A). The semi-quantitative scoring system used to compare goblet cell numbers in *Hyal3*$^{+/+}$ and *Hyal3*$^{-/-}$ lungs showed a trend towards an increase in *Hyal3*$^{-/-}$ airways compared to *Hyal3*$^{+/+}$ airways (Figure 50B), but it was not statistically significant.

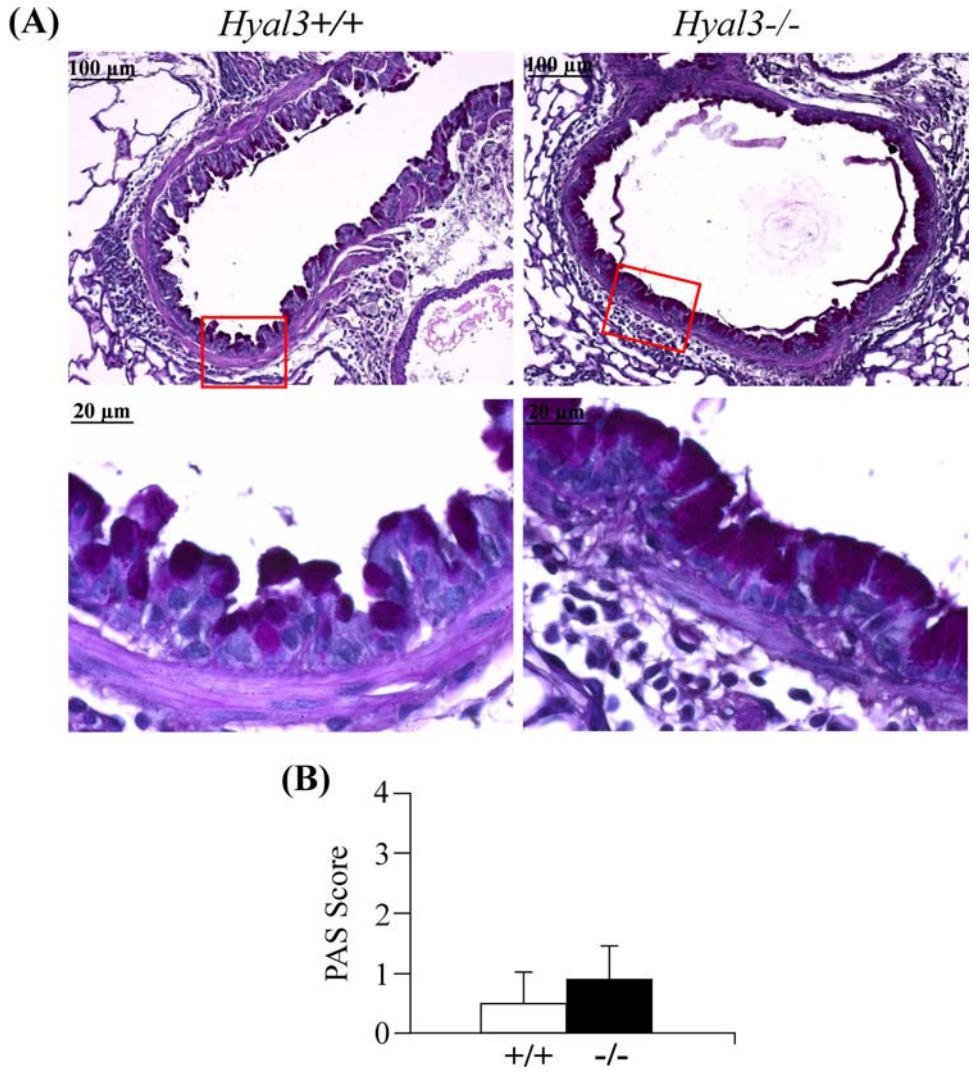

Figure 50: PAS stained lung sections of *Hyal3*$^{+/+}$ and *Hyal3*$^{-/-}$ mice with acute inflammation.

(A) *Hyal3*$^{-/-}$ airways showing slight goblet cell hyperplasia compared to *Hyal3*$^{+/+}$ airways. Red coloured boxes represent the region shown under higher magnification. **(B)** A semi-quantified representation of the goblet cell number in *Hyal3*$^{+/+}$ and *Hyal3*$^{-/-}$ mice. Data represent the mean ± SD (n=4).

1.3 Analysis of serum OVA-specific Ig levels in Hyal3$^{-/-}$ mice with acute inflammation.

OVA-specific Ig levels (IgE, IgG1 and IgG2a) in the serum of *Hyal3*$^{+/+}$ and *Hyal3*$^{-/-}$ mice with acute inflammation were analyzed, and a significant increase in the OVA-IgE levels were observed in *Hyal3*$^{-/-}$ mice compared to *Hyal3*$^{+/+}$ mice (Figure 51A). The ratio of IgG1/IgG2a levels was also increased in *Hyal3*$^{-/-}$ mice compared to *Hyal3*$^{+/+}$ controls suggesting a Th2 specific response (Figure 51B).

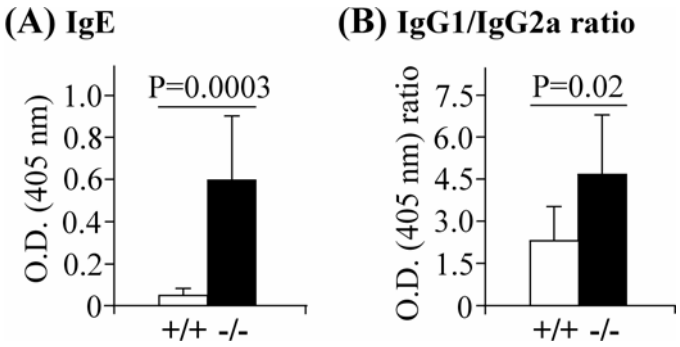

Figure 51: Ig levels in the serum of *Hyal3*$^{+/+}$ and *Hyal3*$^{-/-}$ mice with acute inflammation.

A significant increase in OVA-specific IgE and the ratio of IgG1/IgG2a were observed in *Hyal3*$^{-/-}$ serum. Data represent the mean ± SD (n=8).

1.4 Analysis of BAL fluid cytokine levels in Hyal3$^{-/-}$ mice with acute inflammation

Cytokine levels (IL-9, IL-4, eotaxin-1 and IFN-γ) in the BAL fluid of *Hyal3*$^{+/+}$ and *Hyal3*$^{-/-}$ mice with acute inflammation were analyzed, and a significant increase in IL-9 as well as a trend toward increased IL-4 levels was observed in *Hyal3*$^{-/-}$ mice with acute inflammation compared to similarly treated *Hyal3*$^{+/+}$ mice (Figure 52).

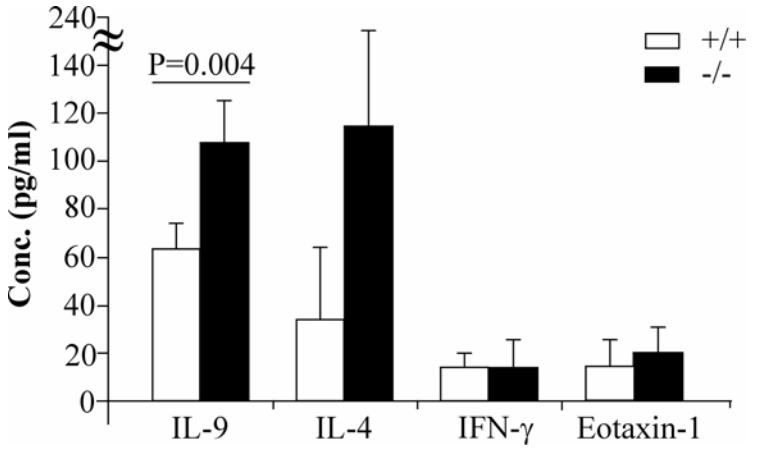

Figure 52: Cytokine levels in the BAL fluid of *Hyal3*$^{+/+}$ and *Hyal3*$^{-/-}$ mice with acute inflammation.

A significant increase in IL-9 and a trend toward increased IL-4 and Eotaxin-1 levels were observed in *Hyal3*$^{-/-}$ BAL fluid. Data represent the mean ± SD (n=4).

1.5 Analysis of collagen thickness in Hyal3$^{-/-}$ *mice with acute inflammation*

To elucidate the effect of *Hyal3*-deficiency on collagen deposition in the acute inflammation model, we compared PSR-stained lung sections of *Hyal3*$^{+/+}$ and *Hyal3*$^{-/-}$ mice with acute inflammation (Simoes et al., 2009). Polarized images and semi-quantitative data derived from the PSR-stained airways of *Hyal3*$^{+/+}$ and *Hyal3*$^{-/-}$ mice with acute allergic inflammation indicated that there was no difference in the collagen thickness (Figure 53A and B).

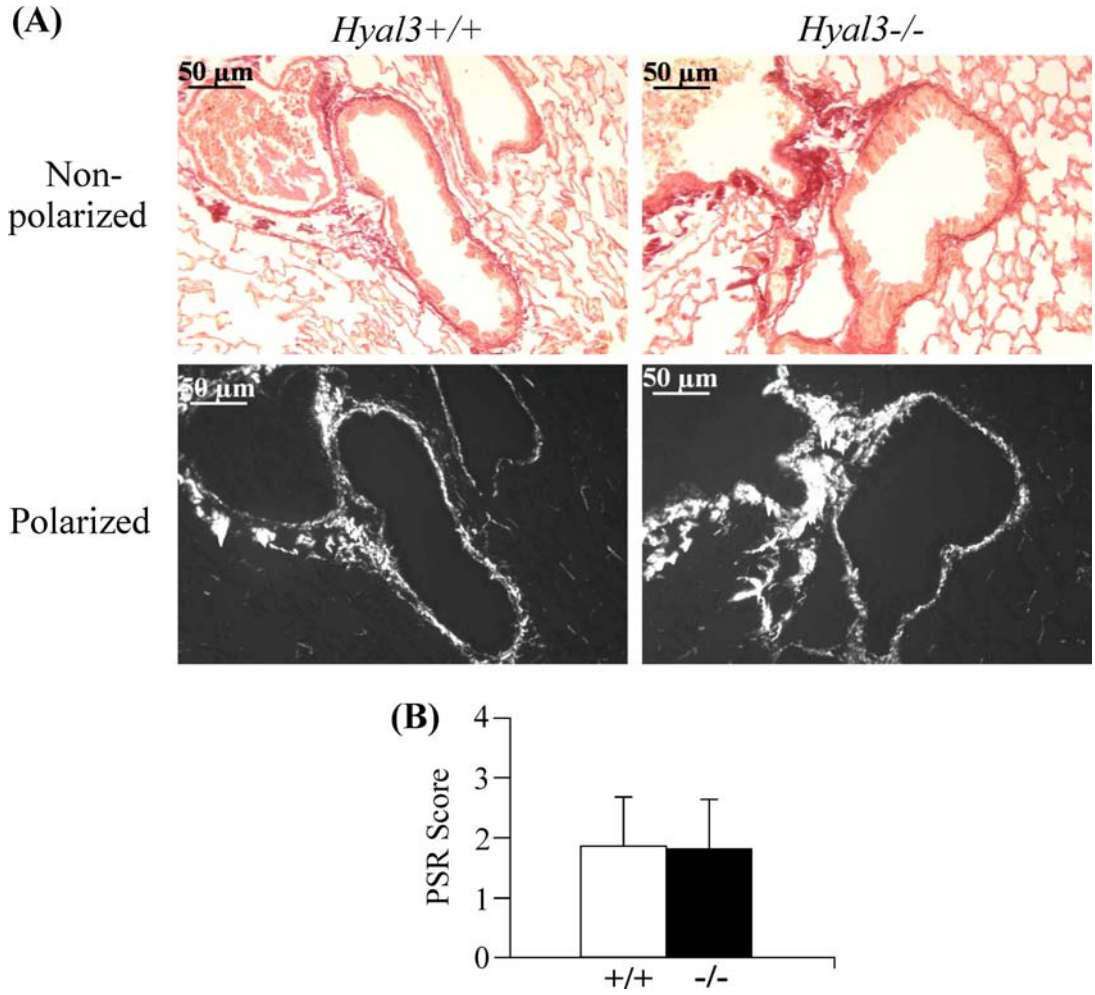

Figure 53: PSR-stained lung sections of *Hyal3*$^{+/+}$ and *Hyal3*$^{-/-}$ mice with acute inflammation.

(A) Non-polarized and polarized images of *Hyal3*$^{+/+}$ and *Hyal3*$^{-/-}$ mice airways. No difference was observed in the collagen thickness of *Hyal3*$^{+/+}$ and *Hyal3*$^{-/-}$ airways. (B) A semi-quantified representation of collagen thickness in *Hyal3*$^{+/+}$ and *Hyal3*$^{-/-}$ airways. Data represent the mean ± SD (n=4).

1.6 Airway resistance in Hyal3$^{-/-}$ *mice with acute inflammation*

The effect of *Hyal3*-deficiency on the development of airway hyper-responsiveness in acute inflammation was assessed by measuring airway resistance of *Hyal3*$^{+/+}$ and *Hyal3*$^{-/-}$ mice in response to increasing doses of methacholine (0, 6, 12.5 and 25 mg/ml). No significant difference was observed between the airway resistance of

Hyal3$^{+/+}$ and *Hyal3*$^{-/-}$ mice with acute inflammation (Figure 54). This indicates that in the acute model, the overall lung function was still normal, despite the mild increase in inflammation.

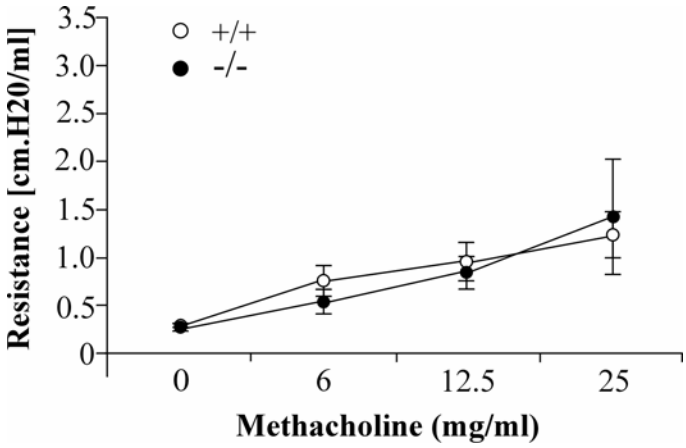

Figure 54: Airway resistance of *Hyal3*$^{+/+}$ and *Hyal3*$^{-/-}$ mice with acute inflammation.
No significant difference was observed in airway resistance of *Hyal3*$^{+/+}$ and *Hyal3*$^{-/-}$ mice. Data represent the mean ± SD (n=8).